eman ta zabal zazu

Universidad del País Vasco

Euskal Herriko Unibertsitatea

DEVELOPING FERRITE BASED NANOCOMPOUNDS FOR BIOMEDICAL APPLICATIONS

Memoria para optar al Grado de DOCTOR

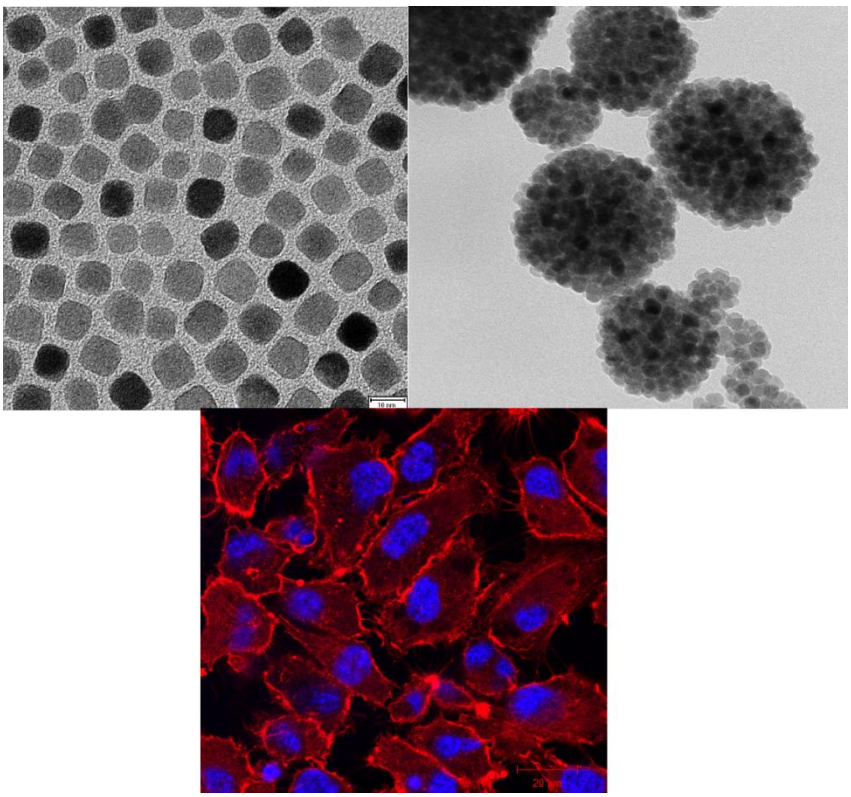

Abril 2017

Xabier Lasheras Aransay

ACKNOWLEDGEMENTS

Imposible reflejar fielmente en unas pocas páginas los méritos de tantas personas que han aportado su empuje directo o indirecto en este trabajo. Además del apoyo directo como puede ser el de directores y colaboradores, muchas veces se olvida que el aporte más importante es el indirecto que ejerce familia, amigos y colegas que con su ejemplo te influencian para querer dar lo mejor de ti y no defraudar su confianza ni sus expectativas en ti.

Antes de nada, quiero agradecer a la fundación BCMATERIALS, ya que su financiación ha hecho posible la consecución de esta tesis. También a mi directora la Dra. Maite Insausti, ya que, sin ninguna duda, no habría iniciado mis estudios doctorales de no ser por su apoyo inicial, así como por su preocupación durante los años de tesis como directora. También agradecer a mi otro director, Jesús Martínez de la Fuente, por su confianza en mí y por abrirme las puertas de su grupo y hacerme sentir como en casa.

No podría relegar sólo a unas líneas a mi "directora en la sombra", la Dra. Laura De Matteis, ya que su aportación directa e indirecta merece al menos un párrafo propio, por no decir una página. Además de dirigirme en mi trabajo con total dedicación y paciencia infinita, indirectamente me ha inculcado valores de seriedad y formalidad en el trabajo, además de no dejarme nunca conformarme con la mediocridad y buscar siempre el máximo. He tenido el privilegio de poder trabajar con una científica y persona inmejorable, de lo que he podido aprender muchísimo. Ha sido para mí un honor, grazie mille per tutti capo.

Y qué decir de mis padres "Cristi" y "Marquitos", llegaron a dudar de mi en mis años "pasotas", pero siempre confiando en mi potencial. Han hecho

que nunca me falte nada de lo que necesite pero sin consentirme "tonterías", lo cual ahora agradezco muchísimo ya que me ha enseñado que las cosas hay que ganárselas. A mis hermanos Andoni e Urko, un refuerzo positivo constante con su ejemplo, que siempre me ha empujado a superarme por tratar de ser como ellos intelectual y personalmente. Puedo decir que más allá de ser mis hermanos, conociéndolos no se puede sentir otra cosa que no sea admiración o respeto. Con ellos quiero agradecer a todos mis abuel@s, ti@s y prim@s por su apoyo. Mención especial para mi "oráculo", durante todos mis años de carrera y tesis hay una persona que jamás ha dudado de mí, mi amama Aurora. En cualquier crisis de confianza, agotamiento o estrés siempre ha bastado una conversación con ella, ya que tras oír su "bah, esto lo pasas sobrado" he salido con plena confianza. Finalmente, siempre he superado todo sobrado sea cual sea su dificultad por no llevarle la contraria. ¿Quién soy yo para dejarte por mentirosa amama? Sin olvidar a Jani, que me ha aguantado durante los larguísimos tiempos de cabreo y desesperación previos a la finalización de esta tesis. Eres un sol amore.

Tras mis diversas colaboraciones tengo muchos compañeros y colegas a los que agradecer su ayuda, compañerismo y por hacer confortable la realización de este proyecto. Del departamento de química Inorgánica (donde he pasado muchísimo tiempo) ha habido mucha gente que ha pasado, pero sólo una que entró a la vez que yo y aún sigue conmigo, Oihane. Siempre está ahí para escuchar y secundar, y he de admitir que por mucho que he intentado lavarle el cerebro jamás lo he conseguido, gran fortaleza mental. Las dos Paulas, tan parecidas y tan diferentes a la vez, Paulita Sanchez siempre con una sonrisa alegrando el día y Serras (otra de las que me ha inculcado la idea del trabajo seria y bien hecho) mutando constantemente de máquina de hacer ciencia en las horas de trabajo a

"macarra" en las horas libres. También está la pareja de Amaias. Iturrospe, con su dulzura y alegría que siempre te ponen de buen humor. Ituorrondo, que con su carácter fuerte y chocante no consigue esconder que es un sol de chavala, la mejor compañera de gym del mundo. El gran Beñat, una máquina dentro y fuera del trabajo, imposible ganarle en conocimientos científicos, aguante a la bebida o al sueño, admirable combinación de dones. Vero me acepto también desde el principio con los brazos abiertos en el grupo y ha sido una ayuda constante, una investigadora con mayúsculas y una amatxu inmejorable para Mikel y Alex. Jago, el currela que nunca te niega un gruñido cuando te lo cruzas por el pasillo y siempre está de buen humor. El tío duro Ricky, que me enseñó cómo sobrevivir en el mundo despiadado de la investigación científica a base de desarrollar una gran fortaleza fundamentada en el ausentismo mental. El señor Wein también merece una mención especial, ya que con su llegada gané un amigo para toda la vida. Una dosis enorme de genialidad, nobleza y humildad en una misma persona, una combinación única. En el campo de las nanopartículas magnéticas he tenido un padre y una madre. El padre, Javi, sabiduría y experiencia hecha carne, nunca me ha negado ayuda o consejo desinteresado. La madre, Idoia, me ha enseñado a usar la imaginación y confiar en mis ideas, ya que si haces bien tu trabajo las cosas salen. Una lección de sacar un trabajo del caos de la ciencia, si sabes cómo. Y por último Itz, que seguirá con este trabajo desde ahora. Estoy contento de decir que se que me harás quedar mal. También han estado Aroa, Ima, Saioa, Maider, Omar, Nahima, Manu, Iker, Luca, Aitor, Dorle, Juan Ignacio, Alberto, Iñaki, Naiara, Ari, Andrés, Nuria, Irati, Sofía, Rober, David, Maite, Anabel y muchos más que en el departamento de inorgánica o en el BCMaterials me han facilitado todo muchísimo. y como no a Manu Barandiarán, Jose Luis Vilas y Naiara Elejalde por aceptarme en el BCMATERIALS. También quiero agradecer a la Dra. Izaskun Gil de Muro por su ayuda con el TEM, así como a Luis Lezama con el EPR y a Eneko Garaio que

ha realizado los experimentos de hipertermia magnética, ya que han sido fundamentales para la consecución de este trabajo. Y al gran y todopoderoso Dr. Iñaki Orue, alias orko, que todo lo sabe y todo lo ve, que siendo técnico de magnetismo puedo decir que el que me haya hecho las medidas magnéticas es lo de menos, ya que no ha dudado en perder todo el tiempo del mundo en explicarme los fundamentos del magnetismo de forma que hasta un simple químico los pueda entender.

Mis estancias en el INA me han procurado toda clase de beneficios. Sin embargo, el primero de todos es el inmerecido privilegio de trabajar junto a científicos de clase mundial, con suerte se me habrá pegado algo de cada uno. Rauch, una auténtica y verdadera máquina científica, obviando el plano personal, en el que le tengo un aprecio enrome, esta rumana con acento de Donosti es una "rock star" en esto de la investigación, me habría encantado poder trabajar con ella, a pesar de que no habría cambiado mi directora de Zaragoza por nadie. Afortunados son sus becarios. Y ya que hablamos del tema, quiero agradecerle a Laura (otra vez, y no haré las 20 menciones que merece por no ser pesado), otra "rock star" italiana con alma alemana por su guía, sabiduría, respeto, seriedad en el trabajo y simpatía dentro y fuera de él. Otra vez, obviando el enorme aprecio personal que siento por ambas, también ha sido un placer tener la oportunidad de trabajar con María Moros y con Graz, son el tipo de personas junto a las cuáles te sientes más listo e incluso mejor persona sólo por influencia del aura que tienen las dos. A pesar de su humildad, por la que de primeras nunca pensarías estar delante de semejante genio, el guiri de m*****, a veces conocido como Scott, también me ha influenciado positivamente en todos los aspectos. Otro ejemplo a seguir. En lo personal María Alleva, Clara e Inés han tenido mucho calado. Cada una de ellas a su manera, con sus caracteres totalmente diferentes, me han influenciado mucho. Clarita con su chispa y su naturalidad turolense,

María con su dulzura y las "pelotas" que le echa a la vida, e Inés de Peñaflor con su nobleza, simpatía y generosidad, un ángel. También quiero agradecer a Vanessa, Vanesa, Laura Asín, Valeria, Carmen, Sara R, Sara P, SoniG, Alvaro, Isa, Gabi, Rafa, Ester, Alfredo, Rodri (alias uruguasho!), Ana Claro, Miriam, Elena, Jorge (alias JD), Mari Carmen (alias MC, mari, rubiaahh, andaluza, sosa, ...), y don Daniel Carmona, entre muchos, por su acogida buen rollo en todo momento. Muchas gracias también a Iñi y a Charlie por el apoyo técnico y personal facilitado los últimos años.

Sin olvidar a mis dos compañeros de piso por excelencia, Yulán y Maciej. Yul, que decir que no sepas, me falta vocabulario para expresar con justicia la pedazo de tía que eres, desde que ya no estás allí Zaragoza nunca volverá a ser lo mismo para mí. Vuelve!!!!!!Maçiej, alias "el polaco", es otro sin el que la vida no es la misma. Un aventurero de la vida y un amigo fiel, siempre nos quedaran los martes locos, you'll never walk alone my friend.

I also had the privilege to work in an exceptional work group in Fribourg, so, first of all, I want to thank Barbara, Alke and Martin for accepting me in their group and for their kindness. Special thanks for Chris, this genuine swiss guy who introduced me in the optimal swissway of working, thanks to you, I'll be the nightmare of my future chiefs and partners. martin, for his patience and great guide through the field of nanotoxicity. And also for all the bionanomaterials research group, Christoph Monier, Christoph Geers, Ana, Sandra, Hanna, Herve, David, Federica, Daniel, Joël, Sandor, Dominic, Leo, Thomas, Laura, Estelle, Savyna, Laetitia, Catherine, Omar, Dimitri and Jose for making this experience great. Great group with awesome people.

Aujourd’hui ma vie ne serait pas le même si je n’aurais pas connu ma famille suisse. Ce sont les personnes que tu crois déjà connaître bien mais ils sont toujours capables de te surprendre. Des personnes qui m´ont ouvert

leur porte de sa maison, qui m'a invitée manger à sa table et connaître sa famille , sans rien demander en retour. De plus, ils ont toujours fait un grand effort s'assurer d'un séjour agréable pour moi.

Je n´imaginais pas non plus que de telles personnes pouvaient exister.Vielen dank Walter, merci beaucoup Noémie, gracias Miguel, merci bien Miriam, merci beaucoup mon swiss neveux Louis et Jeannout, mille fois merci mon ami Jacko, mille merci Silvyanne, merci beaucoup Mateó, merci beaucoup Timoté, merci beaucoup Alicé, muchas gracias Calos et mille fois merci pour mon swiss maman Sonja. Vous rendez le monde meilleur. Vous serez toujours les bienvenus chez moi.

Los amigos también hacen mucho, ya que, si bien no te ayudan directamente, ten por seguro que no lo puedes hacer sin ellos. Mila esker a la kuadrilla, Galder, Isma, Sabin, Aketza, Maider, Idoia, Unai, Saioa, Itxaso, Sancho, Mikelo, Delos, Gotzon, Roi y tambien especialmente a Leire, que ha estado conmigo desde los 9 años hasta ahora, siempre un paso por delante pero tirando de mi para alcanzarla. Mila esker bereziki Kepsentzat frantsesekoitzulketekin laguntzeagatik.

Sería injusto no agradecerles también la gran aportación que han tenido el Señor Paco Pil, Hans Zimmer y Ramin Djandi, ya que sus magníficas obras han sido mi constante hilo musical de fondo durante la escritura.

RESUMEN

La falta de especificidad de muchos tratamientos, tales como la quimioterapia o la radioterapia para tratamientos de cáncer, son el mayor obstáculo para la curación de dichas enfermedades. Tales tratamientos suelen requerir dosis mucho mayores de las en principio necesarias para contrarrestar su falta de especificidad, además de los numerosos efectos secundarios que causan, los cuales a menudo impiden su aplicación. Por ello, el desarrollo de nuevos tratamientos específicos para este tipo de enfermedades es uno de los principales retos que la investigación se ha marcado actualmente.

En las nanopartículas magnéticas (MNP) superparamagnéticas se ha encontrado una opción potencial para solucionar estos problemas. Por una parte, estas nanopartículas podrían usarse como vehículo para transportar fármacos a las zonas deseadas para liberarlos allí, aumentando así su efectividad. Esto permitiría reducir las dosis de estos fármacos, reduciendo a su vez sus efectos secundarios. Además, dichos materiales son capaces de generar calor al verse afectados por un campo magnético alterno, mediante un fenómeno denominado hipertermia magnética. De esta manera, las partículas podrían dirigirse a la zona tumoral, aplicándole entonces un campo magnético alterno para calentar de forma controlada la zona a tratar, matando así las células cancerígenas mediante apoptosis celular. Para alcanzar tales objetivos, hay tres pasos fundamentales que deben llevarse a cabo. 1: el desarrollo de un material magnético nanoestructurado que reúna las condiciones necesarias para generar un gran efecto de hipertermia magnética. 2: modificar la superficie de dicho material para hacerlo biocompatible y funcionalizarlo dependiendo del proceso al que vaya destinado, así como adherir los fármacos a transportar. 3: comprobar su toxicidad mediante ensayos *in vitro* e *in vivo*. En esta tesis se ha transcurrido

por cada uno de estos tres pasos, desarrollando dos materiales con potenciales aplicaciones biomédicas.

Inicialmente, se han sintetizado nanopartículas magnéticas (MNP) de ferrita ($M_xFe_{3-x}O_4$) dopada con cationes de Ni^{2+} o Mn^{2+}, así como distintos sistemas *core shell* alternando capas de ferrita de níquel y magnetita. El motivo de la formación de estas ferritas dopadas y estos sistemas core shell es la posibilidad de obtener valores de hipertermia mayores a los obtenidos con la magnetita (Fe_3O_4), que es el material usado normalmente. Dichos procesos se han llevado a cabo mediante el método de descomposición térmica de precursores metalorgánicos, que consiste en el calentamiento de dichos precursores a altas temperaturas en disolventes orgánicos de alto punto de ebullición y en presencia de ligandos orgánicos. De esta forma, se han obtenido MNPs con tamaños comprendidos entre 8-12 nm. Dado que el tamaño de partícula es un parámetro fundamental para la respuesta de hipertermia, una muestra de cada grupo (ferritas de Ni y ferritas de Mn) ha sido recrecida mediante un método de crecimiento por etapas a partir de semillas de MNPs. Dicho método se basa en la repetición del proceso de formación de las partículas sobre semillas de MNP previamente sintetizadas, aumentando así el tamaño de estas semillas. Los sistemas de core shell también han sido sintetizados mediante este método, alternando capas de diferentes materiales en cada proceso de crecimiento. La caracterización química y estructural ha mostrado que los cationes con los que se ha dopado la ferrita están presentes en las muestras, obteniendo partículas esféricas superparamagnéticas monodominio con una morfología bien definida y cubiertas de cadenas de oleato, lo que estabiliza las partículas en dispersiones coloidales en medio orgánico (apolar). La caracterización magnética ha mostrado que a grados de dopaje mayores de ambos metales la imanación de saturación, a la vez que la constante magnetocristalina,

tienden a decrecer. Esto da una idea de a qué tipo de huecos tiende a ir cada catión, lo que ayuda la comprensión del comportamiento de este tipo de materiales. Del mismo modo, mediante la espectroscopia magnética de resonancia (EMR) se ha comprobado que los tamaños de partícula mayores inducen valores mayores del factor giromagnético efectivo (g_{eff}), lo que es muestra de un mayor comportamiento ferromagnético. Las medidas de hipertermia de todas las muestras han confirmado que el sistema que tiene mayor diámetro, constante magnetocristalina e imanación de saturación es el que da la mayor señal de hipertermia magnética ($Ni_{0.31}Fe_{2.69}O_4$_A). Dicha muestra ha mostrado una respuesta de hipertermia mayor que la de MNP de magnetita de tamaño equivalente. Por ello, esta muestra ha sido seleccionada para continuar con el siguiente paso.

Tal y como se ha comentado, dichas nanopartículas son hidrófobas, y requieren una funcionalización para ser estables en medio fisiológico. En la segunda fase del trabajo, el sistema optimizado en el paso anterior ($Ni_{0.31}Fe_{2.69}O_4$_A) ha sido funcionalizado de dos formas distintas, obteniendo dos tipos diferentes de material que están destinados a una aplicación distinta. Por una parte, las nanopartículas se han recubierto individualmente con el polímero poly(maleic anhydride-alt-1-octadecene) (PMAO) ($Ni_{0.31}Fe_{2.69}O_4$_A_PMAO). De esta forma, las partículas han sido estabilizadas en medio acuoso, obteniendo una carga superficial negativa y siendo destinadas a tratamientos basados en la hipertermia magnética. La presencia de este polímero ha sido demostrada por medidas del diámetro hidrodinámico y de termogravimetría. Dichas partículas no han sufrido cambios en sus propiedades magnéticas en comparación con las partículas recubiertas de oleato ($Ni_{0.31}Fe_{2.69}O_4$_A).

Por otra parte, se ha desarrollado un nuevo mecanismo para encapsular las nanopartículas en el biopolímero quitosano. Dicho método ha sido

optimizado y está basado en la formación de múltiples interacciones hidrófobas entre las cadenas de oleato de la superficie de las NP y el quitosano, seguido de un proceso de coacervación que incremente las interacciones electrostáticas, dotando a las nanoesferas finales de una mayor rigidez. De esta forma, se han obtenido nanoagregados estables de 90 nm de las nanopartículas en este biopolímero de carga positiva (CS-MNS). Al contrario que en la anterior funcionalización, en este caso hay diferencias estructurales y magnéticas notables comparadas con la muestra de MNP de partida. A pesar de que se ha mantenido la imanación de saturación y, aparentemente, las nanoesferas siguen teniendo un comportamiento superparamagnético a temperatura ambiente, la agregación ha inducido interacciones dipolares entre las MNP adyacentes, lo que resulta en un comportamiento más ferromagnético. Los estudios de encapsulación de fluoróforos que se le han realizado, a la vez que los estudios de estabilidad ante diferentes medios, muestran que estas nanoesferas resultan muy apropiadas para el transporte de fármacos.

En el último paso de esta tesis se analiza la toxicidad de estos dos nanosistemas, $Ni_{0.31}Fe_{2.69}O_4$_A_PMAO y CS-MNS. Primero, se ha analizado su citotoxicidad en monocultivos de la línea Vero, poniendo los nanosistemas en contacto con dichos monocultivos durante 24 horas. Los resultados de citotoxicidad obtenidos han demostrando que ninguno de los dos sistemas muestra citotoxicidad en estos cultivos en exposiciones de 24 horas, en las concentraciones testadas (0-0.5 mg/mL). Tras ello, ambos sistemas se han puesto en contacto con un modelo de vaso sanguíneo preparado mediante células endoteliales y macrófagos. En este caso no se ha comprobado sólo la citotoxicidad de los materiales, habiendo comprobado más en profundidad su posible toxicidad. Mediante este experimento se ha demostrado que las nanopartículas individuales $Ni_{0.31}Fe_{2.69}O_4$_A_PMAO penetran en mayor

cantidad en las células que las nanoesferas, debido a su menor tamaño. Ninguno de los dos compuestos muestra ningún tipo de toxicidad (estrés oxidativo, cambios en la morfología celular,...) a excepción de una leve respuesta inflamatoria, que no repercute en gran medida en el metabolismo celular normal, ni tendría que generar ningún efecto visible. Finalmente, se ha analizado el efecto de la muestra CS-MNS en ratones, exponiéndola durante 48 horas. En este caso, además de la toxicidad de las nanoesferas en los ratones, se ha determinado también la biodistribución de éstas por los diferentes órganos. No se ha observado ningún cambio notorio en el peso de los ratones o de alguno de sus órganos debido a la exposición, al margen de un decrecimiento inicial del peso debido al shock derivado de la inyección. En los análisis de sangre sólo se ha observado un leve aumento en los niveles de la encima aspartato aminotransferasa (AST), que podría estar relacionado con daños en el tejido hepático. Sin embargo, el aumento de los niveles de AST no es lo bastante grande como para poder relacionarse con daños severos. La biodistribución de las nanoesferas por los diferentes órganos de los ratones se ha analizado mediante espectroscopía de plasma inductivo (ICP), midiendo las concentraciones de los metales Fe y Ni en los diferentes órganos. En este análisis se ha observado una mayor presencia de las nanoesferas en el hígado, que podría estar filtrando las nanoesferas del flujo sanguíneo.

En conclusión, en estas tesis se han desarrollado dos sistemas nanoestructurados destinados a aplicaciones biomédicas (hipertermia magnética, y transporte de fármacos). Sus propiedades, tanto estructurales como magnéticas, los hacen viables para dichas aplicaciones, ya que no han mostrado una alta toxicidad en los ensayos preclínicos realizados.

ABSTRACT

The lack of specificity of many treatments, such as chemotherapy or radiotherapy, is the main problem for the correct treatment of these illnesses. Such treatments need much higher doses than the necessary to counteract this nonspecificity, besides the many side effects that they induce, which sometimes impede their application.

The magnetic nanoparticles (MNP) are presented as an interesting approach to solvent these problems. On the one hand, these nanoparticles could be used as vehicles to transport the drugs to specific regions, improving their effectiveness. Furthermore, such materials generate heat under the influence of an alternating magnetic field, in a phenomena called magnetic hyperthermia. In this way, the magnetic nanoparticles could be directed to the tumoral tissue. Then, by applying an alternating magnetic field, the generated heat could kill the cells by cellular apoptosis. In order to achieve such objectives, there are three different steps that need to be overtaken: 1.: the development of a nanostructured material which meets the conditions to show a high magnetic hyperthermia response. 2.: the modification of the developed nanoparticle surface to become biocompatible and functionalize it with the desired compound, depending on its especific application. 3.: to analyze its toxicity. In this thesis these three points have been analyzed, developing two different materials with different potential applications.

Initially, Ni^{2+} and Mn^{2+} doped ferrite MNPs have been prepared, as well as core shell systems alternating Ni ferrite and magnetite layers. Such processes have been carried out by means of the thermal decomposition of metalorganic precursors method, obtaining ferrite MNPs with diameters in the 8-12 nm range. Taking into account that the particle diameter has a

mayor significance in the magnetic hyperthermia response, one system of each group (Ni an Mn ferrites) has been growth by a seed mediated one-pot growth process. The core shell systems have also been synthesized through this approach, by forming different material layers. The chemical and structural characterization has demonstrated the presence of the Ni^{2+} and Mn^{2+} cations in the final samples, obtaining oleate covered spherical nanoparticles. The chemical characterization has shown that at both cation higher doping degrees the saturation magnetization, as well as the magnetocrystalline anisotropy, tend to decrease. The electronic magnetic resonance spectroscopy has demonstrated that higher particle diameters induce higher effective gyromagnetic (g_{eff}) values. The hyperthermia measurements have confirmed that the sample which showed the higher diameter, saturation magnetization and magnetocrystalline anisotropy is the one which shows the higher magnetic hyperthermia response ($Ni_{0.31}Fe_{2.69}O_4$_A). For this reason, this sample has been selected to continue with the next step.

Since these nanoparticles are hydrophobic, a functionalization is necessary to make them stable in physiological media. In the second phase of the thesis, the optimized nanoparticles ($Ni_{0.31}Fe_{2.69}O_4$_A) have been functionalized by two different methods, directed to different applications. On the one hand, the MNPS have been coated individually with the poly(maleic anhydride-alt-1-octadecene) (PMAO) polymer, obtaining the $Ni_{0.31}Fe_{2.69}O_4$_A_PMAO sample. In this way, the particles have been stabilized in aqueous media, obtaining a negative surface charge and being directed to magnetic hyperthermia mediated applications. On the other hand, a mechanism to encapsulate the nanoparticles in the chitosan biopolymer has been developed. By this method, 90 nm diameter stable nanoparticle aggregates with positive surface charge have been obtained (CS-MNS). In

contrast to the previously explained functionalization, important differences in the structural and magnetic properties have been observed in this case, comparing with the single nanoparticles ($Ni_{0.31}Fe_{2.69}O_4$_A). The MNP aggregation has generated dipolar interaction between the adjacent particles, inducing a more ferromagnetic behavior. These nanospheres are more suitable to drug delivery and controlled release related applications, according to their structure and properties.

The last step of the synthesis consist in analyzing the toxicity of the prepared nanosystems, $Ni_{0.31}Fe_{2.69}O_4$_A_PMAO and CS-MNS. First, their cytotoxicity in Vero cell monocultures has been analyzed, demonstrating the non-toxicity on both nanocompounds for these cultures for 24 hour exposures. After that, both systems have been putted in contact with a blood vessel model co-culture, prepared by seeding endothelial cells and macrophages. By this experiment, it has been observed that the cellular uptake of the single $Ni_{0.31}Fe_{2.69}O_4$_A_PMAO MNPs is higher than the nanospheres. None of both compounds show any kind of toxicity (oxidative stress, changes in cell morphology,...), excepting a slight inflammatory response. Finally, the effect of CS-MNS nanosphere exposure in mice has been analyzed, exposing them for a 48 hour period. It has not been observed any notorious change in mice or any organ weight due to the exposure. Only a slight increase in the aspartate aminotransferase (AST) levels has been observed in the blood analysis, which could be related to damages in the hepatic tissue. The boidistribution of the nanospheres has been analyzed by means of the inductively coupled plasma spectroscopy (ICP), observing a higher presence of nanospheres in the liver.

In this thesis two different nanostructured materials have been developed, directed to biomedical applications. Their structural and

magnetic properties make them suitable for such applications, as they have not shown high toxicity in the performed assays.

CONTENTS

ABBREVIATIONS

AL Alkaline phosphatase

AST Aspartate transaminase

CS Chitosan

DLS Dynamic Light Scattering

DMEM Dubbelco Modified Eagle Medium

DNA Dexyribonucleic Acid

DTG Derivative Thermogravimetry

EMR Electronic Magnetic Resonance

EPR Enhanced Permeability and Retention

FC Field Cooling

FTIR Fourier Transform Infrared spectroscopy

ICP Inductively Coupled Plasma spectroscopy

IL 8 Interleukin 8

LDH Lactate Dehydrogenase

LSM Laser Scanning Microscope

MNP Magnetic Nanoparticle

MRI Magnetic Resonance Imaging

NP nanoparticle

PBS Phosphate Buffered Saline

PMAO poly(maleic anhydride-alt-1-octadecene)

ROS Reactive Oxygen Species

RPMI Roswell Park Memorial Institute medium

SAR Specific Absorption Rate

SQUID Superconducting Quantum Interference Device

TEM Transmission Electron Microscopy

TG Thermogravimetry

VSM Vibrating Sample Magnetometer

XRD X Ray Diffraction

ZFC Zero Field Cooling

1. INTRODUCTION

Nanoscience is one of the most trending investigation topics nowadays.[1,2,3] The advantages that the material reduction to nanoscale would provide were originally predicted by Richard Feynman in the American Physical Society conference in 1959 with the popular phrase: "there's plenty of room at the bottom".[4] This lecture could be considered as the beginning of the nanoscience, when Feynman described firstly the concept of a nanostructured material and the benefits that its development would provide, as the materials properties could be easily tuned by controlling the parameters involved in nanostructuration. In this way, the research was focused on obtaining and studying nanostructures, which have supposed a new development in materials engineering. However, Feynman also established the challenges that this research had to afford. On the one hand, a way to visualize and to study the materials in the nanometric scale was firstly necessary to be developed, as the instruments available had not enough resolution. Furthermore, instruments being able to interact with materials structure in the atomic scale would provide the ability to develop a new generation of materials.

Feynman´s assertion was *premonitorious* as the development of the Scanning Tunnelling Microscope (STM) in 1981, for which Gerd Binning and Heinrich Rohrer won the Nobel award in 1986, yield a deep study of materials in the atomic range.[5] However, Feynman did not predict the effect that the materials nanoscale reduction would have in the intrinsic properties. In this way, the discovering of new properties that had never been previously observed in bulk state. In other cases, a qualitative modification of their primary properties, supposed a boom in materials chemistry, opening many

new possibilities for materials in the nanoscale.[6,7,8] The increase of surface-to volume ratio induces an important change in final chemical, mechanical, optical, electric and magnetic properties.

Concerning magnetic materials, the reduction to the nanometric scale mixes the properties of ferromagnets and paramagnets, in a behaviour that has been called superparamagnetism.[9,10] These materials maintain the high magnetic susceptibility of ferromagnetic materials and the absence of coercive field and resonant magnetization of paramagnetic materials. These magnetic properties have opened new possibilities in fields as advanced biomedical applications including biosensing, Magnetic Resonance Imaging (MRI) diagnosis, drug delivery and controlled release and cancer treatments by magnetic hyperthermia.[11,12] The present study is focused on this context, the preparation and characterization of different superparamagnetic systems for biomedical applications.

1.1 Chemical, structural and magnetic properties of ferrites

For biomedical applications, the magnetic material with the most suitable properties is the magnetite, $Fe^{3+}{}_2Fe^{2+}O_4$.[13] This ferrimagnetic material shows a great magnetic susceptibility and saturation magnetization with non-reported toxicity in human body, as its decomposition follows the human iron metabolism. Therefore, its use in biomedicine is approved by the Food and Drug Administration (FDA).[14] The partial or total substitution of iron cations for other paramagnetic cations yields different ferrites. Depending on the replacing cations and the doping level, the properties, especially those related to their magnetic behaviour, can be tuned in many different ways.[15,16]

1. Introduction

Ferrite materials are mixed oxides, which present spinel structure (G. E.: Fd-3m). Ferrites composed by Fe^{3+} and Cd^{2+} or Zn^{2}, crystallize as normal spinels, whereas the rest of ferrites present an inverse spinel structure.[17] The inverse spinel structure is formed by 56 ions in the unit cell, with the oxygen anions in a face centred cubic (FCC) arrangement. One eight of the tetrahedral holes (T_d) of the structure (8) are occupied by M^{3+} cations, leading the rest of T_d holes empty. One half of the octahedral (O_h) holes (16) are occupied by M^{3+} cations (8) and M^{2+} cations (8), conforming the unit cell represented in Figure 1.1.[18]

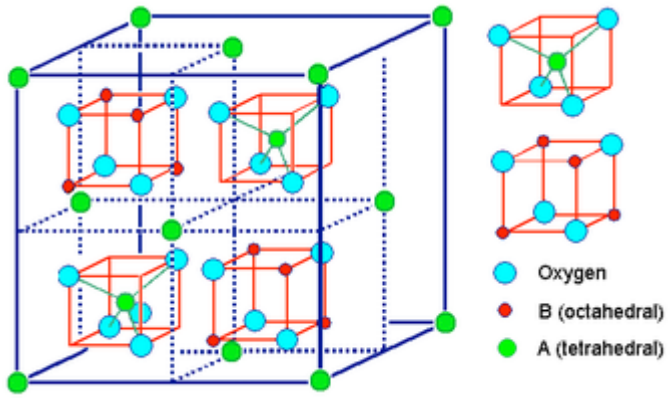

Figure 1.1. *Inverse spinel structure of ferrite materials and configuration of tetrahedral and octahedral holes.*

The M^{2+} and M^{3+} cations proximity and configuration in the crystalline structure induce interexchange interactions between neighbouring cations, which can be ferromagnetic or antiferromagnetic, depending on the spin orientation.[19] Ferrimagnetic materials are induced by unbalanced opposite couplings between spins (antiferromagnetic coupling). Above the Curie temperature (around 858 K for ferrites), ferrimagnets behave as paramagnetic materials, as the mentioned coupling energy has been

overtaken by the external thermal energy, and consequently, magnetic moments are randomly vibrating by the thermal agitation. In this state, the ferrimagnetic material follows the Curie-Weiss law ($\chi = C/(T-\theta)$), in which the magnetic susceptibility decreases linearly with increasing temperature and increases with the applied magnetic field. This paramagnetic behaviour can be defined by the Langevin equation (Figure 1.2A). In this representation, the linear response with magnetic field can be checked for low applied magnetic fields or high temperatures, as $x=\mu H/k_B T$, where k_B is Boltzmann's constant (low x values). In this state, paramagnetic materials show relatively low magnetization values, not being interesting for industrial or biomedical applications. Nevertheless, they do not show remanence magnetization when removing the external magnetic field, as all magnetic moments are randomly oriented by thermal agitation without a preferential orientation, which means that its magnetic behaviour can be controlled.[20]

However, below Curie temperature the interexchange energy overtakes the thermal energy, showing a ferrimagnetic regime. In this state, the interaction between magnetic moments generates an intrinsic molecular magnetic field that induces a spontaneous magnetization. This yields a much higher magnetic response of this kind of materials under the influence of an external magnetic field, comparing with paramagnetic materials. Moreover, the spontaneous generation of magnetic domains inside materials, which are magnetized in random directions, also lead to an hysteresis in the magnetic response due to the anisotropy constant of the material and, specially, to the movement of the magnetic domain walls, called Bloch walls.[18]

Ferrimagnetic behaviour is quite similar to the ferromagnetic one, not differentiable by measuring the magnetic response. In ferromagnetic materials, all interacting magnetic moments in all sublattices are parallel, obtaining a net magnetization by the addition of all contributions. In

contrast, in ferrimagnetic materials, the different sublattices magnetizations do not completely cancel each other, obtaining a spontaneous magnetization that can be much higher than the magnetization shown by paramagnetic compounds and comparable to ferromagnetic materials response. In this case, the final magnetization depends on many factors as the nature of the cations forming the ferrite structure, the net magnetization and the interaction energies between cations. Increasing temperature decreases the net magnetization of the ferrimagnetic system due to the thermal agitation, as can be also observed in ferromagnetic materials.[19,18] The temperature dependence of magnetic moment orientation is schematically illustrated in Figure 1.2B.

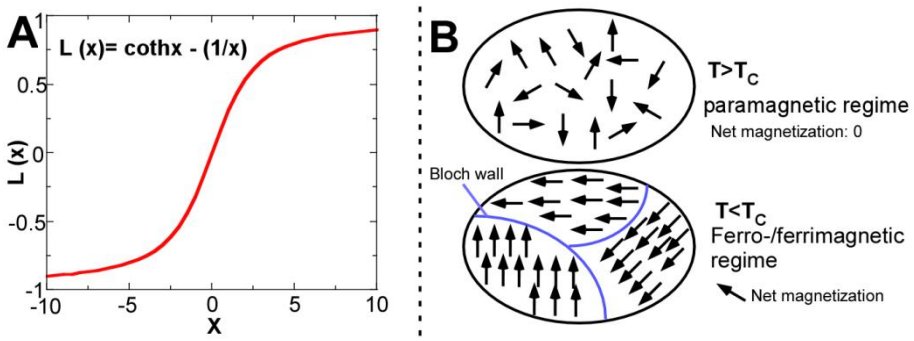

Figure 1.2. *Langevin function representation (A) and illustration of temperature dependant ferro-/ferrimagnetic material magnetic behaviour (B).*

The magnetic response of ferrites can be tuned by modifying the so-called inversion degree which modulates antiferromagnetic coupling interactions between magnetic sublattices.[21,22,23,24,25,26] These changes in the net magnetization value can be predicted by controlling the cation distribution between octahedral and tetrahedral sites. Taking the negative exchange interactions between the tetrahedral and octahedral sites into account, the result between both contributions will be the net magnetization value.[27,16]

In this sense, some ferrites (hard ferrites) show higher values of spontaneous net magnetic moment than others with smaller spontaneous magnetization values (soft ferrites), which defines their optimal application area. Thus, doping with metals such as cobalt, hard ferrites will be obtained, whereas the insertion of nickel or manganese metals, for instance, result in soft ferrite materials. The key factor for obtaining soft or hard materials is the resultant magnetocrystalline anisotropy, which is related to the energy required to turn the direction of the magnetic moment away from an easy direction. This force is generated by the spin-orbital coupling interactions between neighbour ion orbital magnetic moments. In this way, when an external applied magnetic field is changing the spin moments direction, the spin orbitals have to reorient in the same direction. Therefore, depending on the orbitals form and symmetry, it could be more favoured to perform this rotation, which would reduce the magnetocrystalline anisotropy.[28,29,30]

As a summary, ferrite materials structure brings the opportunity of tuning the magnetic response to adequate the material to a specific application. For biomedical applications, high magnetic response is desired, as well as low remanence magnetization values. In this way, the development of nanometric ferrite materials could fulfil these expectations.

1.2 Magnetic nanoparticles, superparamagnetism

As has been previously mentioned, the nanoscale reduction of magnetic materials modifies the magnetic behaviour, inducing the superparamagnetic behaviour.[31] When materials size is below 10^2-10^3 atoms, depending on the material type and shape, the magnetostatic energy is not high enough to favour the formation of Bloch walls and magnetic domains to reduce the spontaneous magnetic energy. Hence, obtaining single domain

(monodomain) compounds one of the main magnetic hysteresis induction sources would be discarded. [10,32]

However, the previously explained magnetocrystalline energy also generates a preferential orientation of magnetic moments that provides magnetic hysteresis. At this point, the magnetocrystalline energy, defined by the anisotropy constant (K), as well as the particle volume V, represents the energy barrier (KV). Energy barrier is the energy limit above the NP net magnetic moment is continuously fluctuating without a preferential orientation. Thus, the nanoparticle would be in the superparamagnetic regime.[28] In absence of an external applied magnetic field, when the energy barrier is higher than the thermal energy, the NP net magnetic moment would be blocked in a specific orientation, whereas when the thermal energy overtakes the NP energy barrier the nanoparticle will be in the superparamagnetic regime, without spontaneous or remanent magnetization, as has been schematically explained in Figure 1.3.[33,10]

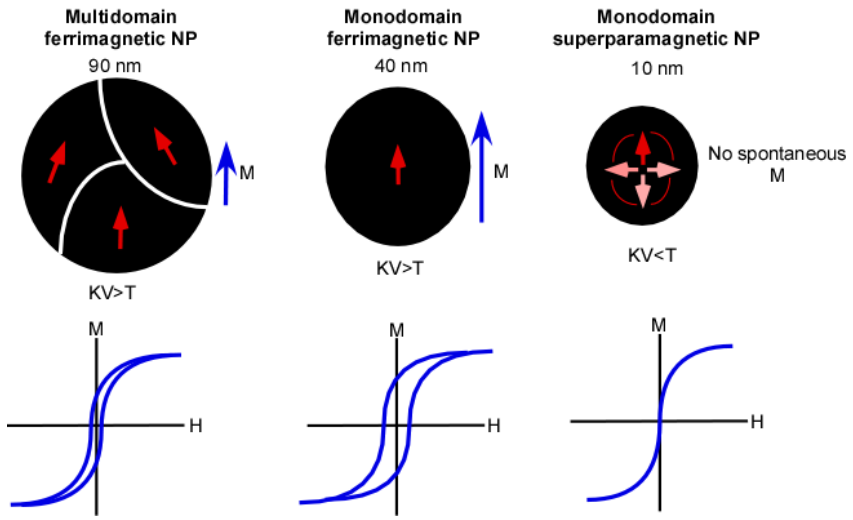

Figure 1.3. *Schematically illustration of a ferrite nanoparticle magnetic behaviour in the superparamagnetic and blocked (ferrimagnetic) regime at room temperature.*

As can be observed in Figure 1.3, in superparamagnetic nanoparticles no hysteresis cycle is observed as they are continuously oscillating by thermal agitation. In blocked NPs, when the energy barrier is higher than the external thermal energy, the presence of hysteresis is observed, as magnetic energy is necessary to overtake the magnetic anisotropy energy that positions the NP in a preferential orientation. Therefore, a NP in the superparamagnetic state behaves as a paramagnetic compound without spontaneous magnetization, yet with an extremely high magnetization under the influence of an external magnetic field.

The superparamagnetic regime of NPs can be altered by reducing the temperature below its energy barrier and blocking the NPs in random orientations. In this way, the temperature in which the NPs energy barrier becomes higher than the thermal energy is called the blocking temperature, T_B. Furthermore, the superparamagnetic regime of a sample in a certain temperature can also be modified by increasing the NP size or by preparing NPs with higher anisotropies. After all, the superparamagnetic state is not an intrinsic property of a material or sample, as it is only an unusual state that can be modified by changing some factors as NP diameter or external temperature.

1.3 Mostly used magnetic NP preparation methods

There is a number of different synthesis methods that have been used for magnetic NP preparation.[9] As usual, the employed mechanism chosen in each case depends on the desired NP properties, as NP size range, shape, surface properties and physical condition (in solid or in colloidal dispersion). Each synthesis method makes possible to obtain also materials with a

hydrophilic or hydrophobic nature. Ultimately, the synthesis method depends on the characteristics necessary for the desired application.

Chemical NP synthesis methods produce NPs directly by chemical routes, being the structure and properties of produced materials strongly dependant on the selected process. Important parameters as grade of crystallinity, size, shape, colloidal stability, functionality or magnetic properties can be starkly different by employing different chemical methodologies. From all possible chemical strategies, the most suitable methods to achieve colloidally stable ferrite nanoparticles are: 1) the co-precipitation method of metallic salts, 2) the solvothermal reaction, 3) the sol-gel synthesis and 4) the thermal decomposition method or the microemulsion.[32,9]

When a biomedical therapeutic nanoparticulate agent is being developed, the surface chemistry of the NPs is as important as the magnetic inorganic core. It provides colloidal stability, avoids the aggregation, stabilizes the NPs in physiological media and possibilities the NP functionalization with drugs or fluorophores adhesion. The covering is sometimes modified in the NP preparation process itself, but in many cases, modifications need to be performed in additional treatments. Concerning ferrite NPs, this coating has the additional function of minimizing the oxidation of the ferrite structure to maghemite due to the high specific surface area of such nanomaterials.

This coating process has been described in literature by employing a large number of different ways as inorganic covers (silica, carbon, gold, silver...), polymer coating and different surfactant and organic molecule adhesion.[32,9] In order to preserve the original magnetic properties of the ferrite material, NPs are usually coated individually, pretending to obtain non interacting single NP water colloidal dispersion. However, recent studies have shown the benefits that controlled NP cluster or aggregate formation could provide.[34,35]

1.4 Biomedical applications of magnetic nanocompounds

Probably, the three most relevant applications for magnetic nanomaterials are electronic devices, magnetic separation (cells, analytes…) and, of course, biomedical applications.[31]

The biomedical applications of magnetic nanocompounds are focused on three main fields: as contrast agents in Magnetic Resonance Imaging (MRI) diagnosis processes, as drug delivery and controlled release agents and as magnetic hyperthermia inductors for cancer treatments.

- **Magnetic Resonance Imaging (MRI)**

The MRI relies on the counterbalance between the small magnetic moment of a proton and the large number of protons in a living tissue. The high magnetization of superparamagnetic NPs disturbs the proton magnetic moment, which yield a measurable effect under the applied magnetic fields, leading to distinguish between different tissues.[33] The NP application as MRI contrast agents has steadily increased over the past decade. Traditionally, paramagnetic ions have been used as contrast agents in MRI, however, due to the their much higher molar relaxivity response, superparamagnetic magnetite NPs are becoming the most used contrast agents nowadays together with gadolinium paramagnetic complexes, as their effect is quite intense at lower concentrations and have been proved to be non toxic at the used doses.[32]

The NPs that have been applied as contrast agents are dextran coated magnetite NPs with average diameters from 3 to 10 nm, to enhance their insertion into the tissues.[36] These NPs are biocompatible and are metabolized via the liver after the treatment. The strong size effect is evident as NPs with diameters above 30 nm are quickly collected by liver and spleen.

They are rapidly identified and removed from the bloodstream by the immune system, whereas NPs around 10 nm or smaller present longer half-life in the bloodstream. This uptake difference also leads to distinguish between different tissues and organs due to the different uptake grade of NPs. Such nanoparticles can also be used to visualize the vascular and nervous systems, by using particles with smaller sizes and specific surfaces. Furthermore, the reticuloendothelial systems of some cancerous cells (comparing with healthy cells) avoid the insertion of the added contrast agents, what also lead us to identify lymph nodes, tumours and brain tumours.[37,32]

- **Magnetic hyperthermia treatments**

Another interesting biomedical application for superparamagnetic NPs is the cancer treatment by means of NPs magnetic hyperthermia. The two main problems that current cancer treatments present are, on the one hand, the low specificity of the employed drugs, being required much higher amounts of drugs than the theoretically necessary needs to achieve the desired effect. Furthermore, the lack of specificity causes severe side effects in many healthy organs and physiological functions. The development of a cancer treatment, which could increase the efficacy, as well as the specificity, is the most followed challenge of the current nanomedicine research.

The tumour treatment by magnetic hyperthermia is one of the mechanisms that are being investigated to treat such diseases efficiently. These treatments are focused on the locally generation of heat by MNPs without damaging the surrounding healthy tissues when applying an alternating magnetic field. Ferro/ferrimagnetic and superparamagnetic particles release heat by hysteresis or relaxation loss under an external alternating magnetic field, depending on their magnetocrystalline

anisotropy, saturation magnetization and particle size. In this sense, the heat generation could be controlled by modifying the synthesis parameters to yield different NPs or by modifying the amplitude (H) and the frequency (v) of the applied alternating magnetic field.[38]

The magnetic hyperthermia cancer treatments are based on the different effects of heat in cancerous and healthy tissues. Although cancerous and healthy cells are biologically and structurally quite similar, some differences in tumour cells as a lower oxygenation, lower pH values or lower vascularisation of tumour tissues, make cancerous tissues more sensitive to high temperatures than the healthy ones.[39,40] Temperatures around 43°C induce protein denaturalization, cell membrane slow decomposition and DNA fragmentation that cause cell death by apoptosis mechanism in cancerous cells. However, temperatures above 46 °C induce the cell death by necrosis mechanism, what is more effective in short times periods, although, the injuries that these thermoablation mechanisms induce in the surrounding healthy tissues are much intense than the apoptosis based methods.[41]

- **Drug delivery and controlled release**

Concerning the biomedical applications, the first step is to perform, a broad analysis of their toxicity.[42] It is important to take into account that the selected synthetic methodology and the further biofunctionalization could influence their toxicity and cellular uptake. This two important features are directly related with the size, shape and surface chemistry of the NPs. In order to prevent any adverse effects induced by the NPs, it is important to determine the therapeutic windows of such new nanoformulations, by means of toxicity studies on cell cultures, complex tissue and finally on complex animals.[43]

1. Introduction

Many developed therapies for cancer, diabetes and cardiovascular diseases with very promising results have a common obstacle related to the side effects induced by lack of specificity of the therapeutic agents.[11] Therefore, the development of mechanisms to transport the therapeutic drug to the specific area to be treated is required. This improvement would lead to increase the efficiency and reduce side effects of the therapeutic agents.

Among the different strategies developed for drug delivery, polymeric nanocapsules are presenting the most promising results. The magnetic NPs could be used in order to direct the magnetic nanocarriers to specific organs. Two main approaches have been proposed: 1) Application of an external magnetic field in order to guide the NP to the target point and 2) insertion of small permanent magnets inside the body. Moreover, the main success on NPs vectorization to tumours is based on the Enhanced Permeability and Retention Effect (EPR effect). This effect is based on the capability of tumoural tissues to absorb higher size objects due to the increase of permeability of the tumoral vasculature.[44]

Furthermore, the functionalization of NPs surface with molecules with affinity for specific tissues can also induce a preferential tumoral cellular uptake of NPs. Then, the release of the drug would take place by the continuous biodegradation of the polymeric NP. The insertion of a magnetic-polymeric composite material would offer a novel mechanism by which the release of the drug can be triggered externally.

Moreover, the insertion of a magnetic component in the nanocarrier also provides a way to control the therapeutic agent release by means of the previously mentioned magnetic hyperthermia response. The temperature increase would stimulate the polymeric shell decomposition, polymer

swelling or induce the rupture of the NP-drug bond or interaction. For instance, Dias *et al* analyzed the temperature gradient caused by magnetic hyperthermia by a fluorophore functionalized DNA denaturalization, as a molecular thermometer.[45] This provides the opportunity to control the drug release by modifying the applied external alternating magnetic field. In the same way, polymeric materials tend to gelify or decompose in relatively low temperatures that can be achieved by magnetic hyperthermia.[46] Otherwise, Kaamyabi *et al* reported the preparation of a pH and thermosensitive polymer for drug delivery applications.[47] The high thermosensibility of this polymer, which decomposes at temperatures above 40 °C, could selectively release the encapsulated only in cancerous cells due to their higher temperature.

With the aim of obtaining the best possible results in future magnetic hyperthermia cancer treatments and drug delivery, two different systems will be developed in the present work. On the one hand, different ferrite systems based on Ni and Mn ferrites and core shell structures will be prepared and characterized in order to obtain samples with intense magnetic hyperthermia response for hyperthermia treatments. On the other hand, the sample with the best magnetic response will be encapsulated in a biopolymer in order to obtain a magnetic NP-biopolymer composite nanosphere, to be applied as drug controlled release agent. Finally, the viability of single and encapsulated NP systems for such applications will be tested by means of *in vitro* and *in vivo* toxicity experiments in cell cultures and animals.

References

(1) Huang, C.; Notten, A.; Rasters, N. Nanoscience and Technology Publications and Patents: A Review of Social Science Studies and Search Strategies. *J. Technol. Transf.* **2011**, 36 (2), 145–172.

(2) Yin, Y.; Alivisatos, a P. Colloidal Nanocrystal Synthesis and the Organic-Inorganic Interface. *Nature* **2005**, 437 (7059), 664–670.

(3) Le Duc, G.; Miladi, I.; Alric, C.; Mowat, P.; Bräuer-Krisch, E.; Bouchet, A.; Khalil, E.; Billotey, C.; Janier, M.; Lux, F.; et al. Toward an Image-Guided Microbeam Radiation Therapy Using Gadolinium-Based Nanoparticles. *ACS Nano* **2011**, 5 (12), 9566–9574.

(4) Richard P. Feynman. There's a Plenty of Room At the Bottom. *Eng. Sci.* **1960**, 23, 22–36.

(5) Hansma, P. K.; Tersoff, J. Scanning Tunneling Microscopy. *J. Appl. Phys.* **1987**, 61 (2), R1.

(6) Haque, M.; Saif, M. B. T. A Review of MEMS-Based Microscale and Nanoscale Tensile and Bending Testing. *Exp. Mech*. **2003**, 43 (3), 248–255.

(7) Kloch, C. C. Nanostructured Materials. Processing, Properties, and Applications, Second edi.; Gary, M., Ed.; William Andrew: Norwich, NY, U.S.A., **2007**.

(8) Liu, H.; Webster, T. J. Nanomedicine for Implants: A Review of Studies and Necessary Experimental Tools. *Biomaterials* **2007**, 28 (2), 354–369.

(9) Faraji, M.; Yamini, Y.; Rezaee, M. Magnetic Nanoparticles: Synthesis, Stabilization, Functionalization, Characterization, and Applications. *J. Iran. Chem. Soc.* **2010**, 7 (1), 1–37.

(10) Knobel, M.; Nunes, W. C.; Socolovsky, L. M.; De Biasi, E.; Vargas, J. M.; Denardin, J. C. Superparamagnetism and Other Magnetic Features in Granular Materials: A Review on Ideal and Real Systems. *J. Nanosci. Nanotechnol.* **2008**, 8 (6), 2836–2857.

(11) Ito, A.; Shinkai, M.; Honda, H.; Kobayashi, T. Medical Application of Functionalized Magnetic Nanoparticles. *J. Biosci. Bioeng*. **2005**, 100 (1), 1–11.

(12) Wu, A.; Ou, P.; Zeng, L. Biomedical Applications of Mmagnetic Nanoparticles. *Nano* **2010**, 5 (5), 245–270.

(13) Pinna, N.; Grancharov, S.; Beato, P.; Bonville, P.; Antonietti, M.; Niederberger, M. Magnetite Nanocrystals: Nonaqueous Synthesis, Characterization, and Solubility. *Chem. Mater*. **2005**, 17 (11), 3044–3049.

(14) Krishnan, K. M. Biomedical Nanomagnetics: A Spin through Possibilities in Imaging, Diagnostics, and Therapy. *IEEE Trans. Magn.* **2010**, 46 (7), 2523–2558.

(15) Mameli, V.; Musinu, A.; Ardu, A.; Ennas, G.; Peddis, D.; Niznansky, D.; Sangregorio, C.; Innocenti, C.; Thanh, N. T. K.; Cannas, C. Studying the Effect of Zn-Substitution on the Magnetic and Hyperthermic Properties of Cobalt Ferrite Nanoparticles. *Nanoscale* **2016**, 8, 10124–10137.

(16) Deepak, F. L.; Bañobre-López, M.; Carbó-Argibay, E.; Cerqueira, M. F.; Piñeiro-Redondo, Y.; Rivas, J.; Thompson, C. M.; Kamali, S.; Rodríguez-Abreu, C.; Kovnir, K.; et al. A Systematic Study of the Structural and Magnetic Properties of Mn-, Co-, and Ni-Doped Colloidal Magnetite Nanoparticles. *J. Phys. Chem. C* **2015**, 119 (21), 11947–11957.

(17) Hill, R. J.; Craig, J. R.; Gibbs, G. V. Systematics of the Spinel Structure Type. *Phys. Chem. Miner*. **1979**, 4 (4), 317–339.

(18) Cullity, B. Introduction to Magnetic Materials; Addison-Wesley: Massachussets, **1972**.

(19) Sòshin Chikazumi. Physics of Ferromagnetism; Oxfod Science Publications: Oxford, U.K., **2009**.

(20) Miyazaki, T.; Hanmin, J. The Physics of Ferromagnetism; Springer: Berlin, **2012**.

(21) Bercoff, P. G.; Bertorello, H. R. Exchange Constants and Transfer Integrals of spine1 Ferrites. *J. Magn. Magn. Mater.* **1997**, 169, 314–322.

(22) Pereira, C.; Pereira, A. M.; Fernandes, C.; Rocha, M.; Mendes, R.; Guedes, A.; Tavares, P. B.; Grene, J.; Arau, P.; Freire, C. Superparamagnetic MFe2O4 (M = Fe , Co , Mn) Nanoparticles: Tuning the Particle Size and Magnetic Properties through a Novel One-Step Coprecipitation Route. *Chem. Mater.* **2012**, 4, 1496–1504.

(23) Chen, R.; Christiansen, M. G.; Anikeeva, P. Maximizing Hysteretic Losses in Magnetic Ferrite Nanoparticles via Model-Driven Synthesis and Materials Optimization. *ACS Nano* **2013**, 7 (10), 8990–9000.

(24) Jia, X.; Chen, D.; Jiao, X.; He, T.; Wang, H.; Jiang, W. Monodispersed Co, Ni-Ferrite Nanoparticles with Tunable Sizes: Controlled Synthesis, Magnetic Properties, and Surface Modification. *J. Phys. Chem. C* **2008**, 112 (4), 911–917.

(25) Jang, J.; Nah, H.; Lee, J.-H.; Moon, S. H.; Kim, M. G.; Cheon, J. Critical Enhancements of MRI Contrast and Hyperthermic Effects by Dopant-Controlled Magnetic Nanoparticles. *Angew. Chem. Int. Ed. Engl*. **2009**, 48 (7), 1234–1238.

(26) McNerny, K. L.; Kim, Y.; Laughlin, D. E.; McHenry, M. E. Chemical Synthesis of Monodisperse γ-Fe–Ni Magnetic Nanoparticles with Tunable Curie Temperatures for Self-Regulated Hyperthermia. *J. Appl. Phys.* **2010**, 107 (9), 09A312.

(27) Thakur, S.; Rai, R.; Sharma, S. Structural Characterization and Magnetic Study of NiXFe3-XO4 Synthesized by Co-Precipitation Method. *Mater. Lett.* **2015**, 139, 368–372.

(28) Zhang, Q.; Castellanos-rubio, I.; Munshi, R.; Orue, I.; Pelaz, B.; Gries, K. I.; Parak, W. J.; Pino, P.; Pralle, A. Model Driven Optimization of Magnetic Anisotropy of Exchange-Coupled Core-Shell Ferrite Nanoparticles for Maximal Hysteretic Loss. *Chem. Mater.* **2015**, 27, 7380–7387.

(29) Sun, S.; Zeng, H.; Robinson, D. B.; Raoux, S.; Rice, P. M.; Wang, S. X.; Li, G. Monodisperse MFe_2O_4 (M = Fe , Co , Mn) Nanoparticles. *J. Am. Chem. Soc*. **2004**, 4 (1), 126–132.

(30) Mazario, E.; Sánchez Marcos, J.; Menéndez, N.; Cañete, M.; Mayoral, A.; Rivera-

Fernandez, S.; De La Fuente, J. M.; Herrasti, P. High Specific Absorption Rate and Transverse Relaxivity Effects in Manganese Ferrite Nanoparticles Obtained by Electrochemical Route. *J. Phys. Chem. C* **2015**, 150304123957002.

(31) Burda, C.; Chen, X.; Narayanan, R.; El-Sayed, M. A. Chemistry and Properties of Nanocrystals of Different Shapes. *Chem. Rev.* **2005**, 105 (4), 1025–1102.

(32) Laurent, S.; Forge, D.; Port, M.; Roch, A.; Robic, C.; Vander Elst, L.; Muller, R. N. Magnetic Iron Oxide Nanoparticles: Synthesis, Stabilization, Vectorization, Physicochemical Characterizations, and Biological Applications. *Chem. Rev.* **2008**, 108 (6), 2064–2110.

(33) Bonnemain, B. Superparamagnetic Agents in Magnetic Resonance Imaging: Physicochemical Characteristics and Clinical Applications A Review. *J. Drug Target.* **1998**, 6 (3), 167–174.

(34) Dutz, S.; Clement, J. H.; Eberbeck, D.; Gelbrich, T.; Hergt, R.; Müller, R.; Wotschadlo, J.; Zeisberger, M. Ferrofluids of Magnetic Multicore Nanoparticles for Biomedical Applications. *J. Magn. Magn. Mater*. **2009**, 321 (10), 1501–1504.

(35) Worsch, C.; Büttner, M.; Schaaf, P.; Harizanova, R.; Rüssel, C.; Schmidl, F.; Seidel, P. Magnetic Properties of Multicore Magnetite Nanoparticles Prepared by Glass Crystallisation. *J. Mater. Sci*. **2013**, 48 (6), 2299–2307.

(36) Müller, K.; Skepper, J. N.; Posfai, M.; Trivedi, R.; Howarth, S.; Corot, C.; Lancelot, E.; Thompson, P. W.; Brown, A. P.; Gillard, J. H. Effect of Ultrasmall Superparamagnetic Iron Oxide Nanoparticles (Ferumoxtran-10) on Human Monocyte-Macrophages in Vitro. *Biomaterials* **2007**, 28 (9), 1629–1642.

(37) Corot, C.; Robert, P.; Idée, J.-M.; Port, M. Recent Advances in Iron Oxide Nanocrystal Technology for Medical Imaging. *Adv. Drug Deliv. Rev*. **2006**, 58 (14), 1471–1504.

(38) Castellanos-Rubio, I.; Insausti, M.; Garaio, E.; Gil de Muro, I.; Plazaola, F.; Rojo, T.; Lezama, L. Fe3O4 Nanoparticles Prepared by the Seeded-Growth Route for Hyperthermia: Electron Magnetic Resonance as a Key Tool to Evaluate Size Distribution in Magnetic Nanoparticles. *Nanoscale* **2014**, 6, 7542–7552.

(39) Corchero, J. L.; Villaverde, A. Biomedical Applications of Distally Controlled Magnetic Nanoparticles. *Trends Biotechnol*. **2009**, 27 (8), 468–476.

(40) Plazaola, F.; Garaio, E.; Collantes, J. M.; Castellanos, I.; Insausti, M.; de Muro, I. G.; Garcia, J. A. Specific Absorption Rate of Magnetite Nanoparticle Powders With and Without Surrounding Organic Ligands. *Journal of Nanoscience and Nanotechnology*. **2012**, pp 7451–7455.

(41) Jordan, A.; Scholz, R.; Wust, P.; Schirra, H.; Thomas Schiestel; Schmidt, H.; Felix, R. Endocytosis of Dextran and Silan-Coated Magnetite Nanoparticles and the Effect of Intracellular Hyperthermia on Human Mammary Carcinoma Cells in Vitro. *J. Magn. Magn. Mater*. **1999**, 194 (1), 185–196.

(42) Mornet, S.; Vasseur, S.; Grasset, F.; Duguet, E. Magnetic Nanoparticle Design for Medical Diagnosis and Therapy. *J. Mater. Chem*. **2004**, 14 (14), 2161.

(43) Moros, M.; Ambrosone, A.; Stepien, G.; Fabozzi, F.; Marcherano, V.; Castaldi, A.; Tino,

A.; M. de la Fuente, J.; Tortiglione, C. Deciphering Intracellular Events Triggered by Mild Magnetic Hyperthermia in Vitro and in Vivo. *Nanomedicine (Lond.)* **2015**, 10 (14), 2167–2183.

(44) Ahmad, Z.; Zahoor, a; Sharma, S.; Khuller, G. K. Inhalable Alginate Nanoparticles as Antitubercular Drug Carriers against Experimental Tuberculosis. *Int. J. Antimicrob. Agents* **2005**, 26 (4), 298–303.

(45) Dias, J. T.; Moros, M.; Del Pino, P.; Rivera, S.; Grazú, V.; de la Fuente, J. M. DNA as a Molecular Local Thermal Probe for the Analysis of Magnetic Hyperthermia. *Angew. Chem. Int. Ed. Engl*. **2013**, 52 (44), 11526–11529.

(46) Jeong, B.; Bae, Y. H.; Lee, D. S.; Kim, S. W. Biodegradable Block Copolymers as Injectable Drug-Delivery Systems. *Nature* **1997**, 388, 860–862.

(47) Kaamyabi, S.; Habibi, D.; Amini, M. M. Preparation and Characterization of the pH and Thermosensitive Magnetic Molecular Imprinted Nanoparticle Polymer for the Cancer Drug Delivery. Bioorganic *Med. Chem. Lett*. **2016**, 26 (9), 2349–2354.

OBJECTIVES

One of the areas of interest of nanomaterials research, nowadays, is directed to exploit the possibilities of magnetic nanomaterials in biomedicine. In this way, this kind of nanosystems, especially those based on Superparamagnetic Iron Oxide Nanoparticles (SPION) are being deeply investigated to be applied as contrast agents in Magnetic Resonance Imaging (MRI), drug delivery, controlled release agents or as magnetic hyperthermia inductors for cancer treatments.

In this research area there are three different issues to be developed: 1) Optimization of the magnetic properties of the nanoparticles nuclei in order to obtain a higher magnetic hyperthermia response; 2) Functionalization of NPs surface to make them stable in physiological conditions, obtain long circulation times in human body and reducing recognition by the immunological system, improving the active targeting to tumour or damaged tissues; 3) Toxicity studies of such nanomaterials.

The present work is focused on developing nanomaterials suitable to be applied in biomedical applications, analyzing all these steps (preparation of magnetic core, functionalization and *in vivo/in vitro* testing) necessary to ascertain its applicability in such areas.

- In order to obtain improved hyperthermia responses, magnetite nanoparticles will be doped with paramagnetic cations (Ni^{2+} and Mn^{2+}). The different doping level of these cations modifies the saturation magnetization and anisotropy constant, and the direct magnetic hyperthermia response will be also affected in some way. Furthermore, some core shell structures composed by magnetite and

Ni ferrite layers are going to be prepared to analyze the significant properties changes induced by the presence of both phases.

- The magnetic nanoparticles with maximum hyperthermia response will be selected as base material and different functionalizations will be performed to make the nanoparticles stable in physiological media. On the one hand, nanoparticles will be coated with the poly (maleic anhydride-alt-1-octadecene) (PMAO) amphiphilic polymer, which covers single NPs by hydrophobic interactions, exposing negative carboxylic groups on the surface. On the other hand, magnetic nanospheres will be formed by the aggregation of NPs with chitosan or fibroin. The functionalization process with such polymers could increase their biocompatibility, besides inducing changes in magnetic properties due to NP agglomeration.

- Finally, the biocompatibility of the samples considered as most suitable for possible applications will be tested in cell culture and in mice. Firstly, the direct cytotoxicity of the prepared compounds in short time period will be tested in Vero cell cultures by the MTT cytotoxicity test. Moreover, in a blood vessel model co-culture, several effects such as oxidative stress or inflammatory response induced by the contact of the nanocompounds will be verified. Finally, the biodistribution of the most promising sample will be analyzed by means of an *in vivo* experiment in mice.

2. NANOCOMPOUND PREPARATION

Different ferrite based nanoparticles have been prepared based on the thermal decomposition bottom up synthetic method. After analyzing the structural and magnetic properties of all obtained NP systems and having tested their magnetic hyperthermia response, the sample which shows the most suitable properties for biomedical applications has been selected as base material for the preparation of biopolymeric magnetic nanospheres. They have been formed by encapsulating the optimal magnetic nanoparticles into different biopolymeric matrices, being the chitosan coated magnetic nanospheres the most deeply studied ones.

2.1 Synthesis of $M_XFe_{3-x}O_4$ magnetic nanoparticles

There is a large number of methods that can be used to prepare NPs, divided in top down and bottom up methods. The bottom up methods are more suitable to prepare ferrite NPs directed to be applied in biomedical applications, as the surface chemistry and colloidal stability can be controlled. According to the literature, ferrite NPs have been commonly synthesized by the co-precipitation method, using the desired metal salts as precursors ($NiCl_2$, $MnCl_2$ or $FeCl_3$) to prepare nickel and manganese ferrites, for instance.[1,2] In some cases, solvothermal and microemulsion mechanisms have also been used to achieve ferrite NPs in colloidal dispersion.[3,4] However, not well defined NP shapes and broad size dispersions are usually obtained by these methods. In this sense, the thermal decomposition method is the most promising one to prepare NPs for such applications, as well defined and homogeneous sized NPs are obtained. The proportion of

the inserted metals can be easily controlled through this method by regulating the amount of each metal precursor.[5] Furthermore, some authors have reported an optimized method to grow the NPs and to prepare core-shell NPs by this chemical route.[6]

The formation of monodisperse NPs (with standard deviations below 5%) in liquid media by chemical methods was described by means of the LaMer diagram (Figure 1.5).[7] It was observed that when the precursors concentration overtakes a certain point (related to the solubility of the precursor compound in the media), the nucleation of NPs spontaneously occurs, reducing the high Gibbs free energy levels of the supersaturated solution, as can be described in the equation 2.1:

$$\Delta G_v = -\frac{kT}{\Omega}\ln\left(\frac{C}{C_0}\right) \quad (2.1)$$

Where C is the solute concentration, C_0 the solubility, T the temperature, Ω the atomic volume and k the Boltzmann constant. When solute concentration (C) overtakes the solubility value (C_0), the Gibbs energy is negative and the nucleation starts spontaneously. Those generated nuclei only would be stable if they reach the critical radius (r*), which is defined by a balance between the total Gibbs energy of the solution and the surface energy (equation 2.2):

$$r^* = -2\frac{\gamma}{\Delta G_v} \quad (2.2)$$

Where γ is the surface energy per unit area. The size and shape of these initial NPs depend strongly on the external conditions during the nucleation as ligands presence, temperature or solvent viscosity. Thus, the used synthesis procedure plays an important role.[8] The nucleation speed is the parameter which defines the diameter of the initially formed NPs, as a fast nucleation yields smaller nanoparticles whereas slower nucleations produce

nanoparticles with larger sizes. The nucleation speed is mainly related to the material. However, this speed can be partially modified by controlling the precursor concentration during the nucleation (Figure 2.1). Hence, at low concentration the nucleation will be slower and the size of the obtained NPs larger while at high precursor concentration a quicker nucleation is induced, obtaining a higher amount of small NPs.

When the precursor concentration decreases below the nucleation concentration value the nucleation process stops and the growth phase begins, in which the formed NP seeds tend to grow by atom diffusion on the surface of the formed NPs and by aggregation of absorbed species on the surface. Thus, the NP formation can be controlled by diffusion or by surface processes. For instance, low precursor concentrations would kinetically favour the diffusion mediated growth mechanism, obtaining homogeneous size dispersions.[8] In this sense, longer growth times would produce larger particles, until a certain point where the precursor concentration reaches the equilibrium. Therefore, the NP growth is not limited and the NP size can be progressively increased by modifying the precursor concentration.[9,6]

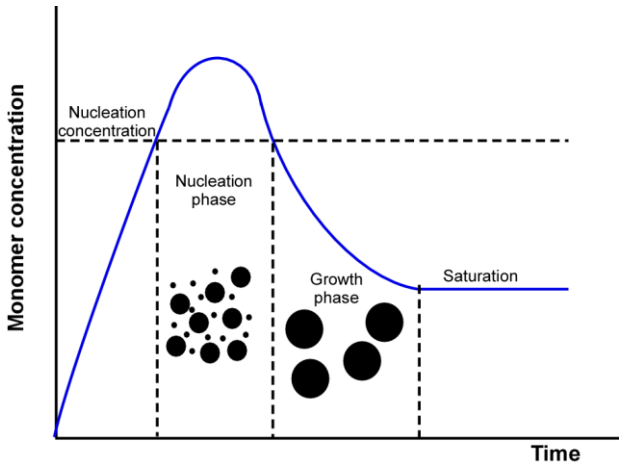

Figure 2.1. *Schematic illustration of nanoparticle formation process in solution (LaMer diagram).*

Although the chemical NP synthesis follows this process, another variables are involved in the mechanism as temperature, pH, fluids ionic strength, presence of surfactants or reactant amounts, which can also affect the nucleation and growth phases. Therefore, this kind of methods always requires an optimization process to achieve an absolute control of the synthesis variables.

2.1.1 Nanoparticle chemical synthesis methods

As previously mentioned, the mostly used chemical methods to prepare homogeneous NPs are the sol-gel, co-precipitation, microemulsion, solvothermal and the thermal decomposition of metalorganic precursors.

- **Sol gel synthesis method**

It is based on the preparation of a diluted solution with the chemical precursors that are necessary to obtain the desired material. In this diluted solution (sol) the gravitational forces are negligible and only surface charges and Van der Waals forces between molecules have influence. When the solvent evaporates a semi-rigid mixture called gel is formed. The proximity between the molecules and ions in the gel solution induces the formation of a continuous network between them, activating the chemical reaction. A calcination process is usually required to favour the polycondensation and enhance the mechanical properties.

In order to prepare NPs, the addition of surfactants and ligands, which limit the particle growth is necessary. However, the sol-gel method is not the best way to prepare NPs to be applied in colloidal dispersion, as the calcination process removes all the surfactants and induces NP aggregation. Thus, although the sol-gel method is usually employed to obtain ceramic

materials as mixed oxides, it is not useful to obtain NP colloidal dispersions.[10,11]

- **Co-precipitation method**

This is probably the mostly used method to obtain ferrite NP colloidal dispersions from aqueous salt solutions. For ferrite materials, this process is performed by the addition of metal ion precursors to a basic solution in the 8-12 pH range:

$$M^{2+} + 2Fe^{3+} + 8OH^{-} \rightarrow MFe_2O_4 + 4H_2O$$

The temperature has an important role in this process, as larger NPs will be obtained at higher reaction temperatures. Furthermore, the size, shape and composition of the obtained NPs depend also on the type of the used metallic salts (chlorides, sulphates and nitrates are the most common ones), the metal ratio, pH value and ionic strength. This synthesis method is representative of the multivariable synthesis process mentioned previously, being a complete optimization and conditions screening necessary to achieve a deep understanding of all variables and to control the final materials properties.[12]

The oxidation tendency of ferrite materials has also to be considered. Therefore, this process needs to be performed under inert (nitrogen or argon) atmospheres to avoid the oxidation process to maghemite (γ-Fe_2O_3) or hematite (α-Fe_2O_3). Ligands which are compatible with NP surface -OH groups can be added to the synthesis process in order to control the surface chemistry of the prepared NPs.[13]

Although this synthesis method shows a number of advantages as its simplicity, colloidal stability of NPs or its functionability, the control of the size and shape of the NPs is not very accurate.

- **Microemulsion method**

The water-in-oil microemulsion method is based on a mixture of water, which contains the NP precursors, surfactants and oil to obtain a transparent uniform solution. In this solution, by the interface tension reduction produced by the surfactant molecules, micro or nanodrops are formed with the reactants inside them, surrounded by surfactant molecules, which form the micelles.

The NP formation synthesis process occurs inside these micelles. The surfactant molecules surrounding water drops act as a wall that avoids or limits the growth of the formed particles, being impossible to overtake the micelle size. Moreover, by changing the water-in-oil mixture range, surfactant or organic phase type, the micelles size and shape can be modified and, therefore, the size and shape of NPs can also be adjusted.[3,14]

As was reported by Vidal-Vidal *et al*, maghemite NPs can be prepared by the microemulsion method, obtaining well defined and homogeneous NPs of 3.5 nm.[15] However, although NPs form a stable colloidal dispersion in water media, the presence of aggregates in colloidal dispersion can be observed through TEM micrographs and DLS measurements. Therefore, their instability might change strongly the NP properties dispersed in liquid media, that is not desirable in biomedical treatments.

- **Solvothermal synthesis**

The solvothermal synthesis process, called hydrothermal when water is used as a solvent, is a usual synthesis process in liquid media. However, it is performed in temperatures above the boiling temperature of the used solvent at high pressures, which can be higher than 2000 psi. The high temperature induces a better formation of the nanocrystals and also the

preparation of nanostructures that do not assemble in the normal liquid temperature range of the used solvent.

Many authors have used this method to prepare ferrite NPs, limiting the particle growth by surfactants and ligands addition.[4,16] In this sense, well formed NPs with average diameters around 40 nm and relatively good magnetic response, not too far from the bulk material response, have been obtained.[17] The high crystallinity and the possibility to obtain specific NP shapes and large sizes present it as an interesting method to produce ferrite NPs for many applications. Nevertheless, in the same way as in the microemulsion method, due to the excessive size of the obtained particles, as well as their low colloidal stability in water media (because of their great tendency to aggregation), the resultant particles are useless for biomedical applications.

- **Thermal decomposition method**

This is, by far, the most widely used method to prepare ferrite NPs for biomedical applications. It was used by Sun *et al* in 2002 to prepare ferrite nanoparticles. The size, shape and structure homogeneity, as well as the high magnetic response of resultant particles, became it the most common ferrite NP synthesis method.[18]

It is based on the decomposition of metal precursors, as acetylacetonates, carbonyls or oleates, at temperatures around 200-300 °C in high boiling point organic solvents, as benzyl ether or octadecene. The presence of dispersants and hydrophobic ligands is required to control NP size and to become stable in organic solvents. The average diameters obtained by this method are in the 4-25 nm range, with quite narrow size dispersions. This average size can be controlled by modifying the nucleation, the growth temperature or the precursors and ligands concentrations. NPs prepared by this method show

magnetic, structural and colloidal properties suitable for biomedical applications. However, the resultant NPs are only stable in non-polar media, therefore, a surface modification process is absolutely necessary to become stable in physiological media.[19,6]

This last method has been chosen for the preparation of the ferrite based $M_XFe_{3-x}O_4$ (M = Ni, Mn) nanoparticles described in this thesis. This technique is also usually used to obtain Fe, Co and Ni metal, metal oxide, sulphide, halogenide and phosphate nanoparticles.[18,20]

The synthesis mechanism is divided in two main steps: in the first step, the solvent containing the metalorganic precursors, surfactants and stabilizing agents is heated applying a constant heating rate to the nucleation temperature (precursor decomposition temperature). After this first nucleation phase, the solution is again heated in a constant heat rate until the boiling point of the solvent. The solution is kept in reflux for certain time (growth phase) and then is cooled to room temperature. All the process must be performed in a close system under inert atmosphere to avoid the spontaneous oxidation.[21]

Many different kind of metalorganic precursors can be used as acetylacetonates, metal cupferronates or carbonyls.[22,23] Depending on the precursors the reaction mechanism could change strongly, since the nanoparticle nucleation process is directly related to the precursor decomposition.[20,22,24,] Another critical factor in this synthesis mechanism is the boiling point of the used organic solvent. Higher boiling points allow higher synthesis temperatures, which modify the nanoparticle growth and directly affect the size and shape of the obtained nanoparticles. In this way, the most used solvents are benzyls and long chain hydrocarbons as octadecene.[25,26,27]

2. Nanocompound preparation

To stabilize the synthesized nanoparticles in the organic solvent, the presence of specific ligands, which interact and cover the nanoparticle surface is necessary. These molecules are usually long aliphatic chain molecules to stabilize NPs in nonpolar media, with functional groups (as carboxylic acid or amine) able to perform strong interactions with nanoparticle surface -OH groups.[28] Furthermore, a stabilization agent, which controls the nanoparticle growth, is also necessary to obtain homogeneous and stable dispersions. Stabilization agents form weak interactions with NP surface to prevent their aggregation during the growth phase of the synthesis by steric repulsions.[23,29]

In this thesis, to obtain ferrite based nanoparticles, the chosen organometallic precursors were acetylacetonate compounds, $Fe(acac)_3$, $Ni(acac)_2$ or $Mn(acac)_2$. The decomposition temperature of these compounds is around 200 °C in all cases, which is suitable to achieve a homogeneous nucleation of NPs. Dibenzyl ether has been chosen as solvent since its boiling temperature (289 °C) is high enough for the nucleation and growth of NPs, and also makes easier the washing process of nanoparticles due to its miscibility with ethanol. Concerning the NP coating agents, the commonly used ligand has been the oleic acid. It has been proved that an additional coating agent as oleylamine induces a competence effect which could improve the size and shape homogeneity of the obtained nanoparticles.[21,29] The presence of a stabilizing agent as 1,2-hexadecanediol has being previously used to increase strongly the size homogeneity.[30] The aim of this compound during the synthesis process is to stabilize and separate the nanoparticles avoiding aggregations by steric effects. The structural formula of all used reagents are represented in Figure 2.2.

In this sense, besides the nature and concentration of the metalorganic reagents, in order to achieve a good control of size, shape, and crystallinity of

final nanoparticles, the concentration of the reagents, the metal precursors and ligands proportion, the amount of stabilizing agent, the heating rate, the boiling temperature and the reflux time are other parameters to take into account.[30]

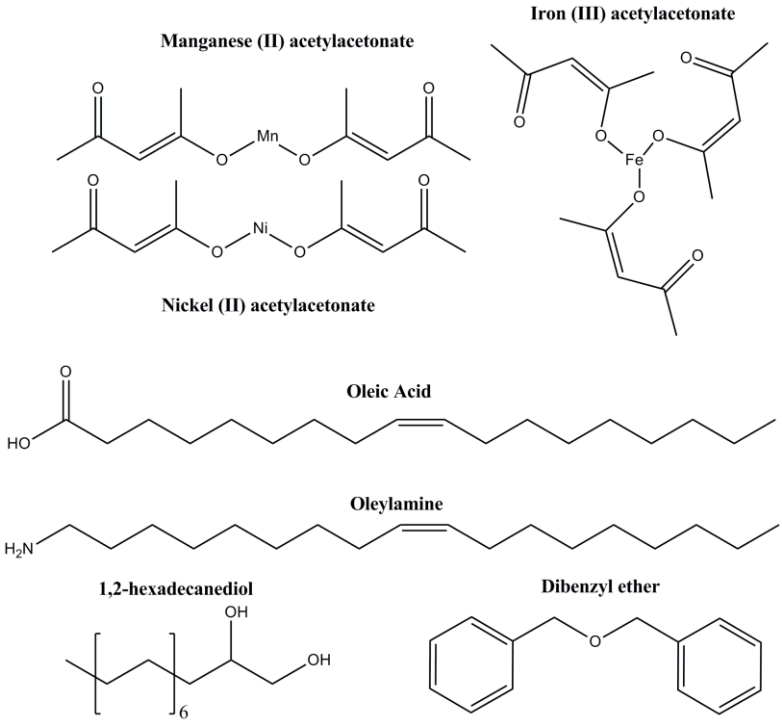

Figure 2.2. *Structural formula of the reagents used during the thermal decomposition synthesis of the prepared ferrite nanoparticles.*

Controlling these parameters, the size of the obtained nanoparticles can be fixed to average diameters in the 8-12 nm range, with narrow size distribution values. However, to achieve a high hyperthermia response, it is necessary to obtain larger particles without increasing the size distribution values. This size increase has been achieved by a multistep seeded-growth technique, which is based on subsequent additions of metalorganic precursor and surfactants on already formed nanoparticle seeds. In previous

studies, this kind of techniques were performed by inducing the NP growth in different synthetic steps.[31] Thus, a standard nanoparticle synthesis is performed following the normal thermal decomposition method and, in a second synthesis process, these nanoparticles are used as seeds and heated again in the presence of metalorganic precursor and surfactants in order to grow these primary nanoparticles. However, it has been recently reported a similar growth effect by means of the one pot method. In this case, instead of washing the nanoparticles to be used as seeds in the growth process, the seed nanoparticles are directly growth in the same synthesis by adding the precursor and the surfactants on the freshly synthesized NPs.[32] By repeating this process several times, controlling the added amount of precursor in each case, the desired sizes can be obtained.[24] This technique also provides an interesting way to produce core shell nanoparticles with different material layers, by adding different precursors in each addition process.

Taking the used metal reagents into account, ferrites with $Ni_xFe_{3-x}O_4$ or $Mn_xFe_{3-x}O_4$ general formula have been prepared. Moreover, in order to modify the anisotropy of the resultant particles core-shell NPs have been prepared by following the previously explained seed mediated growth technique, combining Ni and Mn ferrites layers with magnetite.

2.1.2 Synthesis of nickel ferrite nanoparticles, $Ni_xFe_{3-x}O_4$ (0.3<x<0.9)

Different ferrite nanoparticle samples with different percentages of nickel were prepared by mixing stoichiometric proportions of nickel (II) and iron (III) acetylacetonates. In a standard synthesis process, 2.2 mmol of a $Fe(acac)_3$ ($Fe(C_5H_7O_2)_3$) and $Ni(acac)_2$(($Ni(C_5H_7O_2)_2$) mixture, 1.3 g of oleic acid ($C_{18}H_{34}O_2$, 4.4 mmol), 1.7 g of oleylamine ($C_{18}H_{35}NH_2$, 4.4 mmol), 2.5 g of 1,2-hexadecanediol ($CH_3(CH_2)_{13}CHOHCH_2OH$, 8.8 mmol) and 25 mL of benzyl ether ($(C_6H_5CH_2)_2O$) were mixed and mechanically stirred in a close system

under Ar flow for 15 minutes. The schematic representation of the system appears in Figure 2.3. Then, maintaining the Ar atmosphere, the mixture was first heated to 200 °C at 5.5 °C /min heat rate and kept for 30 min at that temperature for a complete nucleation. Upon heating, the reaction mixture turned black. The solution was then raised to reflux (289 °C) at 3 °C/min and kept for 90 minutes (growth phase). After the growth phase the solution was cooled to room temperature and 50 mL of ethanol were added to destabilize the MNP colloidal dispersion. The mixture was kept at 4 °C overnight for the complete precipitation of the nanoparticles.

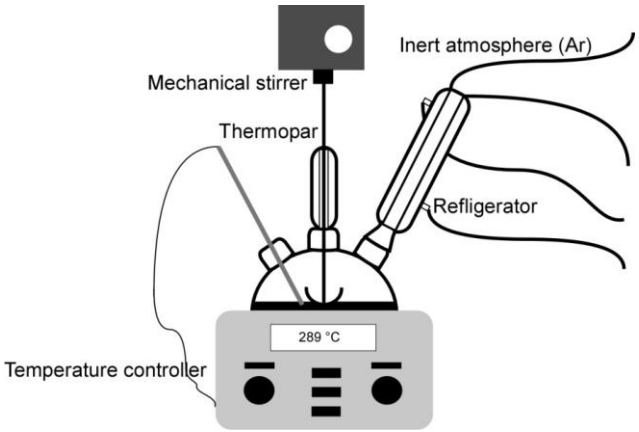

Figure 2.3. *Schematic representation of the system used for the preparation of nickel ferrite, manganese ferrite and core shell nanoparticles.*

By means of a permanent magnet, the MNPs were decanted and resuspended in toluene. Ferrite unstable aggregates were removed by centrifugation at 3000 rpm during 60 minutes. The MNP dispersion was three more times precipitated with ethanol and resuspended in toluene to eliminate the excess of precursor, surfactants and 1,2-hexadecanediol. They were finally resuspended in toluene (in 2 mgFe/mL concentration) with 10 % of oleic acid and oleylamine (to maintain the density of hydrophobic coating)

and were stored at 4 °C to slow down the oxidation. Using the reactant amounts shown in Table 2.1, four different systems were obtained by changing iron-nickel proportions, $Ni_{0.31}Fe_{2.69}O_4$, $Ni_{0.43}Fe_{2.57}O_4$, $Ni_{0.70}Fe_{2.30}O_4$ and $Ni_{0.86}Fe_{2.14}O_4$.

In order to achieve larger NPs for the $Ni_{0.31}Fe_{2.69}O_4$ composition, the previously mentioned seed mediated growth process was carried out. After the initial synthesis process, the solution was cooled and kept at room temperature for 30 minutes. Then, 2.34 mmol of Fe $(acac)_3$, 0.26 mmol $Ni(acac)_2$, 3.02 mmol of oleic acid, 3.02 mmol of oleylamine and 2.25 mmol of 1,2-hexadecanediol were added. This mixture was heated to 200 °C for 30 minutes and to reflux for 90 minutes, as in the first step. After cooling and keeping at room temperature for 30 min, the process was repeated twice increasing the amounts of reagents, as can be observed in the Table 2.1.

During this synthesis process, different diameter particles have been obtained in the different addition processes. In order to isolate these different groups and to obtain monodisperse nanoparticle samples, a separation process needs to be performed. Hence, after the synthesis and washing process, the nanoparticle dispersion was destabilised by means of different toluene:ethanol mixtures. Firstly, nanoparticles were dispersed in 21 mL of toluene and 7 mL of ethanol (3:1 toluene:ethanol). The precipitated NPs were isolated by means of a permanent magnet, resuspended in toluene with 10 % of oleic acid and oleylamine and stored at 4 °C ($Ni_{0.31}Fe_{2.29}O_4$_A). The next nanoparticle group was destabilised by adding a total of 14 mL of ethanol (3:2), and were isolated and resuspended as previously explained ($Ni_{0.31}Fe_{2.29}O_4$_B). This group was only stored to compare its diameter with the largest ones ($Ni_{0.31}Fe_{2.29}O_4$_A). The NPs which did not precipitate were discarded.

Table 2.1. *Amounts of reagents used in all synthesis processes of nickel ferrite nanoparticles and the Fe:Ni metal proportion added in each case.*

SAMPLE	Fe:Ni	n (mmol)				V (mL)	
		$Fe(acac)_3$	$Ni(acac)_2$	Oleic acid	Oleylamine	1,2-Hexadecanediol	Benzyl ether
$Ni_{0.31}Fe_{2.69}O_4$	0.9:0.1	1.97	0.22	4.37	4.37	8.75	25
$Ni_{0.43}Fe_{2.57}O_4$	0.86:0.14	1.88	0.31	4.37	4.37	8.75	25
$Ni_{0.64}Fe_{2.36}O_4$	0.82:0.18	1.79	0.39	4.37	4.37	8.75	25
$Ni_{0.86}Fe_{2.14}O_4$	0.7:0.3	1.53	0.66	4.37	4.37	8.75	25
$Ni_{0.31}Fe_{2.69}O_4\_A$	0.9:0.1	11.51	1.28	14.16	14.16	18.00	55
1st Addition	0.9:0.1	1.97	0.22	4.37	4.37	8.75	25
2nd Addition	0.9:0.1	2.34	0.26	3.02	3.02	2.25	10
3rd Addition	0.9:0.1	3.78	0.42	3.80	3.80	3.50	10
4th Addition	0.9:0.1	3.42	0.38	2.97	2.97	3.50	10

2.1.3 Synthesis of manganese ferrite nanoparticles $Mn_xFe_{3-x}O_4$ (0.1<x<0.4)

The synthesis of manganese ferrite MNPs with different proportions of Mn in the structure was performed following the same method as described for Ni ferrite NP synthesis. In a standard preparation, $Fe(acac)_3$ ($Fe(C_5H_7O_2)_3$) and $Mn(acac)_2$(($Mn(C_5H_7O_2)_2$) mixture (2.2 mmol), 1.3 g of oleic acid ($C_{18}H_{34}O_2$, 4.4 mmol), 1.7 g of oleylamine ($C_{18}H_{35}NH_2$, 4.4 mmol), 2.5 g of 1,2-hexadecanediol ($CH_3(CH_2)_{13}CHOHCH_2OH$, 8.8 mmol) and 25 mL of benzyl ether (($C_6H_5CH_2)_2O$) were mixed and mechanically stirred in a close system under Ar flow for 15 minutes. Then, maintaining the Ar atmosphere, the mixture was first heated to 200 °C at 5.5 °C /min heating rate and kept for 30 min in that temperature for a complete nucleation. Upon heating, the reaction mixture turned black. The solution was then raised to reflux (289 °C) at 3 °C/min and kept for 90 minutes (growth phase). After the growth phase the solution was cooled to room temperature and 50 mL of ethanol were added to destabilize the MNPs. The mixture was kept at 4 °C overnight for a complete precipitation of the nanoparticles. All used reagent amounts are represented in Table 2.2.

As was performed for nickel ferrites, all main manganese ferrites were centrifuged at 3000 rpm during 60 minutes in order to remove the aggregates and the co-phases that could have been formed during the synthesis process. In this case, no co-phases were detected.

Table 2.2. *All amounts of reagents used and the Fe:Mn metal proportion in the synthesis processes of manganese ferrite.*

SAMPLE	Fe:Mn	n (mmol)				V (mL)	
		$Fe(acac)_3$	$Mn(acac)_2$	Oleic acid	Oleylamine	1,2-Hexadecanediol	Benzyl ether
$Mn_{0.13}Fe_{2.87}O_4$	0.90:0.10	1.97	0.22	4.37	4.37	8.75	25
$Mn_{0.18}Fe_{2.82}O_4$	0.86:0.14	1.88	0.31	4.37	4.37	8.75	25
$Mn_{0.27}Fe_{2.73}O_4$	0.82:0.18	1.79	0.39	4.37	4.37	8.75	25
$Mn_{0.36}Fe_{2.64}O_4$	0.70:0.30	1.53	0.66	4.37	4.37	8.75	25
$Mn_{0.18}Fe_{2.82}O_4$_A	0.90:0.10	11.51	1.28	14.16	14.16	18.00	55
1st Addition	0.90:0.10	1.97	0.22	4.37	4.37	8.75	25
2nd Addition	0.90:0.10	2.34	0.26	3.02	3.02	2.25	10
3d Addition	0.90:0.10	3.78	0.42	3.80	3.80	3.50	10
4th Addition	0.90:0.10	3.42	0.38	2.97	2.97	3.50	10

The $Mn_{0.18}Fe_{2.64}O_4$_A sample was prepared by the same seed mediated growth method used for $Ni_{0.31}Fe_{2.69}O_4$_A sample preparation, followed by the same separation process using different ethanol-toluene mixtures. All samples were stored at 4 °C (in a 2 mgFe/mL concentration) and 10% oleic acid toluene dispersions.

2.1.4 Synthesis of core shell mixed nanoparticles

Following the previously described optimized seed mediated growth method, several core-shell NPs have been synthesized. Thus, different metalorganic precursors were added in the different addition steps to form NPs with different composition layers. Four different core-shell NP samples were obtained using this technique composed by magnetite (Fe_3O_4) and nickel ferrite ($Ni_{0.31}Fe_{2.69}O_4$) layers in different configurations (Figure 2.4.). This combination of materials has been chosen based on the magnetic properties observed in the nanoparticles with this Ni proportion and the high magnetic anisotropy of magnetite.

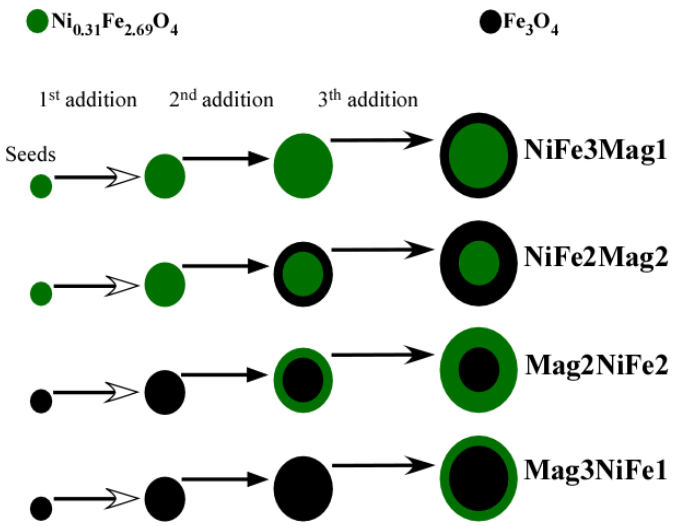

Figure 2.4. *Illustration of the different addition steps for each sample. Green colour represents $Ni_{0.31}Fe_{2.69}O_4$ phase and black colour Fe_3O_4 phase.*

2. Nanocompound preparation

To obtain the $Ni_{0.31}Fe_{2.69}O_4$ phase, $Ni(acac)_2$ and $Fe(acac)_3$ precursors were added in 1:9 proportion, whereas to obtain magnetite phase only $Fe(acac)_3$ precursor was added. In all cases the same total amount of precursor was added (Table 2.3). Same synthesis mechanism used to prepare $Ni_{0.31}Fe_{2.69}O_4$_A and $Mn_{0.18}Fe_{2.64}O_4$_A samples has been employed in this case. As can be observed in Figure 2.4, by changing the precursor addition order 4 different samples were obtained: NiFe3Mag1, NiFe2Mag2, Mag2NiFe2 and Mag3NiFe, where "NiFe" represents the $Ni_{0.31}Fe_{2.69}O_4$ nickel ferrite phase, "Mag" represents the magnetite phase and the numbers represent the number of layers of each phase. The phase codes in the names have been placed in the same order as the order of precursor addition during the synthesis. Thus, for the NiFe3Mag1 core-shell NP synthesis, firstly nickel ferrite NP seeds were prepared, performing two subsequent growth processes to produce two more nickel ferrite layers. However, only iron precursor was added in the last addition process to generate a magnetite layer in the external part of the NP. In order to prepare the second core-shell sample (NiFe2Mag2), nickel ferrite seeds were firstly prepared, followed by an addition of a Ni ferrite layer. The last two additions were performed by adding iron acethylacetonate precursor to form two external magnetite layers. The inverse procedure was followed to prepare the Mag2NiFe2 system, where two magnetite layers were firstly prepared covered by two external Ni ferrite layers. Finally, the last system (Mag3FeNi1) was prepared by synthesizing magnetite seeds with two subsequent iron precursor additions to obtain three magnetite layers. The last addition was performed by mixing Ni and Fe precursors, to obtain the Ni ferrite external layer.

After the synthesis, the separation process between nanoparticles of different sizes was performed in the same way as for the $Ni_{0.31}Fe_{2.69}O_4$_A sample, using only the larger nanoparticles (obtained in the first precipitation

Table 2.3. *Amounts of reagents used to prepare core shell nanoparticles and the Fe:Ni metal proportion added in each addition step.*

SAMPLE	Fe:Ni	n (mmol)				V (mL)	
		$Fe(acac)_3$	$Ni(acac)_2$	Oleic acid	Oleylamine	1,2-Hexadecanediol	Benzylether
NiFe3Mag1	0.93:0.07	11.89	0.9	14.16	14.16	18.00	55
Seeds	0.9:0.1	1.97	0.22	4.37	4.37	8.75	25
1st Addition	0.9:0.1	2.34	0.26	3.02	3.02	2.25	10
2nd Addition	0.9:0.1	3.78	0.42	3.80	3.80	3.50	10
3d Addition	1:0	3.80	0	2.97	2.97	3.50	10
NiFe2Mag2	0.96:0.04	12.31	0.48	14.16	14.16	18.00	55
Seeds	0.9:0.1	1.97	0.22	4.37	4.37	8.75	25
1st Addition	0.9:0.1	2.34	0.26	3.02	3.02	2.25	10
2nd Addition	1:0	4.20	0	3.80	3.80	3.50	10
3d Addition	1:0	3.80	0	2.97	2.97	3.50	10
Mag2NiFe2	0.94:0.06	11.99	0.80	14.16	14.16	18.00	55
Seeds	1:0	2.19	0	4.37	4.37	8.75	25
1st Addition	1:0	2.60	0	3.02	3.02	2.25	10
2nd Addition	0.9:0.1	3.78	0.42	3.80	3.80	3.50	10
3d Addition	0.9:0.1	3.42	0.38	2.97	2.97	3.50	10
Mag3NiFe1	0.97:0.03	12.41	0.38	14.16	14.16	18.00	55
Seeds	1:0	2.19	0	4.37	4.37	8.75	25
1st Addition	1:0	2.60	0	3.02	3.02	2.25	10
2nd Addition	1:0	4.20	0	3.80	3.80	3.50	10
3d Addition	0.9:0.1	3.42	0.38	2.97	2.97	3.50	10

step) for characterization. The samples were stored in toluene dispersions (with a concentration of 2 mgFe/mL) with 10% of oleic at 4 °C.

2.1.5 Biocompatibilization of ferrite nanoparticles.

One of the main disadvantages of the used synthesis method is the hydrophobic nature of the obtained NPs. As these nanoparticles will be applied in biomedicine, a change in the surface chemistry is required to become the NPs stable in physiological media and maintain the colloidal stability during the treatments.[1,33,34] This process is necessary to analyze their toxicity in cell media and simulated tissues, and also to test the NPs as contrast agents for magnetic resonance imaging in *in vitro* relaxivity experiments. For this reason, many studies are focused on nanomaterial surface modification and functionalization using different approaches, as covering the NPs with water compatible inorganic materials, amphiphilic molecules or polymers.[17,35,36] Briefly, the following ones are the most used strategies to biocompatibilize magnetic NPs:

- **Inorganic coating agents**

This kind of coating system is mostly used to isolate magnetic NPs from the outside conditions, according to the high density and stability that these coating agents provide against high temperatures, different pHs and oxidative or reductive conditions. Although many inorganic coating agents can be used, there are two inorganic coating types usually employed for ferrite nanoparticles. Silica shell, because of its high stability and resistance, as well as its functionality, provides a high colloidal and structural stability under extreme conditions.[37,38] On the other hand, the precious metals as silver and, specially, gold also provide stability against external factors as acidity, and also prevent the oxidation.[39,40] Another point to consider is that,

although the lack of toxicity of magnetite material is accepted, silica and precious metals are well known to be inert inside human body.

- **Organic molecules and surfactants**

The hydrophobic NPs could be functionalized with hydrophilic ligands in an additional process after NP synthesis, which attach to NP surface together with the hydrophobic ligands bonded to NP surface during the NP synthesis. In some cases, the functionalization can be carried out by ligand substitution, thus, oleate molecules can be replaced by new ligands as aminoacids or carboxylates. However, the NPs can be partially aggregated during the synthesis process, changing their properties after the treatment.[41,42]

As just explained, surfactants and ligands (organic molecules) are also commonly used in synthesis processes to avoid the NP aggregation and to stabilize NPs in the desired medium. Furthermore, depending on their combination and concentration during the synthesis process the NP growth can be limited. Usually, in order to increase NP colloidal stability or to change the surface charge or functional groups, additional ligand adhesion processes are carried out after synthesis.[43] The most commonly used molecules are carboxylates, aminoacids, phosphates or alkanesulfonic acid.[33]

This kind of molecules present two or more negatively charged functional groups that show a great tendency to assembly to ferrite NP surface, leaving the other negatively charged functional group on the surface. These negative charges lead to charge repulsion between NP surfaces, increasing their colloidal stability in polar media. Furthermore, the stability dependency on ligand chain length has been observed in many studies. Thus, longer ligand chains increase the distance between magnetic nuclei, reducing Van der Waals and magnetic attractive forces between magnetic cores.[41,42]

- **Polymer coating**

In the same way as organic ligands, many polymers are also used in ferrite NP biocompatibilization processes. As has been explained for organic ligands, the longer the coating chain is, the more stable the NP colloidal dispersion will be. In this way, long chain polymers as polyethylene glycol (PEG), polyvinyl alcohol (PVA) or alginate are great candidates to increase NP stability in water media.[44] Furthermore, there are many biopolymers as polysaccharides, proteins or nucleic acids which can be attached to NP surface, providing an extra biocompatibility and increasing strongly the NP internalization in complex organisms. The most common natural polymers are dextran, chitosan, arabic gum and gelatine.[45]

Two methods have been developed to perform this polymer coating after synthesis: firstly, a chemisorption procedure can be used to irreversibly attach polymer chains to NP surface. Furthermore, a polymerization process can be directly performed on NP surface. As this kind of functionalizations can be developed under non-polar conditions, a polymer that is stable in both polar and non-polar media is required. Alternatively, it is possible to functionalize the hydrophobic NPs with non-polar polymers and after proper reactions generate polar groups in the external layers. These approaches have proved to be the most suitable ways to obtain high water stability polymer coated single NPs from hydrophobic NPs.[34,46]

Although polymer coating provides a great colloidal stability to ferrite NPs, it is not the best choice under critical conditions as extreme pH or high temperatures due to their low structural stability in these conditions.

- **Nanoparticle encapsulation**

The encapsulation of nanoparticles in biocompatible polymers constitutes an interesting way to stabilize nanoparticles in physiological media. This relatively novel process is similar to the previously described polymer coating. However, by modifying some chemical parameters as polymer concentration, chain length and NP:polymer ratio and performing some changes in the experimental procedure, the coating process can be controlled to obtain single coated NPs or NP clusters.

This encapsulation can be performed by many different kind of polymers, as co-polymers or natural polymers as proteins or polysaccharides.[47,48] Thus, depending on the used polymer, the surface chemistry of the resultant compound can be controlled, inducing an important impact in the obtained nanosphere functionability, stability and toxicity.[49] The encapsulation procedure, as polymer coating treatments, are mostly carried out after the synthesis process in a post-treatment. This coating is based on the interactions, normally hydrophobic, between the NP surface ligands and polymer chains.

Initially, this kind of surface modifying processes were used to transfer hydrophobic NPs to water media. In fact, the optimization of these treatments is also focused on reducing the interactions between nanoparticles in order to avoid undesired, randomly distributed aggregation effects. Nevertheless, the assembly of the particles based on controlled aggregation could result in interesting changes in the magnetic properties of the whole system. Recent studies are based on the development of multicore systems formed by magnetic nanoparticles which assemble in systems with diameters going from 50 to 200 nm.[50,51] The aim of this strategy is to obtain larger sizes maintaining MNP original properties such as

superparamagnetism and colloidal stability. In this sense, in a homogeneous cluster where the nanoparticles are embedded inside a matrix, magnetic interactions between nanoparticles are increased, tuning the final magnetic properties of the system. In this way, an increased ferromagnetic behaviour can be obtained in larger magnetic systems, avoiding remanence and the formation of magnetic multidomains.[52,47] Furthermore, taking the enhanced permeability and retention effect into account, this size increment could also be interesting for biomedical applications.[53] These systems are also used to encapsulate drugs for delivery and controlled release treatments, by means of the slow decomposition of the polymer shell due to the magnetic hyperthermia induced temperature increase.[54]

Different materials have been used to conform this kind of composite nanostructures; some inorganic materials as silica, gold or silver and different polymers and biopolymers.[39,43] This last option has attracted a great interest since their biocompatibility and physical properties (low transition glass temperatures) make them extremely likely for biomedical applications. Between the used biopolymers, the chitosan is one of the most investigated ones because of its low price, interesting properties and high biocompatibility. However, what makes this polymer interesting for nanoparticle functionalization is its positive surface charge, provided by the primary amino groups of its partially deacetylated structure (Figure 3.1). These primary amino groups are easily functionalizable and allow ionic crosslinking with multivalent anions.[55] Furthermore, it shows a mucoadhesive nature, which increases the stay time at the absorption site, what is another great advantage for the drug delivery and release area. All these promising properties make the chitosan an interesting candidate to perform the encapsulation process of $Ni_{0.31}Fe_{2.69}O_4$_A NPs.

On the other hand, the NP encapsulation in a polymer with negative surface charge would be also interesting in order to compare its functionability and biocompatibility with the positive charged chitosan. In this way, fibroin is a traditionally widely used negative charged biomaterial that is currently being applied in the preparation of nanostructures.[56,57] This natural protein, composed by glycine, alanine and serine in the -Gly-Ala-Gly-Ala-Gly-Ser- sequence forms a semi-crystalline structure (Figure 2.6), and is proved to be histocompatible, less immunogenic and non-toxic.[58] Carbonyl and carboxylic groups provide a strong negative surface charge and an extensive hydrogen bonding, which increases significantly the structural stability of the final compound.[59]

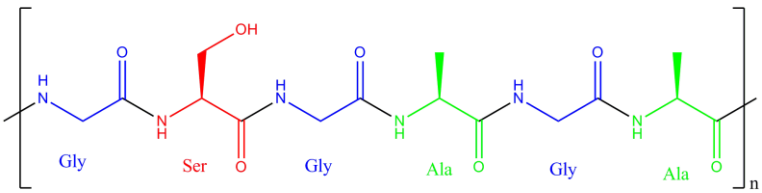

Fibroin

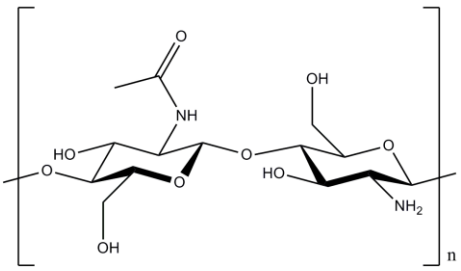

50% deacetylated chitosan

Figure 2.6. *Chemical structures of Fibroin and 50 % deacetylated chitosan.*

Finally, it is to note that before choosing a synthetic route to perform the encapsulation, the ratio between the surface chemistry of the base magnetic

material ($Ni_{0.31}Fe_{2.69}O_4$_A) and the nature of the material to perform the encapsulation must be considered. The previously mentioned biopolymers, chitosan and fibroin, have long chains with different functional groups. The hydrocarbon nature of these chains allows the formation of hydrophobic interactions with the oleate chains of the magnetic nanoparticles.

Taking into account that the aim of these encapsulated nanostructures is the application as magnetic hyperthermia inductors and as drug delivery and release agents, a high magnetic hyperthermia response NP system is required. In this way, the growth $Ni_{0.31}Fe_{2.69}O_4$_A nanoparticles have shown by far the greatest magnetic hyperthermia response maintaining the superparamagnetic behaviour at room temperature. Therefore, these nanoparticles will be transferred to water by using PMAO (direct magnetic hyperthermia inductor) and encapsulated with chitosan and fibroin (drug delivery and release agents).

2.1.5.1 Water transfer of $Ni_{0.31}Fe_{2.69}O_4$_A nanoparticles by PMAO amphiphilic polymer

Water transfer of $Ni_{0.31}Fe_{2.69}O_4$_A nanoparticles was performed by a polymer coating process developed by Moros *et al*,[46] using the poly(maleic anhydride-alt-1-octadecene) ($(C_9H_{12}O_3)_n$, PMAO) polymer. This method is based on the addition of an amphiphilic molecule. This compound interacts with the hydrophobic oleate molecules of the nanoparticle surface, forming a bilayer cover and exposing the polar groups on the NP surface. These molecules present long aliphatic chains which are able to interact with the NP surface oleate molecules by multiple hydrophobic Van der Waals forces.[34] Nevertheless, the PMAO hydrophobic polymer presents non-polar functional groups (anhydrides) that should be modified after the coating process to obtain a polar group. In this case, the $Ni_{0.31}Fe_{2.69}O_4$_A nanoparticles were first

functionalized by PMAO polymer, keeping the anhydride groups in the surface. After the coating process, the anhydride molecules were hydrolyzed in basic medium to form carboxylic polar groups, becoming the NPs stable in water media. The process is represented in Figure 2.5.

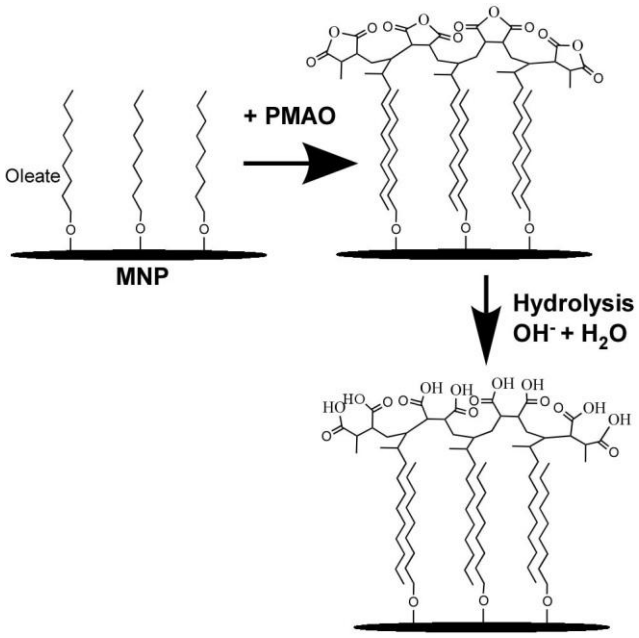

Figure 2.5. *Basic scheme of the polymer coating with PMAO amphiphilic polymer performed in $Ni_{0.31}Fe_{2.69}O_4$_A sample*.

In a typical reaction, 150 mg of PMAO polymer were dissolved in 100 mL of $CHCl_3$ solvent in a 250 mL flat bottom boiling-flask. A total of 2 mg of $Ni_{0.31}Fe_{2.69}O_4$_A nanoparticles were precipitated with ethanol and redispersed in 2 mL of chloroform. This nanoparticle solution was added dropwise to PMAO solution under sonication during 2 minutes. The MNP-PMAO mixture was then kept under sonication for 15 minutes (covered to prevent the chloroform evaporation). After that, the chloroform was slowly evaporated at 40 °C by means of a rotary evaporator, ensuring that the

sample would not completely dry out (≈5 mL of chloroform left). The hydrolysis process of the anhydride groups was carried out by quick simultaneous addition of 20 mL of NaOH 0.1 M and 20 mL of distilled H_2O. For a complete hydrolysis, the nanoparticle solution was stirred under vacuum at 60 °C in the rotary evaporator until no bubbles appeared in the solution. The obtained solution was then filtered in a 0.2 µm pore size filter to eliminate the possibly formed aggregates. To remove the excess of PMAO polymer, three washing cycles were performed, adding 30 mL of distilled water in each one. To perform the washing processes, the nanoparticles were centrifugated in a Beckman Coulter ultracentrifuge at 24000 rpm for 2 hours. The resultant sample was named as **$Ni_{0.31}Fe_{2.69}O_4$_A_PMAO**.

2.2 Encapsulation process of $Ni_{0.31}Fe_{2.69}O_4$_A magnetic nanoparticles

$Ni_{0.31}Fe_{2.69}O_4$_A nanoparticle encapsulation tests have been performed using chitosan (CS), fibroin and chitosan/fibroin mixtures to check differences in the surface properties induced by the presence of different charged polymers.

2.2.1 Formation of chitosan magnetic nanospheres

An optimization process of $Ni_{0.31}Fe_{2.69}O_4$_A@Chitosan nanosphere formation was carried out to obtain a different parameter screening in order to find the best conditions for nanosphere formation.

The synthesis of the desired composite material is based on the interaction of non-polar MNP surface oleate molecules with the chitosan chains.[29] These interactions could be electrostatic, between the carboxylic groups of the oleic acid molecules intercalated between the ones

coordinated to the inorganic surface and the chitosan amino groups (positively charged under proper pH conditions). Moreover, hydrophobic interactions between oleic acid and chitosan chains could be established.[59] Because of these interactions, it is supposed that the chitosan could act as a binder to keep the MNP together in the nanosphere but, at the same time, keeping the inorganic nuclei separated to maintain their original superparamagnetic properties. Moreover, a coacervation treatment is applied at the end of the synthesis process to complete the condensation of the chitosan matrix, as this treatment is commonly used in literature for chitosan nanoparticle production.[60]

In this process, MNPs dispersed in an organic solvent were used as seeds for the polymeric matrix formation. A chitosan aqueous solution was added to the NPs under sonication and was kept sonicating for 2 minutes. The second part of the synthesis process consist on the coacervation treatment. The pre-nanospheres were added to a 50 mM sodium sulphate solution to obtain well defined and stiff nanospheres, which form a stable colloidal dark dispersion in distilled water.[61]

Firstly, in order to obtain water stable chitosan magnetic nanospheres with controlled size and well defined spherical morphology, an optimization of the synthesis process was carried out. Thus, a screening of some parameters of the process, that is, solvent polarity, water:organic solvent proportion and MNP:chitosan weight ratio was carried out (Figure 2.7).

As the first step, different solvents for MNPs have been tested based on their polarity; hexane (Polarity index P.I.: 0), toluene (P.I.: 2.4), tetrahydrofurane (THF) (P.I.: 4) and ethanol (P.I.: 5.2). This parameter is quite important since the synthesis process is mainly based on the mixture between the NP organic suspension and the chitosan aqueous solution. THF

has been selected as the optimal solvent since its low polarity is able to maintain the MNPs in stable colloidal dispersion. Moreover, it is completely miscible with water, which makes possible to obtain a stable mixture of MNP dispersion with the chitosan solution. Using THF as solvent for MNP suspension, water stable spherical nanospheres with a quite homogeneous diameter around 100 nm were obtained. When hexane and toluene were used as solvents for MNP suspension, MNP aggregates were obtained as can be observed in Figure 2.7a, being the size and shape of the obtained composite spheres heterogeneous and uncontrollable. A similar result has been obtained in the case of ethanol. In spite of the higher compatibility of this solvent with water, it did not allow the formation of stable MNP dispersions.

The second step of the optimization process was carried out by testing four different THF/H_2O volume ratios (1:32, 1:16, 1:2 and 2:1), performed by modifying the NP concentration in THF to keep the NP:CS relation stable. It was observed that at high THF content (THF:H_2O 2:1), nanospheres presented a not well defined morphology. Thus, small MNP aggregates with no homogeneous shape and with a strong tendency to aggregation were obtained (Figure 2.7b). On the other hand, at THF proportions lower than 1:16, the magnetic nanoparticles were destabilized and agglomerated before the synthesis as a result of their high concentration in the organic medium.

In this way, the optimal THF:H_2O ratio is in the 1:15-1:3 range, considering the 1:7 middle value as the ideal ratio.

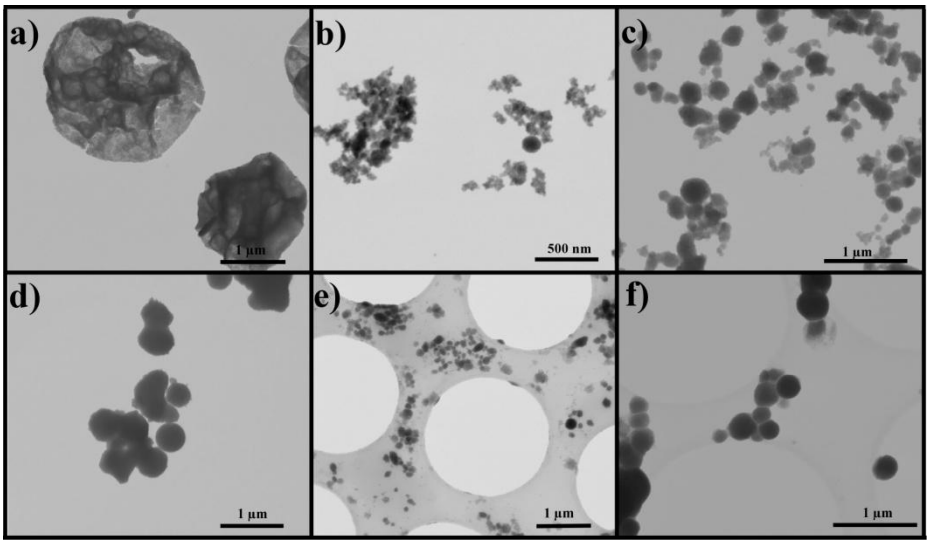

Figure 2.7. *STEM micrographs of chitosan magnetic nanospheres synthesized in different steps of condition screening. Obtained by, (a) using hexane as MNP solvent, (b) using 2:1 ratio in THF:H2O mixture, (c) by 1:2 of Fe:CS ratio, (d) by 1:5 of Fe:CS ratio, (e) without and (f) with coacervation final step.*

As the final optimization step, different MNP:CS ratios were tested by changing the concentration of the chitosan solution, keeping the NP dispersion concentration stable. The NP dispersion concentration was measured by colorimetric determination with subsequent iron thiocyanate ($Fe^{3+}(SCN)^{-3}$) red compound formation, after NP digestion. In this way, four different Fe:CS weight ratios, 2:1, 1:2, 1:5 and 1:8 were tested. The obtained results showed that the diameter and the shape of nanospheres depend also on the Fe and CS ratio. As can be observed in Figure 2.7c, using metal:chitosan ratios below 1:2 the amount of chitosan is not high enough to obtain a complete coating of nanoparticle aggregates to form spheres and MNPs appeared to be heterogeneously coated, without well defined morphology. When using metal:chitosan ratios above 1:5, the mean diameter of the obtained magnetic nanospheres increased to 500 nm and

the stability of colloidal dispersion strongly decreased (Figure 2.7d). In order to avoid these effects, the proper metal/chitosan ratio was fixed in 1:3.

Finally, a coacervation treatment by mixing the chitosan magnetic spheres with a sodium sulphate solution was carried out. It has been reported that sodium sulphate increases the interactions between polymer chains by favouring electrostatic interactions and hydrogen bonds, improving the compactness of chitosan matrix around the MNP multicores.[60] As can be observed by comparing Figure 2.7e (not coacervated spheres) and Figure 2.7f (coacervated ones), the treatment highly increased the density of the obtained chitosan nanospheres and probably also the mechanical and structural stability of the multicore assembled structure.

Taking the studied parameters into account, the following experimental process for optimized chitosan nanosphere formation was carried out. Firstly, a 0.5 mg/mL chitosan aqueous solution was prepared in a 1% acetic acid media. A total of 1.5 mg of $Ni_{0.31}Fe_{2.69}O_4$_A nanoparticles were cleaned twice with THF, precipitated with ethanol and resuspended in 100 µL of THF in a 2 mL eppendorf tube. Under sonication, a total of 750 µL of 0.5 mg/mL chitosan solution was added dropwise to the $Ni_{0.31}Fe_{2.69}O_4$_A nanoparticle suspension and the mixture was sonicated for 2 min. At this point, the magnetic nanospheres have been formed by means of a large number of small hydrophobic interactions between chitosan-oleate and chitosan-chitosan molecules. After that, the mixture was added dropwise to 5 mL of 50 mM Na_2SO_4 under sonication and the mixture was sonicated for another 2 min. The full mechanism of the optimized synthesis process is represented in Figure 2.8.

Three washing processes were carried out to discard the chitosan excess. The magnetic nanospheres were dispersed in 1 mL of distilled water and

separated by magnetic decantation and finally dispersed in 2 mL of distilled water. The sample was labelled as **CS-MNS**.

Figure 2.8. *Schematic representation of the magnetic nanosphere formation mechanism.*

In view of a mechanism for drug association in magnetic nanospheres needs to be developed, the best way to perform it was by encapsulating fluorophores in the nanospheres. In literature, a widely used method to control the distribution or the location of a inserted compound in an animal or a tissue is by associating a fluorophore as Alexa®, Tamra, Rhodamine or Nile Red.[62,63] In this way, the compound can be located by the fluorophore emission detection. Furthermore, other authors have associated fluorophores as molecular "thermometers" to NP surface in order to control the emitted heat by magnetic or optical hyperthermia by controlling the fluorophore release.[64] In our case, the fluorophores would replace drugs in the encapsulation tests considering that the functionalization of nanospheres with fluorophores, can be easily monitored by quantifying the amount of associated fluorophore molecules by fluorescence or absorption measurements of supernatants.

However, depending on the chemistry nature of the drug that needs to be encapsulated the association mechanism will be completely different. For

this reason, encapsulation processes for hydrophilic and hydrophobic molecules have been developed: Nile Red and Rhodamine b isothiocyanate (Figure 2.9).

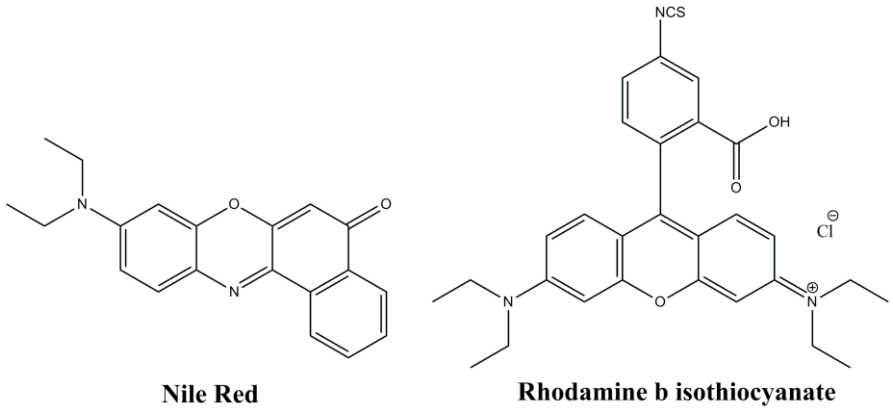

Figure 2.9. *Chemical structures of fluorophores associated to magnetic nanospheres.*

To achieve the association of both molecules to magnetic nanospheres, different functionalization mechanisms would be necessary, being a good starting point to link real specific drugs in future works.

2.2.1.1 Nile Red encapsulation in CS-MNS magnetic nanospheres

Nile Red fluorophore is an excellent candidate for encapsulation since its hydrophobic nature makes it compatible with nickel ferrite nanoparticles and makes it suitable to be internalized with the nanoparticles inside the chitosan shell during the nanosphere formation process. Nile Red is a commercially available and widely used hydrophobic fluorophore with a maximum absorption/emission wavelength of 553/636 nm (in methanol).[62]

The same process used in the formation of CS-MNS nanospheres has been followed dissolving different amounts of Nile Red fluorophore in THF (100 µL) with nickel ferrite magnetic nanoparticles (1.5 mg) as can be seen in

(Figure 2.10). The sample names and added amounts of Nile Red are described in Table 2.4. The supernatants obtained in the washing processes were stored in order to determine the amount of non encapsulated Nile Red.

Table 2.4. *Amounts of Nile Red encapsulated in each sample*.

SAMPLE	CS-MNS-NL200	CS-MNS-NL100	CS-MNS-NL50	CS-MNS-NL20	CS-MNS-NL15	CS-MNS-NL10
$n_{Nile\ Red}$ (nmol)	200	100	50	20	15	10

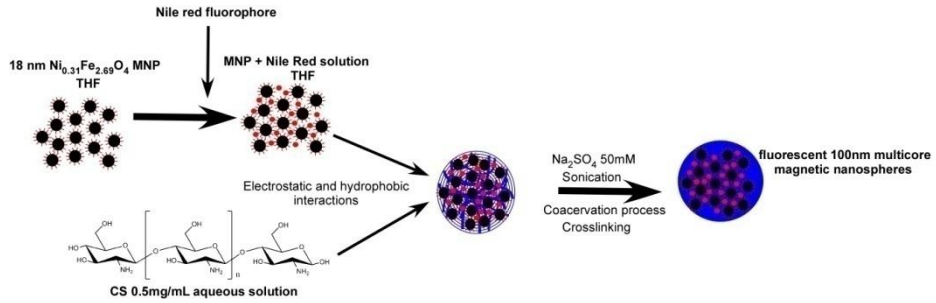

Figure 2.10. *Synthesis mechanism of magnetic nanospheres with encapsulated Nile Red*.

2.2.1.2 Functionalization of CS-MNS nanospheres with Rhodamine B isothiocyanate

Rhodamine B isothiocyanate is a positively charged mixture of 5- and 6-isocyanate isomers, with a maximum absorption/emission wavelength of 543/580 nm (in methanol). The positively charged structure provides a high solubility in water media (15 g/L), being broadly used as protein fluorophore tracer, specially as a monitoring tool in biodistribution experiments.[63]

2. Nanocompound preparation

The affinity of Nile Red compound with the hydrophobic surface of the magnetic nanoparticles makes it easy to encapsulate inside the nanospheres, since its nature is compatible with the hydrophobic core of the chitosan magnetic nanospheres. Nonetheless, the hydrophilic nature of rhodamine molecule makes impossible to encapsulate it inside the nanosphere. Therefore, the best way to associate the fluorophore to nanosphere is by linking it to the hydrophilic surface by electrostatic interactions between the positive amino groups of chitosan and the negatively charged rhodamine B isothiocyanate molecules.[65]

Thus, 0.6 mg of CS-MNS were dispersed in 1.5 mL pH 8 solution with 1% of tween ($C_{58}H_{114}O_{26}$). The pH was chosen to favor the electrostatic interaction between the fluorophore and the amino groups of nanosphere surface. The purpose of tween surfactant was to avoid the aggregation of nanospheres during the functionalization. A specific amount of rhodamine B isothiocyanate was added (Table 2.5) and the mixture was mechanically stirred for 30 min. Then, the nanospheres were washed twice with distilled water and the supernatants were stored to measure the absorbance and determine the amount of associated dye.

Table 2.5. *Amounts of rhodamine B isothiocyanate added in each sample.*

SAMPLE	CS-MNS-RH25	CS-MNS-RH50	CS-MNS-RH75
$n_{Nile\ Red}$ (nmol)	25	50	75

2.2.2 Formation of fibroin and chitosan-fibroin magnetic nanospheres

The optimized synthesis mechanism for chitosan CS-MNS nanospheres was used as starting point for fibroin nanosphere development since the primary formation mechanism is based on the same kind of interactions in both cases. Additionally, some magnetic nanospheres combining chitosan and fibroin polymers have also been prepared. In this way, a basic study of surface chemistry of fibroin and fibroin-chitosan magnetic nanospheres was carried out.

Fibroin was gently dissolved in milliQ water in 0.5 mg/mL concentration, as concentrations above 1 mg/ml result in the gelation of fibroin. Thus, in order to obtain fibroin magnetic nanospheres, 1.5 mg of $Ni_{0.31}Fe_{2.69}O_4$_A nanoparticles were washed twice and dispersed in 100 µL of THF. To this dispersion, 750 µL of 0.5 mg/mL fibroin solution were added dropwise under sonication and kept for 2 min. A coacervation process with 5 mL of 50 mM Na_2SO_4 was carried out with three subsequent washes with distilled water. The obtained sample was labelled as **Fi-MNS**.

The fibroin-chitosan mixed magnetic nanospheres were synthesized by the same mechanism as the fibroin and chitosan magnetic nanospheres. However, a great number of different shells could be obtained by changing the addition way and order of different polymers. Therefore, different proportions of fibroin:chitosan were tested to check possible differences in the surface chemistry of final nanospheres. Thus, the surface charge of the obtained nanospheres could be tuned by using different proportions of positively and negatively charged polymers. So as to find the most suitable synthesis method, three different attempts were carried out changing the addition order of biopolymers:

- Fi-CS1: In this case, the main objective was to prepare a core-shell structure nanosphere by first forming a chitosan layer around MNP cluster and subsequent addition of a fibroin solution. First, chitosan magnetic nanospheres (CS-MNS) were synthesized by the previously explained method. Under sonication, 750 µL of fibroin 0.5 mg/mL solution were added and kept under sonication for 2 min. Finally, a coacervation process was developed with 5 mL of 50 mM Na_2SO_4 and washed three times with distilled water. The sample was labelled as **Fi-CS1.**

- Fi-CS2: Another approach to obtain the CS-Fi core shell structure was attempted by adding both polymers subsequently before the coacervation process. Thus, 750 µL of 0.5 mg/mL chitosan solution was added dropwise to 1.5 mg of $Ni_{0.31}Fe_{2.69}O_4$_A magnetic nanoparticles dispersed in 100 µL of THF under sonication. Immediately, 750 µL of 0.5 mg/mL fibroin solution were added dropwise and sonicated for 2 min. Finally, a coacervation procedure (previously described) was performed followed by three washing processes with distilled water. The sample was labelled as **Fi-CS2.**

- **Fi-CS3**: In this case, an aqueous solution of both biopolymers was directly added to the MNP dispersion in THF in order to form magnetic nanospheres with both polymers in the structure. 750 µL of Fi:CS polymer mixture were added dropwise to 4.5 mg of $Ni_{0.31}Fe_{2.69}O_4$_A magnetic nanoparticles dispersed in 100 µL of THF under sonication. The synthesis was completed with a coacervation process and three washing processes with distilled water. Four different Fi:CS relations were tested: 50:50 (**Fi-CS3.1**), 40:60 (**Fi-CS3.2**), 35:65 (**Fi-CS3.3**) and 15:85 (**Fi-CS3.4**), which correspond to 0.5:0.5, 0.33-0.5, 0.26-0.5 and 0.09-0.5 mg/mL of Fi-CS polymer added concentration, respectively.

A brief scheme of the synthesized fibroin-chitosan nanospheres is illustrated in Figure 2.11.

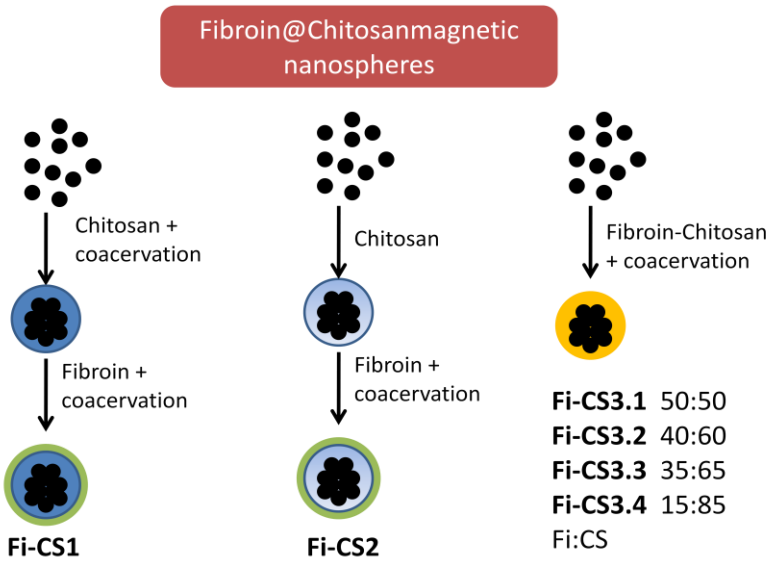

Figure 2.11. *Schematic description of prepared chitosan-fibroin magnetic nanospheres.*

2.3 Summary

First, different ferrite nanoparticles have been successfully prepared. In order to obtain monodisperse, controlled sized and high crystalline NPs an optimized thermal decompositions method has been used. This method is based on the decomposition of metalorganic precursors at high temperatures in high boiling point organic solvents. Thus, ferrites with different Ni^{2+} and Mn^{2+} cation doping degrees have been prepared to analyze their effect in the magnetic response and magnetic hyperthermia. Furthermore, a seed mediated growth process has been carried out in one sample of each group, to test the size effect in the magnetic hyperthermia

response. Based on this seed mediated growth process, some core shell systems have been prepared by alternating Ni ferrite and magnetite layers.

However, these NPs present a hydrophobic surface, what it means that a functionalization is necessary to make them stable in physiological media. Two different kind of functionalizations have been carried out to one of the prepared NP systems ($Ni_{0.3}Fe_{2.69}O_4$_A), focused on obtaining two different nanocompounds. Firstly, a polymer coating has been performed with the PMAO polymer in order to obtain single water stable nanoparticles ($Ni_{0.3}Fe_{2.69}O_4$_A_PMAO). On the other hand, a NP encapsulation mechanism has been developed with chitosan biopolymer, to obtain CS-MNS nanospheres. A deep optimization of this encapsulation process has been performed to achieve a great control of the nanosphere formation process. Based on this mechanism, some fibroin and CS-fibroin nanospheres have also been prepared.

References

(1) Rana, S.; Gallo, A; Srivastava, R. S.; Misra, R. D. K. On the Suitability of Nanocrystalline Ferrites as a Magnetic Carrier for Drug Delivery: Functionalization, Conjugation and Drug Release Kinetics. *Acta Biomater.* **2007**, *3* (2), 233–242.

(2) Thakur, S.; Rai, R.; Sharma, S. Structural Characterization and Magnetic Study of $Ni_xFe_{3-X}O_4$ Synthesized by Co-Precipitation Method. *Mater. Lett.* **2015**, *139*, 368–372.

(3) Mathew, D. S.; Juang, R. S. An Overview of the Structure and Magnetism of Spinel Ferrite Nanoparticles and Their Synthesis in Microemulsions. *Chem. Eng. J.* **2007**, *129* (1–3), 51–65.

(4) Blanco-Gutiérrez, V.; Virumbrales, M.; Saez-Puche, R.; Torralvo-Fernandez, M. J. Superparamagnetic Behaviour of MFe2O4 Nanoparticles and MFe_2O_4/SiO_2 Composites (M: Co, Ni). *J. Phys. Chem. C* **2013**, *117*, 20927–20935.

(5) Deepak, F. L.; Bañobre-López, M.; Carbó-Argibay, E.; Cerqueira, M. F.; Piñeiro-Redondo, Y.; Rivas, J.; Thompson, C. M.; Kamali, S.; Rodríguez-Abreu, C.; Kovnir, K.; et al. A Systematic Study of the Structural and Magnetic Properties of Mn-, Co-, and Ni-Doped Colloidal Magnetite Nanoparticles. *J. Phys. Chem. C* **2015**, *119* (21), 11947–11957.

(6) Cheng, H.-W.; Luo, J.; Zhong, C.-J. An Aggregative Growth Process for Controlling Size, Shape and Composition of Metal, Alloy and Core–shell Nanoparticles toward Desired Bioapplications. *J. Mater. Chem. B* **2014**, *2* (40), 6904–6916.

(7) Arshadi, S.; Moghaddam, J.; Eskandarian, M. LaMer Diagram Approach to Study the Nucleation and Growth of Nanoparticles Using Supersaturation Theory. *Korean J. Chem. Eng.* **2014**, *31* (11), 2020–2026.

(8) Cao, G. (University of W. *Nanostructures & Nanomaterials Synthesis, Properties and Applications*, First edit.; Imperial College: London, 2004.

(9) Margulis-Goshen, K.; Magdassi, S. Organic Nanoparticles from Microemulsions: Formation and Applications. *Curr. Opin. Colloid Interface Sci.* **2012**, *17* (5), 290–296.

(10) Deng, Y. H.; Wang, C. C.; Hu, J. H.; Yang, W. L.; Fu, S. K. Investigation of Formation of Silica-Coated Magnetite Nanoparticles via Sol-Gel Approach. *Colloids Surfaces A Physicochem. Eng. Asp.* **2005**, *262* (1–3), 87–93.

(11) Toksha, B. G.; Shirsath, S. E.; Patange, S. M.; Jadhav, K. M. Structural Investigations and Magnetic Properties of Cobalt Ferrite Nanoparticles Prepared by Sol-Gel Auto Combustion Method. *Solid State Commun.* **2008**, *147* (11–12), 479–483.

(12) Hervé, K.; Douziech-Eyrolles, L.; Munnier, E.; Cohen-Jonathan, S.; Soucé, M.; Marchais, H.; Limelette, P.; Warmont, F.; Saboungi, M. L.; Dubois, P.; et al. The Development of Stable Aqueous Suspensions of PEGylated SPIONs for Biomedical Applications. *Nanotechnology* **2008**, *19* (46), 465608.

(13) Pereira, C.; Pereira, A. M.; Fernandes, C.; Rocha, M.; Mendes, R.; Guedes, A.; Tavares, P. B.; Grene, J.; Arau, P.; Freire, C. Superparamagnetic MFe_2O_4 (M = Fe , Co , Mn) Nanoparticles: Tuning the Particle Size and Magnetic Properties through a Novel One-Step Coprecipitation Route. *Chem. Mater.* **2012**, *4*, 1496–1504.

(14) Ammar, S.; Helfen, A.; Jouini, N.; Fiévet, F.; Rosenman, I.; Villain, F.; Molinié, P.; Danot, M. Magnetic Properties of Ultrafine Cobalt Ferrite Particles Synthesized by Hydrolysis in a Polyol Medium. *J. Mater. Chem.* **2001**, *11* (1), 186–192.

(15) Vidal-Vidal, J.; Rivas, J.; Lopez-Quintela, M. A. Synthesis of Monodisperse Maghemite Nanoparticles by the Microemulsion Method. *Colloids Surfaces A Physicochem. Eng. Asp.* **2006**, *288* (1–3), 44–51.

(16) Köseoğlu, Y.; Bay, M.; Tan, M.; Baykal, A.; Sözeri, H.; Topkaya, R.; Akdoğan, N. Magnetic and Dielectric Properties of $Mn_{0.2}Ni_{0.8}Fe_2O_4$ Nanoparticles Synthesized by PEG-Assisted Hydrothermal Method. *J. Nanoparticle Res.* **2011**, *13* (5), 2235–2244.

(17) Wang, J.; Sun, J.; Sun, Q.; Chen, Q. One-Step Hydrothermal Process to Prepare Highly Crystalline Fe_3O_4 Nanoparticles with Improved Magnetic Properties. *Mater. Res. Bull.* **2003**, *38* (7), 1113–1118.

(18) Sun, S.; Zeng, H. Size-Controlled Synthesis of Magnetite Nanoparticles. *J. Am. Chem. Soc.* **2002**, No. 31, 8204–8205.

(19) Stefanou, G.; Sakellari, D.; Simeonidis, K.; Kalabaliki, T.; Angelakeris, M.; Dendrinou-samara, C.; Kalogirou, O. Tunable AC Magnetic Hyperthermia Efficiency of Ni Ferrite Nanoparticles. *IEEE Trans. Magn.* **2014**, *50* (12), 4601207–4601207.

(20) Cannas, C.; Musinu, A.; Ardu, A.; Orrù, F.; Peddis, D.; Casu, M.; Sanna, R.; Angius, F.; Diaz, G.; Piccaluga, G. $CoFe_2O_4$ and $CoFe_2O_4$ /SiO_2 Core/Shell Nanoparticles: Magnetic and Spectroscopic Study. *Chem. Mater.* **2010**, *22* (11), 3353–3361.

(21) Lu, A.-H.; Salabas, E. L.; Schüth, F. Magnetic Nanoparticles: Synthesis, Protection, Functionalization, and Application. *Angew. Chem. Int. Ed. Engl.* **2007**, *46* (8), 1222–1244.

(22) Chen, R.; Christiansen, M. G.; Anikeeva, P. Maximizing Hysteretic Losses in Magnetic Ferrite Nanoparticles via Model-Driven Synthesis and Materials Optimization. *ACS Nano* **2013**, *7* (10), 8990–9000.

(23) Laurent, S.; Forge, D.; Port, M.; Roch, A.; Robic, C.; Vander Elst, L.; Muller, R. N. Magnetic Iron Oxide Nanoparticles: Synthesis, Stabilization, Vectorization, Physicochemical Characterizations, and Biological Applications. *Chem. Rev.* **2008**, *108* (6), 2064–2110.

(24) Castellanos-Rubio, I.; Insausti, M.; Garaio, E.; Gil de Muro, I.; Plazaola, F.; Rojo, T.; Lezama, L. Fe_3O_4 Nanoparticles Prepared by the Seeded-Growth Route for Hyperthermia: Electron Magnetic Resonance as a Key Tool to Evaluate Size Distribution in Magnetic Nanoparticles. *Nanoscale* **2014**, *6*, 7542–7552.

(25) Eslaminejad, T.; Nematollahi-Mahani, S. N.; Ansari, M. Synthesis, Characterization, and Cytotoxicity of the Plasmid EGFP-p53 Loaded on Pullulan-Spermine Magnetic Nanoparticles. *J. Magn. Magn. Mater.* **2016**, *402*, 34–43.

(26) Sun, S.; Zeng, H.; Robinson, D. B.; Raoux, S.; Rice, P. M.; Wang, S. X.; Li, G. Monodisperse MFe_2O_4 (M = Fe , Co , Mn) Nanoparticles. *J. Am. Chem. Soc.* **2004**, *4* (1), 126–132.

(27) Salado, J.; Insausti, M.; Gil de Muro, I.; Lezama, L.; Rojo, T. Synthesis and Magnetic Properties of Monodisperse Fe_3O_4 Nanoparticles with Controlled Sizes. *J. Non. Cryst. Solids* **2008**, *354* (47–51), 5207–5209.

(28) Burda, C.; Chen, X.; Narayanan, R.; El-Sayed, M. A. Chemistry and Properties of Nanocrystals of Different Shapes. *Chem. Rev.* **2005**, *105* (4), 1025–1102.

(29) Faraji, M.; Yamini, Y.; Rezaee, M. Magnetic Nanoparticles: Synthesis, Stabilization, Functionalization, Characterization, and Applications. *J. Iran. Chem. Soc.* **2010**, *7* (1), 1–37.

(30) Lu, L. T.; Dung, N. T.; Tung, L. D.; Thanh, C. T.; Quy, O. K.; Chuc, N. V; Maenosono, S.; Thanh, N. T. K. Synthesis of Magnetic Cobalt Ferrite Nanoparticles with Controlled Morphology, Monodispersity and Composition: The Influence of Solvent, Surfactant, Reductant and Synthetic Conditions. *Nanoscale* **2015**, *7* (46), 19596–19610.

(31) Levy, M.; Quarta, A.; Espinosa, A.; Figuerola, A.; Wilhelm, C.; García-hern, M.; Genovese, A.; Falqui, A.; Alloyeau, D.; Cozzoli, P. D.; et al. Correlating Magneto-Structural Properties to Hyperthermia Performance of Highly Monodisperse Iron Oxide Nanoparticles Prepared by a Seeded-Growth Route. *Chem. Mater.* **2011**, *23*, 4170–4180.

(32) Park, J.; Lee, E.; Hwang, N.-M.; Kang, M.; Kim, S. C.; Hwang, Y.; Park, J.-G.; Noh, H.-J.; Kim, J.-Y.; Park, J.-H.; et al. One-Nanometer-Scale Size-Controlled Synthesis of

Monodisperse Magnetic Iron Oxide Nanoparticles. *Angew. Chem. Int. Ed. Engl.* **2005**, *44* (19), 2873–2877.

(33) Thanh, N. T. K.; Green, L. a. W. Functionalisation of Nanoparticles for Biomedical Applications. *Nano Today* **2010**, *5* (3), 213–230.

(34) Lin, C. A. J.; Sperling, R. a.; Li, J. K.; Yang, T. Y.; Li, P. Y.; Zanella, M.; Chang, W. H.; Parak, W. J. Design of an Amphiphilic Polymer for Nanoparticle Coating and Functionalization. *Small* **2008**, *4*, 334–341.

(35) El-Fiqi, A.; Kim, J.-H.; Kim, H.-W. Osteoinductive Fibrous Scaffolds of Biopolymer/Mesoporous Bioactive Glass Nanocarriers with Excellent Bioactivity and Long-Term Delivery of Osteogenic Drug. *ACS Appl. Mater. Interfaces* **2015**, *7* (2), 1140–1152.

(36) Sundar, S.; Kundu, J.; Kundu, S. C. Biopolymeric Nanoparticles. *Sci. Technol. Adv. Mater.* **2010**, *11* (1), 14104.

(37) Bumb, a; Brechbiel, M. W.; Choyke, P. L.; Fugger, L.; Eggeman, a; Prabhakaran, D.; Hutchinson, J.; Dobson, P. J. Synthesis and Characterization of Ultra-Small Superparamagnetic Iron Oxide Nanoparticles Thinly Coated with Silica. *Nanotechnology* **2008**, *19* (33), 335601.

(38) Insin, N.; Tracy, J.; Lee, H.; Zimmer, J. Incorporation of Iron Oxide Nanoparticles and Quantum Dots into Silica Microspheres. *ACS Nano* **2008**, *2* (2), 197–202.

(39) Salado, J.; Insausti, M.; Lezama, L.; Gil de Muro, I.; Moros, M.; Pelaz, B.; Grazu, V.; de la Fuente, J. M.; Rojo, T. Functionalized Fe_3O_4@Au Superparamagnetic Nanoparticles: In Vitro Bioactivity. *Nanotechnology* **2012**, *23* (31), 315102.

(40) Xu, Z.; Hou, Y.; Sun, S. Magnetic Core/Shell Fe_3O_4 /Au and Fe_3O_4 /Au/Ag Nanoparticles with Tunable Plasmonic Properties. *J. Am. Chem. Soc.* **2007**, *129* (28), 8698–8699.

(41) Lu, Y.; Yin, Y.; Mayers, B. T.; Xia, Y. Modifying the Surface Properties of Superparamagnetic Iron Oxide Nanoparticles through a Sol-Gel Approach. *Nano Lett.* **2002**, *2* (3), 183–186.

(42) Hill, H. D.; Mirkin, C. A. The Bio-Barcode Assay for the Detection of Protein and Nucleic Acid Targets Using DTT-Induced Ligand Exchange. *Nat. Protoc.* **2006**, *1* (1), 324–336.

(43) Berry, C. C.; Curtis, A. S. G. Functionalisation of Magnetic Nanoparticles for Applications in Biomedicine. *J. Phys. D. Appl. Phys.* **2003**, *36* (13), R198–R206.

(44) Mukhopadhyay, A.; Joshi, N.; Chattopadhyay, K.; De, G. A Facile Synthesis of PEG-Coated Magnetite (Fe_3O_4) Nanoparticles and Their Prevention of the Reduction of Cytochrome C. *ACS Appl. Mater. Interfaces* **2012**, *4* (1), 142–149.

(45) Chen, W.; Yi, P.; Zhang, Y.; Zhang, L.; Deng, Z.; Zhang, Z. Composites of Aminodextran-Coated Fe_3O_4 Nanoparticles and Graphene Oxide for Cellular Magnetic Resonance Imaging. *ACS Appl. Mater. Interfaces* **2011**, *3* (10), 4085–4091.

(46) Moros, M.; Pelaz, B.; López-Larrubia, P.; García-Martin, M. L.; Grazú, V.; de la Fuente, J. M. Engineering Biofunctional Magnetic Nanoparticles for Biotechnological

Applications. *Nanoscale* **2010**, *2* (9), 1746–1755.

(47) De Matteis, L.; Fernández-Pacheco, R.; Marquina, C.; Ibarra, M. R.; De La Fuente, J. M. Nanostructural Characterization of Biomagnetic Cobalt Ferrite-Alginate Nanospheres. *Part. Part. Syst. Charact.* **2013**, *30* (12), 1018–1023.

(48) Grumezescu, A. M.; Andronescu, E.; Holban, A. M.; Ficai, A.; Ficai, D.; Voicu, G.; Grumezescu, V.; Balaure, P. C.; Chifiriuc, C. M. Water Dispersible Cross-Linked Magnetic Chitosan Beads for Increasing the Antimicrobial Efficiency of Aminoglycoside Antibiotics. *Int. J. Pharm.* **2013**, *454* (1), 233–240.

(49) Bigall, N. C.; Curcio, A.; Leal, M. P.; Falqui, A.; Palumberi, D.; Di Corato, R.; Albanesi, E.; Cingolani, R.; Pellegrino, T. Magnetic Nanocarriers with Tunable pH Dependence for Controlled Loading and Release of Cationic and Anionic Payloads. *Adv. Mater.* **2011**, *23* (47), 5645–5650.

(50) Schaller, V.; Wahnström, G.; Sanz-Velasco, A.; Gustafsson, S.; Olsson, E.; Enoksson, P.; Johansson, C. Effective Magnetic Moment of Magnetic Multicore Nanoparticles. *Phys. Rev. B - Condens. Matter Mater. Phys.* **2009**, *80* (9), 1–4.

(51) Dutz, S.; Kuntsche, J.; Eberbeck, D.; Müller, R.; Zeisberger, M. Asymmetric Flow Field-Flow Fractionation of Superferrimagnetic Iron Oxide Multicore Nanoparticles. *Nanotechnology* **2012**, *23* (35), 355701.

(52) Yoon, T. J.; Lee, H.; Shao, H.; Hilderbrand, S. a.; Weissleder, R. Multicore Assemblies Potentiate Magnetic Properties of Biomagnetic Nanoparticles. *Adv. Mater.* **2011**, *23* (41), 4793–4797.

(53) Meng, H.; Xue, M.; Xia, T.; Ji, Z.; Tarn, D. Y.; Zink, J. I.; Nel, A. E. Use of Size and a Copolymer Design Feature to Improve the Biodistribution and the Enhanced Permeability and Retention Effect of Doxorubicin-Loaded Mesoporous Silica Nanoparticles in a Murine Xenograft Tumor Model. *ACS Nano* **2011**, *5* (5), 4131–4144.

(54) Dutz, S.; Clement, J. H.; Eberbeck, D.; Gelbrich, T.; Hergt, R.; Müller, R.; Wotschadlo, J.; Zeisberger, M. Ferrofluids of Magnetic Multicore Nanoparticles for Biomedical Applications. *J. Magn. Magn. Mater.* **2009**, *321* (10), 1501–1504.

(55) Agnihotri, S. a.; Mallikarjuna, N. N.; Aminabhavi, T. M. Recent Advances on Chitosan-Based Micro- and Nanoparticles in Drug Delivery. *J. Control. Release* **2004**, *100*, 5–28.

(56) Cao, T.-T.; Zhou, Z.-Z.; Zhang, Y.-Q. Processing of β-Glucosidase-Silk Fibroin Nanoparticle Bioconjugates and Their Characteristics. *Appl. Biochem. Biotechnol.* **2014**, *173* (2), 544–551.

(57) Deng, M.; Huang, Z.; Zou, Y.; Yin, G.; Liu, J.; Gu, J. Fabrication and Neuron Cytocompatibility of Iron Oxide Nanoparticles Coated with Silk-Fibroin Peptides. *Colloids Surf. B. Biointerfaces* **2014**, *116*, 465–471.

(58) Altman, G. H.; Diaz, F.; Jakuba, C.; Calabro, T.; Horan, R. L.; Chen, J.; Lu, H.; Richmond, J.; Kaplan, D. L. Silk-Based Biomaterials. *Biomaterials* **2003**, *24* (3), 401–416.

(59) Wydro, P.; Krajewska, B.; Hac-Wydro, K. Chitosan as a Lipid Binder: A Langmuir Monolayer Study of Chitosan-Lipid Interactions. *Biomacromolecules* **2007**, *8* (8), 2611–2617.

(60) Jonassen, H.; Kjøniksen, A.-L.; Hiorth, M. Effects of Ionic Strength on the Size and Compactness of Chitosan Nanoparticles. *Colloid Polym. Sci.* **2012**, *290* (10), 919–929.

(61) Kim, B.-S.; Taton, T. A. Multicomponent Nanoparticles via Self-Assembly with Cross-Linked Block Copolymer Surfactants. *Langmuir* **2007**, *23* (4), 2198–2202.

(62) Greenspan, P.; Mayer, E. P.; Fowler, S. D. Nile Red: A Selective Fluorescent Stain for Intracellular Lipid Droplets, J. Cell Biol. 100 (1985) 965–973. *J. Cell Biol.* **1985**, *100* (10), 965–973.

(63) Jang, H.; Lee, C.; Nam, G.-E.; Quan, B.; Choi, H. J.; Yoo, J. S.; Piao, Y. In Vivo Magnetic Resonance and Fluorescence Dual Imaging of Tumor Sites by Using Dye-Doped Silica-Coated Iron Oxide Nanoparticles. *J. Nanoparticle Res.* **2016**, *18* (2), 41.

(64) Dias, J. T.; Moros, M.; Del Pino, P.; Rivera, S.; Grazú, V.; de la Fuente, J. M. DNA as a Molecular Local Thermal Probe for the Analysis of Magnetic Hyperthermia. *Angew. Chem. Int. Ed. Engl.* **2013**, *52* (44), 11526–11529.

(65) Urries, I.; Muñoz, C.; Gomez, L.; Marquina, C.; Sebastian, V.; Arruebo, M.; Santamaria, J. Magneto-Plasmonic Nanoparticles as Theranostic Platforms for Magnetic Resonance Imaging, Drug Delivery and NIR Hyperthermia Applications. *Nanoscale* **2014**, *6* (15), 9230–9240.

2. Nanocompound preparation

3. NANOCOMPOUND CHEMICAL, STRUCTURAL AND MAGNETIC CHARACTERIZATION

The results obtained from the chemical, structural and magnetic characterizations of the prepared samples have been divided in different sections, according to the nature of the analyzed materials. First, the chemical, structural and magnetic properties of the synthesized ferrite magnetic nanoparticles were analyzed. From this study, the optimal sample to perform future functionalizations and *in vitro* and *in vivo* cytotoxicity tests has been selected.

In the second main section, the chemical and structural properties and magnetic behaviour of the prepared nanospheres have been analyzed, being the chitosan nanospheres the most deeply studied ones. The stability and the functionalization with fluorophores have also been analyzed for the chitosan nanospheres.

Finally, the samples which have shown the most promising magnetic and structural properties were selected to perform some preclinical *in vitro* and *in vivo* experiments. The direct effects of the nanocompounds in simulated tissues have been analyzed by an *in vitro* cellular uptake and toxicity study in monocultures and blood vessel model co-cultures. Furthermore, a

preliminary *in vivo* study has been performed in mice to analyze the nanocompound toxicity and biodistribution in animals. From these experiments, the effects of the synthesized nanocompounds in cell cultures and animals were studied to ascertain the symptoms that the nanocompounds could induce. The procedure followed in this study is schematically illustrated in Figure 3.1.

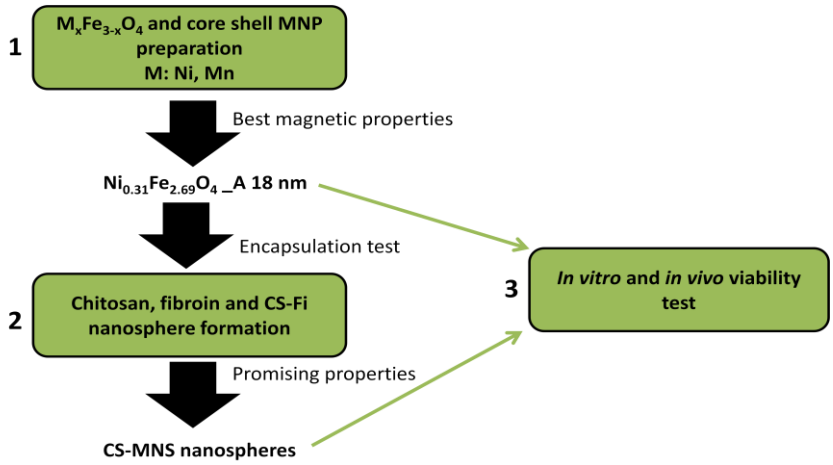

Figure 3.1. *Schematic illustration of the procedure followed during this study.*

3.1 Ferrite magnetic nanoparticles

The synthesized magnetic nanoparticles were divided in three different groups depending on their nature: nickel ferrite nanoparticles ($Ni_xFe_{3-x}O_4$), manganese ferrite nanoparticles ($Mn_xFe_{3-x}O_4$) and core-shell nanoparticles ($Ni_{0.31}Fe_{2.69}O_4$@Fe_3O_4). Nanoparticle samples have been structurally and chemically characterized by the Inductively Coupled Plasma spectroscopy (ICP-MS), Transmission Electron Microscopy (TEM), Dynamic Light Scattering (DLS), X Ray Diffraction (XRD) and Thermogravimetric analysis (TG). The magnetic properties have been analyzed by field dependent magnetization (M (H)) measurements, temperature dependent magnetization (M (T))

measurements, Electronic Magnetic Resonance spectroscopy (EMR) and magnetic hyperthermia measurements.

3.1.1 Chemical and structural properties of MNPs

Firstly, a basic chemical and structural characterization of Ni, Mn ferrites and Ni ferrite@magnetite core shell nanoparticles was carried out by ICP, TEM, DLS, XRD and TG. Thus, their Ni and Mn doping degree, structure, size, shape and oleic acid coating level has been assessed. Most of these factors are expected to be similar in every case (excepting the size and doping levels), since the materials should be structurally similar between them.

3.1.1.1 NP composition

As it has been previously explained, the doping level was managed by controlling the amount of different metal precursors added during the synthesis process. However, the amount of the internalized metal in each case could be different than the added one, due to the possible formation of secondary phases or different metal diffusion kinetics. The nominal chemical structures of NPs were determined by ICP measurements of all the metals (Fe, Ni and Mn) present in each sample.

To perform the chemical analysis, the synthesized magnetic nanoparticles were first digested overnight in aqua regia ($HCl:HNO_3$ 3:1) at room temperature. After that, the samples were diluted 10 times with milliQ water before measure the amount of dissolved metals by means of an ELAN 9000 ICP-MS (PerkinElmer SCIEX) spectrophotometer. The obtained results for Ni, Mn ferrites and core shell NPs are presented in Table 3.1, as relative to total metal amount in each sample.

In this way, the amounts of measured Ni levels for Ni ferrites are in the 8-30% range, almost the same as the theoretical values, added in the synthesis.

In fact, the obtained relative values are exactly the same as the added in the synthesis in many cases, as for $Ni_{0.31}Fe_{2.69}O_4$ and $Ni_{0.43}Fe_{2.57}O_4$ samples. This means that, apparently, all the added Ni^{2+} has been incorporated to the nanoparticle structure.

Table 3.1. *Theoretical amount of added magnetic metal in each synthesis and the final amount determined by ICP, when M=Ni or Mn in each case.*

SAMPLE	Fe (% mol)	M_{ICP} (% mol)	M_{THEOR} (% mol)
$Ni_{0,31}Fe_{2,69}O_4$	89.7	10.3	10
$Ni_{0,43}Fe_{2,57}O_4$	85.5	14.5	14
$Ni_{0,70}Fe_{2,30}O_4$	78.7	21.3	18
$Ni_{0,86}Fe_{2,14}O_4$	71.4	28.6	30
$Ni_{0,31}Fe_{2,69}O_4$_A	92.0	8.0	10
$Mn_{0,13}Fe_{2,87}O_4$	96.3	3.7	10
$Mn_{0,18}Fe_{2,82}O_4$	94.5	5.5	14
$Mn_{0,27}Fe_{2,73}O_4$	90.7	9.3	18
$Mn_{0,36}Fe_{2,64}O_4$	88.4	11.6	30
$Mn_{0,13}Fe_{2,87}O_4$_A	95.2	4.8	10
FeNi2Mag2	94.8	5.2	4
Mag2FeNi2	93.1	6.9	6

In contrast, the relative amounts of Mn obtained from the Mn ferrite ICP analysis are quite lower than the theoretical ones (around 3 times lower). There are two possible reasons that could explain this phenomenon: on the one hand, the formation of a secondary phase (manganese (IV) oxide) which could have been removed during the washing process. On the other hand, the higher size of Mn^{2+} (91 pm) comparing with Fe^{2+} (82 pm) could reduce the probability of Mn^{2+} cations to occupy the tetrahedral or octahedral sites of the inverse spinel structure.

The relative values of Ni and Fe obtained for core shell samples, which are a combination of Fe_3O_4 and $Ni_{0.31}Fe_{2.69}O_4$ layers, are very close to the metal amounts added during the synthesis. Unfortunately, it is not possible to verify the amounts of Ni cation in the different layers from these results.

3.1.1.2 Nanoparticle size and shape analysis

- **Transmission Electron Microscopy (TEM)**

The direct way to determine the size and shape of the prepared NP samples is by means of Transmission Electronic Microscopy (TEM). TEM micrographs of the prepared samples were obtained using a Philips CM200 microscope at an acceleration voltage of 200 kV, in the conditions described in Appendix I. TEM micrographs of the Ni ferrite samples can be observed in Figure 3.2. The NP main diameters vary from 8 to 12 nm for samples prepared with different Ni:Fe proportion, being 18 nm for the $Ni_{0.31}Fe_{2.69}O_4$_A growth sample.

It is to note that the applied seed mediated one pot growth method has yield proper results, since the obtained main diameter in the growth sample is in good agreement with the expected. In this kind of processes multimodal size dispersions are usually obtained, therefore, an effective method to separate different NP diameter groups was necessary in order to obtain homogeneous samples.[1] In our case, the separation method used after the synthesis process and previously described, has achieved a perfect separation of sizes.

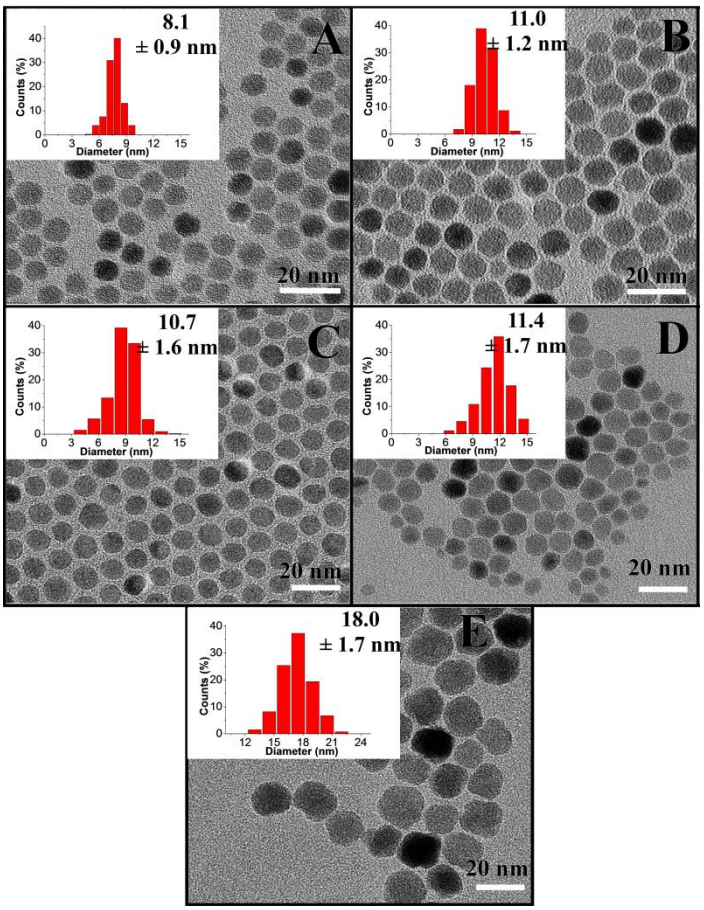

Figure 3.2. *TEM micrographs of $Ni_{0.31}Fe_{2.69}O_4$ (A), $Ni_{0.43}Fe_{2.57}O_4$ (B), $Ni_{0.70}Fe_{2.30}O_4$ (C), $Ni_{0.86}Fe_{2.14}O_4$ (D) and $Ni_{0.31}Fe_{2.69}O_4$_A (E), together with the size distributions.*

Thus, depending on the colloidal dispersion stability, different sized NP aliquots could be obtained from a polydisperse sample. For instance, a smaller size aliquot ($Ni_{0.31}Fe_{2.69}O_4$_B) has been obtained from the sample synthesized by the seed mediated growth method, isolated by applying different toluene:ethanol ratios (Figure 3.3). This mechanism shows an interesting way to obtain monodisperse aliquots whatever the polydispersity of the synthesized sample is.

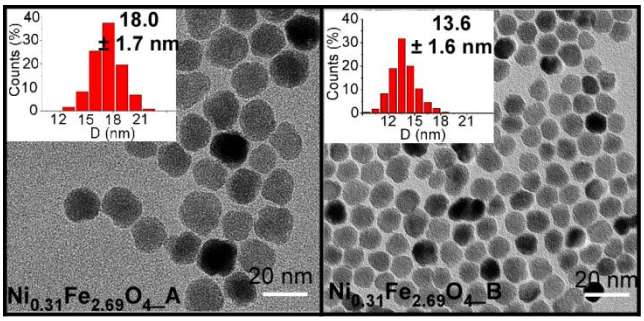

Figure 3.3. *TEM micrographs of $Ni_{0.31}Fe_{2.69}O_4$_A and $Ni_{0.31}Fe_{2.69}O_4$_B aliquots obtained from the same seed mediated growth sample*.

The size dispersions are in the 1-2 nm range in every instance and the size distributions fit to Gaussian profiles (Table 3.2). These deviations are in good agreement with other ferrite nanoparticles synthesized by the same method.[1,2] The Ni ferrite nanoparticle shape is generally spherical, specially for $Ni_{0.31}Fe_{2.69}O_4$, $Ni_{0.43}Fe_{2.57}O_4$, $Ni_{0.70}Fe_{2.30}$ and $Ni_{0.86}Fe_{2.14}O_4$ samples. However, a slight deviation from the spherical shape can be appreciated in the $Ni_{0.31}Fe_{2.69}O_4$_A growth sample, as a more prism like shape can be observed. Similar morphological changes in NPs have been previously observed in literature when the NP size rises from lower diameters to higher.[3]

Similar results have been obtained for Mn ferrite nanoparticle series. The average diameters, measured from the histograms presented in Figure 3.4, vary from 7 to 11 nm for $Mn_{0.13}Fe_{2.87}O_4$, $Mn_{0.18}Fe_{2.82}O_4$, $Mn_{0.27}Fe_{2.73}O_4$ and $Mn_{0.36}Fe_{2.64}O_4$ samples, in a similar range as the Ni ferrites. NP size distributions fit also to a Gaussian profile, with deviations around 1.5 nm. In this way, Ni and Mn precursors do not strongly affect the synthesis process, as in both cases the NP size and shape are similar.

3. Nanocompound characterization

As it was performed for Ni ferrite series, one of the samples ($Mn_{0.13}Fe_{2.87}O_4$) was also growth by means of the seed mediated one pot growth mechanism. Nonetheless, the diameter increase was not as high as in the growth Ni sample, rising from 10 nm of the $Mn_{0.13}Fe_{2.87}O_4$ seed sample to 16 nm of the $Mn_{0.13}Fe_{2.87}O_4$_A growth sample (Table 3.2). Furthermore, a great difference in the NP shape can be appreciated in the Figure 3.4 for this growth sample. As it was checked in the Ni ferrite growth sample, the NP shape tends to shift to anisotropic morphologies at diameters higher than 16 nm.[4] The increase of spin couplings in nanoparticles at higher particle diameters is related to a higher ferromagnetic behaviour of NP, which induces anisotropy in the particles. This anisotropy increase, together with the size homogeneity, can also be verified by the strong tendency of self assembling that the nanoprisms show (Figure 3.4).

Finally, the micrographs of the core shell samples (FeNi2Mag2 and Mag2FeNi2) are shown in Figure 3.5. The main diameters of both samples are around 15 nm, with standard deviations of ±2 nm. As it has been explained in chapter 2, these core shell samples have been prepared by means of a seed mediated growth procedure, thus, their diameter can only be compared with other growth samples ($Mn_{0.13}Fe_{2.87}O_4$_A and $Ni_{0.31}Fe_{2.69}O_4$_A). The main diameters of the core shell NP samples are slightly lower than the Ni and Mn growth ferrites, but quite similar between them. The spherical shape observed in smaller NPs has been lost, and a prism like morphology can be observed in some cases.

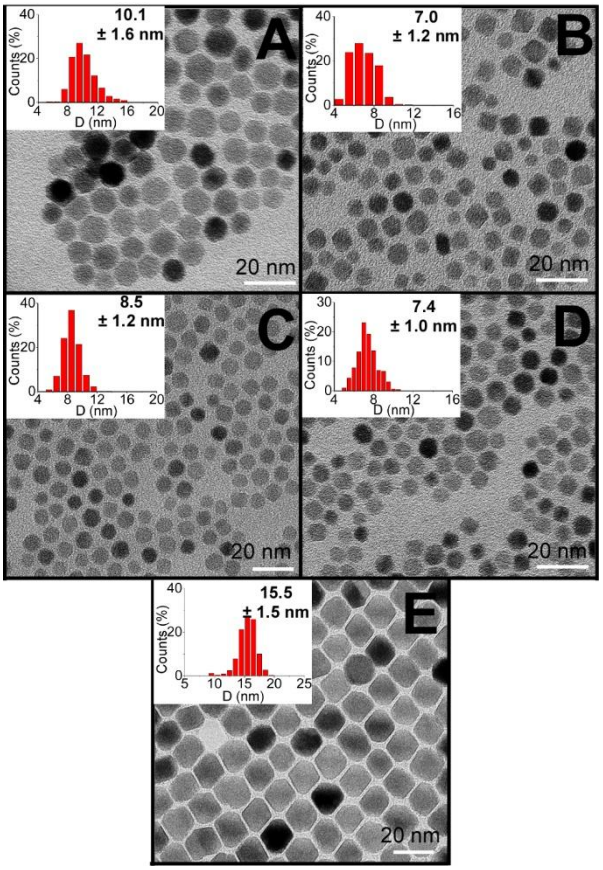

Figure 3.4. *TEM micrographs of $Mn_{0.13}Fe_{2.87}O_4$ (A), $Mn_{0.18}Fe_{2.82}O_4$ (B), $Mn_{0.27}Fe_{2.73}O_4$ (C), $Mn_{0.36}Fe_{2.64}O_4$ (D) and $Mn_{0.13}Fe_{2.87}O_4$_A (E), together with size distributions.*

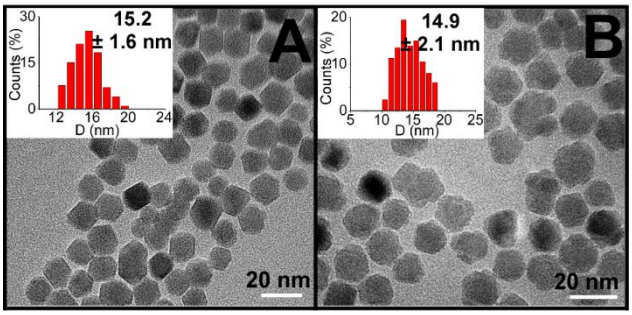

Figure 3.5. *TEM micrographs of Ni2Mag2(A) and Mag2FeNi2(B) samples, together with the size distributions.*

As a conclusion, there are no evidences of NP size dispersion or morphology changes due to Ni or Mn doping. However, a significant nanoparticle shape change has been observed in the $Mn_{0.13}Fe_{2.87}O_4$_A growth sample, probably induced by the intrinsic anisotropy increase.

- **Size analysis by Dynamic Light Scattering (DLS)**

As these materials are expected to be applied in colloidal dispersion in biomedical applications, the NP size in colloidal dispersion also needs to be checked. In this way, Dynamic Light Scattering (DLS) is an useful technique since, based on the size dependent light dispersion angle on particles, the dynamic NP sizes can be determined in colloidal suspension.

The aggregation effect in stable colloidal dispersions can be determined by comparing the particle diameter measured by electronic microscopy with the obtained from the light scattering by DLS. This colloidal stability is mainly based on the repulsion forces between particles. For hydrophobic nanoparticles, as our ferrite NPs, the final stability depends strongly on the oleate coating grade of the NPs, since the hydrophobic repulsions which avoid the aggregation increase with oleate density in the NP surface. For hydrophilic NPs, the key point lies on the charge density of NP surface, as the repulsion between same charges keeps the NPs isolated from each other.

As it can be observed in Figures 3.6, 3.7, 3.8 and Table 3.2, the values obtained from the DLS measurements are in good agreement with those obtained from the TEM analysis. In Ni ferrite size distribution curves shown in Figure 3.6, the size distribution values are also in the same value range of the obtained from TEM analysis. Generally, the average dynamic diameters might be higher than values obtained from microscopy depending on the coating agent. Considering the length of oleic acid chains, which form the NP surface, the length rise should be only about 1 nm, thus, the obtained results

support this surmise. As it was expected, the highest dynamic diameter was shown for the $Ni_{0.31}Fe_{2.69}O_4$_A growth sample.

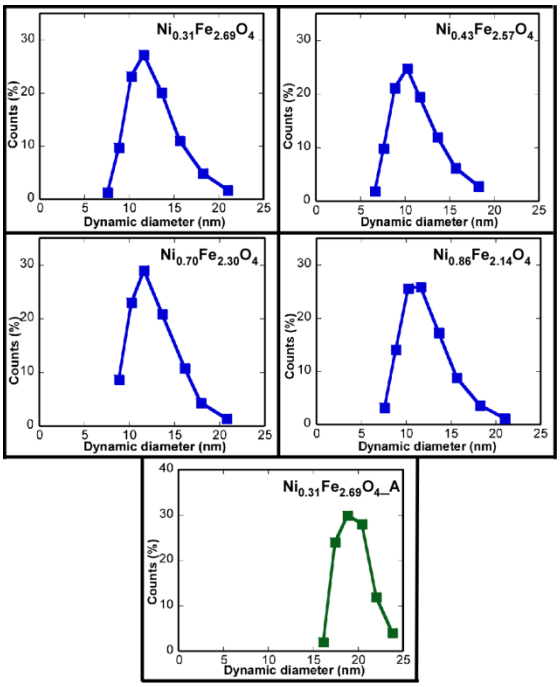

Figure 3.6. *Dynamic size distributions of $Ni_{0.31}Fe_{2.69}O_4$, $Ni_{0.43}Fe_{2.57}O_4$, $Ni_{0.70}Fe_{2.30}O_4$, $Ni_{0.86}Fe_{2.14}O_4$ and $Ni_{0.31}Fe_{2.69}O_4$_A samples measured by DLS.*

Similar results can be observed in Figure 3.7 for the Mn ferrite samples, as the measured average diameters are in good agreement with the TEM measurements. Although a light increase of the dynamic diameters can be appreciated for these ferrites, excepting for $Mn_{0.27}Fe_{2.73}O_4$ sample, it is not high enough to be caused by an aggregation effect. The size dispersion for the $Mn_{0.13}Fe_{2.87}O_4$_A growth sample is slightly higher than the obtained for the other growth sample ($Ni_{0.31}Fe_{2.69}O_4$_A), which could be due to their high shape anisotropy.

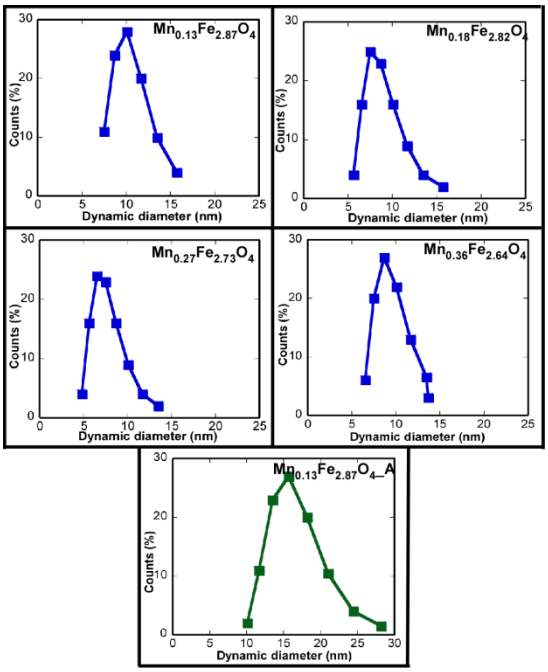

Figure 3.7. *Dynamic diameters for $Mn_{0.13}Fe_{2.87}O_4$, $Mn_{0.18}Fe_{2.82}O_4$, $Mn_{0.27}Fe_{2.73}O_4$, $Mn_{0.36}Fe_{2.64}O_4$ and $Mn_{0.13}Fe_{2.87}O_4$_A samples measured by DLS.*

Finally, the DLS results for the core shell NPs represented in Figure 3.8 show the expected dynamic diameters for both samples. The size dispersion is slightly broader for the FeNi2Mag2 core shell sample than for the Mag2FeNi2. This effect could be induced by the anisotropic shape of these NPs, previously observed in TEM measurements (Figure 3.5). It is to note that the size dispersion values are comparable to those obtained from the TEM micrographs, discarding any aggregation process.

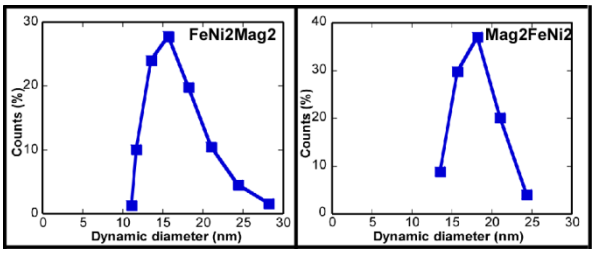

Figure 3.8. *Dynamic size distributions of FeNi2Mag2 and Mag2FeNi core shell NPs measured by DLS.*

Table 3.2. *Average diameter and standard deviations of Ni ferrite, Mn ferrite and core shell NP samples measured by TEM and DLS.*

SAMPLE	D_{TEM} (nm)	D_{DLS} (nm)
$Ni_{0,31}Fe_{2,69}O_4$	8.1 ± 0.9	10.9 ± 2.2
$Ni_{0,43}Fe_{2,57}O_4$	11.0 ± 1.2	10.6 ± 2.5
$Ni_{0,70}Fe_{2,30}O_4$	10.7 ± 1.6	12.2 ± 2.5
$Ni_{0,86}Fe_{2,14}O_4$	11.4 ± 1.7	11.5 ± 2.4
$Ni_{0,31}Fe_{2,69}O_4$_A	18.0 ± 1.7	19.4 ± 1.8
$Mn_{0,13}Fe_{2,87}O_4$	10.1 ± 1.6	10.0 ± 2.0
$Mn_{0,18}Fe_{2,82}O_4$	7.0 ± 1.2	8.7 ± 2.1
$Mn_{0,27}Fe_{2,73}O_4$	8.5 ± 1.2	7.5 ± 1.8
$Mn_{0,36}Fe_{2,64}O_4$	7.4 ± 1.0	9.3 ± 2.0
$Mn_{0,13}Fe_{2,87}O_4$_A	15.5 ± 1.5	16.1 ± 3.1
FeNi2Mag2	15.2 ± 1.6	16.3 ± 3.2
Mag2FeNi2	14.9 ± 2.1	17.8 ± 2.6

3.1.1.3 X Ray Diffraction analysis

The X Ray Diffraction (XRD) technique was employed to verify the presence of the inverse spinel structure and to check the presence of possible impurities or secondary phases. Furthermore, an increase of Ni or Mn doping level in the inverse spinel structure could modify the unit cell

parameters of the crystalline structure. The obtained diffractograms for all samples are shown in Figure 3.9.

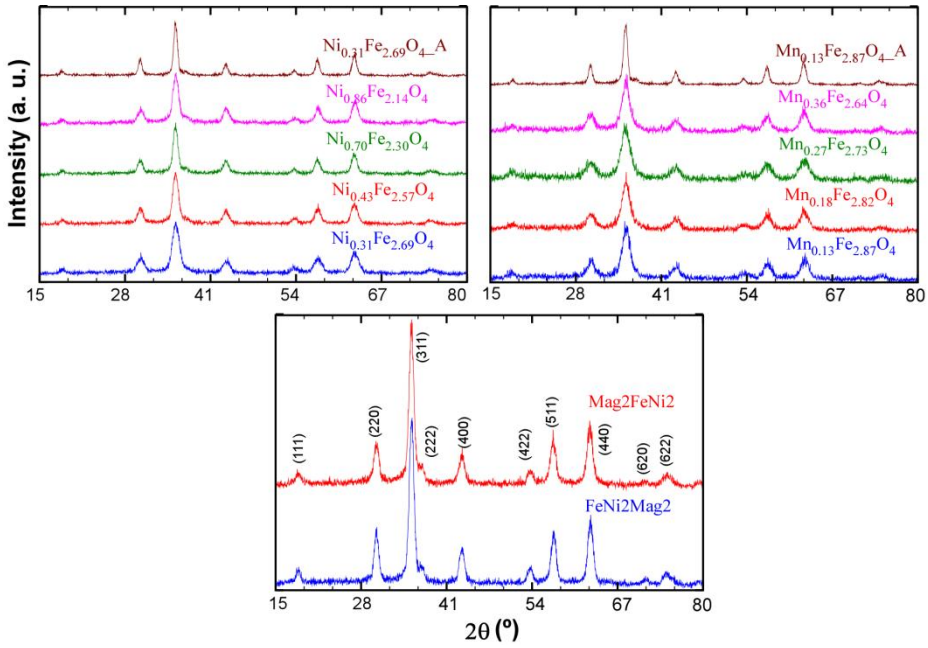

Figure 3.9. *X ray diffraction measurements of Ni, Mn ferrite and core shell nanoparticles.*

As it can be observed in Figure 3.9, all the diffraction peaks correspond to the inverse spinel face centred cubic based structure (S.G.: Fd-3m, PDF number 89-0691). No extra peaks have been observed in any sample, thus, the absence of any secondary phases at proportions higher than 5 % in mass can be ensured.

In order to verify the possible displacement of the diffraction peaks due to the Ni or Mn substitution, the fitting of the most intense peak (311) has been performed by means of WinPLOTR software. The fitting of the (311) reflexion peak for Ni ferrite samples is represented in Figure 3.10, and the

obtained 2θ values for all samples are represented in Table 3.3. Peak fitting for Mn ferrite and core shell samples were performed in the same way.

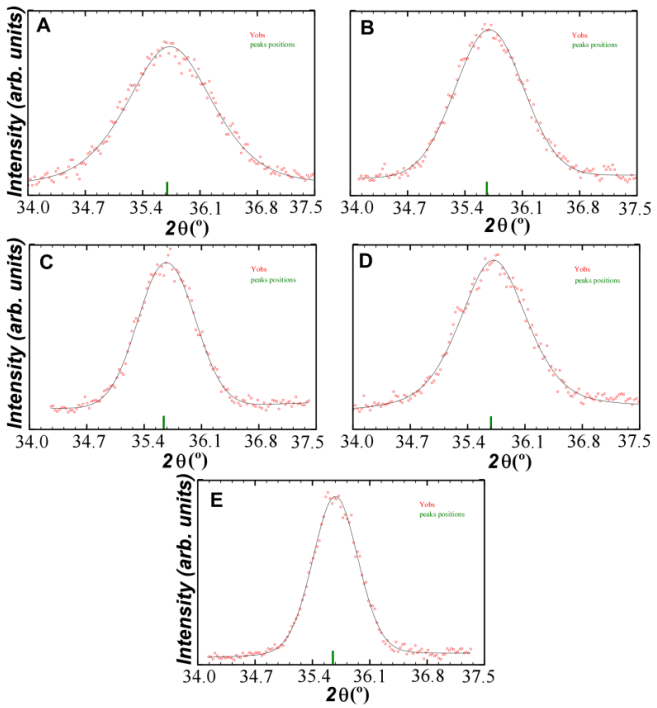

Figure 5.10. *(311) peak fitting for Ni ferrite NPs. A: $Ni_{0.31}Fe_{2.69}O_4$, B: $Ni_{0.43}Fe_{2.57}O_4$, C: $Ni_{0.70}Fe_{2.30}O_4$, D: $Ni_{0.86}Fe_{2.14}O_4$, E: $Ni_{0.31}Fe_{2.69}O_4$_A.*

From these fittings, differences in unit cell parameters can be obtained. Moreover the crystal size can be estimated by means of the Scherrer's equation from the peak width at half height.[5] All obtained results are represented in Table 3.3.

Table 3.3. *2θ positions of (311) planes and crystal sizes calculated by means of Debye Scherrer equation for NP samples.*

SAMPLE	311 (2θ °)	Size (nm)
$Ni_{0,31}Fe_{2,69}O_4$	35.70	8.0
$Ni_{0,43}Fe_{2,57}O_4$	35.67	10.6
$Ni_{0,64}Fe_{2,36}O_4$	35.64	11.0
$Ni_{0,86}Fe_{2,14}O_4$	35.68	10.6
$Ni_{0,31}Fe_{2,69}O_4$_A	35.64	17.7
$Mn_{0,13}Fe_{2,87}O_4$	35.63	11.7
$Mn_{0,18}Fe_{2,82}O_4$	35.59	11.8
$Mn_{0,27}Fe_{2,73}O_4$	35.55	10.2
$Mn_{0,36}Fe_{2,64}O_4$	35.58	12.1
$Mn_{0,13}Fe_{2,87}O_4$_A	35.52	19.5
FeNi2Mag2	35.65	16.3
Mag2FeNi2	35.62	16.2

No great differences between ferrites with different proportions of Ni or Mn cations can be observed in the 2θ values, due to the similar radius of the cations (78 pm for Ni^{2+}, 75 pm for Fe^{2+} and 81 pm for Mn^{2+}) (Table 3.3). Furthermore, an estimation of crystal diameter can be performed from the peak widths. Considering the nanoparticles as monodomain systems, the crystal size is directly related to the particle diameter by means of the Scherrer's equation (3.1):

$$\tau = \frac{K\lambda}{\beta_\tau cos\theta} \qquad (3.1)$$

Where τ represents the crystal domain (the particle diameter in monodomain spherical NPs), K is the shape factor (1 for spherical NP), λ is the applied wavelength (1.54178 Å for copper Kα radiation), βτ is the peak width at half height and θ is the peak angle position. This is only an estimation of the crystal size, since there are other variables as the shape factor that are difficult to determine precisely, and could change the final

value. In this way, the obtained crystalline diameters shown in Table 3.3 prove that the obtained nanosystems are monodomain in every case, and fit perfectly with the values measured from TEM micrographs. This monodomain nature of nanoparticles is crucial for a superparamagnetic behaviour, as the presence of magnetic domains induce remanent magnetization.[6] This confirmation is specially relevant for the core shell NPs, since the formation of magnetic domains by interaction of different phases in the same nanoparticle has been refused.

3.1.1.4 Nanoparticle coating analysis

In the same way as the chemistry and structure analysis, it is also important to obtain information about the NP cover. This coating stabilises the NPs in colloidal dispersion, which is absolutely essential to eventually be applied in biomedical applications. The mass evolution of the organic matter with the temperature has been studied by means of thermogravimetric measurements performed in Ar atmosphere, applying a 10 °C/min heating rate in a the 25-800 °C temperature range (Figure 3.11).

Thermogravimetric curves show a well-defined mass loss profile over the temperature range of 200-600 °C, attributed to the decomposition of the organic ligands attached to the particle surface. As can be seen, the mass loss profile is similar in all samples. The profile is related to the decomposition of the organic matter, what happens in the same way in all prepared NPs. Losses below 150 °C correspond to the adsorbed humidity, which is present in all samples, especially in core shell and Mn ferrite samples. Slight mass losses can also be appreciated below 300 °C in most samples correlated with benzyl ether solvent reminders, which boiling temperature is 290 °C.

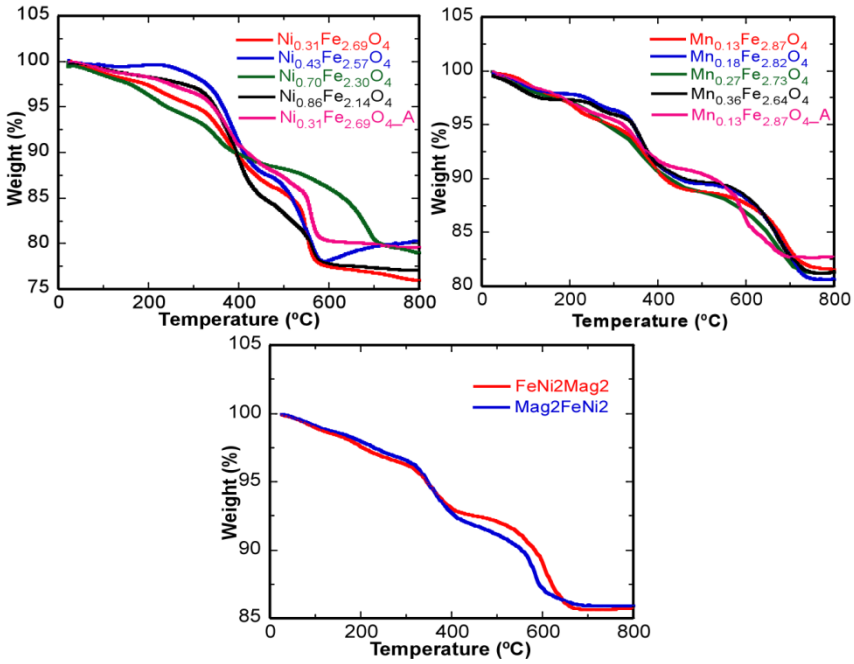

Figure 3.11. *Thermogravimetric curves of Ni, Mn ferrites and core shell nanoparticles in 25-800 °C range.*

The presence of two different slopes at 400 and 550 °C suggests two different kind of interactions between oleic acid and NP surface, which produces different dissociations at two different temperatures. Oleic acid molecules are chemically absorbed on the surface of the ferrite nanoparticles though the chemical interaction between their -COOH groups and the -OH surface groups. Some authors have attributed this two step degradation to a double oleate layer in the NP surface, whereas other authors argued that these two decomposition temperatures correspond to two different dissociations. In our point of view, both hypothesis could be possible.[2] An excess of oleic acid could induce the formation of a new oleic acid layer by Van der Waals's interactions between oleate chains, which would be the reason of the two different dissociation temperatures.

The organic mass losses are summarized in Table 3.4. No great changes can be appreciated between similar NPs. Higher diameter NPs, which have been synthesized by the seed mediated growth method ($Ni_{0.31}Fe_{2.69}O_4$_A, $Mn_{0.13}Fe_{2.87}O_4$_A, FeNi2Mag2 and Mag2Fe3Ni2 samples) show the lowest amount of organic mass. Thus, the coating proportion of nanoparticles is directly related to their size and shape, as these factors limit the proportion of superficial area available to be functionalized. In contrast, the smallest samples show the highest percentage of organic coating, as can be clearly observed in the Ni ferrite series, where the highest size sample ($Ni_{0.31}Fe_{2.69}O_4$_A) presents the lowest organic mass percentage.

As conclusion, the high percentage of organic matter of all synthesized magnetic nanoparticles is indicative of a complete coating by ligands, which is the reason of their high colloidal stability.

Table 3.4. *Organic mass percentage losses calculated from the thermogravimetric analysis for the NPs.*

SAMPLE	Org. Mat. (%)
$Ni_{0,31}Fe_{2,69}O_4$	24
$Ni_{0,43}Fe_{2,57}O_4$	20
$Ni_{0,64}Fe_{2,36}O_4$	20
$Ni_{0,86}Fe_{2,14}O_4$	22
$Ni_{0,31}Fe_{2,69}O_4$_A	18
$Mn_{0,13}Fe_{2,87}O_4$	18
$Mn_{0,18}Fe_{2,82}O_4$	20
$Mn_{0,27}Fe_{2,73}O_4$	19
$Mn_{0,36}Fe_{2,64}O_4$	19
$Mn_{0,13}Fe_{2,87}O_4$_A	18
FeNi2Mag2	14
Mag2FeNi2	14

3.1.2 Magnetic properties of prepared NPs

As it has been explained, the aim of the prepared particles is to be applied as magnetic hyperthermia inductors in future medical treatments. For this purpose, after their chemical and structural properties have been analyzed and their colloidal stability has been verified, their capability to induce magnetic hyperthermia response needs to be studied. The magnetic behaviour of NPs was analyzed by different methods, as field and temperature dependent magnetization measurements M (H) and M (T), and Electron Magnetic Resonance (EMR) spectroscopy. These tools have been selected based on the previous experience, focusing on achieving a proper understanding of NP magnetic behaviour before testing the magnetic hyperthermia induced heat generation.

3.1.2.1 Field dependent magnetization measurements of NPs, M (H)

By this experiment, materials net magnetization is measured while applying a variable magnetic field. Firstly, the saturation magnetization of the material can be calculated from the maximum saturation of the magnetization loop. Furthermore, for nanoparticle samples, the superparamagnetic behaviour can be checked at different temperatures by the absence of magnetic remanence in the M (H) cycles. All samples were measured in powder (≈ 15 mg) in a Vibrating Sample Magnetometer (VSM) from Cryogenic Ltd. up to a maximum field of 100 kOe in a 5-300 K temperature range. Sample powder was compressed in a gelatine capsule to avoid vibrations during the measurement. The matrix effect in the final magnetization value has been discarded by deducting the mass corresponding to the organic matter determined by the thermogravimetric analysis (Table 3.4). The obtained M (H) signals at 5 and 300 K for Ni and Mn

ferrites and core shell nanoparticles are present in Figure 3.12. The obtained M_s and H_c values are represented in Table 3.5.

From the hysteresis loops measured at 300 K the absence of remanent magnetization can be noticed for most of the prepared nanoparticles, characteristic of a superparamagnetic behaviour.[7] By Ni and Mn addition soft ferrites have been obtained. A reduction of the coercive field is obtained for these bulk ferrites comparing with the magnetite, thus, inducing a higher superparamagnetic behaviour for soft ferrite nanostructured materials, comparing with equal Fe_3O_4 NPs. The opposite effect has been observed in literature for hard ferrite nanoparticles, as Co ferrites.[8] In this case, the introduction of Co^{2+} cations into the inverse spinel structure induces a broadening effect of the M (H) cycle by increasing strongly the anisotropy constant of the material. In fact, the loss of superparamagnetic behaviour in small Fe_3O_4 nanoparticles has been checked by doping with very small proportions of Co^{2+}.[9,10]

The heat generation by applying an external magnetic field is directly related to the saturation magnetization value. Consequently, the effects of the Ni and Mn doping in the saturation magnetization (M_s) values need to be analysed. As it can be seen in Figure 5.12 and Table 3.5, the magnetization of ferrites at an applied constant magnetic field was higher at 5 K, since the absence of thermal fluctuation allows the blocking of magnetic moments oriented to the magnetic field. For Ni ferrites, M_s values at 5 K vary from 75 to 100 emu/$g_{Ferrite}$, depending on the nickel content of the structure. Samples with lower nickel proportions ($Ni_{0.31}Fe_{2.69}O_4$ and $Ni_{0.31}Fe_{2.69}O_4$_A) present slightly higher saturation magnetizations (100 emu/g) than magnetite bulk materials (98 emu/g).[11]

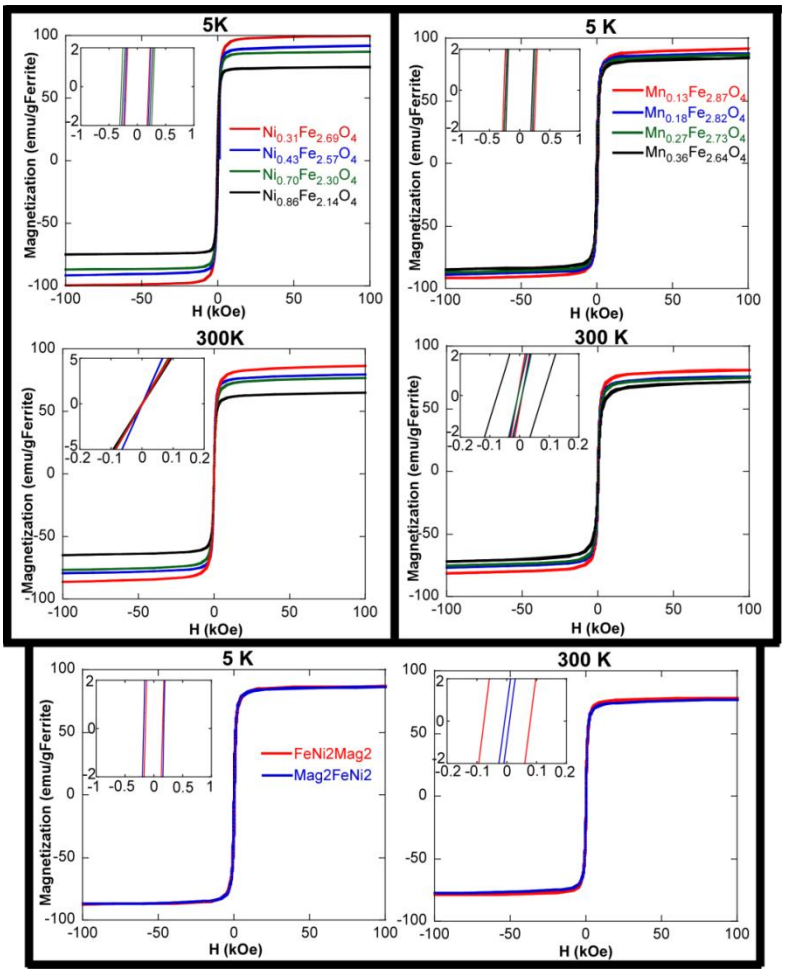

Figure 5.12. *M (H) cycles for all nanoparticles measured at 5 and 300 K. The central part is enlarged to visualize Hc.*

However, the M_s value decreases drastically when increasing the nickel percentage, as it can be observed in $Ni_{0.43}Fe_{2.57}O_4$, $Ni_{0.70}Fe_{2.30}O_4$ and $Ni_{0.86}Fe_{2.14}O_4$ samples. This could be explained by the modification of the antiferromagnetic interactions between T_d and O_h sites.[11] In structures with low Ni^{2+} proportions (2 μ_B), these cations would occupy the T_d sites, inducing partial removal of the antiferromagnetic coupling interactions between Fe^{3+} (5 μ_B) ions and increasing M_s values. At higher nickel amounts, these cations

would fill the octahedral holes, balancing the ferrimagnetic structure spin amounts by Fe^{2+} (4 μ_B) cation substitution and, therefore, decreasing the net magnetization value.[12] The possible effects of Ni^{2+} cation insertion in the ferrite magnetization final value are schematically illustrated in Figure 3.13.

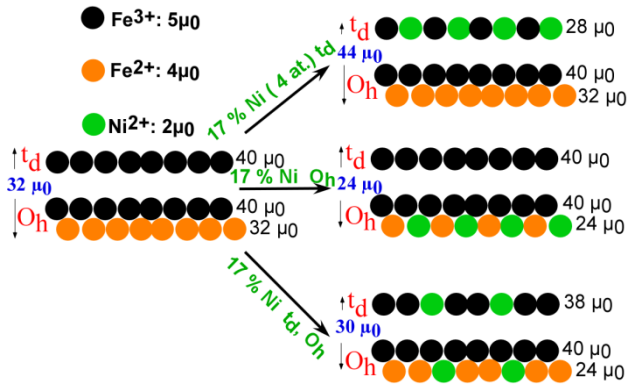

Figure 3.13. *Schematic illustration of the possible effects Ni^{2+} doping in magnetite. First atom row represents the eight tetrahedral holes and second and third rows the 16 octahedral holes of an inverse spinel structure.*

Similar effects can be observed in Mn ferrite samples. As it can be seen in Table 3.5, the M_s reached a maximum value of 92 emu/gFerrite in the lowest Mn ratio ($Mn_{0,13}Fe_{2,87}O_4$ and $Mn_{0,13}Fe_{2,87}O_4$_A) at 5 K. Although this value is quite high for ferrite NPs, it is slightly lower than the values obtained for the Ni ferrites. The trend of M_s values at higher Mn ratios is not as clear as in the Ni ferrites. The hypothesis used to explain the decrease of magnetization at high Ni^{2+} ratios is not suitable for Mn^{2+} doping, since the substitution of Fe^{2+} (4 μ_B) cations for Mn^{2+} (5 μ_B) has not the same effect as the Ni^{2+} (2 μ_B) insertion. In this case, the M_s value seems to be almost constant whatever the ratio of Mn^{2+} is, having detected a very slight M_s decreasing when increasing the Mn^{2+} doping grade.[7] Changes in the Mn oxidation state during this kind of synthesis to conform more stable compounds have been

reported in literature.[13] Hence, the oxidation from Mn^{2+} to Mn^{3+} could yield a net magnetization decrease in the same way as has been observed for the Ni^{2+} insertion in the octahedral holes.

In the same way, both core-shell magnetic nanoparticles have similar M_s values, being slightly lower than values corresponding to the bulk magnetite. The nickel ammount in these cases is too low to induce a measurable effect in the total M_s of the core-shell material. Furthermore, the different configuration of both layers (Fe_3O_4 and $Ni_{0.31}Fe_{2.69}O_4$) does not seem to have measurable influence in M_s value.

Most of the sample cycles presented in Figure 5.12 show H_c values around 200 Oe, being slightly higher for the $Mn_{0,13}Fe_{2,87}O_4$_A and FeNi2Mag2 samples. However, the H_c values obtained from the VSM measurements are not accurate enough to take them into account. The NPs in powder have great dipolar and magnetic interactions between them, which skews the magnetization value at low applied magnetic fields. To avoid this kind of interactions, M (H) measurements at 5 K were performed in a commercial Superconducting Quantum Interference Device (SQUID) magnetometer (Quantum Design (MPMS-7T), equipped with a 7 T superconducting magnet) by depositing the NP toluene colloidal dispersions (0.05 mgFe/mL) on filter paper (Figure 3.14 and Table 3.5). Thus, the obtained coercive fields are more reliable. Nevertheless, similar values to those obtained from the VSM measurements have been deduced for Ni and Mn ferrites and core shell samples. The softening effect theoretically induced by the Ni^{2+} and Mn^{2+} cation presence in the ferrites cannot be verified by the H_c measurements in this case.

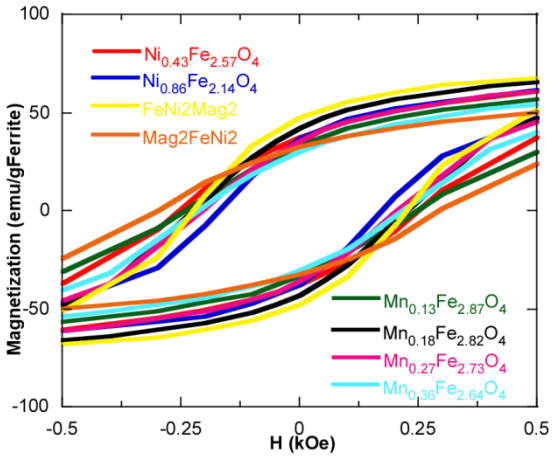

Figure 3.14. *Field dependent magnetization measurements, measured at 5 K in samples dispersed in filter paper.*

Table 3.5. *Saturation magnetization (M_s) values at 5 and 300 K (measured in the VSM) and coercive fields (H_c) measured in the VSM and the SQUID at 5K.*

SAMPLE	M_s 5 K/300 K (emu/gFerrite)	H_c VSM (Oe) 5 K	H_c SQUID (Oe) 5 K
$Ni_{0,31}Fe_{2,69}O_4$	100/87	202	-
$Ni_{0,43}Fe_{2,57}O_4$	92/79	222	255
$Ni_{0,64}Fe_{2,36}O_4$	73/77	280	-
$Ni_{0,86}Fe_{2,14}O_4$	75/65	250	171
$Ni_{0,31}Fe_{2,69}O_4$_A	98/86	203	-
$Mn_{0,13}Fe_{2,87}O_4$	92/81	262	251
$Mn_{0,18}Fe_{2,82}O_4$	88/76	237	224
$Mn_{0,27}Fe_{2,73}O_4$	87/75	235	206
$Mn_{0,36}Fe_{2,64}O_4$	85/72	208	215
$Mn_{0,13}Fe_{2,87}O_4$_A	96/86	169	-
FeNi2Mag2	87/79	148	225
Mag2FeNi2	86/77	165	298

To summarize, high saturation magnetization values have been obtained in every case and all samples have shown superparamagnetic behaviour at

room temperature. Moreover, the influence of Ni and Mn cation insertion has been verified. The most promising sample would be the $Ni_{0,31}Fe_{2,69}O_4$_A growth sample, since its highest saturation magnetization could provide a great magnetic hyperthermia response.

3.1.2.2 Temperature dependant magnetization M(T) measurements of NPs

For ferro-, ferri- and antiferromagnetic materials, the magnetization value evolution with the temperature provides useful information about their nature and properties. In this way, the synthesized ferrites are expected to show high magnetic susceptibility and ferromagnetic behaviour below Curie's temperature (T_C), which is around 585 °C for bulk Fe_3O_4 system. Above this temperature the thermal energy overcomes the spin coupling energy, and the ferrimagnetic material behaves as a paramagnet.

As it has been checked by M (H) measurements, the synthesized materials show superparamagnetic behaviour at room temperature, and behave as a high magnetic susceptibility paramagnetic material. However, there is a temperature where the anisotropy energy of NPs overcomes the thermal energy, called blocking temperature (T_B). Below this point, even being monodomain systems without magnetic domains, the NPs behave as ferrimagnetic materials as their magnetic moments are anchored. By performing the temperature dependent magnetization experiment, this blocking temperature can be calculated. Furthermore, the sample homogeneity can also be evaluated from the T_B distribution. Thus, magnetization measurements as a function of temperature after cooling at zero field (ZFC curve) and 10 Oe field (FC curve) were performed in the SQUID. NPs diluted in toluene dispersion (0.05 mgFe/mL), were dyed in a filter paper to avoid dipolar and magnetic interactions between NPs. The

diamagnetic contribution of the filter paper was removed. The FC-ZFC curves obtained for all the samples are represented in Figure 3.15.

Above blocking temperature, magnetic moments are fluctuating between both directions of the easy magnetization axis, making the net magnetization zero in absence of an applied magnetic field. This is called the superparamagnetic behaviour, where the high thermal energy overcomes the anisotropy energy. However, these fluctuating magnetic moments align with the applied magnetic fields, showing a great magnetization value, far higher than paramagnetic materials values. After cooling the sample below the T_B without applying magnetic field (ZFC), these fluctuant magnetic moments will anchor equally in both directions of the easy magnetization axis, also obtaining a zero net magnetization value. However, at the beginning of the ZFC curve, a week magnetization can be observed due to the slight orientation of the magnetic moments with the applied magnetic field (10 Oe), defined by the previously mentioned Stoner-Wolhfart model.[14] At increasing temperatures, smallest NPs overcomes their blocking temperatures and align with magnetic field. Taking the existence of particle moment distribution (which comes from the size distribution) into account, the macroscopic net magnetization depends on this magnetic distribution ($f(\mu)$), which causes a blocking temperature distribution ($f(T_B)$). The distribution of the energy barriers can be obtained by a direct subtraction of the field cooled and zero field cooled branches of the magnetization *versus* temperature measurements. This difference is proportional to the number of particles in the blocked regime (ferrimagnetic behaviour), that decreases with temperature when the thermal energy overcomes the anisotropy energy of each nanoparticle.[15] In this way, the net magnetization gradually increases with temperature until most of the NPs are unblocked and the ZFC magnetization branch reaches a maximum, ideally the average T_B. From this

point, increasing temperature induces higher thermal agitation of the magnetic moments, which progressively decreases the magnetization value.

At this point, the system is again cooled under a 10 Oe magnetic field and the temperature dependent magnetization is measured again. Cooling the NPs under a constant magnetic field below blocking temperature the magnetic moments are anchored only in the direction of the magnetic field, instead of in both directions of the easy magnetization axis as in the ZFC curve. Thus, all magnetic moments are oriented with the magnetic field with a minimum thermal agitation force. Consequently, the magnetization value reaches its maximum. Increasing the temperature, the unblocking process of the NPs starts as happened in the ZFC branch. When the thermal rotation of the magnetic moments is activated, the net magnetization value starts progressively decreasing due to the increase of the magnetic moment fluctuation. The point where the ZFC and FC curves converge is called the irreversibility temperature (T_{irr}) and refers to the unblocking of the higher size magnetic NPs, or the NPs which present the highest anisotropy energy. In this way, the difference between T_B and T_{irr} is related to the size distribution, or the aggregation state.

As it can be checked in Figure 3.15, all measured samples present superparamagnetic behaviour at room temperature, with several differences between their average blocking temperatures and T_B distributions. The original equation for explaining the magnetic behaviour of monodomain magnetic particles was developed by Stoner and Wohlfarth, relating the saturation magnetization (M_S), anisotropy energy constant (K) and coercive field (H_c) (3.2 equation):

$$H_C = 0.48\frac{2K}{M_S}\left[1 - \left(\frac{T}{T_B}\right)^{1/2}\right] \quad (3.2)$$

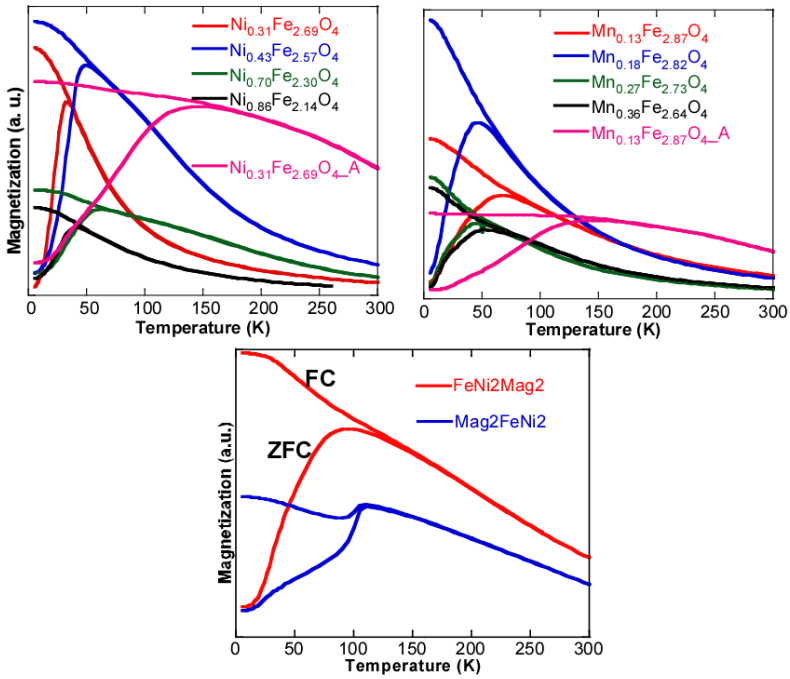

Figure 3.15. *Temperature dependent magnetization curves of prepared NPs measured after zero field (ZFC) and field (FC) cooling.*

Where 0.48 is the constant calculated from the average of easy magnetization axes distribution in the system, T is the measurement temperature and T_B the NP average blocking temperature. This equation was designed for T=0 K, but can be applied at 5 K, by a temperature correction.[14] From fitting the former curves, the mean blocking temperatures and anisotropy constants for all samples have been obtained. The T_B and K values for all NPs are shown in Table 3.6.

From all these data several conclusions can be obtained. The direct dependence of the T_B value with the particle diameter has been verified. All samples that have been prepared by the one pot seed mediated growth process have shown considerably higher blocking temperatures due to their higher main diameter. The $Ni_{0.31}Fe_{2.69}O_4$_A sample (19 nm), for instance,

shows a T_B of 99 K whereas its 8 nm seeds ($Ni_{0.31}Fe_{2.69}O_4$) show a T_B of 16 K. Furthermore, the observed blocking temperatures are significantly lower than those corresponding magnetites,[3] mainly due to the softening effect that the Ni^{2+} cation presence induces in the inverse spinel crystalline structure, aiding the easy rotation of the NP magnetic moment in both directions of the easy magnetization axis. Although different nickel content seems not to affect strongly the blocking temperature, it can be observed that anisotropy constant, which are independent of particle size, decrease at higher nickel concentration. A weaker coupling between the magnetic moments is caused by the insertion of Ni^{2+} cations into the ferrite structure, which decreases the anisotropy barrier value (KV). This softening process is well known and is caused by the lower intrinsic anisotropy of Ni^{2+} cations.[11,16]

For the small Ni ferrite samples, narrow ZFC signals were obtained due to the homogeneity of the particle sizes. However, the $Ni_{0.31}Fe_{2.69}O_4$_A ferrite growth sample shows a broadening of the ZFC branch maximum, which is related to the strong dependence of the T_B with the particle diameter (proportional to D^3), as well as to the increase of magnetic interactions between the higher NPs.[17]

A similar effect can be observed for Mn ferrites. However, although the amount of Mn atoms in the ferrite structure is almost the middle of the Ni atoms in the Ni ferrites, nearly similar anisotropy constants have been obtained in both series. Some paramagnetic cations as Ni^{2+}, Mn^{2+}, Mn^{3+} or Co^{2+} have a great influence in the magnetic remanence and coercive values of the inverse spinel structure of the resultant ferrites, obtaining hard ferrites (higher M_r and H_c values than Fe_3O_4) or soft ferrites (lower M_r and H_c values than Fe_3O_4.[18] Depending on the orbital shape, the spins would be more directed to an specific orientation. Thus, due to their orbital shapes, less spin preferential orientation is caused by the presence of Ni and Mn

atoms in the ferrite structure comparing with the Fe^{2+} orbitals. Therefore, the anisotropy of the material is reduced by the presence of such cations.[12]

Table 3.6. *Blocking temperatures and anisotropy constant values for each sample obtained from FC-ZFC experiments and particle sizes measured from the TEM micrographs.*

SAMPLE	T_B (K)	K (kJ/m^3) (T_B)	$SIZE_{TEM}$ (nm)
$Ni_{0,31}Fe_{2,69}O_4$	16	21.06	8.1 ± 0.9
$Ni_{0,43}Fe_{2,57}O_4$	27	17.99	11.0 ± 1.2
$Ni_{0,64}Fe_{2,36}O_4$	31	16.48	10.7 ± 1.6
$Ni_{0,86}Fe_{2,14}O_4$	22	14.20	11.4 ± 1.7
$Ni_{0,31}Fe_{2,69}O_4$_A	99	20.24	18.0 ± 1.7
$Mn_{0,13}Fe_{2,87}O_4$	34	20.11	10.1 ± 1.6
$Mn_{0,18}Fe_{2,82}O_4$	26	20.17	7.0 ± 1.2
$Mn_{0,27}Fe_{2,73}O_4$	26	20.26	8.5 ± 1.2
$Mn_{0,36}Fe_{2,64}O_4$	28	16.49	7.4 ± 1.0
$Mn_{0,13}Fe_{2,87}O_4$_A	75	21.03	15.5 ± 1.5
FeNi2Mag2	42	7.86	15.2 ± 1.6
Mag2FeNi2	65	11.97	14.9 ± 2.1

An anomalous peak can be observed in the ZFC curve of FeNi2Mag2 and Mag2FeNi2 samples at around 125 K. This peak has been identified as the Verwey's transition, related to a structural distortion. This structure transition below ≈120 K for extra pure ferrites was discovered by Verwey on 1939, and has been recently confirmed.[19] The order of the Fe^{2+} and Fe^{3+} cations in the crystalline structure changes below 120 K to a lower density phase due to the alignment of three octahedral Fe^{2+} units. This alignment avoids the electron hopping between Fe^{3+} and Fe^{2+} cations and reduces strongly material conductivity.[20] The presence of this transition has no effect on the magnetic behaviour of these materials at room temperature, neither in the saturation magnetization value measured at 5 K. Nevertheless, the

phase transition impeded the blocking temperature determination from the FC-ZFC experiment. Therefore, the obtained anisotropy values for both core shell samples cannot be compared with the other samples or with the data obtained from the literature. The presence of this transition is not common in the synthetically prepared ferrites, which also supports the crystalline purity of the obtained samples.[21]

3.1.2.3 Electron Magnetic Resonance (EMR) analysis

The Electron Magnetic Resonance (EMR) has a broad use in the study of the magnetic behaviour of materials with paramagnetic ions. Moreover, this technique has also been revealed as a really useful tool to analyse microscopic interactions in superparamagnetic nanoparticles.

The theoretical basis of the EMR are quite similar to the Nuclear Magnetic Resonance. The main difference is that in this case the unpaired spins are being excited instead of the nuclei. By this technique, microwaves are absorbed by materials with unpaired electrons under an external magnetic field that achieves the resonant condition under a certain magnetic field. This fact limits the range of application of this technique as no signal is produced by diamagnetic materials. This limitation makes the method more specific, as possible interferences coming from diamagnetic materials are automatically removed. The EMR technique is generally focused on the identification of paramagnetic systems. However, its usefulness to analyze the electronic microscopic interactions extends the applicability of this techniques to ferro-, antiferromagnetic materials and spin glasses and is starting to be widely used for magnetic nanoparticle analysis.[22,23,3]

In this way, in NP superparamagnetic systems, some important parameters as NP size, system homogeneity, magnetic anisotropy and magnetic interactions between NPs can be studied by this technique. The

magnetic moments achieve the resonant condition at a specific magnetic field which has enough energy to change the magnetic moment orientations. This resonance magnetic field in this kind of uniaxial anisotropy superparamagnetic systems present contributions from the applied magnetic field and from the internal anisotropy. The EMR in this kind of superparamagnetic nanoparticles was studied by Raikher and Stepanov and defined by this equation (3.3):[24]

$$H_r = \frac{\hbar\nu}{g} - \frac{H_a}{2}\frac{1}{L(x)}\left[1 - \frac{3L(x)}{x}\right](3cos^2\vartheta - 1) \quad (3.3)$$

Where H_a is the internal anisotropy field ($2K/M_s$), L (x) is the Langevin function, ϑ represents the angle between the applied magnetic field and the NP anisotropy axis and H_r is the resonant magnetic field. From this resonant magnetic field the electronic gyromagnetic effective factor (g_{eff}) can be obtained. This factor represents the proportionality between the angular momentum and the magnetic moment of e^-.

Hence, different magnetic nanoparticles with different net magnetic moments will show different resonant magnetic fields. This heterogeneity can be induced by differences in the NP magnetocrystalline anisotropy, size or shape. Furthermore, the short time window of this experiment, comparing with M (H) or M (T) measurements, offers the possibility to detect microscopic interactions that are no detected by other techniques. The time window of this kind of measurements is in the same range of the NP magnetic moment spontaneous rotation, therefore, the time window of the used measurement technique could change completely the perception as superparamagnetic or ferromagnetic system. The measurement techniques with time windows below the NP magnetic moment rotation time would identify the NP as ferromagnetic, whereas the techniques with time windows above would be detected as superparamagnetic. As conclusion, the

superparamagnetic nature of a system can only be ensured under certain conditions (a specific magnetic field, temperature). Mn, Ni ferrite and core shell nanoparticle samples have been measured by Dr. Luis Lezama in a Bruker ELESYS spectrometer in the conditions explained in Appendix I.

The absence of interparticle interactions is essential to analyze the NP samples in a single particle regime. Hence, the samples have been measured in 0.05 mgFe/mL toluene dispersion to avoid dipolar interactions between NPs. The obtained EMR spectra for all the systems are represented in Figure 3.16.

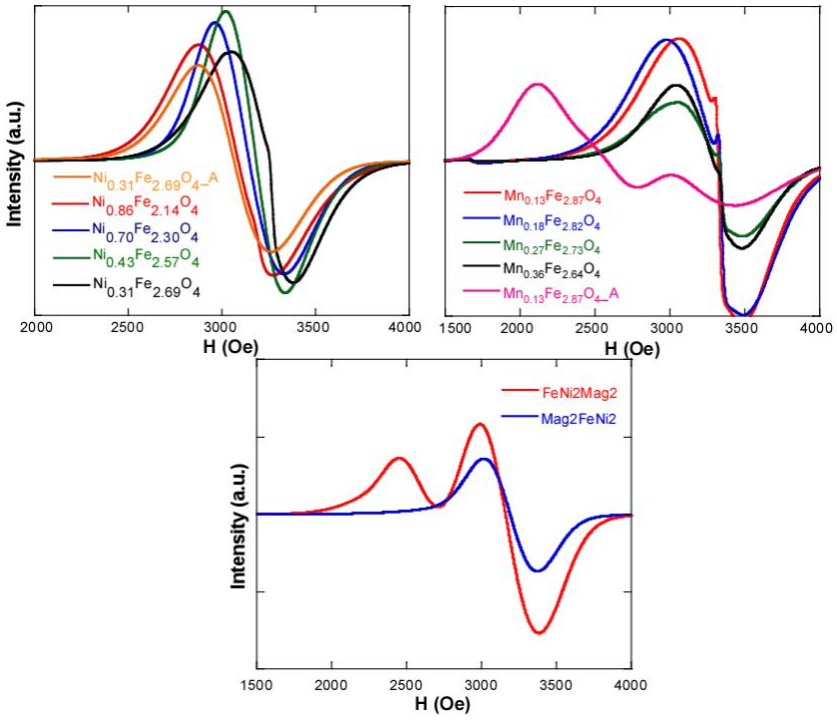

Figure 3.16. *Electronic Magnetization Resonance spectroscopy measurements for all prepared NPs in toluene dispersions at room temperature.*

As it can be seen in Figure 3.16, most spectra show single peaks (double in $Mn_{0.13}Fe_{2.87}O_4$_A and FeNi2Mag2 samples), which fit to a gaussian profile. The broadness of the obtained signals is related to differences in resonant magnetic fields (H_r) between the NPs present in the sample. This H_r value can be strongly influenced from differences in NP size, shape or in the crystalline structure (the Ni and Mn doping in our case). Thus, heterogeneity in size, shape or Mn or Ni doping levels would lead to a great broadening effect in the EMR signal. In some cases where two different NP groups are present in the same sample, two different signals can be detected, as in the FeNi2Mag2 sample. The peak to peak distances (ΔH_{pp}) have been measured fitting the signals to a gaussian profile (Table 3.7). The ΔH_{pp} values are slightly lower for Ni ferrite samples than for Mn ferrites, probably due to the higher heterogeneity of the Mn ferrite samples. As it can be observed in Figure 3.16, the FeNi2Mag and $Mn_{0.13}Fe_{2.87}O_4$_A samples show two different peaks. The presence of these two peaks could be due to different groups of particle sizes, shapes or chemistry ($Ni_xFe_{3-x}O_4$ and Fe_3O_4). For the rest of Ni ferrite and core shell samples, the homogeneity in the magnetic response of samples can be ensured. A small peak can be observed in most of Mn ferrite samples at a 3300 Oe applied magnetic field. This signal appears frequently in the EMR spectra of NP samples and is representative of a little population of small size (≈4 nm) particles.

The ferromagnetic contribution for each sample can be tested by measuring the deviation of the effective gyromagnetic factor (g_{eff}) from the ideal value for a free electron without orbital contributions, that is 2.0023.[15] Considering that the Ni^{2+} cation has an orbital contribution (d^8), a displacement of the g_{eff} value is expected to higher values. On the other hand, no displacements are expected by the presence of the Mn^{2+} cation (d^5), as its orbitals are balanced, annulling the orbital contribution in this

case.[25] Furthermore, considering that the previously discussed M (T) experiments have proved the effect of Mn and Ni doping in the NP anisotropy value, it also could have an effect in the NP rotation in the EMR analysis. In this way, any small interparticle interaction affects its orientation with magnetic fields by producing preferential orientations, and it might have an influence in the final result.[15,3,25]

The effective gyromagnetic factor has been calculated by means of this equation, that is a simplified version of previously exposed Raikher and Stepanov equation (3.4) (Table 3.7).

$$\Delta E = \hbar\nu = g\mu_B H_r \rightarrow g_{eff} = \frac{\hbar\nu}{\mu_B H_r} \quad (3.4)$$

Where h is planks constant, ν is the frequency of the magnetic field, μ_B is Bohr magneton ($9.27 \cdot 10^{-21}$ erg/G) and H_r is the resonant field, what comes from the zero intensity point in the EMR spectra. For the previously mentioned FeNi2Mag2 and $Mn_{0.13}Fe_{2.87}O_4$_A samples, the resonant magnetic fields and g_{eff} factor for both peaks have been calculated.

Regarding the g_{eff} factor values obtained for Ni ferrites, there is a clear association between the obtained gyromagnetic factor and the particle size. The $Ni_{0.31}Fe_{2.69}O_4$_A samples g_{eff} value (g=2.21) is much higher than the g_{eff} value obtained for its seed sample ($Ni_{0.31}Fe_{2.69}O_4$, g=2.06) (Table 3.7). This correlation has been previously detected in some magnetite samples, in such a way that the dependence can be fitted to a simple exponential function.[3] The great difference in the g_{eff} values of two samples with the same morphology, phase and magnetocrystalline anisotropy makes evidence of the effect of the NP size on the EMR signal.

Table 3.7. *Peak width (ΔH_{pp}) value extracted from EMR spectra, g_{eff} factors calculated from mean resonant magnetic field in each case and compared with means size and size dispersion obtained from TEM micrographs.*

SAMPLE	g_{eff}	D_{TEM} (nm)	ΔH_{pp} (Oe)
$Ni_{0,31}Fe_{2,69}O_4$	2.06	8.1 ± 0.9	450
$Ni_{0,43}Fe_{2,57}O_4$	2.11	11.0 ± 1.2	370
$Ni_{0,70}Fe_{2,30}O_4$	2.09	10.7 ± 1.6	397
$Ni_{0,86}Fe_{2,14}O_4$	2.18	11.4 ± 1.7	493
$Ni_{0,31}Fe_{2,69}O_4$_A	2.21	18.0 ± 1.7	429
$Mn_{0,13}Fe_{2,87}O_4$	2.02	10.1 ± 1.6	720
$Mn_{0,18}Fe_{2,82}O_4$	2.01	7.0 ± 1.2	1072
$Mn_{0,27}Fe_{2,73}O_4$	2.01	8.5 ± 1.2	883
$Mn_{0,36}Fe_{2,64}O_4$	2.04	7.4 ± 1.0	628
$Mn_{0,13}Fe_{2,87}O_4$_A	2.6/-	15.5 ± 1.5	756
FeNi2Mag2	2.48/2.12	15.2 ± 1.6	412/351
Mag2FeNi2	2.10	14.9 ± 2.1	398

However, taking the strong dependence of the g_{eff} value with the particle size into account, the g_{eff} variations cannot be directly ascribed to the nickel doping but also to small differences in particle sizes. In order to perform a proper analysis of the g_{eff} value displacement by influence of Ni doping, many monodisperse samples with exactly the same diameter and shape but different Ni doping levels would be necessary. However, in the case of the Ni^{2+} cation, there is a δN^{+} orbital contribution, which leads to higher g effective values due to the orbital interaction with the spin.

The presence of one unique peak without a great broadening effect in the $Ni_{0.31}Fe_{2.69}O_4$_A growth spectrum comparing with smaller samples demonstrates the efficiency of the aliquot separation process performed after the synthesis (explained in the 2nd chapter). Many previous works have revealed the sensibility of this technique to small populations of different

size particles,[3] what makes it an exhaustive quality control for this kind of monodisperse NP systems.

The conclusions obtained from the g_{eff} values of Mn ferrites go in the same direction as the obtained for the Ni ferrites. Firstly, the g effective value of the $Mn_{0.13}Fe_{2.87}O_4$_A sample is far higher than its seed sample. However, the extremely high g_{eff} value, as well as the presence of two peaks in the spectrum, indicates that this increase has also been induced by other factors. Once again, different factors which are having influence in the final result as particle size, shape and doping level make impossible to analyze properly the Mn doping influence in the main g_{eff} value.

Finally, as it was expected, the core shell nanoparticles have shown relative large g_{eff} values, taking their high particle size into account. The gyromagnetic ratio values are around 2.1 for both samples, nevertheless, two well differentiated peaks can be observed in the FeNi2Mag2 sample spectra (at g=2.48 and 2.12). There are many different reasons that could generate this phenomenon. The most common one for this kind of results, checked previously for similar samples in literature,[3] is the presence of two different particle size groups. Although the EMR spectroscopy has revealed as more sensitive technique to detect small particle groups, such big particle group should have been detected by some of these techniques. On the other hand, the higher g_{eff} ratio peak could represent a group of aggregated particles. The aggregation is another way to increase the interparticle interactions and, therefore, to rise the g_{eff} value. The EMR peak of this sample was expected to be in the same range of Mag2FeNi2 sample. In fact, the less displaced g_{eff} value (2.12) fits perfectly with the value of the Mag2FeNi2 sample (2.10), as its diameter is slightly higher. This supports this last theory to explain the presence of the most displaced group, as a partial

particle aggregation phenomena would explain the appearance of a higher g_{eff} value peak.

On balance, lower g_{eff} values have been obtained for Mn ferrite nanoparticles, due to its lack of orbital contribution, comparing with core shell and Ni ferrite samples. However, as has been explained, the performed analysis has not yield to acquire undeniable evidences of Mn and Ni cation influence in the NP g_{eff} factor. The main conclusion that can be obtained from this analysis is the confirmation of the homogeneous magnetic response of all Ni ferrite and core shell NPs, excepting the FeNi2Mag2 sample. The Mn ferrites can also be considered as homogeneous samples, however, a signal corresponding to small size particles has been detected in most of Mn ferrite NP samples.

3.1.3 Magnetic hyperthermia response of MNPs

The magnetic hyperthermia response of NPs is the key factor to determine their potential applicability in future magnetic hyperthermia anticancer therapies. By these measurements, the thermal energy produced by each sample under an alternating magnetic field is measured at different conditions (different frequencies and magnetic fields).

Basically, magnetic nanoparticles interact with the applied resonant magnetic field and release the absorbed energy as thermal energy. The magnetic hyperthermia response of a material is described as the Specific Absorption Rate (SAR), which defines the amount of produced thermal energy. Two different approaches can be used to measure the experimental SAR value of colloidal dispersion samples. On the one hand, the specific absorption rate can be determined by direct measurement of the time dependent temperature change under an AC magnetic field (3.5 equation):

$$SAR = \frac{C}{m}\frac{\Delta T}{\Delta t} \quad (3.5)$$

Where ΔT/Δt is the time dependent temperature evolution, m is the sample mass (represented as g_{Fe3O4}, g_{sample} or g_{Fe}) and C is the specific heat capacity of the fluid (1.72 $J \cdot g^{-1} \cdot K^{-1}$ for toluene) and material (0.16 $J \cdot g^{-1} \cdot K^{-1}$ for magnetite). However, the accuracy of this method to analyze the intrinsic material behaviour is poor, since many factors as NP internal temperature gradients and thermal the energy absorption of the smallest nanoparticles generate distortions, making impossible to obtain a clear measurement of the NP heat generation.

The other approach, and the one used in this thesis, is based on the time dependent NP dynamic magnetization measurement obtained from the integral of the time dependent magnetization value with the applied magnetic field amplitude (equation 3.6):

$$SAR = -\frac{f}{c}\mu_0 \oint M(t) \cdot dH = \frac{f}{c}\mu_0 \pi H_0^2 \cdot \chi'' \quad (3.6)$$

By this method, the NP SAR value is directly measured from the AC field dependent magnetization response, that is characteristic from the material. The amount of heat depends on many different factors as NP size, homogeneity, anisotropy and applied conditions. Under an alternating magnetic field all the magnetic materials tend to absorb this magnetic energy, however, the amount of absorbed energy and how this energy is released depends on the material. On the one hand, the monodomain or multidomain character of the material is essential to analyze the magnetic hyperthermia response. A great part of the thermal energy generated by magnetic hyperthermia of multidomain materials is absorbed by Bloch walls movement, which needs much more energy (or time) to orient with the applied magnetic field than the single magnetic moments.[6]

On the other hand, depending on the physical state of the ferrimagnetic material, in solid state or in a colloidal dispersion, the magnetic hyperthermia generation mechanisms will be different. Solid materials only show one kind of hyperthermia mechanism, Nèels mechanism, whereas colloidal dispersions will release thermal energy by means of two mechanisms, Nèel and Brown. Nèels mechanism refers to the orientation of the magnetic moments with the applied magnetic field, which induces a rotation of these magnetic moments inside the NP. As it has been previously explained, the rotation of intrinsic NP magnetic moment is influenced by its size, shape and anisotropy constant. These three factors define the magnetic energy that is necessary to induce the rotation of the magnetic moments or, in other words, the time necessary to orient these magnetic moments to a magnetic field, that is the Nèels relaxation time (τ_N). This relaxation time can be defined as an intrinsic material property and can be calculated by the following equation (3.7):

$$\tau_N = \frac{\tau_0}{2}\sqrt{\frac{\pi k_B T}{KV}}e^{KV/k_B T} \qquad (3.7)$$

Where K is the material anisotropy constant, V the particle volume, T the temperature, k_B the Boltzmann constant and τ_0 the attempt time. The attempt time is related to the probability of the magnetic moment spontaneous inversion in the easy magnetization axis, and is about 10^{-10} s for this kind of materials, as an estimation. The KV factor represents the rotation energy barrier of the NP, while the first part of the equation is related to the probability of this spontaneous rotation at this temperature. Thus, this relaxation time is strongly influenced by the anisotropy constant and particle volume.

The other magnetic hyperthermia mechanism, the Brownian mechanism, has only effect in colloidal dispersions. This mechanism refers to the physical

rotation of the NPs by applying the AC magnetic field and to the energy generated by the friction of the NPs with the surrounding fluid. This relaxation time is defined by the Debye's equation, and depends on the hydrodynamic diameter of the NP (r_h), the fluid viscosity (η) and the temperature (equation 3.8):

$$\tau_B = \frac{4\pi\eta r_h^3}{k_B T} \quad (3.8)$$

As the Brownian relaxation mechanism is related to the friction between the NP surface and the fluid, the relaxation time will depend on the NP surface area and the solvent viscosity. Both relaxation mechanisms are schematically illustrated in Figure 3.17.

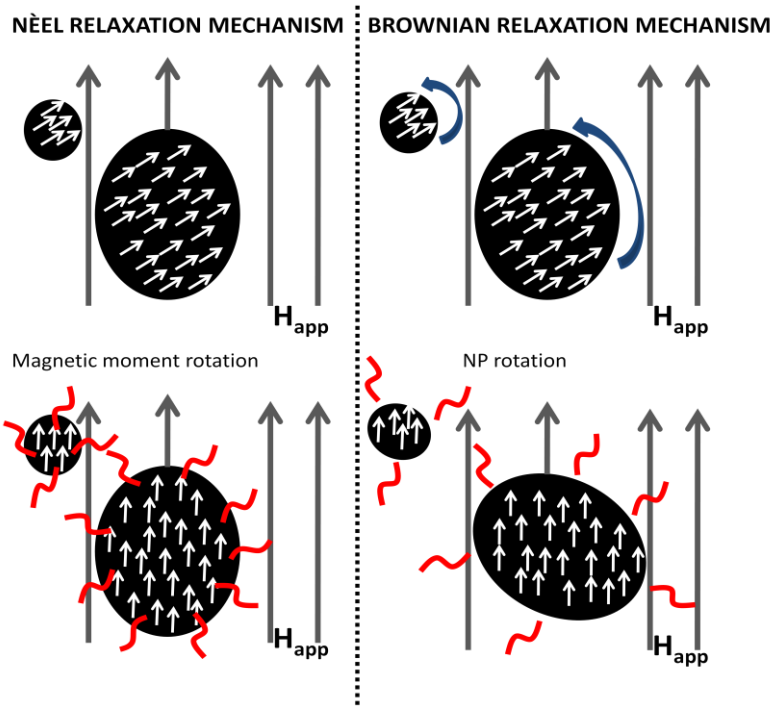

Figure 3.17. *Schematic illustration of the two mechanisms for magnetic hyperthermia generation, in ferrofluids.*

The efficiency of the hyperthermia response under an applied magnetic field can be predicted by comparing different relaxation times with the constant frequency of the applied magnetic field (Figure 3.18A).

To analyze the total hyperthermia response of a material, both relaxation times must be considered to obtain the effective relaxation time (τ_{eff}) (equation 3.9):

$$\frac{1}{\tau_{eff}} = \frac{1}{\tau_N} + \frac{1}{\tau_B} \quad (3.9)$$

Both mechanisms have different contributions to the effective relaxation time, and are differently influenced by the NP properties. For small NPs, with diameters around 4-6 nm, the main relaxation mechanism is the Brown one since the heat generated by the short amount of magnetic moments inside NPs is negligible. However, the thermal energy generated by Brown mechanism in this kind of small NP samples is also negligible. Thus, these small sized systems are not able to produce a measurable response. However, Nèels mechanism gains relevance with the particle size, as the higher number of magnetic moments increases exponentially the generated thermal energy (Figure 3.17). The nanoparticles considered for magnetic hyperthermia treatments have diameters around 16-20 nm. In this size range, the contribution of Brown mechanism can be considered negligible (depending on the mediums viscosity), and only Nèel's mechanism is taken into account.

The relaxation times of the NPs are directly related to their magnetic hyperthermia response. In order to induce a measurable response, relaxation times need to be comparable to the period time of the applied magnetic field, as it can be seen in Figure 3.18A. The time window of the hyperthermia experiments, defined by the time period of the applied AC

magnetic field, defines the character of the NP as ferrimagnetic or superparamagnetic. Particles will behave as superparamagnetic at effective relaxation times shorter than the magnetic field time period, whereas at higher relaxation times the NP net magnetic moment does not have enough time to orient with the magnetic field. Consequently, the NP behaves as a blocked ferrimagnetic particle. In this way, the maximum hyperthermia efficiency occurs when the NP effective relaxation time has the same value as the magnetic field time period (Figure 3.18A). At this point, the NP magnetic moment is in resonance condition with the applied magnetic field. For instance, for a 15 nm magnetite NP ($K \approx 14$ kJ/m^3) with an effective relaxation time of $1.4 \cdot 10^{-8}$ s the maximum magnetic hyperthermia efficiency will be achieved by applying a 71.5 MHz magnetic field.

The thermal energy generated by the superparamagnetic NPs is related to the delay of the magnetization response regarding to the magnetic field phase. Hence, the magnetization response of the NP is considered as linearly proportional to the applied magnetic field. However, under an AC dynamic magnetic field, this magnetization value is time dependent and the magnetic susceptibility is a complex number where the χ'' imaginary part represents the non phased part related to the magnetic energy absorption (equation 3.10):

$$M(t) = \chi H \chi = \chi^{'} - j\chi'' \quad (3.10)$$

The value of χ'' can be solved by means of the Shliomis equation (3.11):

$$\chi^{''} = \chi_0 \frac{\omega \tau_{eff}}{1+(\omega \tau_{eff})^2} \quad (3.11)$$

The experimental Specific Absorption Rate (SAR) expression depends also on the size distribution, adding the contribution of all sized nanoparticles (equation 3.12):

$$SAR = \int_0^{D_{max}} P(D, f, K) f(D) dD \quad (3.12)$$

Where f (D) represents the diameter distribution and P (D,f,K) the absorbed potency at an specific frequency. From the effective relaxation time, the power generated by the NP dispersion can be estimated for a NP by means of the following equation (3.13):

$$P\left(\frac{W}{g}\right) = P(W/m^3) = \frac{\pi \mu_0^2 f M_s^2 H^2 V}{3 k_B T}\left(\frac{f\tau_{eff}}{1+(f\tau_{eff})^2}\right) \quad (3.13)$$

Where μ_0 is the vacuum magnetic permeability, f the frequency of the applied magnetic field (H_{app}), M_s the saturation magnetization, H the magnetic field amplitude, V the particle volume, k_B the Boltzmann's constant and τ_{eff} the effective relaxation time.[11]

Concerning biomedical applications, there are some limitations for the magnetic fields to be applied to human tissues. However, there is not a unified criterion about the specific limit of the frequency and amplitude of the magnetic field to be applied used without inducing serious damages in the human body. The large number of factors which influence the final absorbed radiation is the source of this uncertainty. The so-called eddy currents that form in the tissues by influence of the absorbed electric field produce a thermal energy that could damage the tissues if the currents are intense enough. Obviously, the frequency and the amplitude of the applied magnetic field directly influence the Eddy currents formation. Moreover, the geometry and the area where the radiation is being applied have also to be considered, besides the geometry of the magnetic field generator. In this way, an estimation can be perform, considering the geometrical factors, to ascertain the f·H limit of the applied magnetic field (equation 3.14):[26]

$$H_{app} \cdot f < \frac{1}{R}\sqrt{\frac{2W_E^{max}}{\mu_0^2 \pi^2 \sigma}} \quad (3.14)$$

Where R represent the radius of the treated part (whole body, limb, specific part...), W_E is the maximum power density dissipated by the Eddy currents, μ_0 is the vacuum magnetic permeability and σ represents the tissue conductivity. As a general estimation, it was accorded that the H·f relation should not lead the $4.85x10^8$ $A \cdot m^{-1} \cdot s^{-1}$ value.[27]

Firstly, according to the previously explained equations, Neèl, Brown and effective relaxation times were calculated for all NP samples in order to understand which is the predominant mechanism in each case, and to ascertain the highest hyperthermia response (Table 3.8). The NP shapes have been considered spherical in order to perform the relaxation time estimation.

Table 3.8. *Nèel (τ_N), Brown (τ_B) and effective (τ_{eff}) relaxation times at room temperature calculated for all prepared samples according to previously described equations. NP shape has been taken as spherical for all samples to obtain this estimation.*

SAMPLE	τ_n (s)	τ_B (s)	τ_{eff} (s)
$Ni_{0,31}Fe_{2,69}O_4$	$3.06 \cdot 10^{-9}$	$1.13 \cdot 10^{-7}$	$2.98 \cdot 10^{-9}$
$Ni_{0,43}Fe_{2,57}O_4$	$1.05 \cdot 10^{-8}$	$2.83 \cdot 10^{-7}$	$1.01 \cdot 10^{-8}$
$Ni_{0,70}Fe_{2,30}O_4$	$7.11 \cdot 10^{-9}$	$2.60 \cdot 10^{-7}$	$6.92 \cdot 10^{-9}$
$Ni_{0,86}Fe_{2,14}O_4$	$7.75 \cdot 10^{-9}$	$3.14 \cdot 10^{-7}$	$7.57 \cdot 10^{-9}$
$Ni_{0,31}Fe_{2,69}O_4$_A	$6.88 \cdot 10^{-4}$	$1.24 \cdot 10^{-6}$	$1.24 \cdot 10^{-6}$
$Mn_{0,13}Fe_{2,87}O_4$	$7.51 \cdot 10^{-9}$	$2.19 \cdot 10^{-7}$	$7.26 \cdot 10^{-9}$
$Mn_{0,18}Fe_{2,82}O_4$	$2.27 \cdot 10^{-9}$	$7.28 \cdot 10^{-8}$	$2.20 \cdot 10^{-9}$
$Mn_{0,27}Fe_{2,73}O_4$	$3.40 \cdot 10^{-9}$	$1.30 \cdot 10^{-7}$	$3.32 \cdot 10^{-9}$
$Mn_{0,36}Fe_{2,64}O_4$	$2.24 \cdot 10^{-9}$	$8.60 \cdot 10^{-8}$	$2.19 \cdot 10^{-9}$
$Mn_{0,13}Fe_{2,87}O_4$_A	$5.58 \cdot 10^{-6}$	$7.90 \cdot 10^{-7}$	$6.92 \cdot 10^{-7}$
FeNi2Mag2	$1.55 \cdot 10^{-8}$	$7.45 \cdot 10^{-7}$	$1.52 \cdot 10^{-8}$
Mag2FeNi2	$5.90 \cdot 10^{-8}$	$7.02 \cdot 10^{-7}$	$5.44 \cdot 10^{-8}$

As it can be observed in Table 3.8, the NP size has a great influence in the τ_N values, as was expected according to the exponential dependence with the volume and the anisotropy constant. The relaxation process is dominated by Nèel mechanism in most of cases. However, growth samples, according to their higher volume, show much higher τ_N values, especially for $Ni_{0,31}Fe_{2,69}O_4$_A growth sample. This Ni ferrite sample has an estimated Nèel relaxation time above $6 \cdot 10^{-4}$ s, much higher than experiments time window, which goes from $6.7 \cdot 10^{-6}$ to $9.7 \cdot 10^{-7}$ s in the typical applied frequencies.

The effective relaxation times obtained by combining contributions of both mechanisms show that the growth NPs ($Ni_{0,31}Fe_{2,69}O_4$_A, $Mn_{0,13}Fe_{2,87}O_4$_A, FeNi2Mag2 and Mag2FeNi2) are the most promising samples for the hyperthermia treatments due to their higher NP main diameter that lead to τ_{eff} values similar to the resonance condition.

By applying the 3.13 equation, the SAR values for different relaxation times at a specific magnetic field amplitude and frequency ((H: 10 kA/m, f 532 kHz) can be estimated. Thus, the resonant condition of a sample at a specific applied alternating magnetic field can be determined, as it can be observed in Figure 3.18A. In this graph the SAR has been represented for the $Ni_{0,31}Fe_{2,69}O_4$_A sample in a large relaxation time value range. The calculated SAR at values close to the usual magnetic hyperthermia experiments time window (from 10^{-7} to 10^{-5} s) the line fits to a Gaussian profile, which reaches the maximum value at $\tau_{eff}=1.9 \cdot 10^{-6}$ s, that is the resonant condition. Although this graph only represents the SAR response of the $Ni_{0,31}Fe_{2,69}O_4$_A sample, all NP samples follow the same behaviour.

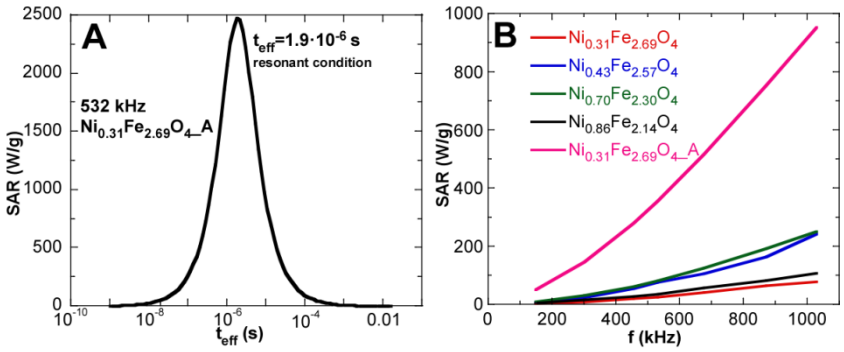

Figure 3.18. *SAR value evolution with effective relaxation time for $Ni_{0.31}Fe_{2.69}O_4$_A sample at 532 kHz and 10 kA/m magnetic field simulated applying the 3.13 equation (A) and magnetic field frequency dependent SAR values for Ni series ferrite samples at 20 kHz magnetic field amplitude (B).*

The thermal energy generated by different samples (Ni ferrites, Mn ferrites and core shell nanoparticles) has been measured at different frequencies and magnetic field amplitudes. These measurements have been carried out by Dr. Eneko Garaio in a homemade instrument developed in the Departamento de Electricidad y Electrónica of UPV/EHU.[28]

The SAR values of Ni ferrite samples have been measured in the 150-1000 kHz range, under a magnetic field amplitude of 20 kA/m. As it can be observed in the spectra shown in Figure 3.18B, the SAR values of Ni ferrite samples exponentially rise with increasing frequency, in good agreement with the previously studied relation between the τ_{eff} values and the experiment time window. The slope is higher for the $Ni_{0.31}Fe_{2.69}O_4$_A sample as its effective relaxation time (1.24·10^{-6} s) is closer to the resonant condition. Hence, this sample would yield the greatest magnetic hyperthermia response. For the rest of the samples, the obtained results fit

perfectly to the estimated effective relaxation time values. However, the hyperthermia response also depends on the saturation magnetization, NP shape and size dispersions. These factors have induced the small differences in the SAR values between the non growth Ni ferrite samples.

The produced thermal energy also depends on the amplitude of the H_{app}, in a different way as the frequency dependence, since the SAR value is linearly proportional to the magnetic field amplitude (SAR (W/g) α H^2), at low applied magnetic field amplitudes. This relation has been checked by measuring the SAR value of the prepared samples under a constant AC magnetic field frequency of 532 kHz at magnetic field amplitudes from 1 to 28 kA/m. As it can be observed in Figure 3.19A, B and C, all SAR values increase with the field amplitude. The SAR values are in the same range in all samples, excepting in $Mn_{0,13}Fe_{2,87}O_4$_A and $Ni_{0,31}Fe_{2,69}O_4$_A growth samples, which show much higher magnetic hyperthermia response.

According to the particle main diameter influence in the hyperthermia response, it was expected to obtain higher responses from FeNi2Mag2 and Mag2FeNi2 core shell samples. The low SAR values obtained could be related to the lower sample homogeneity checked in the EMR characterization. Previous works have demonstrated the negative influence of high size dispersions in this hyperthermia response.[3] The thermal energy production efficiency is much lower in small NPs, as the heat generated could be negligible. Moreover, from this magnetic field dependent SAR evolution, an estimation of the anisotropy constant can be carried out to check their agreement with the values determined from the M (T) analysis. These data have been obtained by fitting the H dependent SAR values in the linear response at low H values, generally below 10 kA/m as can be observed in Figure 3.20A and B.

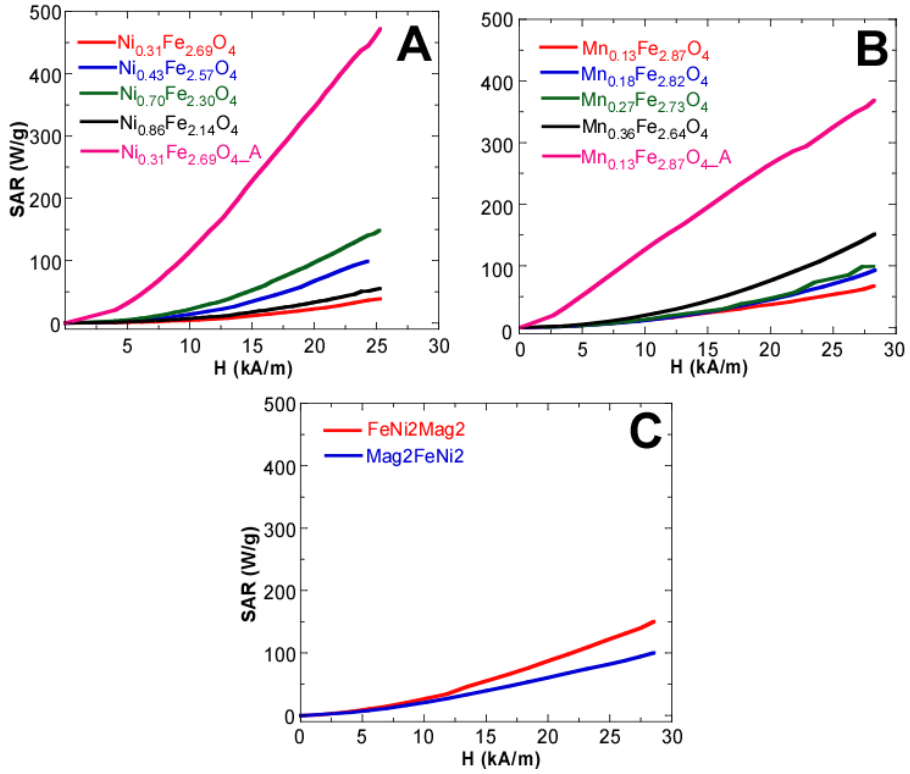

Figure 3.19. *Magnetic field amplitude dependent SAR measurements at 1 mg/mL concentration in toluene for NP samples at 532 kHz frequency magnetic field (A Ni ferrite series, B Mn ferrite series and C core shell series).*

These anisotropy constant values (Table 3.9) have been obtained by means of an estimation of the H vs SAR slope that theoretically the system should follow for a known field frequency, average diameter, size dispersion, saturation magnetization, dynamic diameter, material density and medium viscosity. This fitting has been performed with the collaboration of Dr. Iñaki Orue (sgiker, UPV/EHU). As it can be observed in Figure 3.20A and B, this estimation fits well with the experimental data.

Table 3.9. *Anisotropy constants for all samples estimated from the H vs SAR slope fitting and compared with the values determined from the FC-ZFC analysis.*

SAMPLE	D_{TEM} (nm)	K (kJ/m^3) (FC-ZFC)	K (kJ/m^3) (SAR)
$Ni_{0,31}Fe_{2,69}O_4$	8.1 ± 0.9	21.1	24.8
$Ni_{0,43}Fe_{2,57}O_4$	11.0 ± 1.2	18.0	14.7
$Ni_{0,70}Fe_{2,30}O_4$	10.7 ± 1.6	16.5	17.9
$Ni_{0,86}Fe_{2,14}O_4$	11.4 ± 1.7	14.2	11.5
$Ni_{0,31}Fe_{2,69}O_4$_A	18.0 ± 1.7	20.2	5.6
$Mn_{0,13}Fe_{2,87}O_4$	10.1 ± 1.6	20.1	18.0
$Mn_{0,18}Fe_{2,82}O_4$	7.0 ± 1.2	20.2	24.3
$Mn_{0,27}Fe_{2,73}O_4$	8.5 ± 1.2	20.3	18.8
$Mn_{0,36}Fe_{2,64}O_4$	7.4 ± 1.0	16.5	18.4
$Mn_{0,13}Fe_{2,87}O_4$_A	15.5 ± 1.5	21.0	9.3
FeNi2Mag2	15.2 ± 1.6	7.9	6.9
Mag2FeNi2	14.9 ± 2.1	12.0	6.9

Although the anisotropy constants estimated from the SAR measurements do not suit perfectly with the ones obtained from the FC-ZFC measurements, all non growth NP samples are in the same value range. Thus, the well concordance of the obtained results with the non interacting superparamagnetic model can be assured for non growth samples. In contrast, all growth samples show much lower anisotropy values than it was expected. This effect could be induced by dipolar and ferromagnetic interactions between particles with bigger sizes, according to their relatively high effective relaxation times.

The SAR value evolution could be displaced from the linear response at high magnetic field amplitudes in this kind of measurements. In order to verify this fact, $Ni_{0.31}Fe_{2.69}O_4$_A sample magnetization cycles under a constant field frequency (532 kHz) at different field amplitudes have been represented in Figure 3.20C.

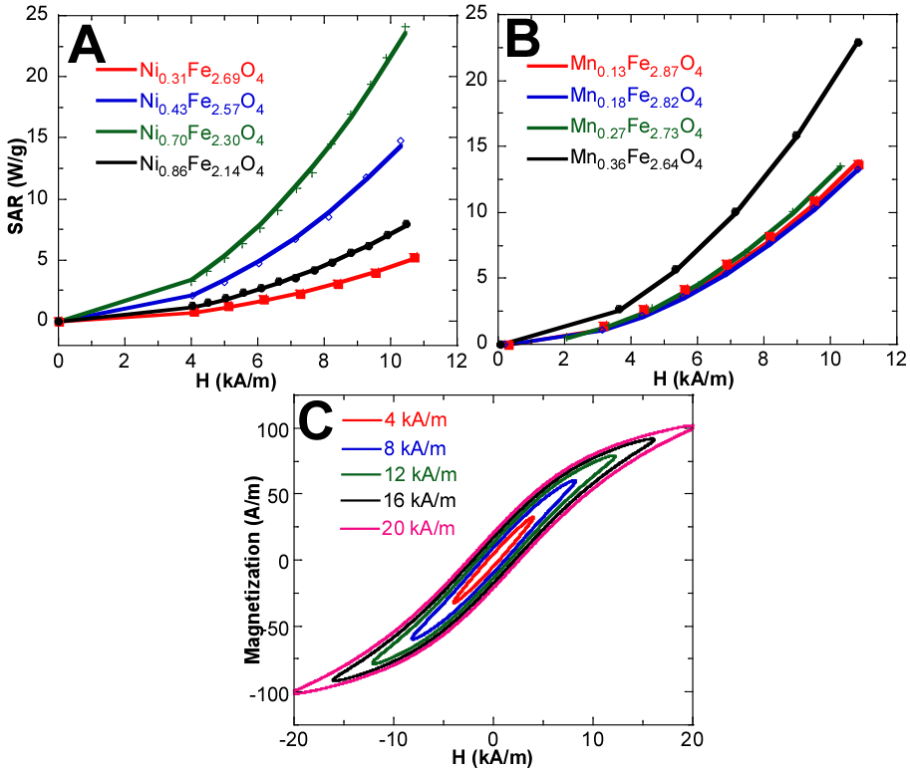

Figure 3.20. *SAR vs H curves fitting for Ni ferrite (A) and Mn ferrite (B) non growth samples, below 10 kA/m H_{app}. Measured experimental data values are represented as points and theoretical fittings as lines. Magnetic field dependent magnetization measurements at different magnetic field amplitudes for the $Ni_{0.31}Fe_{2.69}O_4$_A sample (C).*

On the one hand, a strong magnetization hysteresis increase at higher H_{app} can be observed. This increase is directly related to the specific absorption rate, as the area inside each cycle represents the absorbed magnetic energy. On the other hand, the linear relation between the SAR and the H_{app} can be observed in these cycles by the ellipse shape magnetization curves. This elliptical cycle shape can only be observed in the cycle measured at the lowest field amplitude, 4 kA/m. This cycle shows by far the lowest magnetic hyperthermia response as the area inside the cycle is much smaller than the others. However, the ellipsoidal shape of M (H) slope

fits to the linear response theory, previously explained. At higher field amplitude measurements the area inside cycles rises powerfully, what implies a greater absorbed magnetic energy. But these intense magnetic fields induce also a displacement from the linear response as a consequence of the saturation of magnetic moments.

Although the $Ni_{0.31}Fe_{2.69}O_4$_A ferrite sample seems to have the highest SAR value, it is necessary corroborate the SAR values under an H_{app} suitable to be applied in humans. Consequently, the SAR values under a 149 kHz and 4 kA/m AC magnetic field have been measured and represented in Table 3.10.[26,27]

These values represent the effect that would be obtained in a hyperthermia therapeutic treatment, avoiding the distortion that an in vivo environment would induce (viscosity, immunological response, aggregation,...). The low hyperthermia response of the non growth ferrite NP samples is related to their small size, being completely useless in a therapeutic hyperthermia treatment. The only two samples which show a hyperthermia response suitable to be applied as magnetic hyperthermia inductor agents are the $Ni_{0.31}Fe_{2.69}O_4$_A and $Mn_{0,13}Fe_{2,87}O_4$_A samples. The values shown in Table 3.10 seem to be quite low comparing with other values provided in literature for this kind of NPs.[29,13] However, the SAR data appearing in literature are mainly measured under high frequencies and amplitudes that do not represent realistically the response that the samples would present in an *in vivo* experiment. In this way, the sample that has been revealed as the best candidate for the following experiments is the $Ni_{0.31}Fe_{2.69}O_4$_A sample.

Table 3.10. *SAR values of samples under a human compatible AC magnetic field (149 kHz and 4 kA/m) at a 1 mg/mL concentration in toluene.*

SAMPLE	SAR (W/g) 149 kHz, 4 kA/m
$Ni_{0,31}Fe_{2,69}O_4$	1.80
$Ni_{0,43}Fe_{2,57}O_4$	2.77
$Ni_{0,64}Fe_{2,36}O_4$	3.63
$Ni_{0,86}Fe_{2,14}O_4$	2.15
$Ni_{0,31}Fe_{2,69}O_4$_A	22.53
$Mn_{0,13}Fe_{2,87}O_4$	2.40
$Mn_{0,18}Fe_{2,82}O_4$	2.28
$Mn_{0,27}Fe_{2,73}O_4$	2.67
$Mn_{0,36}Fe_{2,64}O_4$	3.36
$Mn_{0,13}Fe_{2,87}O_4$_A	18.46
FeNi2Mag2	4.21
Mag2FeNi2	3.36

3.1.4 Chemical and structural characterization of $Ni_{0.31}Fe_{2.69}O_4$_A_PMAO sample

As it has been previously explained, $Ni_{0.31}Fe_{2.69}O_4$_A is the sample which has been chosen to be tested in *in vitro* and *in vivo* tests. Consequently, it has been transferred to water media with PMAO polymer to obtain the **$Ni_{0.31}Fe_{2.69}O_4$_A_PMAO** sample. This treatment has not influence in the magnetic properties, and could have only a small effect in its hyperthermia response, due to the increase of the hydrodynamic diameter. Thus, in order to verify the correct association of the PMAO polymer, TEM, TGA and DLS characterizations were carried out after the water transfer treatment. These characterizations are summarized in Figure 3.21.

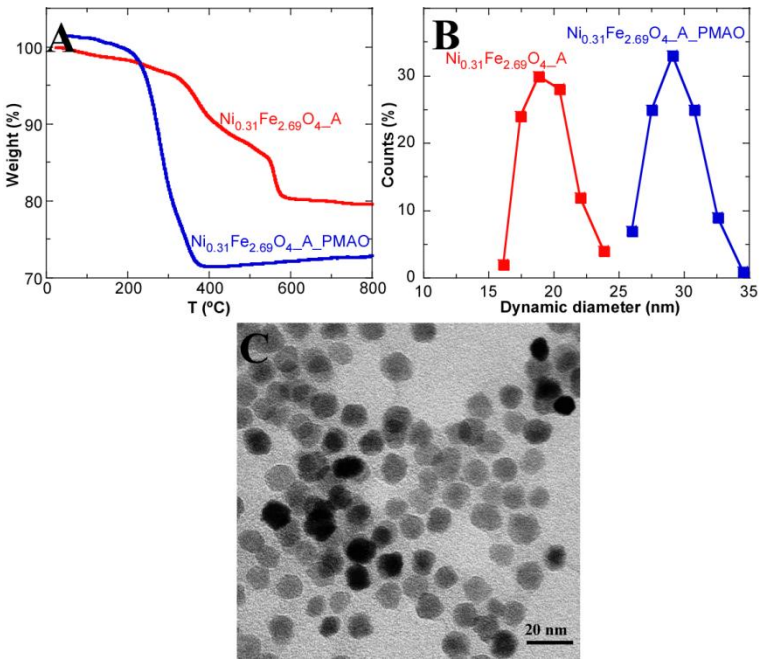

Figure 3.21. *Thermogravimetric analysis (A) and dynamic light scattering (B) of $Ni_{0.31}Fe_{2.69}O_4$_A and $Ni_{0.31}Fe_{2.69}O_4$_A_PMAO samples and TEM micrograph of $Ni_{0.31}Fe_{2.69}O_4$_A_PMAO sample (C).*

As it can be observed in Figure 3.21A, an important increase of the organic matter amount has occur after polymer coating, from 18 % in the $Ni_{0.31}Fe_{2.69}O_4$_A oleate coated sample to 28 % in the PMAO coated sample. This value is in good agreement with literature data for similar samples, suggesting a successful polymer coating.[1,30]

The comparison of the dynamic diameter before and after the polymer coating process (Figure 3.21B) shows an important increase of the average dynamic diameter, from 18 to 30 nm, without changing the standard deviation (≈ ±3) nm. This increase would be related to the increment of the dynamic diameter by coupling large chain polymers on the surface. Furthermore, the constancy of the standard deviation value also indicates

that mostly single particles have been coated, instead of forming nanoclusters composed by more than one NP. Finally, any changes in NP inorganic nucleus size or shape have been discarded when visualizing the $Ni_{0.31}Fe_{2.69}O_4$_A_PMAO water transferred sample by TEM (Figure 3.21C).

3.2 Biopolymeric magnetic nanospheres

The previously characterized $Ni_{0.31}Fe_{2.69}O_4$_A NP sample has been chosen as the magnetic core material for the developing of NP-biopolymer magnetic nanospheres. As it has been previously explained, the aim has been to obtain biopolymeric based magnetic materials to be applied as drug delivery and release agents more than to be applied as direct magnetic hyperthermia inductors. In this way, the designed release system would be based on the biopolymeric nanosphere decomposition by means of heat generation by magnetic hyperthermia. Consequently, the NPs with the highest magnetic hyperthermia response have been selected for this purpose.

Two polymers have been chosen to conform the nanospheres. Firstly, chitosan was used to develop the magnetic nanosphere formation by encapsulating the $Ni_{0.31}Fe_{2.69}O_4$_A NPs with chitosan shells, as has been explained (CS-MNS). A complete chemical, structural and magnetic characterization has been performed for these nanospheres. Furthermore, some stability experiments by modifying different conditions as temperature, pH and enzyme presence have been carried out. After that, different fibroin nanospheres were synthesized by following the same mechanism developed for the CS nanosphere formation. In this case, only a superficial characterization was carried out for these fibroin nanospheres to test their potential usefulness for future projects.

3.2.1. Chemical and structural characterization of CS-MNS

3.2.1.1 Transmission Electron Microscopy (TEM) and Environmental Scanning Electron Microscopy (ESEM) of CS-MNS

Size and shape analysis of CS-MNS nanospheres were carried out by means of ESEM and TEM microscopy. The ESEM microscopy has been used for this sample characterization as its high size makes possible to check the nanosphere diameters. However, the resolution of the ESEM microscope is not high enough to visualize properly the NP assembly inside the nanospheres, therefore, TEM microscopy has been also used to determine the presence and organization of the NPs inside the CS shells.

For ESEM and TEM measurements, one drop of CS-MNS 0.05 mgFe/mL water dispersion was dried on a carbon covered copper grid. The measurement conditions are described in the appendix I. The obtained micrographs by ESEM and TEM microscopy are shown in Figure 3.22, as well as the histograms.

As it can be observed in Figure 3.22A, well defined spherical nanospheres have been obtained. The size distribution of the CS nanospheres varies from 30 to 200 nm with an average size of 92 nm (Figure 3.22D). This size distribution is broader than the obtained for magnetic NPs, as it has also been reported in literature for other nanocluster formation.[31,32,33] Only the inorganic core of the nanosphere can be observed by the transmission detector, hence, the secondary electron scanning has been employed to analyze the chitosan shell. As it can be observed in Figure 3.22B, the chitosan shells also present a perfect spherical morphology. The lack of porosity and its compactness proves the strong interactions between the chitosan chains. Furthermore, there are not magnetic NPs in the nanosphere surface, verifying that all the NPs are encapsulated in the internal inorganic core.

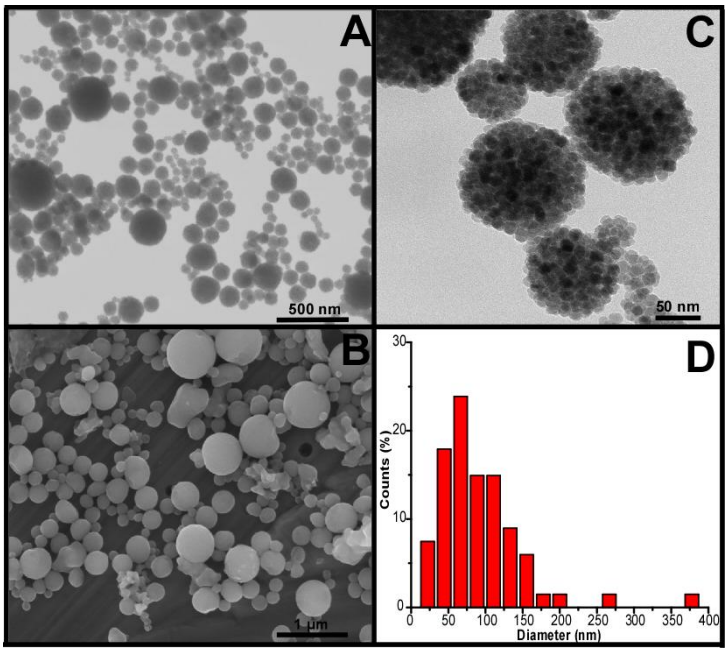

Figure 3.22. *ESEM micrographs obtained by means of transmission (A) and secondary electron dispersion (B) detectors, TEM micrograph (C) and histogram of the CS-MNS sample.*

The NP assembly inside the nanospheres is also an interesting point, as the nanosphere magnetic behaviour depends on the magnetic couplings and dipolar interactions between the nanoparticles inside the nanosphere. As it can be observed in the TEM micrograph (Figure 3.22C), the NPs are really close to each other forming a close packaging inside the nanospheres, only separated by the oleate chains. In this way, it seems that the chitosan chains do not induce an important separation between the NPs due to sterical repulsions, being impossible to measure the amount of NPs inside each nanosphere. The average NP amount inside nanospheres will be estimated from other sources, as it cannot be determined from the micrographs. Although specific assemblies cannot be appreciated in most of the nanospheres, the tendency of the NPs to form linear self-assemblies can be observed in some cases (Figure 3.23).

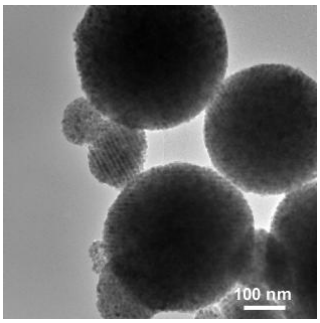

Figure 3.23. *TEM micrograph of a CS-MNS sample where NP self-assembly can be observed.*

This phenomena could be related to the small distances and the magnetocrystalline anisotropy energy of the NPs, which induces a higher ferromagnetic behaviour due to the increasing magnetic interactions between the NPs.[34] The control of this self-assembly would open many new possibilities for these materials, as the final magnetic properties could be tuned.

3.2.1.2 CS-MNS hydrodynamic diameter and Zeta potential analysis by Dynamic Light Scattering (DLS)

The DLS and Zeta potential measurements have been performed in a BI 90 Plus Particle Size Analyser (Brookhaven Instruments Corporation). The hydrodynamic diameter has been obtained using particle sizing software by means of the photocorrelation spectroscopy (PCS) technique (Appendix I). The concentration of the CS-MNS water solution (0.01 mgFe/mL) was the same as the previously used for NP measurements.

The hydrodynamic size distribution shown in Figure 3.24 assesses once again that, although some nanosphere aggregation can be observed in Figure 3.22, single nanospheres are forming the water colloidal dispersion. The size distribution range varies from 100 to 150 nm and fits to a log normal profile,

with an average hydrodynamic diameter of 130 nm. As it was expected, the main hydrodynamic diameter is considerably higher (41 % higher) than the main diameter measured from the micrographs due to the presence of the chitosan shell.

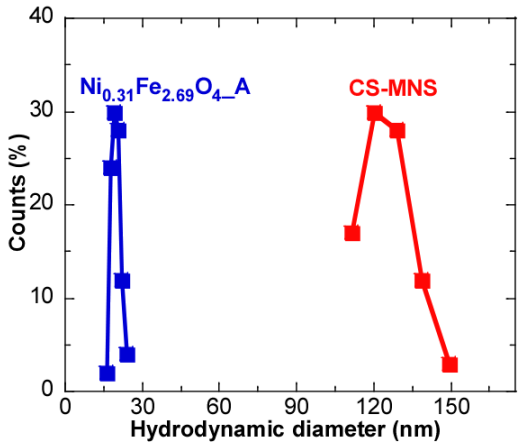

Figure 3.24. *Hydrodynamic size distributions of the $Ni_{0.31}Fe_{2.69}O_4$_A inorganic core sample and the CS-MNS magnetic nanospheres.*

Comparing the DLS data obtained for $Ni_{0.31}Fe_{2.69}O_4$_A inorganic core NPs and CS-MNS nanospheres a high diameter and size dispersion increase can be verified in Figure 3.24. Apparently, the impact of the coating agent on the hydrodynamic diameter is different in both cases. Furthermore, the CS chains are not covalently bonded to the nanoparticles, what it means that many polymer chains can interact with the inorganic core, making even more thick the polymer shell.

As it has been explained, for materials that are going to be applied in colloidal dispersion, a wide knowledge about the surface charge is essential to have a proper control of its behaviour in different media. Hence, a pH dependant Zeta potential (ζ) analysis has also been performed. The Zeta

potential measurements have been carried out in the BI 90 Plus Particle Size Analyser using the Zeta PALS software. In the conditions described in appendix I, the CS-MNS nanospheres were measured in 0.01 mgFe/mL 10 mM KCl colloidal suspension at different pHs (from 2 to 12, 6 points). The Zeta potential values at different pHs have been represented in Figure 3.25.

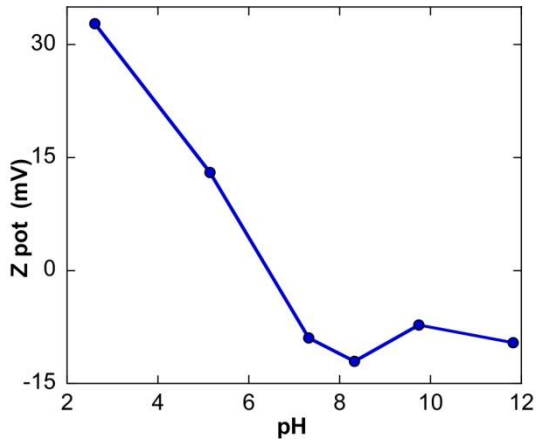

Figure 3.25. *Zeta potential measurements of CS-MNS at 0.01 mgFe/mL concentration in 10 mM KCl solutions at different pHs.*

As it can be observed in Figure 3.25, the value of zero charge has been established at pH 6.25. This isoelectric point is referred to the pH value where the magnetic nanospheres lose all the surface charge. At this pH, the magnetic and dipolar attractive forces between nanospheres overtake the repulsion forces, inducing the aggregation and precipitation of the nanospheres. This fact is inconvenient considering that this pH is close to the pH value of the physiological fluid. However, as it can observed in Figure 3.25, the ζ absolute value rises quickly above and below the isoelectric point, explaining the high colloidal stability of nanospheres in neutral pH.

In any case, due to the high amino groups density on the surface, these nanospheres are more stable in acid pHs. The high potential values registered at pHs below 6 can be explained by the pKa value (6.3) of the amino groups of chitosan. Below this pH the amino groups are positively charged, increasing the repulsion forces and avoiding their aggregation.[35] At higher pH values, the colloidal stability decreases because of the amino group deprotonation. Therefore, these nanospheres only will be stable in neutral or acid water colloidal dispersions.

3.2.3 Thermogravimetric analysis (TG) of CS-MNS

The coating grade of CS nanospheres has been analyzed by means of the thermogravimetric analysis, as it was performed for the magnetic NPs. Taking into account that more than one organic contribution is present in the sample (oleate and chitosan), their specific degradation points need to be known to ascertain their specific proportions in the sample. Furthermore, once that the proportions of each material present in the nanospheres has been obtained, an estimation of the NP amount inside the nanospheres can be deduced. Hence, the CS-MNS nanospheres and the $Ni_{0.31}Fe_{2.69}O_4$_A NPs which form the nanosphere magnetic nuclei, as well as the oleic acid and the chitosan, have been analyzed by means of a NETZSCH STA 449C equipment. The measurements were performed under Argon atmosphere to avoid oxidation processes. The measurement conditions are described in appendix I.

The thermogravimetric analysis corresponding to CS-MNS nanospheres and $Ni_{0.31}Fe_{2.69}O_4$_A NPs can be observed in Figure 3.26A. The CS-MNS profile shows three weight losses at 160, 225 and 330 °C, being 36 % the total organic mass loss. This is significantly higher than the proportion of organic matter recovering the $Ni_{0.31}Fe_{2.69}O_4$_A NPs (11 %) which form the nanosphere

magnetic core. This strong organic matter proportion increase indicates that the CS represents a large part of the nanosphere volume, as its density is considerably lower than the ferrites (5.2 g/cm^3 for Fe_3O_4 and 0.255 g/cm^3 for CS). In order to check the accurate weight loss points, the derivative thermogravimetry (DTG) analysis of the CS-MNS nanospheres, chitosan and oleic acid have been compared in Figure 3.26B. There is not a good agreement between the decomposition points of chitosan, oleic acid and CS-MNS DTG peaks. However, it is usual that interacting materials have different decomposition profiles than the non-interacting ones. As it was previously explained, some of the oleate chains are covalently bonded to magnetic nanoparticles, modifying strongly its decomposition pathway. Moreover, the hydrophobic interactions between CS chains and the oleate molecules, as well as the H bonds formed between the CS alcoholic groups, also modify strongly the decomposition kinetic and the thermodynamic.

No humidity has been absorbed by the CS nanospheres, as no mass losses occur at 100 °C. The first mass loss, corresponding to the chitosan starting degradation point, is located between 100 and 200 °C. The decomposition of the oleate coating layer starts at higher temperatures than the CS decomposition, as can be observed in the $Ni_{0.31}Fe_{2.69}O_4$_A profile in Figure 3.26A. The next two mass losses, from 200 to 400 °C, represent the second step of the chitosan degradation and also the decomposition of the MNP surface oleate layer.[36] The chitosan layer decomposition, as well as it has been previously explained for the oleate decomposition, occurs in two different steps. In the first step (in the 100-200 °C range), the loss of the chitosan chains that are only attached to other CS chains occur, whereas the CS chains attached to the intrinsic oleate layer are decomposed at higher temperatures (around 300 °C).[37,2] Based on the comparison between the CS-MNP magnetic nanospheres and the NPs, the chitosan content of the

magnetic nanospheres was estimated to be the 28 % of the total CS-MNP sample weight.

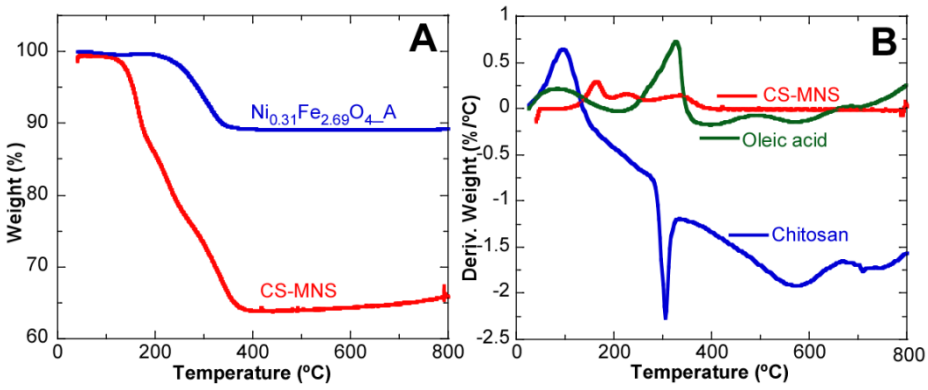

Figure 3.26. *Thermogravimetric curves of CS-MNS and $Ni_{0.31}Fe_{2.69}O_4$_A samples (A) and DTG curves of CS-MNS, chitosan powder and oleic acid (B).*

This information makes possible an estimation of the NP amount inside each magnetic nanosphere, using the density of the materials (ferrite, oleic acid and chitosan), and the average volume of magnetic nanospheres and NPs. Thus, by a comparison between the nanoparticle and CS-MNS weigh, 90 MNPs per nanosphere can be estimated:

$$V_{NP} = 3053.63nm^3 \xrightarrow{d=4.7g\cdot cm^{-3}} \mathbf{1.4432 \cdot 10^{-17}\ g/NP}$$

$$V_{CS-MNS} = 523598nm^3 \xrightarrow[(72\%\ NP)\ \mathbf{1.3066 \cdot 10^{-15} g/CSMNS}]{d=3.5g\cdot cm^{-3}} 1.8248 \cdot 10^{-15} g/CSMNS$$

Where d was calculated taking the proportion of each material (ferrite, oleic acid and CS) into account:

$$d_{NP} = 5.2\frac{g}{cm^3} \cdot 0.89 + 0.895\ \frac{g}{cm^3} \cdot 0.11 = 4.726\ \frac{g}{cm^3}$$

$$d_{CS-MNS} = 4.726\frac{g}{cm^3} \cdot 0.72 + 0.225\ \frac{g}{cm^3} \cdot 0.28 = 3.466\ \frac{g}{cm^3}$$

$$\frac{1.3066 \cdot 10^{-15} g/CSMNS}{1.4432 \cdot 10^{-17} g/NP} = 90\ NP/CSMNS$$

However, this number is always hugely conditioned by the size dispersion of magnetic nanospheres, which changes greatly the number of nanoparticles inside each nanosphere.

3.2.1.4 Fourier Transform Infrared Spectroscopy (FTIR) of CS-MNS magnetic nanospheres

Although the presence of chitosan can be assumed by the stability of the nanospheres in water or the increase of the organic matter in the TG analysis, not direct evidences of the chitosan presence have been obtained. In this sense, Fourier Transform Infrared Spectroscopy (FTIR) would provide information about the functional groups present in the sample. The FTIR analysis of the $Ni_{0.31}Fe_{2.69}O_4$_A magnetic nanoparticles and CS-MNS magnetic nanospheres (Figure 3.27) was performed to obtain a wider understanding of the nanosphere surface chemistry, and also to study the interactions between NPs and CS after the nanosphere formation. The chitosan powder spectrum is also reported for comparison in Figure 3.27. The measurements were performed in powder in the conditions described in Appendix I.

The CS polymer spectrum shows a broad band in the range of 3400-3200 cm^{-1} corresponding to ν_{OH} stretching vibrations from the chitosan chains. The same band can be recognized in the CS-MNS sample, proving the presence of the polymer in the magnetic nanospheres.

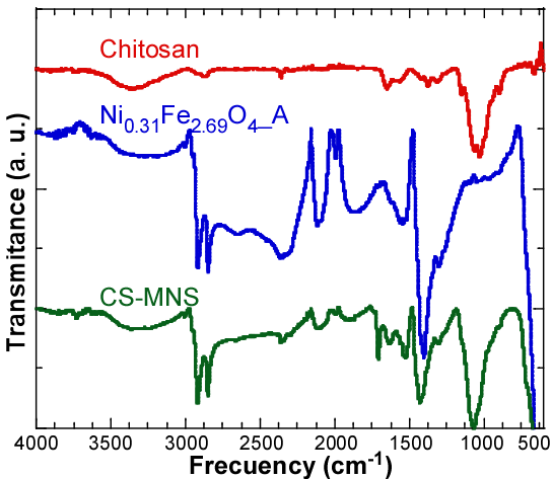

Figure 3.27. *FTIR analysis of CS-MNS nanosphere sample compared with $Ni_{0.31}Fe_{2.69}O_4$_A NPs and chitosan powder.*

Nevertheless, the presence of this band might also be caused by the absorbed humidity, as it can be also identified in the $Ni_{0.31}Fe_{2.69}O_4$_A sample spectrum. The presence of chitosan can also be verified in the CS-MNS spectrum by the intense peak at 1025-1050 cm^{-1}, corresponding to the $\nu_{C\text{-}N}$ stretching vibration of the primary amino groups. Furthermore, the large intensity of this peak in the nanosphere spectra is also related to the noteworthy presence of the primary amine groups on the surface.

In both $Ni_{0.31}Fe_{2.69}O_4$ and CS-MNS spectra, the presence of the oleic acid molecules could be checked by two bands in the 2800-3000 cm^{-1} range, corresponding to ν_{CH2} stretching vibrations. The interaction of the magnetic NP surface oleate molecules can be disclosed by analysing the distance between the peaks at 1635 and 1523 cm^{-1}. These bands can be recognized in both $Ni_{0.31}Fe_{2.69}O_4$ and CS-MNS sample spectra and correspond to asymmetric (ν_{as}) and symmetric (ν_s) COO- stretching vibrations, respectively.[2] By the presence of these bands, a chelating bidentate interaction between the

oleate molecules and ferrite nanoparticles can be ensured in CS-MNS nanospheres.

Thus, the FTIR characterization not only has corroborated the presence of chitosan in the nanospheres, but has also shown that the encapsulation process did not change the NP conformation.

3.2.1.5 Surface amino group determination

Despite the presence of surface amino groups in the chitosan nanospheres has been already confirmed, a quantification of these amino groups would be also interesting. A quantification of the amino group surface density is key for the future surface functionalization of the CS-MNS. There are a number of different chemical-colorimetric methods for amino group quantification.[38,39] A mostly used one is based on the Orange II salt association to nanosphere surface primary amino groups at low pHs. The release of this dye can be achieved at basic pHs. Thus, by measuring the absorbance of supernatants the amount of the associated orange molecules can be determined and, therefore, the amount of the surface primary amino groups.

The surface amino groups quantification of the CS-MNS sample has been performed by measuring the pH-dependent adsorption of Orange II sodium salt dye. This determination is based on the electrostatic interactions between the positively charged amino groups and the negatively charged sulfonate groups at acid media, using the Orange II sodium salt dye spectroscopic determination.[38] First of all, an Orange II salt calibration curve was carried out in the 0.003-0.03 mM range at pH 3 by measuring the absorbance at 484 nm in a Cary 50 prove UV-VISIBLE VARIAN spectrophotometer (Figure 3.28).

In a typical experiment, a total of 0.6 mg of CS-MNS magnetic nanospheres were mixed with an excess of Orange II sodium salt dye (2 µmol) in 1 mL of HCl solution (pH 3) and mechanically stirred for 30 minutes at 40 °C. This dye interacts electrostatically with the amino groups in acid media. Then, four washing steps were performed with 1 mL of a pH 3 solution in each case until all the unbound dye is removed. In order to to release the absorbed dye, another three washing steps were performed with a pH 12 NaOH solution. At these basic pHs the Orange II salt is released from nanosphere surface due to the decay of the electrostatic interactions. Finally, the absorption of the supernatants (which have the disengaged dye) was measured, obtaining the concentration of the Orange salt dye, representative of the amino groups surface concentration in the CS-MNS nanospheres. The pH of these solutions must be adjusted to pH 3 before measuring the absorbance at 484 nm, since the calibration curve was performed at this pH.

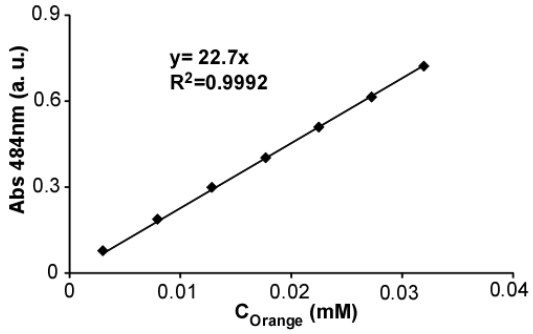

Figure 3.28. *VIS spectra of Orange (II) salt calibration at pH3 for surface amino group quantification experiment.*

The obtained amount of surface primary amino groups was 264.90 nmol-NH_2/mg nanosphere, with a standard deviation of ±19.69 nmol-NH_2/mg. Considering the previously calculated nanosphere weight ($1.81 \cdot 10^{-15}$ g/CS-

MNS), it has been established that there are $289 \cdot 10^3$ -NH_2 groups/nanosphere on the nanosphere surface. This number would represent the amount of active functional amine groups for functionalization, also providing colloidal stability. This amino group amount should be taken into account when performing future functionalizations. An excessive functionalization of these available amino groups would lead to a colloidal stability loss and to the nanosphere aggregation, due to the surface charge reduction. Moreover, the toxicity usually shown by compounds with high density of amino groups, makes this data relevant for future biomedical applications.

The results obtained from previously performed chemical and structural characterizations are resumed in Table 3.11.

Table 3.11. *Main chemical and structural data determined for CS-MNS sample, compared with the data obtained for $Ni_{0.31}Fe_{2.69}O_4$_A NPs.*

SAMPLE	$Ni_{0.31}Fe_{2.69}O_4$_A	CS-MNS
$Size_{TEM}$ (nm)	18.0 ± 1.7	92.0 ± 37
$SIZE_{DLS}$ (nm)	19.4 ± 1.8	152.5 ± 28
Zeta Pot. pH 7 (mV)	-	-11
Isoelectric point	-	6.25
Organic matter (%)	11	36
Weight (g)	$1.44 \cdot 10^{-17}$ g/NP	$1.81 \cdot 10^{-15}$ g/CS-MNS
NP/CS-MNS	-	90
-NH_2/nanosphere	-	$289 \cdot 10^3$

Summarizing, the successful formation of well defined spherical chitosan nanospheres has been verified. The DLS and Zeta potential measurements have shown that the nanospheres form stable colloidal dispersions in neutral water media, but are even more stable at acid pHs, whereas their stability at

basic pHs decreases strongly. Although the amount of the NPs inside each nanosphere could not be calculated from the electron microscopy, this amount was estimated from the thermogravimetric analysis. Thus, an average of 90 NPs per nanosphere, with $289 \cdot 10^3$ of superficial amino group (-NH_2) per nanosphere have been estimated. The high amount of NPs inside the nanosphere suggests the present of dipolar and magnetic interactions inside nanospheres, hence, a modification of the magnetic properties is expected for the CS-MNS nanospheres comparing with the $Ni_{0.31}Fe_{2.69}O_4$_A single NPs.

3.2.2 Magnetic properties of CS-MNS chitosan nanospheres

The same magnetic characterization as the performed for the ferrite magnetic NPs has been carried out for the CS-MNS, always comparing with the NPs which form the nanosphere inorganic nuclei ($Ni_{0.31}Fe_{2.69}O_4$_A). Hence, M (H), M (T) and EMR characterization have been performed for the nanospheres. In contrast to the ferrite NPs, this kind of materials could be more suitable as drug delivery and release agents or as contrast agents for Magnetic Resonance Imaging (MRI). Therefore, their relaxivity value will also be measured. Their application as drug delivery agents will be analyzed by the association of two different fluorophores.

3.2.2.1 Magnetization measurements of CS-MNS

Field dependent magnetization M(H) measurements have been performed at room temperature in a home-made VSM magnetometer up to a maximum field of 18 kOe with high field resolution. This instrument is more accurate than the used for the ferrite and core shell NPs to analyze small changes in magnetization values at low H_{app}. Thus, it is more suitable to determine the presence of coercive field and to verify its superparamagnetic behaviour. The samples have been measured in powder after compressing in

gelatine capsules, as in ferrite NP analysis. The obtained field dependant CS-MNS magnetization cycle, as well as the obtained for the $Ni_{0.31}Fe_{2.69}O_4$_A nanoparticles is represented in Figure 3.29.

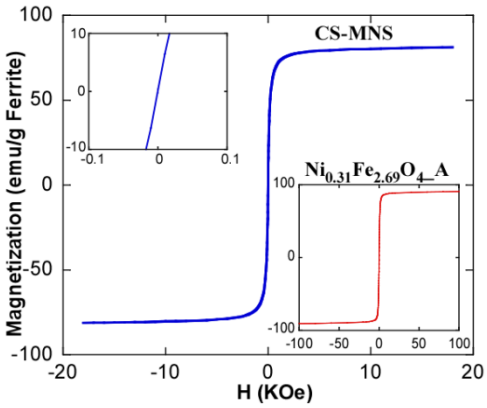

Figure 3.29. *M (H) cycles of CS-MNS nanospheres at R.T., compared with the cycle obtained for $Ni_{0.31}Fe_{2.69}O_4$_A core nanoparticles. The central part is enlarged to visualize the H_c.*

As it can be observed in Figure 3.29, the superparamagnetic behaviour can be confirmed by the absence of coercivity. In this sense, the presence of interparticle interactions between NPs inside the nanosphere cannot be assured by this technique. This fact indicates that the NP assembly into chitosan nanospheres does not modify the anisotropy of single NPs at the time window of this experiment. It is clear by this coercivity absence that all NPs in the inorganic core of the nanosphere do not behave as a unique large magnetic particle. Such a large magnetic particle should show an enormous remanence magnetization value and different susceptibility and saturation magnetization due to the generated great demagnetizing field.[40] In fact, the magnetic nanocluster rarely have induced a significant modification in the coercive field or remanent magnetization.[31,33,32] However, the presence of dipolar and magnetic interactions between NPs cannot be discarded, as could be detected by other techniques with shorter time windows.

As expected, the saturation magnetization value (M_s) is 81 emu/gFerrite (51.8 emu/gSample) for the CS-NMS nanospheres, that it is comparable to the 84.6 emu/gFerrite of the $Ni_{0.31}Fe_{2.69}O_4$_A NPs. Hence, the ferrite intrinsic magnetization has not suffered an important modification after the encapsulation treatments. In this kind of surface modification treatments temperature increases should always be avoided, as these phases are sensitive to the oxidation under air atmosphere at high temperatures.

The temperature dependent magnetization evolution will provide further information about differences induced by the NP agglomeration inside the nanospheres. Once again, the FC-ZFC experiments for CS-MNS nanospheres and $Ni_{0.31}Fe_{2.69}O_4$_A nanoparticles were performed in a commercial Superconducting Quantum Interference Device (SQUID) magnetometer as described in Appendix I. The samples diluted in toluene (in the case of $Ni_{0.31}Fe_{2.69}O_4$_A sample) or water (CS-MNS) dispersions (0.05 mgFe/mL) were dried on a filter paper to avoid dipolar and magnetic interactions between NPs. The diamagnetic contribution of the filter paper has been removed. The FC-ZFC curves of both samples are shown in Figure 3.30A.

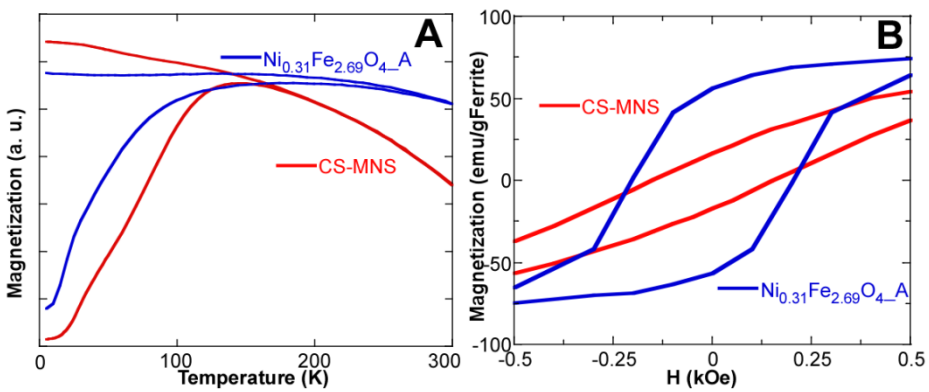

Figure 3.30. *Temperature dependant magnetization measurements after zero field (ZFC) and field (FC) cooling (A) and hysteresis loops at 5 K measured in samples dispersed on a filter paper (B) of* $Ni_{0.31}Fe_{2.69}O_4$*_A NPs and CS-MNS nanospheres.*

The CS-MNS sample shows a higher broadness effect in the ZFC peak and higher separation between ZFC and FC curves. The blocking temperatures have been determined in the same way as explained for the ferrite NPs, and the anisotropy constants were calculated by means of Stoner-Wohlfarth equation (3.15):[41]

$$K = \frac{25 k_B T_B}{V} \quad (3.15)$$

As it can be observed in Table 3.12, both samples show nearly identical blocking temperatures and anisotropy constants, which supports that NPs are single and independent magnetic nanosystems inside the nanosphere instead of behaving as one single big particle. Otherwise, if the diameter of the nanosphere would be taken as 92 nm (the main diameter of the CS-MNS), the obtained anisotropy constant value would be 1.24 kJ/m^3. Thus, the CS-MNS behaviour fits much better to a cluster of multiple independent magnetic NPs than to a one single 92 nm particle system. In order to relief the data obtained from the FC-ZFC analysis, the anisotropy constants have also been calculated from coercive fields of the hysteresis loops measured at 5 K dispersed in filter paper (Figure 3.30B). The anisotropy constants are in the same value range as the obtained from the blocking temperatures and are in good agreement with the expected values.

Table 3.12. *Blocking temperature (T_B), coercive field (H_C) and anisotropy constant values obtained from different sources of $Ni_{0.31}Fe_{2.69}O_4$_A and CS-MNS samples.*

SAMPLE	$Ni_{0.31}Fe_{2.69}O_4$_A	CS-MNS
T_B (K)	72	66
H_C (Oe)	204	162
K (ZFC-FC) (kJ/m^3)	20.06	18.76
K (H_C) (kJ/m^3)	28.28	22.17

In spite of the similar blocking temperature, coercive field and anisotropy constant values obtained for nanospheres and NPs, the broadening effect in the FC-ZFC maximum of CS-MNS has to be considered. This broad curve could be related to the presence of dipolar interactions between NPs. In literature, the broadening of the ZFC blocking temperature peak, as well as the increase of the difference between the T_B maximum and the T_{irr} point (as in this case), is usually attributed to an aggregation effect. This possibility must be considered taking the high number of NPs inside each nanopshere into account.[16,17]

3.2.2.2 Electronic Magnetic Resonance (EMR) analysis of CS-MNS

The Electronic Magnetic Resonance (EMR) spectroscopy has been revealed as a useful tool to determine small changes in the magnetic response, as well as the heterogeneity in this response.[7,8] For this reason, this is the best way to verify the interparticle interactions deduced from the FC-ZFC experiments. The magnetic couplings between the adjacent NPs will be evidenced in the EMR analysis by an increase of the g_{eff} value, induced by the slower NP rotation because of the increase of these magnetic couplings. The CS-MNS nanospheres and $Ni_{0.31}Fe_{2.69}O_4$_A NPs have been measured in aqueous (nanospheres) and toluene (NPs) 0.05 mgFe/mL colloidal dispersions at room temperature, as described in Appendix I. The obtained EMR spectra for both samples are represented in Figure 3.31.

Both spectra show a single narrow band in the 2000-3000 Oe range, as it can be observed in Figure 3.31. This single peak supports that the CS-MNS nanospheres behave like a homogeneous magnetic system. The peak to peak line widths (ΔH_{pp} values) of both bands, 410 Oe for $Ni_{0.31}Fe_{2.69}O_4$_A and 620 for CS-MNS, are in good accord with the homogeneity of the magnetic systems. However, a displacement of the g_{eff} value (2.19 for $Ni_{0.31}Fe_{2.69}O_4$_A)

to higher values (g = 2.45 for CS-MNS) can be observed. In this case, the presence of dipolar or magnetic interactions between the NPs has been detected, which would increase the NP relaxation time and originate ferromagnetic interactions.[15]

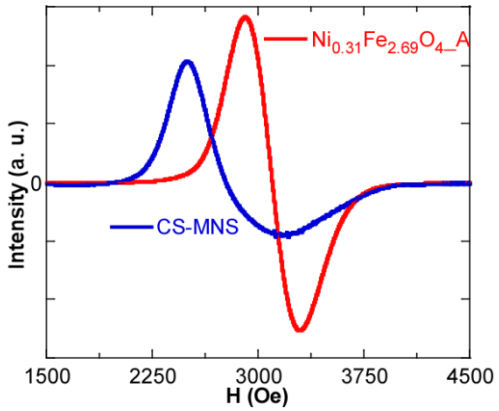

Figure 3.31. *Electronic Magnetic Resonance spectra of CS-MNS nanospheres and $Ni_{0.31}Fe_{2.69}O_4$_A NPs in colloidal dispersion.*

Nevertheless, if all the NPs inside the nanosphere would be behaving as one single big NP, the g_{eff} increase would be much higher, since this value rises exponentially with the diameter as was reported by Castellanos et al.[3] Therefore, the higher g_{eff} value would be related to weak interparticle interactions between magnetic moments. These couplings decrease the NP net magnetic moment rotation, that would need more energy to orient with the magnetic field.

Another interesting point that should be considered is that the relative high size dispersion of the CS-MNS does not seem to affect this displacement, as the signal homogeneity of the $Ni_{0.31}Fe_{2.69}O_4$_A sample has maintained. Therefore, the explained interparticle magnetic couplings would only occur between adjacent particles instead of between all NPs forming

the nanosphere. Magnetic couplings between all the NPs inside nanospheres would had yield great differences between nanospheres with different sizes, providing an extremely broad EMR peak. In this way, the presence of small magnetic interactions between neighbouring NPs inside nanospheres can only be assumed.[23]

3.2.2.3 Magnetic relaxivity measurements of CS-MNS and $Ni_{0.31}Fe_{2.69}O_4$_A_PMAO samples.

The sample response in the Magnetic Resonance Imaging (MRI) diagnosis is usually tested by measuring the relaxivity behaviour. Basically, the MRI relies on the counterbalance between the small magnetic moment on a proton and the high proton amount in the environment, as in biological tissues, which are mostly composed by water. Thus, the signal is based on the of water protons signals, what it means that the signal would be completely different in different mediums. Although the signal of each proton at an applied magnetic field is quite small (it is estimated that only the 0.0003 % of protons align with the applied magnetic field) the high amount of protons in aqueous samples and wet tissues makes the signal detectable.[42] Under a constant magnetic field (B_0), a transverse radiofrequency field is also applied to excite the oriented protons. The protons tend to align again with the B_0 magnetic field (relaxation). The presence of magnetic nanocompounds disturbs the normal alignment of the protons, producing an easily detectable contrast effect.[43]

The proton relaxation can be produced by two different mechanisms: on the one hand, the longitudinal relaxation, T_1, which represents the time required for the 63 % of the excited H^1 to align with the B_0. In this case, the absorbed energy during the radiofrequency excitation is released to the surrounding tissues. The transverse relaxation, T_2, refers to the relaxation

between the excited spins, which magnetic fields interacts between them, resulting in an energy exchange between the proton spins. Thus, T_2 refers to the time in which the transversal magnetization value (induced by the applied radiofrequency) decrease to 37% of its initial value. Examples of T_1 and T_2 relaxation are represented in Figure 3.32.

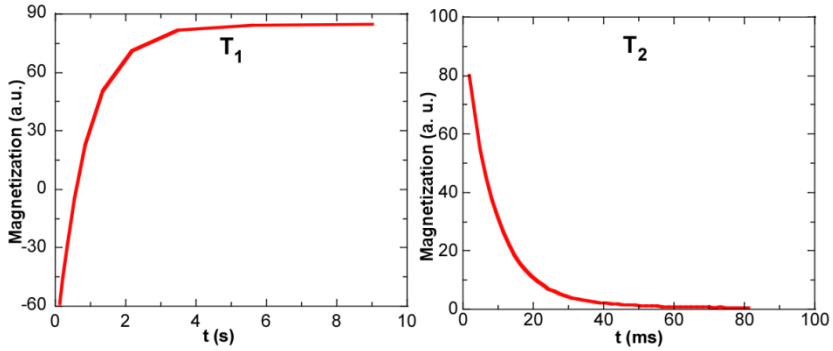

Figure 3.32. *Longitudinal T_1 and transversal T_2 relaxation slopes for $Ni_{0.31}Fe_{2.69}O_4$_A_PMAO sample at 0.5 mM Fe concentration dispersed in 10% gelatin solutions.*

Magnetic relaxivity measurements were performed using a minispec m1-one Analyzer from Bruker at 1.41 T (appendix I). The longitudinal (T_1) and transversal (T_2) relaxation times have been measured at five different iron concentrations in the 0.1-1 mgFe/mL range for $Ni_{0.31}Fe_{2.69}O_4$_A_PMAO and CS-MNS samples. Both nanocompounds have been dispersed in 10 % gelatine aqueous solution in order to obtain a more suitable *in vivo* media. The water transferred $Ni_{0.31}Fe_{2.69}O_4$_A_PMAO NPs have been measured in order to compare with nanospheres relaxivity.[44] The zero concentration solution (10 % gelatine aqueous solution) was measured and its contribution was deducted from the measured values in the different nanocompound concentrations. Four different measurements of T_1 and T_2 were performed for every sample and concentration for a statistical correction. The T_1 values were determined by the inversion-recovery method and T_2 values by the

Carr-Purcell-Meirboom-Gill sequence.[45] The longitudinal (r_1) and transversal (r_2) relaxivity values were calculated from the slope of the linear plot of longitudinal and transversal relaxation times ($1/T_1$ and $1/T_2$) with the iron concentration. The *in vitro* relaxation times (T_1 and T_2) of CS-MNS and $Ni_{0.31}Fe_{2.69}O_4$_A_PMAO samples at different concentrations are represented in Figure 3.33.

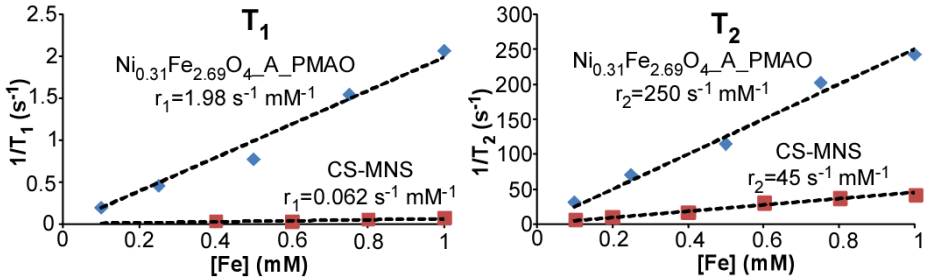

Figure 3.33. *Longitudinal (T_1) and transversal (T_2) relaxation times at different concentrations obtained for $Ni_{0.31}Fe_{2.69}O_4$_A_PMAO (squares) and CS-MNS (rhombus) samples*.

As it corresponds to superparamagnetic nanoparticles, the longitudinal r_1 relaxivity (1.98 $s^{-1}mMFe^{-1}$ for NPs and 0.062 $s^{-1}mMFe^{-1}$ for CS-MNS) resulted to be smaller than the r_2 transversal one (250 $s^{-1}mMFe^{-1}$ for NPs and 45 s^{-1} $mMFe^{-1}$ for CS-MNS) for both samples. This also can be checked in the example represented in Figure 3.32 for $Ni_{0.31}Fe_{2.69}O_4$_A_PMAO sample at 0.05 mM concentration, where the time shown in x axis is around 100 lower in T_2 than in T_1. As superparamagnetic nanocompounds behave as paramagnets with high magnetization values, they lose the magnetization at the moment when the transversal magnetic field is removed, being the transversal T_2 relaxation time much quicker than the longitudinal one.[46] For this reason, superparamagnetic particles are considered as T_2 contrast agents, thus, the r_1 values are negligible comparing with the r_2 values. Actually, the CS-MNS sample did not present T_1 relaxivity at all. Hence, both

samples behave as high magnetization superparamagnetic compounds, suitable for be applied as MRI contrast agents. Nevertheless, the calculated slope (r_2) from the linear fitting of the $1/T_2$ values is, as well as the r_1 values, higher for the $Ni_{0.31}Fe_{2.69}O_4$_A_PMAO single NPs than for the CS-MNS nanospheres. In contrast, some studies in literature supports that the NP assembly, caused by the aggregation, increases its effectiveness as T_2 relaxation agent.[47] However, this effect has not been observed in our CS-MNS nanospheres. The confirmation by EMR measurements of the presence of magnetic couplings between the NPs inside nanospheres is in good accord with the measured lower relaxivities. Furthermore, the lower net magnetization of the nanospheres due to their higher organic matter content would have affected their relaxation. The combination of these effects could be the reason of the relaxivity value decrease after the nanospheres formation. In any case, the relaxivity values obtained for both samples are in the usual range for this kind of nanoparticles, being even higher in the case of the $Ni_{0.31}Fe_{2.69}O_4$_A_PMAO NPs.[37,42,43]

3.2.3 Structural stability of CS-MNS magnetic nanospheres

As a previous step before testing the nanocompounds in *in vitro* and *in vivo* experiments, it is useful to study the stability of the nanocompounds in different conditions. Hence, their structural and colloidal stability at extreme pH solutions, as well as high ionic strength solutions, should be known. Furthermore, the effects that some biologic fluids (intestinal and gastric fluids) could induce in the nanosphere structural and colloidal stability should also be predicted.[48,49,50] For this purpose, some solutions which simulates these conditions have been prepared.[51,36] The effects that some chitosan specific enzymes have in the nanosphere structure were also studied.[50,52] In fact, the encapsulation of such kind of enzymes inside the nanospheres it is being considered in order to provide an alternative

controlled release mechanism.[53] Finally, the temperature dependant evolution would give information about the structural configuration and the density of the CS shell, as well as the shell decomposition temperature, which would be useful to control the release mechanism.[54,55]

Hence, with the aim of achieving a broader understanding of the structural and chemical changes that some factors can induce in the chitosan nanospheres, different stability tests were carried out at different temperatures, pH solutions, simulated physiological fluids and enzymes.

3.2.3.1 CS-MNS stability tests at different pH and simulated physiological fluids

A broad knowledge of the nanosphere stability at different pH is necessary to be applied in future *in vivo* experiments. Depending on the part of the human body where the nanospheres are going to be applied, there is a wide range of pHs that the nanospheres could be in contact with. These changes could induce the decomposition or the aggregation of the CS-MNS.

Thus, the CS-MNS sample was incubated in 2 mL solutions at different pHs (1, 3, 5, 7, 9 and 12), in 0.4 mg/mL concentration at 37 °C for 90 min under stirring. In the same conditions, the nanospheres were dispersed also in 2 mL of simulated gastric fluid (80 μM sodium taurocholate, 20 μM lecithin, 34.2 mM NaCl, pH 1.6) and simulated intestinal fluid (3 mM sodium taurocholate, 0.2 mM lecithin, 19.12 mM maleic acid, 34.8 mM sodium hydroxide, 68.62 mM sodium chloride, pH 6.5).[56] After the incubation, the nanospheres were centrifuged at 13000 rpm for 5 min and separated from the supernatant. Finally, the nanospheres were washed twice and analysed by ESEM microscopy to check the effects of the fluid in the nanosphere structure. Furthermore, so as to verify if the chitosan of the nanosphere shell has been partially decomposed and dissolved, the amount of chitosan

dissolved in the supernatant was measured by a modified Schales method using potassium ferricyanide.[57,58] After the 90 min of incubation, a total of 1.5 mL of the centrifuged supernatants were mixed with a 2 mL solution of 0.5 M Na_2CO_3 and 0.05 % potassium ferricyanide. This mixture was incubated at 80 °C for 30 min and the absorbance was measured at 420 nm in a Cary 50 UV-VISIBLE VARIAN spectrophotometer. Glucosamine concentration in solution was calculated by previously performed calibration curve in the 0.001-0.03 mM range.

ESEM micrographs of the nanospheres incubated at different pH values and in different simulated physiological solutions are reported in Figure 3.34. The magnetic CS nanospheres maintained their colloidal and structural stability at acidic and neutral pH values and also at slightly basic media. This pH response is in good agreement with the results obtained in the pH dependant Zeta potential analysis. However, the Zeta potential values only referred to the surface charge value of the nanocompounds, not providing any information about the structural condition. At pH values below 6.2 (point of zero charge) the surface amino groups are positively charged, that assures the necessary repulsion forces to maintain a good colloidal stability, as can be observed at pH 1, pH 3 and pH 5 micrographs in Figure 3.34. At high pH values, the nanospheres appear completely aggregated due to the strong dipolar and magnetic interactions between NP, being the amino groups deprotonated, as it can be observed in Figure 3.34. Apparently, although the colloidal stability has been lost, no substantial changes in the nanosphere structure can be appreciated in those incubated at pH 9 and pH 12.

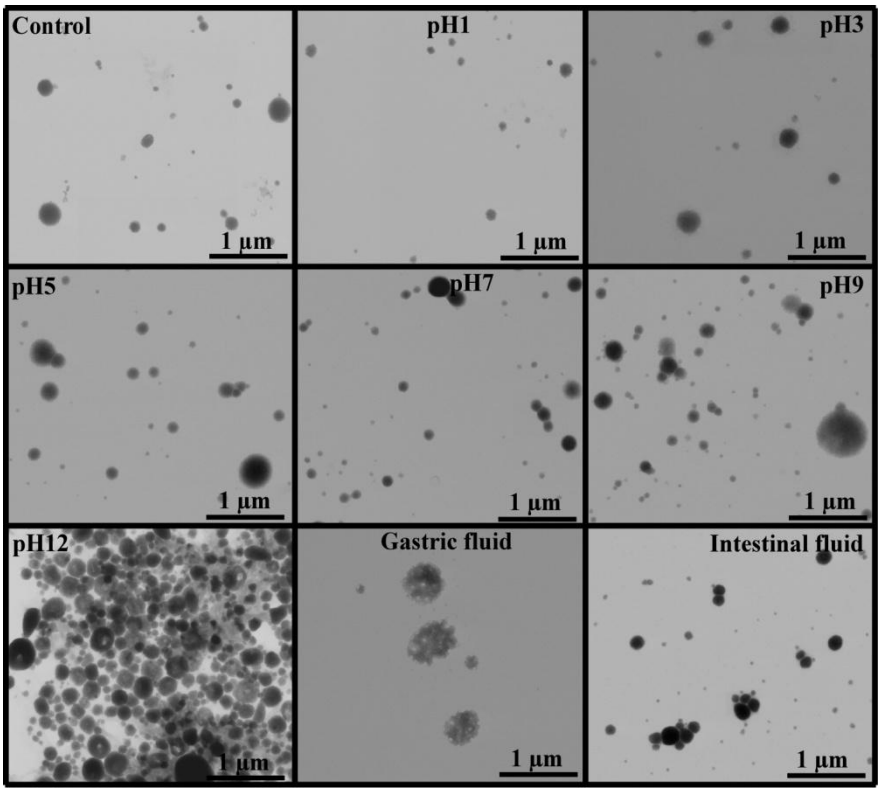

Figure 3.34. *ESEM micrographs of CS-MNS nanospheres after being incubated at 37 °C at different pHs and physiological fluids for 90 min.*

Additionally, the stability in gastric and intestinal simulated solutions (GS and IS respectively) was tested. The magnetic nanospheres are structurally stable in IS (pH 6.8), but the polymeric coating resulted partially dissolved after the incubation in gastric solution. In this case, the high salt concentration in addition to the extremely low pH value of this fluid produces the partial solubilisation of chitosan. From the micrograph shown in Figure 3.34, this effect can be recognized by the presence of some porosity in the nanosphere structure. The acid media, in addition to the high salt concentration, could cause the disruption of dipolar interactions between the CS chains, as well as the o-glycosidic bonds breaking, producing the

release of chitosan oligomers.[50,59] To support this hypothesis, the analytical determination of free chitosan present in supernatants after nanosphere separation from the incubation medium was carried out by a redox reaction of glucosamine by potassium ferricyanide.[58]

In good agreement with the electron microscopy evidences, the analytical method only revealed a detectable amount of chitosan in the GS incubation supernatant. A total of 0.06 mg of glucosamine, which comes from the chitosan breaking, were detected in the GS supernatant, which represents the 40% of the initial chitosan amount in the nanosphere sample. No glucosamine presence has been detected in the other supernatants, hence, the nanosphere decomposition was no severe in the other cases.

3.2.3.2 CS-MNS stability testing in contact with chitosanase specific enzyme

Before testing the magnetic nanospheres in complex organisms, it is necessary to have a general knowledge about their behaviour in contact with chitosan specific enzymes as chitosanase. This enzyme selectively hydrolyses the glycosidic bonds, inducing the degradation of the chitosan chains.[60] This enzyme can be obtained from many different bacteria and fungi as *Bacillus circulans, fusarium solani* or *Matsuebacter chitosanotabidus*.[61,62] For this study, chitosanase from the *Streptomyces griseus* was selected. The incubation conditions used during the treatment have been chosen focused on obtaining the greatest performance of the enzyme, being these conditions compatible with a physiological environment. Thus, sodium acetate buffer has been chosen as dispersion media to increase the enzyme activity, and the incubation temperature was 37 °C to simulate the physiological conditions.[63]

Chitosanase is the enzyme that specifically endohydrolyses the β-1,4-bonds between glucosamine monomers in partially acetylated chitosan.[60] A

total of 1.3 mg/mL of CS-MNS magnetic nanospheres were incubated in sodium acetate buffer (0.1 M at pH 5.75) at 37 °C in the presence of 0.008 U/mL (0.12 U) of chitosanase during 15 hours under stirring.[63] The enzymatic activity was stopped by heating the solution at 100 °C for 5 minutes. The incubated sample was then centrifuged at 13000 rpm to isolate the supernatant. The glucosamine amount in the supernatants was measured by spectrophotometric determination by potassium ferricyanide assay as it was previously described.[64] The presence of chitosan and glucosamine in the supernatant was also checked by Thin Layer Chromatography (TLC). After the incubation with chitosanase, 8 µL of supernatant were placed in a silica gel plate (Silica gel 60, Merk) with glucosamine (1 mM) and chitosan (0.5 mg/mL) as controls. A mixture of n-propanol:H_2O:ammonia (30%) 70:15:15 was used as developing solvent.[63] The spots were made visible by a ninhidrine solution, which stains the chitosan amino groups.

The measured amount of dissolved glucosamine in the supernatant was 25 µg, which represents the 3% of the initial nanosphere chitosan. A control experiment at the same conditions was performed using dissolved chitosan to check the enzymatic activity. In this control experiment, a significant amount of the added chitosan, the 28 %, was disrupted under the enzymatic activity. In this way, the 3% of the discomposed chitosan in the chitosan nanospheres represents a negligible nanosphere decomposition, compared with the 28% of decomposed dissolved chitosan.

Moreover, the presence of chitosan and glucosamine in supernatants was also checked by Thin Layer Chromatography (TLC) (Figure 3.35). As control, the marks corresponding to glucosamine and enzyme have also been represented. As can be observed, only glucosamine has produce an observable mark in the plate. The CS-MNS (S in Figure 3.35) does not show any evidences of glucosamine presence, thus, the decomposition of the CS

nanospheres induced by the chitosanase enzyme activity has been again discarded.

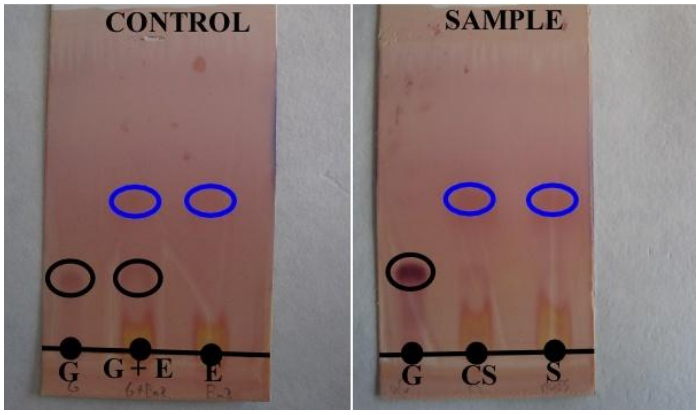

Figure 3.35. *TLC plates of the control performed with glucosamine (G), glucosamine + enzyme (G+E) and enzyme (E) and the sample (S) plate compared with glucosamine and chitosan marks.*

These results suggest that, in the case of the CS-MNS magnetic nanospheres, the chitosanase was not able to decompose the chitosan once it is forming the nanosphere shell. This is probably due to the stiffness of the structure. Nevertheless, it cannot be excluded that this low digestion degree could be due to the low accessibility of chitosan to the enzyme once it is forming the shell of the sphere. Thus, when the CS is dissolved as in the control the enzyme activity is more direct, whereas when is forming the nanosphere shell the enzyme has not direct access to the β-1,4-bonds. In any case, nanospheres have shown a great structural stability under the activity of this specific enzyme.

3.2.3.3 Temperature dependant CS-MNS stability

The study of the CS-MNS colloidal behaviour in different temperatures will provide important information about the structural effects of the temperature in the nanospheres. This would be useful in order to understand the effects of the magnetic hyperthermia in the nanospheres and also in the colloidal stability.

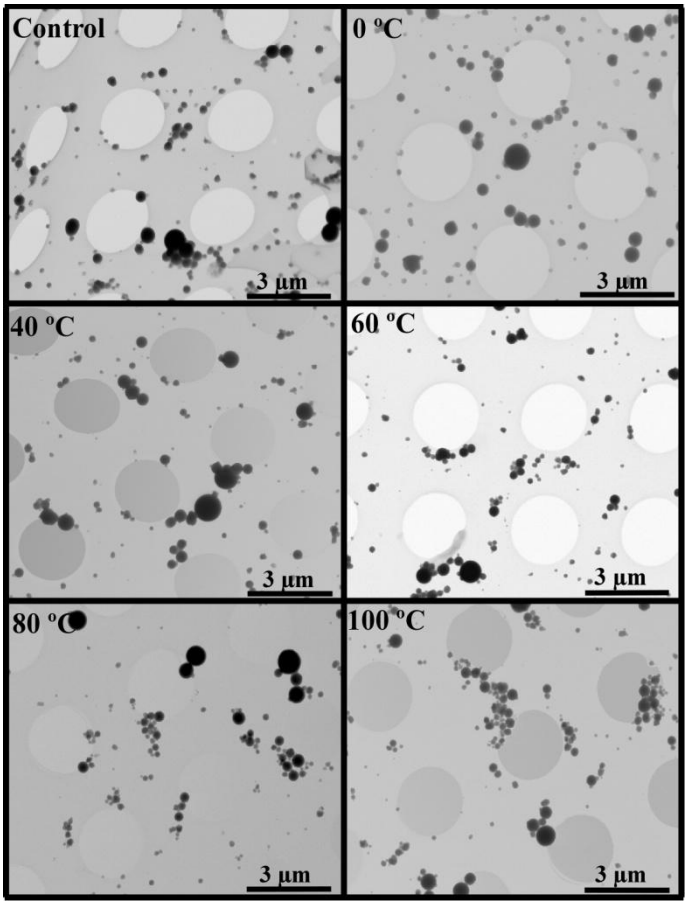

Figure 3.36. *Micrographs of CS-MNS nanospheres after have been treated at different temperatures for 90 minutes.*

Thus, the CS-MNS magnetic nanospheres were incubated in 0.4 mg/mL concentration in 2 mL of milliQ water at 0, 40, 60, 80 and 100 °C for 90 min. After the incubation, possible changes in the nanosphere structure and diameter were checked by ESEM microscopy. The obtained micrographs for the exposed nanospheres to different temperatures are shown in Figure 3.36.

As it can be observed in the ESEM micrographs, no structural changes can be detected in any of the exposed nanospheres. Even after the incubation at 100 °C, no morphological changes can be observed in the nanospheres, in terms of shape and apparent stiffness. Although the nanospheres could have suffered some changes not detected by ESEM, the thermal stability of the prepared CS-MNS seems to be high.

3.2.4 Fluorophore association with CS-MNS magnetic nanospheres

As it has been previously explained, two fluorophores, Nile Red and Rhodamine b isothiocyanate, were chosen to associate with the nanospheres due to their dissimilar nature and different association mechanisms, since Nile Red is hydrophobic and Rhodamine is hydrophilic. The association grade of these polymers will test the capability of the CS-MNS nanospheres to encapsulate this kind of drugs and the mechanism and efficiency of this association.

3.2.4.1 Nile Red encapsulation in CS-MNS

Different amounts of Nile Red (from 10 to 200 nmol) were encapsulated inside the CS-MNS nanospheres during the nanosphere formation, together with the NPs. The amount of the encapsulated Nile Red has been calculated by an indirect determination. Thus, the non-encapsulated Nile Red has been determined by fluorescence measurements of the supernatants obtained

from the washing processes after the encapsulation. Firstly, the absorption/emission spectra (Figure 3.38A) has been performed in a 75:25 CH_3OH:H_2O mixture solvent to determine the optimum excitation and emission wavelength, which are Ex: 572 nm and Emi: 644.17 nm for this solvent mixture. After that, the calibration of Nile Red in the 0.2-4 µM range at 572 nm excitation wavelength in this solvent mixture was performed (Figure 3.38B).

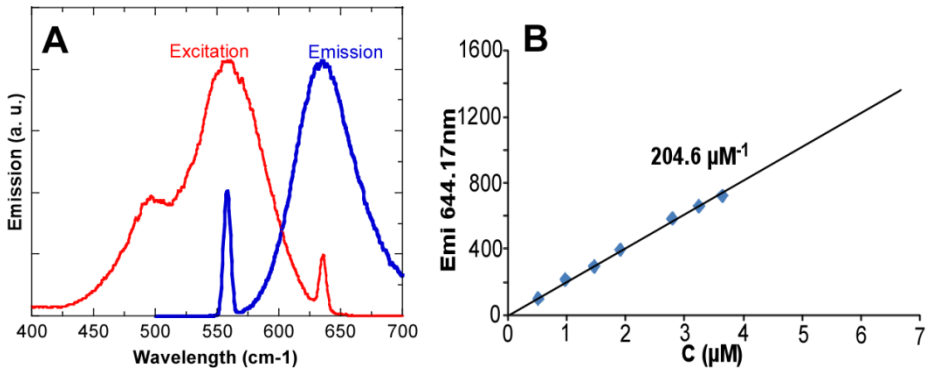

Figure 3.38. *A: excitation/emission spectra of Nile Red in 75:25 CH_3OH:H_2O and B: Nile Red calibration in the 0.2-4 µM range at 572 nm of excitation and 644 nm of emission wavelengths.*

Based on this calibration, the amounts of non-encapsulated fluorophore were measured and, hence, the encapsulated Nile red and the encapsulation efficiency were calculated (Table 3.13).

The obtained encapsulation amounts, as well as the efficiency values, show that the encapsulation process was successful in all the tested amounts of Nile Red. Furthermore, the presence of Nile Red has not induced any change in the normal nanosphere formation.

Table 3.13. *Obtained emission values and calculated amounts of encapsulated Nile Red and encapsulation efficiency.*

SAMPLE	Added Nile Red (nmol)	Supernatant $Emission_{644.17nm}$ Intensity (a. u.)	Encapsulated Nile Red (nmol)	Efficiency (%)
CS-MNS-NL200	200	8	199.7	99.5
CS-MNS-NL100	100	28.79	98.9	98.9
CS-MNS-NL50	50	13.28	49.5	99.0
CS-MNS-NL20	20	24.25	19.1	95.5
CS-MNS-NL15	15	16.17	14.4	96
CS-MNS-NL10	10	17.25	9.3	93

Consequently, it seems that the encapsulation of hydrophobic drugs would be suitable with these nanospheres. However, in order to visualize the Nile Red inside nanospheres a fluorescence optic microscope has been used. Although Nile Red was easily detected in all samples, in CS-MNS-NL200 and CS-MNS-NL100 samples Nile Red aggregates were observed inside the nanospheres. Therefore, the easy encapsulation of the hydrophobic compounds has been proved. Nevertheless, it was also found that at concentrations higher than 50 nmol, the internal distribution of the compound could be heterogeneous. Thus, an excessive amount of drug encapsulations should be avoided.

3.2.4.2 CS-MNS functionalization with rhodamine B isothiocyanate

The same procedure used for Nile Red encapsulation has been tried to apply for the rhodamine B fluorophore. Nevertheless, due to the polar nature of the fluorophore, the rhodamine has been attached to the nanosphere surface by a sulfenamide N-S bond.[65] As it was previously explained, a key feature that should be taken into account when a

functionalization is being carried out is the amount of the amine groups that are being blocked. Depending on the amount of functionalized amino groups, the net surface charge of the nanosphere could change, changing the colloidal stability.

As it can be observed in Table 3.14, three different amounts of rhodamine have been added in three different experiments, 25, 50 and 75 nmol. The amounts below 25 nmol of rhodamine in nanospheres were undetectable by the fluorescence optic microscope. on the other hand, at the highest tested amount, 75 nmol, the stability limit was exceeded (reducing excessively the net surface charge) and the nanospheres were aggregated and precipitated. The same procedure as in Nile Red experiments has been followed to ascertain the amount of the functionalized rhodamine. Thus, after performing a calibration of rhodamine dye absorption in the 1-20 µM range (Figure 3.39), the absorbance of the supernatants obtained after washing processes was measured at 550 nm. The non associated and associated rhodamine amounts, together with the association process efficiency (Table 3.14) has been calculated.

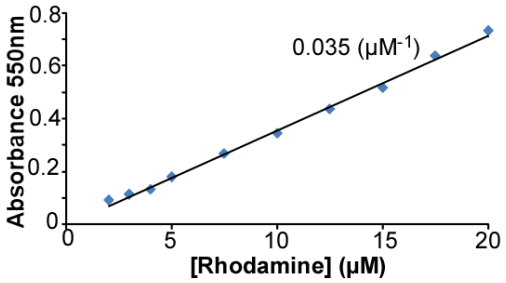

Figure 3.39. *Calibration of rhodamine B isothiocyanate dye absorbance at 550 nm in water in 1-20 µM range.*

Since the CS-MNS-RH75 nanospheres precipitated during the functionalization process, their functionalization grade could not be determined. As it has been explained, the amount of added rhodamine was too high in this case, blocking a great proportion of the nanosphere surface amino groups. This excessive amino group blocking reduced the net positive charge of the nanospheres. In this point, the van der Waals and magnetic attractive interactions between the nanospheres overtook the electrostatic repulsion forces between the positively charged nanospheres, inducing their aggregation. Despite the great difference between the added rhodamine amounts in the CS-MNS-RH25 and CS-MNS-RH50 sample preparation, the obtained efficiency values were similar in both cases. Hence, the proportion between the added and associated amounts of rhodamine seems to be constant whatever the added amount is. However, the efficiency in both cases, 39 and 38 %, is far from the high efficiency grade obtained for the Nile Red encapsulation, which was around the 100 % in every instance. Thus, the efficiency of the developed functionalization process with rhodamine is quite lower than the developed one for Nile Red.

Table 3.14. *Amounts of added and functionalized rhodamine, association efficiency and calculated relative amount of rhodamine per total amount of amino groups in one nanosphere.*

SAMPLE	Added rhodamine (nmol)	Functionalized rhodamine (nmol)	Efficiency (%)	rhodamine/-NH_2 (%)
CS-MNS-RH25	25	9.7	39	6.3
CS-MNS-RH50	50	19.2	38	12
CS-MNS-RH75	75	-	-	-

Furthermore, by applying the previously calculated relations ($1.81 \cdot 10^{-15}$ g/nanosphere and $289 \cdot 10^{3}$ -NH_2/nanosphere), the percentage of the

functionalized amino groups has been calculated. As it can be observed in Table 3.14, the percentage of the occupied amino groups was the 6 % for the CS-MNS-RH25 and the 12 % for the CS-MNS-RH50 sample. Although these proportions seem to be low, the consequent surface charge decrease would be important. In this way, this fact could explain the nanosphere aggregation when higher amounts of rhodamine were added in the CS-MNS-RH75 sample preparation.

3.2.5 Chemical and structural properties of prepared fibroin nanospheres

The chemical and structural stability of the previously prepared fibroin and fibroin-chitosan nanospheres have been tested. Among all the preparations performed for obtaining different chitosan-fibroin nanospheres, only the Fi-CS3.1, Fi-CS3.2, Fi-CS3.3 and Fi-CS3.4 samples, as well as the fibroin nanospheres (Fi-MNS), have shown enough stability to continue with characterization. In this sense, these nanospheres have been characterized by ESEM and zeta potential measurements at neutral pH, to achieve a general knowledge about their surface chemistry and morphology. All samples were measured in 0.01 mgFe/mL concentration.

One of the greatest achievements that this Fi-CS mixed nanospheres could provide would be the ability to control the surface charge of the resultant compound, as both biopolymers have opposite charges. The ESEM micrographs, besides the Zeta potential values at pH 6.8, are shown in Figure 3.40.

As it can be seen, the nanospheres prepared by mixing both polymers have lost the well defined spherical shape that was obtained for the CS-MNS nanospheres.

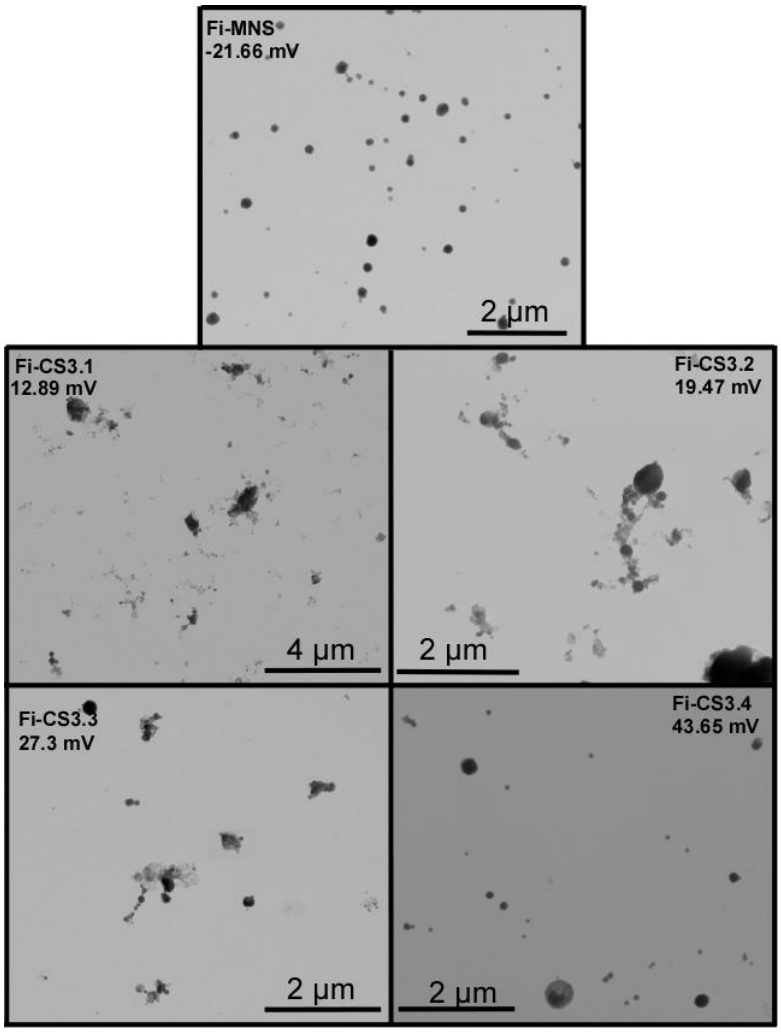

Figure 3.40. *ESEM micrographs and Zeta potential values measured at pH 6.8 of fibroin nanospheres and Fi:CS mixed nanospheres.*

In fact, the sample with the highest fibroin proportion (Fi-CS3.1, 50%) has completely lost its spherical morphology, as only amorphous polymer coated NP aggregates can be observed in the micrograph. Better defined spherical morphologies have been obtained by reducing the fibroin proportion in the nanospheres, being perfectly defined in the sample with the lowest fibroin

proportion (Fi-CS3.4, 15%). However, this effect is not due to the presence of the fibroin, as the Fi-MNS shows a perfectly defined spherical morphology, with an average diameter of 97 nm, quite similar to the diameter of the CS nanospheres. This effect could be related to the interactions between different polymer chains, which would not allow the proper formation of the nanospheres.

The presence of both polymers has been evidenced by the Zeta potential values obtained for the different samples, as this value decreases when increasing the fibroin proportion in nanosphere structure (43.65 mV (15%), 27.3 mV (35%), 19.47 mV (40%), 12.89 mV (50 %) and -21.66 mV (100%)). This fact demonstrates the presence of fibroin in the structure, and the correlation between the amount of fibroin and the surface charge. However, even at a 50% of fibroin proportion, the surface charge is still positive. Consequently, higher amounts of fibroin would be needed to obtain negatively charged mixed nanospheres. Furthermore, so as to analyze properly the new Fi-MNS fibroin nanospheres surface chemistry, an infrared spectra measurement has been performed (Figure 3.41).

The fibroin nanosphere FTIR spectra can be observed in Figure 3.41, where the most characteristic fibroin bands are represented. The peak at 3280 cm^{-1} is attributed to the ν(N-H) stretching band. The presence of one single band confirms that only secondary amide groups are present in the sample, as primary amide groups produce two differentiated bands. The alkene group of the oleate chains is represented by the small band at 2950 cm^{-1} corresponding to the ν(=C-H) stretching band.

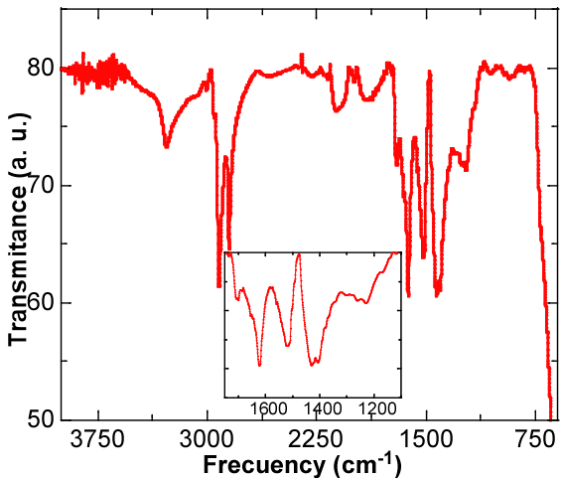

Figure 3.41. *FTIR spectra of the Fi-MNS fibroin magnetic nanospheres*.

Its low intensity is due to the small proportion of oleate chains in the sample, besides that the oleate chains only have one unique alkene group. The multiple bands in the 2800-3000 cm^{-1} frequency range correspond to the ν(C-H) stretching vibrations of oleate and fibroin chains, assuming that the most intense bands are due to the presence of C-H bonds in the fibroin structure (from glycine and alanine aminoacids). However, the presence of these multiple ν(C-H) bands, together with the presence of the alkene group, demonstrates that the organic ligand of the magnetic nuclei is included in the polymeric matrix after the nanosphere formation.

The characteristic bonds of the fibroin multiple amide groups can be appreciated in the 1700-1200 cm^{-1} range. These bands represent the amide bond corresponding to the ν(NC=O) stretching vibrations, which are related to the secondary and tertiary protein structures. In this way, three different amide bands can be observed in the extended region of Figure 3.41, representing the different amide groups of the fibroin chemical structure (3

totally).[66] The presence and position of these groups is related to the β-sheet protein secondary conformation.[67] However, the presence of an intense double peak at 1407 and 1430 cm^{-1} is also indicative of the random-coil conformation existence in the fibroin structure.[66,68]

In summary, the fibroin and fibroin:nanosphere preparation experiments have achieved promising results, as negatively charged fibroin nanospheres have been obtained. Nevertheless, so as to control the formation of the mixed polymer nanospheres a deep study and optimization would be necessary.

3.3 Summary

The presence of the Ni^{2+} and Mn^{2+} cations in the final samples has been demonstrated by the ICP measurements. The TEM and DLS analysis have shown that the obtained diameters are in the 8-12 nm range for the main samples, being considerably higher for the growth samples. The prepared NPs showed spherical shape, excepting the $Mn_{0,13}Fe_{2,87}O_4$_A sample which present prismatic shape. Their monodomain and superparamagnetic nature has been confirmed by the crystal size estimation performed from the XRD analysis and by the lack of coercive field in the field dependant magnetization measurements. Both cations have a great influence in the magnetic properties, as lower M_s and K values have been obtained at increasing doping degrees. The EMR analysis only has demonstrated the high size dependence of the g_{eff} value. Finally, the $Ni_{0.31}Fe_{2.69}O_4$_A sample has shown the highest magnetic hyperthermia response due to its higher size, M_s and K values, and it has been selected to be functionalized.

3. Nanocompound characterization

The $Ni_{0.31}Fe_{2.69}O_4$_A nanoparticles have been successfully functionalized with the poly(maleic anhydride-alt-1-octadecene) (PMAO) polymer, obtaining the $Ni_{0.31}Fe_{2.69}O_4$_A_PMAO negatively charged single NPs. On the other hand, a mechanism to encapsulate the nanoparticles in the chitosan biopolymer has been developed. By this method, 90 nm diameter stable nanoparticle spherical aggregates with positive surface charge have been obtained (CS-MNS). Important differences in the structural and magnetic properties have been observed comparing with the single NPs. The proximity between the NPs has generated dipolar interaction, inducing a more ferromagnetic behaviour, detected by the temperature dependant magnetization and the EMR.

References

(1) Huang, J.-H.; Parab, H. J.; Liu, R.-S.; Lai, T.-C.; Hsiao, M.; Chen, C.-H.; Sheu, H.-S.; Chen, J.-M.; Tsai, D.-P.; Hwu, Y.-K. Investigation of the Growth Mechanism of Iron Oxide Nanoparticles via a Seed-Mediated Method and Its Cytotoxicity Studies. *J. Phys. Chem. C* **2008**, *112* (40), 15684–15690.

(2) Zhang, L.; He, R.; Gu, H. C. Oleic Acid Coating on the Monodisperse Magnetite Nanoparticles. *Appl. Surf. Sci.* **2006**, *253* (5), 2611–2617.

(3) Castellanos-Rubio, I.; Insausti, M.; Garaio, E.; Gil de Muro, I.; Plazaola, F.; Rojo, T.; Lezama, L. Fe_3O_4 Nanoparticles Prepared by the Seeded-Growth Route for Hyperthermia: Electron Magnetic Resonance as a Key Tool to Evaluate Size Distribution in Magnetic Nanoparticles. *Nanoscale* **2014**, *6*, 7542–7552.

(4) Oyarzún, S.; Tamion, A.; Tournus, F.; Dupuis, V.; Hillenkamp, M. Size Effects in the Magnetic Anisotropy of Embedded Cobalt Nanoparticles: From Shape to Surface. *Sci. Rep.* **2015**, *5* (August), 14749.

(5) Patterson, A. L. The Scherrer Formula for X-Ray Particle Size Determination. *Phys. Rev.* **1939**, *56* (10), 978–982.

(6) Schrefl, T., J. Fidler, H. K. Remanence and Coercivity in Isotropic Nanocrystalline Permanent Magnets. *Phys. Rev. B* **1974**, *49* (9), 6100–6113.

(7) Deepak, F. L.; Bañobre-López, M.; Carbó-Argibay, E.; Cerqueira, M. F.; Piñeiro-Redondo, Y.; Rivas, J.; Thompson, C. M.; Kamali, S.; Rodríguez-Abreu, C.; Kovnir, K.; et al. A Systematic Study of the Structural and Magnetic Properties of Mn-, Co-, and Ni-

Doped Colloidal Magnetite Nanoparticles. *J. Phys. Chem. C* **2015**, *119* (21), 11947–11957.

(8) Sabale, S.; Jadhav, V.; Khot, V.; Zhu, X.; Xin, M.; Chen, H. Superparamagnetic MFe_2O_4 (M = Ni, Co, Zn, Mn) Nanoparticles: Synthesis, Characterization, Induction Heating and Cell Viability Studies for Cancer Hyperthermia Applications. *J. Mater. Sci. Mater. Med.* **2015**, *26* (3).

(9) Lu, L. T.; Dung, N. T.; Tung, L. D.; Thanh, C. T.; Quy, O. K.; Chuc, N. V; Maenosono, S.; Thanh, N. T. K. Synthesis of Magnetic Cobalt Ferrite Nanoparticles with Controlled Morphology, Monodispersity and Composition: The Influence of Solvent, Surfactant, Reductant and Synthetic Conditions. *Nanoscale* **2015**, *7* (6), 19596–19610.

(10) Jeppson, P.; Sailer, R.; Jarabek, E.; Sandstrom, J.; Anderson, B.; Bremer, M.; Grier, D. G. Cobalt Ferrite Nanoparticles : Achieving the Superparamagnetic Limit by Chemical Reduction. *J. Appl. Phys.* **2006**, *100*, 114324.

(11) Cullity, B. *Introduction to Magnetic Materials*; Addison-Wesley: Massachussets, 1972.

(12) Sòshin Chikazumi. *Physics of Ferromagnetism*; Oxfod Science Publications: Oxford, U.K., 2009.

(13) Chen, R.; Christiansen, M. G.; Anikeeva, P. Maximizing Hysteretic Losses in Magnetic Ferrite Nanoparticles via Model-Driven Synthesis and Materials Optimization. *ACS Nano* **2013**, *7* (10), 8990–9000.

(14) E. C. Stoner, E. P. W. A Mechanism of Magnetic Hysteresis in Heterogeneous Alloys. *phylosophical Trans. R. Soc. A Math. Phys. Eng. Sci.* **1948**, *240* (826), 599.

(15) Salado, J.; Insausti, M.; Lezama, L.; Muro, I. G. De; Goikolea, E. Preparation and Characterization of Monodisperse Fe_3O_4 Nanoparticles : An Electron Magnetic Resonance Study. *Chem. Mater.* **2011**, *23*, 2879–2885.

(16) Blanco-Gutiérrez, V.; Virumbrales, M.; Saez-Puche, R.; Torralvo-Fernandez, M. J. Superparamagnetic Behaviour of MFe2O4 Nanoparticles and MFe_2O_4/SiO_2 Composites (M: Co, Ni). *J. Phys. Chem. C* **2013**, *117*, 20927–20935.

(17) Vargas, J. M.; Nunes, W. C.; Socolovsky, L. M.; Knobel, M.; Zanchet, D. Effect of Dipolar Interaction Observed in Iron-Based Nanoparticles. *Phys. Rev. B - Condens. Matter Mater. Phys.* **2005**, *72* (18), 2–7.

(18) Chiba, K.; Chikazumi, S. Magnetocrystalline Anisotropy of Magnetite. *J. Magn. Magn. Mater.* **1983**, *31–34* (PART 2), 813–814.

(19) Senn, M. S.; Wright, J. P.; Attfield, J. P. Charge Order and Three-Site Distortions in the Verwey Structure of Magnetite. *Nature* **2011**, *481* (7380), 173–176.

(20) Miyazaki, T.; Hanmin, J. *The Physics of Ferromagnetism*; Springer: Berlin, **2012**.

(21) Yu, Q.; Mottaghizadeh, A.; Wang, H.; Ulysse, C.; Zimmers, A.; Rebuttini, V.; Pinna, N.; Aubin, H. Verwey Transition in Single Magnetite Nanoparticles. *Phys. Rev. B - Condens. Matter Mater. Phys.* **2014**, *90* (7), 1–7.

(22) Salado, J.; Insausti, M.; Gil de Muro, I.; Lezama, L.; Rojo, T. Synthesis and Magnetic

Properties of Monodisperse Fe3O4 Nanoparticles with Controlled Sizes. *J. Non. Cryst. Solids* **2008**, *354* (47–51), 5207–5209.

(23) Salado, J.; Insausti, M.; Lezama, L.; Gil de Muro, I.; Moros, M.; Pelaz, B.; Grazu, V.; de la Fuente, J. M.; Rojo, T. Functionalized Fe_3O_4@Au Superparamagnetic Nanoparticles: In Vitro Bioactivity. *Nanotechnology* **2012**, *23* (31), 315102.

(24) Raikher, Y. L.; Stepanov, V. I. Ferromagnetic Resonance in a Suspension of Single-Domain Particles. *Phys. Rev. B* **1994**, *50* (9), 6250–6259.

(25) Bercoff, P. G.; Bertorello, H. R. Exchange Constants and Transfer Integrals of spine1 Ferrites. *J. Magn. Magn. Mater.* **1997**, *169*, 314–322.

(26) Hergt, R.; Dutz, S.; Müller, R.; Zeisberger, M. Magnetic Particle Hyperthermia: Nanoparticle Magnetism and Materials Development for Cancer Therapy. *J. Phys. Condens. Matter* **2006**, *18* (38), S2919–S2934.

(27) Brezovich, I., A. Low Frequency Hyperthermia: Capacitive and Ferromagnetic Thermoseed Methods. *Med. Phys. Monogr.* **1988**, *16*, 82–111.

(28) Garaio, E.; Sandre, O.; Collantes, J.-M.; Garcia, J. A.; Mornet, S.; Plazaola, F. Specific Absorption Rate Dependence on Temperature in Magnetic Field Hyperthermia Measured by Dynamic Hysteresis Losses (Ac Magnetometry). *Nanotechnology* **2015**, *26* (1), 015704-.

(29) Zhang, Q.; Castellanos-rubio, I.; Munshi, R.; Orue, I.; Pelaz, B.; Gries, K. I.; Parak, W. J.; Pino, P.; Pralle, A. Model Driven Optimization of Magnetic Anisotropy of Exchange-Coupled Core-Shell Ferrite Nanoparticles for Maximal Hysteretic Loss. *Chem. Mater.* **2015**, *27*, 7380–7387.

(30) Moros, M.; Pelaz, B.; López-Larrubia, P.; García-Martin, M. L.; Grazú, V.; de la Fuente, J. M. Engineering Biofunctional Magnetic Nanoparticles for Biotechnological Applications. *Nanoscale* **2010**, *2* (9), 1746–1755.

(31) Abbasi, A. Z.; Guti, L.; Mercato, L. L.; Herranz, F.; Chubykalo-fesenko, O.; Veintemillas-verdaguer, S.; Parak, W. J.; Hernando, A.; Presa, P. De. Magnetic Capsules for NMR Imaging : Effect of Magnetic Nanoparticles Spatial Distribution and Aggregation. *J. Phys. Chem. C* **2011**, No. 115, 6257–6264.

(32) Balasubramaniam, S.; Kayandan, S.; Lin, Y.-N.; Kelly, D. F.; House, M. J.; Woodward, R. C.; St Pierre, T. G.; Riffle, J. S.; Davis, R. M. Toward Design of Magnetic Nanoparticle Clusters Stabilized by Biocompatible Diblock Copolymers for T_2-Weighted MRI Contrast. *Langmuir* **2014**, *30* (6), 1580–1587.

(33) De Matteis, L.; Fernández-Pacheco, R.; Marquina, C.; Ibarra, M. R.; De La Fuente, J. M. Nanostructural Characterization of Biomagnetic Cobalt Ferrite-Alginate Nanospheres. *Part. Part. Syst. Charact.* **2013**, *30* (12), 1018–1023.

(34) Bigall, N. C.; Wilhelm, C.; Beoutis, M.; Garc, M.; Khan, A. A.; Giannini, C.; Sa, A.; Materia, M. E.; Garcia, M. A. Colloidal Ordered Assemblies in a Polymer Shell: A Novel Type of Magnetic Nanobeads for Theranostic Applications. **2013**, 7–14.

(35) Park, J. W.; Park, K. K. Acid-Base Equilibria and Related Properties of Chitosan. *Bulletion Korean Chem. Soc.* **1983**, *4* (2), 68–72.

(36) Qin, C. Q.; Du, Y. M.; Xiao, L. Effect of Hydrogen Peroxide Treatment on the Molecular Weight and Structure of Chitosan. *Polym. Degrad. Stab.* **2002**, *76* (2), 211–218.

(37) Lasheras, X.; Insausti, M.; Gil de Muro, I.; Garaio, E.; Plazaola, F.; Moros, M.; De Matteis, L.; M. de la Fuente, J.; Lezama, L. Chemical Synthesis and Magnetic Properties of Monodisperse Nickel Ferrite Nanoparticles for Biomedical Applications. *J. Phys. Chem. C* **2016**, *120*, 3492–3500.

(38) Noel, S.; Liberelle, B.; Robitaille, L.; Crescenzo, G. De; Hc, C. Quantification of Primary Amine Groups Available for Subsequent Biofunctionalization of Polymer Surfaces. *Bioconjug. Chem.* **2011**, *22*, 1690–1699.

(39) Rosen, H. A Modified Ninhydrin Colorimetric Analysis for Amino Acids. *Arch. Biochem. Biophys.* **1957**, *67* (1), 10–15.

(40) Gudoshnikov, S. A.; Liubimov, B. Y.; Popova, A. V.; Usov, N. A. The Influence of a Demagnetizing Field on Hysteresis Losses in a Dense Assembly of Superparamagnetic Nanoparticles. *J. Magn. Magn. Mater.* **2012**, *324* (22), 3690–3694.

(41) Stoner, E. C.; Wohlfarth, E. P. A Mechanism of Magnetic Hysteresis in Heterogeneous Alloys. *Philos. Trans. R. Soc. London A Math. Phys. Eng. Sci.* **1948**, *240* (826), 599–642.

(42) Corot, C.; Robert, P.; Idée, J.-M.; Port, M. Recent Advances in Iron Oxide Nanocrystal Technology for Medical Imaging. *Adv. Drug Deliv. Rev.* **2006**, *58* (14), 1471–1504.

(43) Mornet, S.; Vasseur, S.; Grasset, F.; Duguet, E. Magnetic Nanoparticle Design for Medical Diagnosis and Therapy. *J. Mater. Chem.* **2004**, *14* (14), 2161.

(44) Pierre, T. G. S.; Clark, P. R.; Chua-anusorn, W.; Fleming, A. J.; Jeffrey, G. P.; Olynyk, J. K.; Pootrakul, P.; Robins, E.; Lindeman, R.; St Pierre, T. G.; et al. Noninvasive Measurement and Imaging of Liver Iron Concentrations Using Proton Magnetic Resonance. *Blood* **2005**, *105* (2), 855–861.

(45) Bonnemain, B. Superparamagnetic Agents in Magnetic Resonance Imaging: Physicochemical Characteristics and Clinical Applications A Review. *J. Drug Target.* **1998**, *6* (3), 167–174.

(46) Search, H.; Journals, C.; Contact, A.; Iopscience, M.; Address, I. P. Applications of Magnetic Nanoparticles in Biomedicine. *J. Phys. D. Appl. Phys.* **2003**, *167*, R167–R181.

(47) Roch, A.; Gossuin, Y.; Muller, R. N.; Gillis, P. Superparamagnetic Colloid Suspensions: Water Magnetic Relaxation and Clustering. *J. Magn. Magn. Mater.* **2005**, *293* (1), 532–539.

(48) Bigall, N. C.; Curcio, A.; Leal, M. P.; Falqui, A.; Palumberi, D.; Di Corato, R.; Albanesi, E.; Cingolani, R.; Pellegrino, T. Magnetic Nanocarriers with Tunable pH Dependence for Controlled Loading and Release of Cationic and Anionic Payloads. *Adv. Mater.* **2011**, *23* (47), 5645–5650.

(49) Wen, Y.; Oh, J. K. Dual-Stimuli Reduction and Acidic pH-Responsive Bionanogels: Intracellular Delivery Nanocarriers with Enhanced Release. *RSC Adv.* **2014**, *4* (1), 229.

(50) Cabrera, J. C.; Van Cutsem, P. Preparation of Chitooligosaccharides with Degree of Polymerization Higher than 6 by Acid or Enzymatic Degradation of Chitosan. *Biochem.*

Eng. J. **2005**, *25* (2), 165–172.

(51) Stippler, E.; Kopp, S.; Dressman, J. Pharmacopeia Simulated Intestinal Fluid TS (without Pancreatin) and Phosphate Standard Buffer pH 6.8, TS of the International Pharmacopoeia with Respect. *Dissolution Technol.* **2004**, No. May, 6–10.

(52) Zhang, H.; Neau, S. H. In Vitro Degradation of Chitosan by a Commercial Enzyme Preparation: Effect of Molecular Weight and Degree of Deacetylation. *Biomaterials* **2001**, *22* (12), 1653–1658.

(53) Dowling, M. B.; Bagal, A. S.; Raghavan, S. R. Self-Destructing "mothership" capsules for Timed Release of Encapsulated Contents. *Langmuir* **2013**, *29* (25), 7993–7998.

(54) Neto, C. G. T.; Giacometti, J. a.; Job, a. E.; Ferreira, F. C.; Fonseca, J. L. C.; Pereira, M. R. Thermal Analysis of Chitosan Based Networks. *Carbohydr. Polym.* **2005**, *62* (2), 97–103.

(55) Zou, H.; Yuan, W. Temperature- and Redox-Responsive Magnetic Complex Micelles for Controlled Drug Release. *J. Mater. Chem. B* **2014**, *3* (2), 260–269.

(56) Marques, M. R. C.; Loebenberg, R.; Almukainzi, M. Simulated Biological Fluids with Possible Application in Dissolution Testing. *Dissolution Technol.* **2011**, *18* (3), 15–28.

(57) Schales, O. A Simple Method for the Determination of Glucose in Bood. *Arch. Biochem.* **1945**, *8* (2), 285–292.

(58) Imoto, T.; Yagashita, K. Activity Measurement of Lysozyme. *Agr. Biol. Chem.* **1971**, *35* (7), 1154–1156.

(59) Zamani, A.; Jeihanipour, A.; Edebo, L.; Niklasson, C.; Taherzadeh, M. J. Determination of Glucosamine and N-Acetyl Glucosamine in Fungal Cell Walls. *J. Agric. Food Chem.* **2008**, *56* (18), 8314–8318.

(60) Thadathil, N.; Velappan, S. P. Recent Developments in Chitosanase Research and Its Biotechnological Applications: A Review. *Food Chem.* **2014**, *150*, 392–399.

(61) Henrissat, B.; Vegetales, M.; Grenoble, F. A Classification of Glycosyl Hydrolases Based Sequence Similarities Amino Acid. *Biochem. J.* **1991**, *280* ((Pt 2)), 309–316.

(62) Henrissat, B.; Bairoch, a. New Families in the Classification of Glycosyl Hydrolases Based on Amino Acid Sequence Similarities. *Biochem. J.* **1993**, *293 (Pt 3* (January), 781–788.

(63) Tanabe, T.; Morinaga, K.; Fukamizo, T.; Mitsutomi, M. Novel Chitosanase from Streptomyces Griseus HUT 6037 with Transglycosylation Activity. *Biosci. Biotechnol. Biochem.* **2003**, *67* (2), 354–364.

(64) Jarle Horn, S.; Eijsink, V. G. H. A Reliable Reducing End Assay for Chito-Oligosaccharides. *Carbohydr. Polym.* **2004**, *56* (1), 35–39.

(65) Ghanadzadeh, A.; Zanjanchi, M. A. Self-Association of Rhodamine Dyes in Different Host Materials. *Spectrochim. Acta Part A Mol. Biomol. Spectrosc.* **2001**, *57* (9), 1865–1871.

(66) Um, I. C.; Kweon, H.; Park, Y. H.; Hudson, S. Structural Characteristics and Properties of the Regenerated Silk Fibroin Prepared from Formic Acid. *Int. J. Biol. Macromol.* **2001**, *29* (2), 91–97.

(67) Chen, X. I. N.; Li, W.; Yu, T. Conformation Transition of Silk Fibroin Induced by Blending Chitosan. *J. Polym. Sci. B* **1997**, *35*, 2293–2296.

(68) Shao, J.; Zheng, J.; Liu, J.; Carr, C. M. Fourier Transform Raman and Fourier Transform Infrared Spectroscopy Studies of Silk Fibroin. *J. Appl. Polym. Sci.* **2005**, *96* (6), 1999–2004.

4. IN VITRO AND IN VIVO EXPERIMENTS

The final objective of this thesis is to develop nanocompounds which could be helpful in the treatment of some significant human diseases. The prepared nanosystems are specially focused on cancer treatments by drug delivery and controlled release or by direct application of magnetic hyperthermia in tumours.[1] Thus, the heating ability of the nanocompounds, their theoretical lack of toxicity and the absence of remanence magnetization provide interesting ways to achieve these goals. Moreover, the suitability of this kind of nanocompounds in the diagnosis area has also been previously proven in the literature.[2] In fact, magnetite nanoparticles have currently been using as contrast agents in magnetic resonance imaging.[3,2]

However, there are many previous steps to be overtaken in order to develop new therapeutical applications of novel nanomedicines. Firstly, it is important to estimate the safety of the nanocompounds using simple cytotoxicity studies in basic cell culture assays. Comparing the toxic effect of such nanomaterials with control cultures will allow us to exclude those preparation with high toxicity and also to establish the tolerability of the cells to them.

In order to increase the complexity of model systems for toxicity evaluation before going to complex animals, more complex cell co-cultures need to be optimized. These co-cultures mimic more accurately the natural tissues. However, there are not perfect model systems, and animal

experimentation is required in order to study the biodistribution and fate of such nanomaterials.

Considering all the synthesized nanoparticles and nanospheres, the $Ni_{0.31}Fe_{2.69}O_4$_A_PMAO nanoparticles and the CS-MNS magnetic nanospheres were chosen to be tested as candidates for biomedical applications due to these reasons:

$Ni_{0.31}Fe_{2.69}O_4$_A_PMAO is the best candidate for magnetic hyperthermia treatments due to its high specific absorption rate (SAR). on the other hand, CS-MNS could be used as drug delivery and control release platforms due to their high loading efficiency.

It is worthy to mention that both systems have opposite superficial charge. Ni ferrite nanoparticles present strong negative surface charge, whereas the chitosan nanospheres are positively charged. These changes on superficial charge could also affect their interactions with living systems.

4.1 Stability test of $Ni_{0.31}Fe_{2.69}O_4$_A_PMAO and CS-MNS in cell culture media

It is important to take into account that the physico-chemical properties of nanocompounds could be affected by physiological media such as cell culture media in *in vitro* experiments. The high ionic strength, changes in pH and the presence of a huge variety of proteins in such solutions can cause nanoparticles aggregation.[4] Hence, their stability in these conditions needs to be previously tested. Thus, $Ni_{0.31}Fe_{2.69}O_4$_A_PMAO nanoparticles and CS-MNS nanospheres stability were evaluated by means of hydrodynamic diameter and Z potential measurements using non-supplemented and

supplemented (10% foetal bovine serum (FBS), penicillin (100 U/mL), streptomycin (100 μg/mL) and glutamine (2 mM)) Dubelcco's Modified Eagle's Medium (DMEM) cell culture media.

The hydrodynamic diameter of this kind of samples cannot be determined by conventional Dynamic Light Scattering (DLS) measurements, as the high protein concentration of the cell culture interferes strongly with the light dispersion. There are other techniques that are commonly used to evaluate the NP physico-chemical properties and the dispersion level in such conditions.[4] The depolarized DLS (DDLS) extends the DLS technique to particles with optical or shape anisotropy, being also useful to eliminate artefacts that appear in polydisperse samples.[5] By this technique, the hydrodynamic diameter of the NPs suspension in DMEM media was obtained by means of a 3D LS Spectrometer (LS Instruments AG, Switzerland. 90°, 6 runs and 3 min/run).

Furthermore, the Zeta potential value was measured in non-supplemented and supplemented DMEM at pH 4 and pH 7 in order to explore stability behaviour of NPs at different physiological pHs. The Zeta potential was measured in a BI 90 Plus Particle Size Analyser (Brookhaven Instruments Corporation) using the Zeta PALS software in 0.01 mg Fe/mL concentration. Control samples (nanocompounds dispersed in water media) were dispersed in a 10 KCl mM solution.

The obtained hydrodynamic diameters and Zeta potential values for the $Ni_{0.31}Fe_{2.69}O_4$_A_PMAO and CS-MNS samples dispersed in non-supplemented and supplemented DMEM are resumed in Table 4.1, and compared with the values in water.

Table 4.1. *Average values of hydrodynamic diameter and Zeta potentials (in pH 4 and pH 7) of $Ni_{0.31}Fe_{2.69}O_4$_A_PMAO and CS-MNS samples in miliQ water, non-supplemented and supplemented DMEM.*

	$Ni_{0.31}Fe_{2.69}O_4$_A_PMAO			CS-MNS		
	H_2O	DMEM	Supl. DMEM	H_2O	DMEM	Supl. DMEM
Hydrodynamic diameter (nm)	20.6 ±8.4	524.3 ±234.1	74.7 ±49.3	161.3 ±79.5	160.0 ±46.3	109.7 ±50.5
Zeta pot. (mV) pH 4	-30.2	-34.4	0.2	46.1	32.8	0.9
Zeta pot. (mV) pH 7	-23.7	-23.4	-9.9	-7.3	-2.7	-11.5

The $Ni_{0.31}Fe_{2.69}O_4$_PMAO magnetic nanoparticles are aggregated in non-supplemented culture media, as it can be observed by changes in the hydrodynamic diameter (from 21 nm in H_2O to 524 nm in non-supplemented DMEM). The obtained Zeta potential (ζ) value at pH 7 was in this case the same as in water media (-23 mV). Therefore, the strong aggregation could be caused by the effect of the high DMEM ionic strength (calcium chloride, ferric nitrate, potassium chloride or sodium phosphate). The great impact of phosphate salts in negatively charged nanoparticle colloidal stability has been documented in literature.[6] The high ionic strength induces the collapse of the colloidal system by compression of the repulsive electrostatic NP double layer.[7] Surprisingly, the same Ni ferrite NPs dispersed in supplemented DMEM show only a small aggregation effect. The measured hydrodynamic diameter in this case was slightly higher (75 nm) than the diameter in water media, but nowhere near as high as the observed in non-supplemented DMEM. The aggregation effect in this case is correlated with a decrease in the Zeta potential value at pH 7 (-9 mV). However, according to the results obtained in not supplemented DMEM, the aggregation effect was expected to be much higher. The high protein concentration of the added

bovine serum would have induced the NP protein adsorption, which would cover the NP surface and also avoids the aggregation by steric repulsion. This combination of electrostatic and steric repulsion between NPs, induced by the adhered proteins, could lead to a steric stabilization of nanoparticles in the high ionic strength solution.[8,9]

On the other hand, the CS-MNS nanospheres show quite similar main hydrodynamic diameter and ζ values in DMEM (both non-supplemented and supplemented at pH 7) and in H_2O. In this case, the amino groups of the nanosphere surface were not affected by the high ionic strength of the DMEM media, neither by the high protein concentration of the foetal bovine serum of the supplemented DMEM. Therefore, both hydrodynamic diameter and ζ values at pH 7 are in good agreement with the obtained values in water.

The Zeta potential values of both samples at low pH (pH 4) are similar to the values in water, in the case of non-supplemented DMEM. The ionic strength increase seems to have less impact on the NPs at acid media. In contrast, the ζ values for both samples decrease drastically in supplemented DMEM indicating colloidal instability. This instability should be taken into account when inserting these NPs in acid biological media. Thus, the Ni ferrite nanoparticles and CS nanospheres seem to have not suffered great changes in supplemented DMEM at pH7, as only a small aggregation of the $Ni_{0.31}Fe_{2.69}O_4$_A_PMAO sample has been noticed. Besides, such NPs are suitable for further *in vitro* studies due to their stability in cell culture media.

4.2 Nanocompound cytotoxicity in Vero cells

Usually, the first biocompatibility test to be carried out for a new developed material is a cytotoxicity assay in a 2D cell culture. This kind of assay allows to discard highly toxic compounds or to determine the tolerated dose of nanomaterials. It is important to select well the cell line to be tested in order to be similar to the target tissue. One of the main limitation of these assays is the short time periods to be studied, depending on the cell line, it can go from one to three days in average. Other important issue to take into account is the number of replicates to be carried out in order to obtain statistically significant results.

In order to test the cytotoxicity of new compounds in simple cell monocultures, different assays can be used.[10] Most of them are based on metabolic changes in the cell function after apoptosis, or on the release of some intracellular compounds due to degradation of the cell membrane.[11,12]

One of the most widely used test is based on the presence of the NAD(P)H oxidoreductase enzyme.[13] This colorimetric assay uses a tetrazolium salt (MTT, (3-(4,5-dimethylthiazol-2-yl)-2,5-diphenyl tetrazolium bromide) (Figure 4.1) which reacts with the mitochondrial NAD(P)H oxidoreductase enzyme and producing water insoluble dark blue formazan crystals ($C_{14}H_{15}ClN_4$). Such crystals can be dissolved in dimethyl sulfoxide (DMSO). The absorbance of the resulting crystal solution (in DMSO) is directly proportional to the amount of living cells in the analysed cell culture.

Thus, the cell viability, after the Ni ferrite nanoparticles and CS nanosphere exposures, was tested in Vero cells (African green monkey kidney epithelial cells) and analysed by means of 3-[4,5-dimethylthiazolyl-2]-2,5-diphenyltetrazolium bromide (MTT) colorimetric assay.[11]

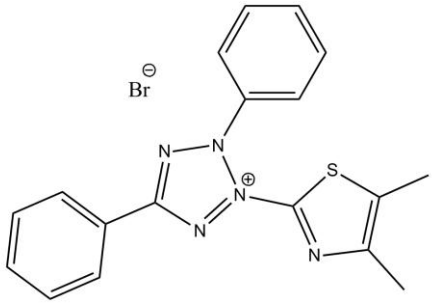

MTT
(3-(45-dimethylthiazol-2-yl)-2,5-diphenyl tetrazolium bromide

Figure 4.1. *Chemical structure of MTT dye salt used in cytotoxicity assays.*

The Vero cells were purchased from the American Type Culture Collection, number CCL-81 and grown at 37 °C in a 5% CO_2 atmosphere in DMEM supplemented with 10% foetal bovine serum (FBS), penicillin (100 U/mL), streptomycin (100 µg/mL) and glutamine (2 mM) (following the standard procedure for cell growth used in literature).[14] The supplementation products were added to the cell media in order to improve the cell growth and to prevent possible bacterial contamination.

A total of 5 000 cells were seeded using a standard 96-well plate (TPP). After 24 h of incubation in a humidified atmosphere containing 5 % CO_2, the cell medium was replaced with 200 µL of new medium containing 6 different concentrations (0.01, 0.02, 0.05, 0.1, 0.25 and 0.5 mg/mL) of the different nanocompounds ($Ni_{0.31}Fe_{2.69}O_4$_A_PMAO and CS-MNS). A negative control (cell media without MNPs) and positive control (cells treated with a Triton X100 0.2% solution in PBS) were also evaluated. Each concentration was repeated 6 times. After 24 h, the medium was replaced with fresh medium containing the MTT solution to a final concentration of 0.5 mg/mL in DMEM. After 2 h of incubation at 37 °C and 5 % CO_2, the medium was removed and the formed water-insoluble formazan crystals were dissolved in 200 µL of

DMSO. The absorbance was read on a microplate reader (Thermo Scientific Multiskan GO UV/Vis Microplate) at 570 nm. The relative cell viability (%) related to negative control wells containing cells without nanoparticles was calculated by $[[A]_{test}-[A]_{control}/[A]_{control}]$ x 100. The obtained results are illustrated in Figure 4.2.

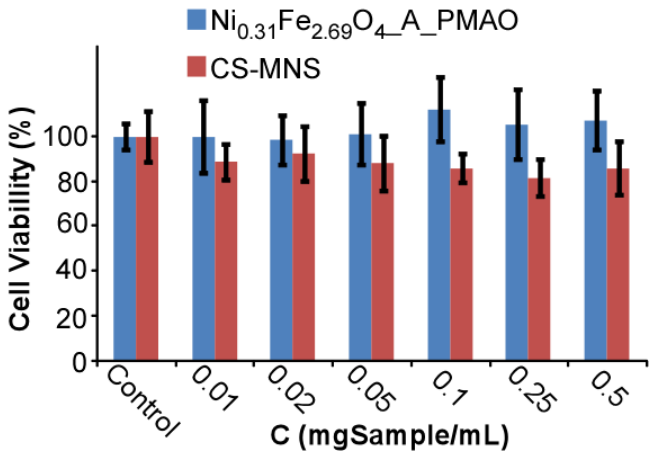

Figure 4.2. *MTT Cytotoxicity experiments of $Ni_{0.31}Fe_{2.69}O_4$_A_PMAO and CS-MNS samples, exposed to Vero cells for 24 hours in the 0.01-0.5 mg/mL concentration range.*

Both samples have neglectable effect on the cell viability at the used concentrations and exposed times.

4.3 Nanocompound exposures to blood vessel model co-culture

In order to increase the complexity of the *in vitro* model system, we have tested a co-culture of cells simulating blood vessel tissue.

4. *In vitro* and *in vivo* experiments

Basically, the human blood vessels are composed by an endothelial cell thin layer in the inside part (in direct contact with bloodstream) and macrophages in the external part of the vessel. The endothelial cells form a single cell layer that aligns all blood vessels and regulates exchanges between the bloodstream and the surrounding tissues. This layer also acts as a barrier between the bloodstream and the internal tissues. Signals from endothelial cells organize the growth and development of connective tissue cells that form the surrounding layers of the blood vessel wall.[15] There is an elastic fibber called internal elastic lamina, which separates the endothelial cell layer form the rest of the tissues. Macrophages also play an important role in the blood vessel function. Macrophages remove the debris through the process of phagocytosis, which prevents secondary necrosis and inflammation by removing apoptotic bodies before their decomposition.[16,17]

Using this model system, not only the cytotoxicity of the nanocompounds in the cell culture was determined, many other possible effects such as changes in the cell morphology, permeability of the cell layer, oxidative stress and inflammatory response were also analysed.

Thus, to predict the effects of our nanocompounds in the blood vessels, the $Ni_{0.31}Fe_{2.69}O_4$_A_PMAO nanoparticles and the CS-MNS nanospheres were exposed to a simulated blood vessel model co-culture. This co-culture is composed by endothelial cells and macrophages (Figure 4.3). In order to compare the effects of our nanocompounds in the co-culture, the experiment was also performed in endothelial cell monocultures, under the same conditions. This comparison could provide useful information about the role of the macrophages in the system.

As in previous cytotoxicity experiments, the $Ni_{0.31}Fe_{2.69}O_4$_A_PMAO nanoparticles and the CS-MNS magnetic nanospheres have been tested in

the blood vessel co-culture model in different concentrations (5, 10 and 20 µg/mL), according to literature.[14,18]

4.3.1 Endothelial cell monoculture and endothelial cell-macrophage co-culture preparation

The co-culture was formed by EAhy296 human endothelial cells and human monocyte derived macrophages. The EAhy296 human endothelial cells were obtained from the American Type Culture Collection, and were grown in DMEM supplemented with 10 % foetal bovine serum, 1 % L-glutamine and 1 % penicillin/streptomicyn. The Monocytes for macrophages were isolated from healthy donors (blood donation service, Bern, Switzerland),[19] and cultured in phenol red free RPMI medium supplemented with 10 % foetal bovine serum, 1 % L-glutamine and 1 % penicillin/streptomicyn.

The co-cultures and monocultures were prepared using special inserts with 3 µm porous PET layers (BD Falcon cell culture inserts with a surface area of 4.2 cm^2 and transparent PET membranes with 3 µm pores) to simulate the intermediate internal elastic lamina. Thus, the endothelial cells (10^6 cells) were seeded on one part of this membrane in a monolayer to be in direct contact with the nanocompounds. After 48 h of incubation (37 °C, 5 % CO_2), the macrophages (50 000 cells) were seeded on the flipside of the membrane. Thus, the inserts were located in 6 well plates, with the macrophages on the upper part. The scheme of the prepared co-culture is shown in Figure 4.3. The structure of the endothelial cell monoculture system is the same, without the macrophages.

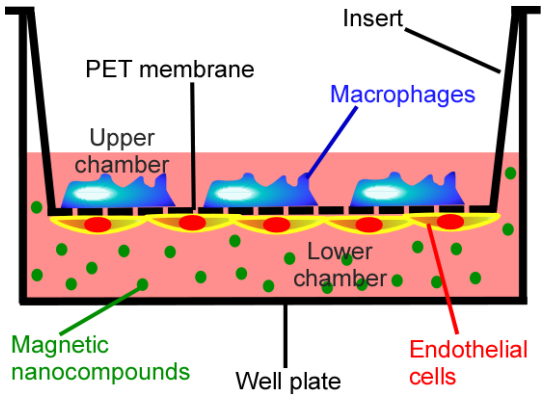

Figure 4.3. *Illustration of the human blood vessel in an "in vitro" model.*

In a typical blood vessel model co-culture and an endothelial cell monoculture preparation, one million of endothelial cells were seeded on the lower side (in direct contact with the nanocompounds) of the inserts and placed in 6 well plates. In the case of the co-cultures, after 48 hours of incubation at 37 °C and 5 % CO_2 in DMEM, 50 000 macrophages were seeded on the upper chamber of the insert and incubated for 24 hours at 37 °C and 5 % CO_2 in 6 well plates (in a 70:30 DMEM:RPMI compound medium, 3 mL in the lower chamber and 2 mL in the upper chamber of the insert).

4.3.2 Nickel ferrite nanoparticle and chitosan magnetic nanosphere exposures

After preparing the blood vessel model co-cultures, the colloidal dispersions of $Ni_{0.31}Fe_{2.69}O_4$_A_PMAO nanoparticles and CS-MNS nanospheres were added in DMEM at three different concentrations (5, 10 and 20 µgFe/mL). These concentrations were chosen according to previous studies.[18,14] The specific amounts of the exposed nanoparticles and nanospheres are represented in Table 4.2. A total of 3 mL of nanocompound DMEM dispersions were added to the lower chamber of the insert, the upper

chamber was filled with 2 mL of fresh DMEM. The cultures were left exposed to the nanocompounds for 24 hours at 37 °C and 5% CO_2. All experiments were carried out three times for a statistical validation. After that, different analysis were performed to determine the effects of the nanocompounds in the mono- and co-cultures. The process is schematically described in Figure 4.4.

Table 4.2. *Amounts of $Ni_{0.31}Fe_{2.69}O_4$_A_PMAO nanoparticles and CS-MNS nanospheres exposed to mono- and co-cultures in each concentration*.

Sample	[Fe] (µg/mL)	Total amount (nanoparticles, nanospheres)
$Ni_{0.31}Fe_{2.69}O_4$_PMAO	5	$2739 \cdot 10^5$ MNP
	10	$5478 \cdot 10^5$ MNP
	20	$1096 \cdot 10^6$ MNP
CS-MNS	5	$2134 \cdot 10^5$ MNS
	10	$4269 \cdot 10^5$ MNS
	20	$8538 \cdot 10^5$ MNS

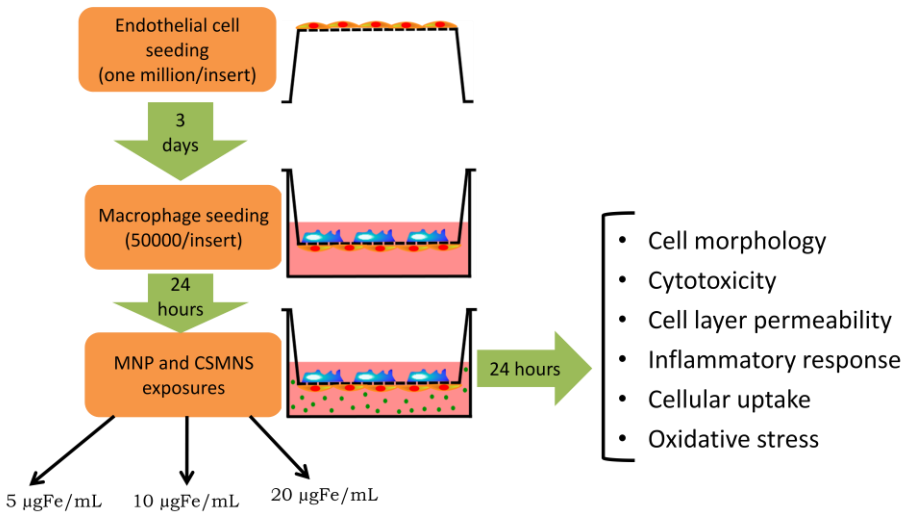

Figure 4.4. *Schematic illustration of the different steps carried out for $Ni_{0.31}Fe_{2.69}O_4$_A_PMAO and CS-MNS exposure experiments*.

4.3.3. Cell morphology analysis

The interaction between the magnetic nanocompounds and the cell cultures could modify the cell morphology or cause several damages in the cell membrane, nucleus or cytoskeleton. The interaction should be stronger with the endothelial cell layer, since it is in direct contact with the nanocompound suspension. These hypothetical changes in cell morphology after exposures were checked by visualizing the co-cultures and monocultures in an inverted laser scanning confocal microscope (LSM) 710 (Axio Observer.Z1, Carl Zeiss). For this purpose, the cells were fixed on the PET membrane and stained with DAPI and phalloidin to identify the nucleus and actin fibres respectively.

After the exposures, the mono- and co-cultures were washed with phosphate buffered saline (PBS) to remove the cell media and the nanocompounds. Then, the cells were fixed for 15 min in 3 % paraformaldehyde (PFA) in PBS solution. After that, the fixed cells were treated with 0.1 M glycine in PBS for another 15 min. 0.3 % Triton X-100 solution in PBS was added for 15 minutes to permeabilize the cell layers. Then, the cell nuclei were stained with 4',6-diamidino-2-phenylindole (DAPI) fluorophore and the cytoskeletons with phalloidin rhodamine (phRh). This stain was performed by exposing the cell membranes to a 1 % bovine serum albumin (BSA) 0.1 % triton X-100 solution in PBS with 1:100 proportion of phRh and 1:50 proportion (in volume) of DAPI, for 60 min in darkness and humidity. This procedure was performed by following the fixation-staining procedures previously reported in the literature.[20]

The obtained micrographs for mono and co-cultures are illustrated in Figure 4.5. The cell nuclei are marked in blue colour (stained by DAPI dye) and the cell cytoskeleton in red (stained by rhodamine-phalloidin dye).

As it can be observed in Figure 4.5A, comparing all exposed cell co-cultures with the negative control, the absence of any morphological changes or cell layer damages can be confirmed. Similar behaviour can be observed in Figure 4.5B for the exposed endothelial cell monocultures. The micrographs show a dense endothelial cell monolayer with the typical endothelial cell elongated morphology. The cytoskeleton density and nuclei definition do not present any appreciable changes. Apparently, the nanocompound interaction with the cytoskeleton has not induced any damages by protein denaturalization or cell layer decomposition.

In contrast, lower cytoskeleton density and less cells can be observed in the positive control (cell culture treated with triton X-100 0.2% solution in PBS). The triton surfactant is known to damage the cell layer by creating holes in the membrane, consequently, a great cytoskeleton deterioration is caused by its interaction in both monoculture and blood vessel model co-culture.[21] These damages also induce cell necrosis, as it can be appreciated in the low cell density present in the positive control micrographs.

Thus, by comparing the positive control damaged cells with the apparently intact exposed cell cultures, the interaction between $Ni_{0.31}Fe_{2.69}O_4$_A_PMAO and CS-MNS with blood vessel model cell co-cultures apparently cause no macroscopic damages in the cell integrity, in 24 hour exposure time and in the tested concentration range.

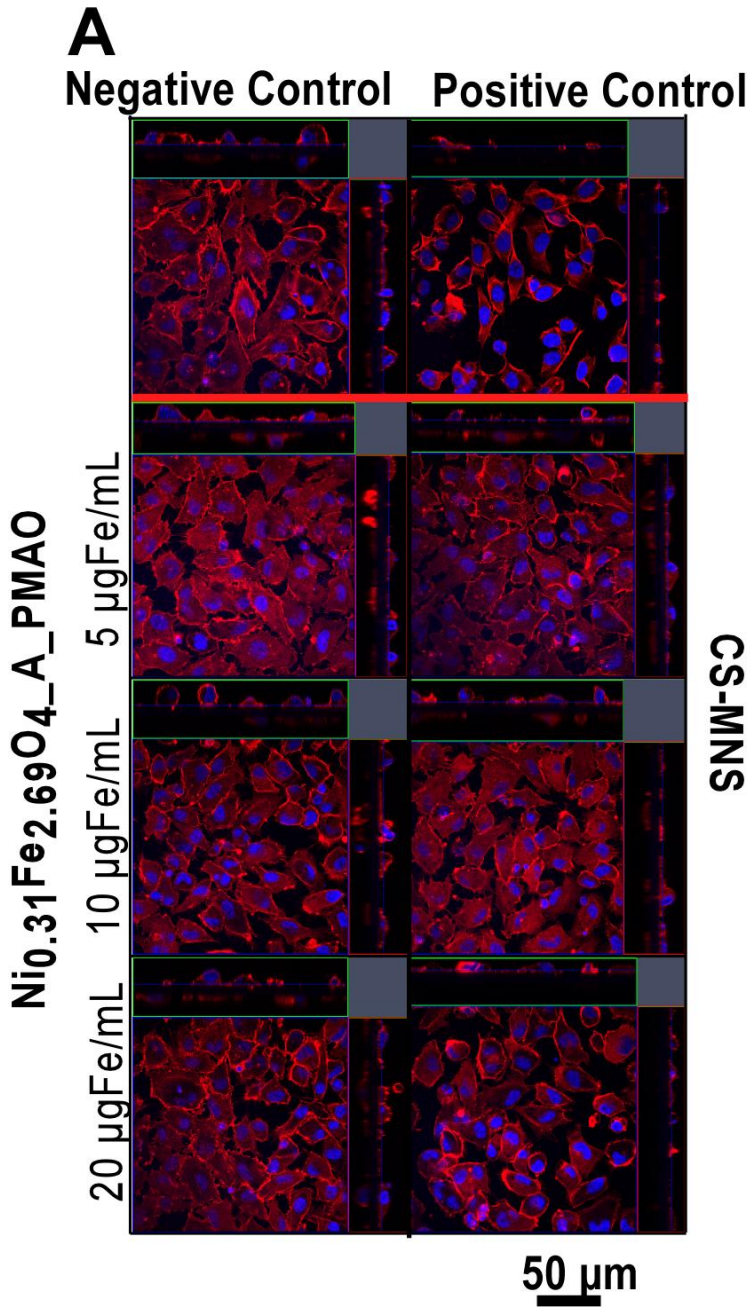
A
Negative Control
Positive Control
Ni0.31Fe2.69O4_A_PMAO
5 µgFe/mL
10 µgFe/mL
20 µgFe/mL
SNW-SC
50 µm

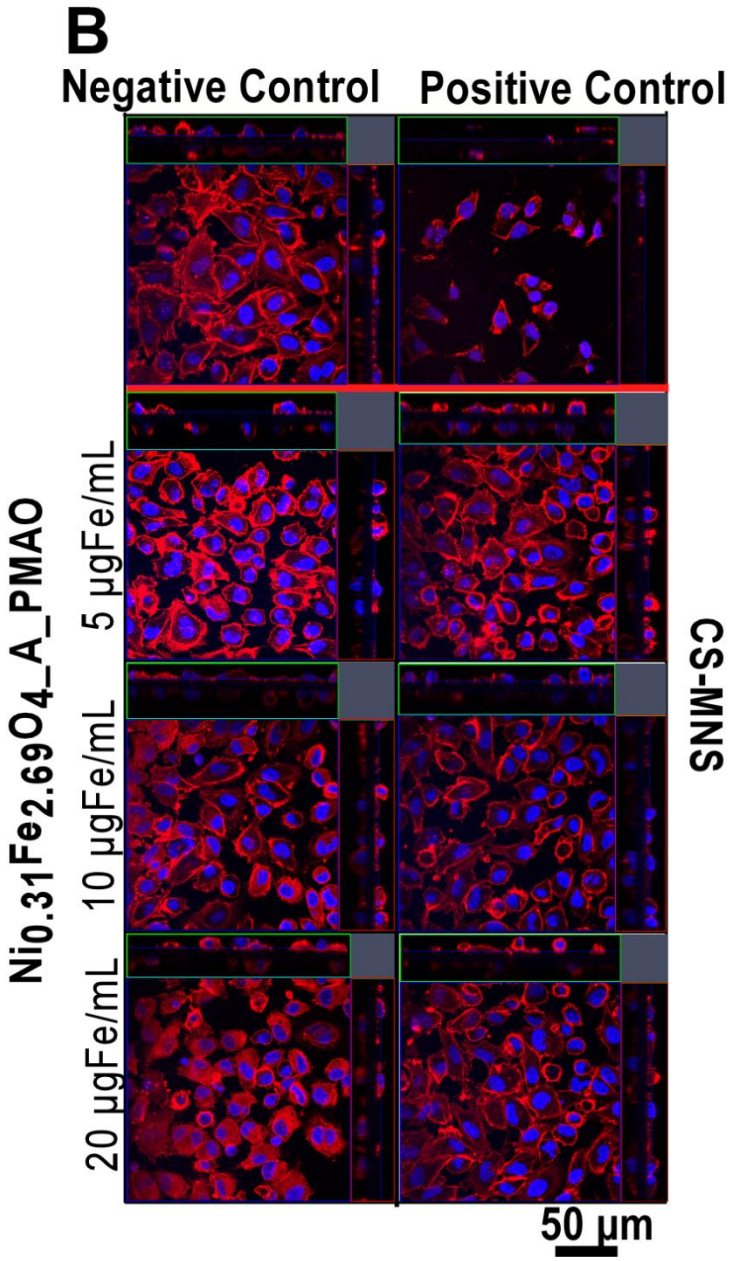

Figure 4.5. *LSM images of $Ni_{0.31}Fe_{2.69}O_4$_A_PMAO and CS-MNS exposed co-cultures (A) and monocultures (B), compared with a non-exposed negative control and a positive control treated with a 0.2% triton PBS solution.*

4.3.4. Cellular uptake of nanocompounds

$Ni_{0.31}Fe_{2.69}O_4$_A_PMAO nanoparticle and CS-MNS nanosphere internalization was quantified by ICP measurements of the Fe and Ni metals present in the cell cultures.[22,23] It was expected a different cellular uptake for both samples taking into account the different size and superficial charge of both samples.

After the incubation with both nanocompounds, the samples were washed with PBS five times in order to remove all remaining nanocompounds. The cell were then pre-digested with 300 µL of 2:1 HNO_3:H_2O_2 v/v solution in a six well plate for 3 h. The plates were sonicated for 15 min at 50 °C to avoid the effervescence of the gases in the next digestion step. Then, 400 µL of HCl were added to the wells and the cell cultures were digested overnight at room temperature. The solutions were extracted from the 6 well plates and diluted to 15 mL.

The Fe and Ni concentrations were measured by means of an ICP-MS (7700x, Agilent Technologies) spectrometer using a MicroMist micro-uptake glass concentric nebulizer (Glass Expansion). The results obtained are represented in Figure 4.6.

As it can be observed in Figure 4.6, the same metal amount increase tendency inside the cell co-cultures (also in monocultures) is measured when higher concentrations of nanocompounds have been exposed. This fact indicates that the cells are not still saturated by nanocompounds. This increase tendency also verifies that the presence of Fe and Ni is due to the nanocompound exposure.

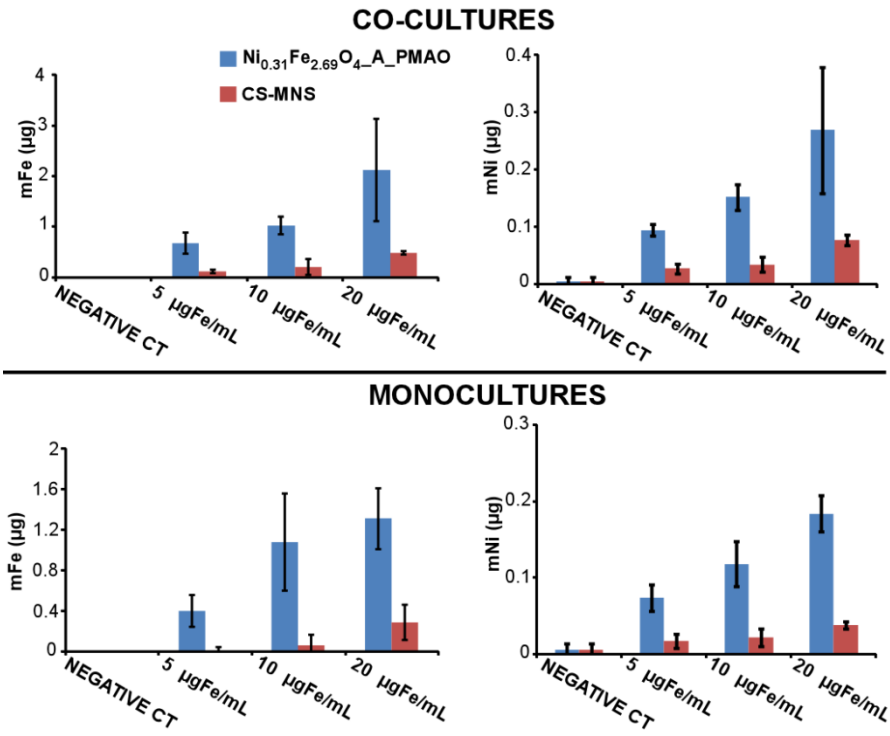

Figure 4.6. *Iron and nickel content co-cultures (up) and monocultures (down) after have been exposed to different concentrations of $Ni_{0.31}Fe_{2.69}O_4$_A_PMAO and CS-MNS nanocompounds, compared with negative control.*

It must be considered that some cells could present traces of iron ions, although no such high amounts. Furthermore, the Fe and Ni presence in negative controls is negligible for co-cultures and monocultures. The amounts of the internalized nanocompounds have been calculated from the iron content of cultures, taking into account the weight of each nanocompound calculated in chapter 3.2 ($1.59 \cdot 10^{-17}$ g/$Ni_{0.31}Fe_{2.69}O_4$_A_PMAO and $1.99 \cdot 10^{-15}$ g/CS-MNS, (g/NP)) and the specific weight of Fe in each material. The internalized particle amounts are presented in Table 4.3 (for co-cultures) and Table 4.4 (for monocultures).

In good agreement with their lower size, the amount of the internalized $Ni_{0.31}Fe_{2.69}O_4$_A_PMAO nanoparticles in the blood vessel model co-cultures is much higher than the internalized CS-MNS, as it can be observed in Table 4.3. In this case, the smaller size of the Ni ferrite magnetic nanoparticles increases its internalization into the cells, since the permeability of the cell membrane is much higher for particles with diameters in the 10-50 nm range.[24] Nonetheless, the negatively charged Ni ferrite nanoparticle surface should theoretically induce less uptake than the positively charged equivalents. The electrostatic attractive interactions with the negatively charged cell membrane surface should increase the kinetic of the positively charged NP absorption.[24] In spite of that, some studies have revealed that the cell internalization of negatively charged NP is possible by means of a clustering process of NPs on cationic sites of the plasma membrane, and final internalization by an endocytosis mechanism.[25]

Table 4.3. *Concentrations of exposed nanocompounds in each blood vessel model co-culture exposure experiment and calculated rates of uptaken and exposed nanocompound and internalized nanocompound per cell.*

SAMPLE	Exposed NP (µgFe)	Uptaken NP (µgFe)	Uptaken NP/exposed NP (%)	Uptaken NP/cell
$Ni_{0.31}Fe_{2.69}O_4$_A_PMAO	15	0.68	4.55	$6.34 \cdot 10^4$
	30	1.03	3.42	$9.52 \cdot 10^4$
	60	2.12	3.53	$1.97 \cdot 10^5$
CS-MNS	15	0.13	0.84	$1.29 \cdot 10^2$
	30	0.22	0.72	$2.23 \cdot 10^2$
	60	0.49	0.81	$4.99 \cdot 10^2$

The higher cellular uptake of $Ni_{0.31}Fe_{2.69}O_4$_PMAO NPs demonstrates the higher influence of the NP size comparing with the surface charge in the

cellular internalization. In fact, the amount of the internalized nanoparticles is 500 times higher than the internalized CS nanospheres in the lower exposed concentration, while in the higher exposed concentration the uptake amount is 400 times higher.

Table 4.4. *Concentrations of exposed nanocompounds in endothelial cell monoculture exposure experiment and calculated rates of uptaken and exposed nanocompound and internalized nanocompound per cell.*

SAMPLE	[exposed NP] (µgFe/mL)	Uptaken mFe (µg)	Uptaken NP/exposed NP (%)	Uptaken NP/cell
$Ni_{0.31}Fe_{2.69}O_4$_A_PMAO	5	0.40	2.66	$3.70 \cdot 10^4$
	10	1.08	3.59	$1.00 \cdot 10^5$
	20	1.31	2.18	$1.21 \cdot 10^5$
CS-MNS	5	0	0	0
	10	0.06	0.21	66.5
	20	0.29	0.48	$2.94 \cdot 10^2$

Finally, as it can be observed in Table 4.4, the amount of the internalized nanocompounds is lower for monocultures than for co-cultures, specially for CS-MNS nanospheres. This comparison has even more relevance in this case, as the obtained associated nanocompound differences verifies the well formation of the blood vessel model. Hence, this big difference proves the great influence of macrophages in the control of strange compounds in the bloodstream, as most of our nanocompounds have been phagocyted by the macrophages. This explains the obtained differences in the uptake level between the monocultures and co-cultures.

4.3.5. LDH cytotoxicity assays

In order to determine the cytotoxicity of nanocompounds in mono- and co-cultures, the lactate dehydrogenase (LDH) intracellular enzyme level assay was used. Higher concentrations of LDH in supernatants is associated to damages in the cell membranes and to cell necrosis.[26,27] The cell medium from the upper and lower chambers after exposures was analysed using a LDH cytotoxicity detection kit (Roche Applied Science) following the protocol described in the manufacturer's manual (Appendix III).

The LDH concentration was quantified by measuring the absorbance at 490 nm (reference wavelength, 630 nm to maintain the same background). All samples were measured by triplicate. For positive control, mono- and co-cultures were exposed for 24 hours to a Triton X-100 0.2% solution in PBS, as was previously explained. The positive control was diluted 10 times before measuring its absorption. The LDH release results obtained for the exposed co-cultures and monocultures have been represented in Figure 4.7.

As it can be observed in Figure 4.7, the LDH levels of all exposed blood vessel model cell cultures are in the same range as the negative control. Furthermore, the measured relative LDH release for the Triton 0.2 % PBS treated co-cultures is around 20 times higher than the nanocompound exposed cell cultures and negative control. Moreover, non-significant differences can be observed between cultures exposed to different nanocompounds, nor to different concentrations. Only the co-cultures exposed to the highest NP and nanosphere concentrations show slightly higher LDH release, around 1.5, but still too far from the release level of the positive control.

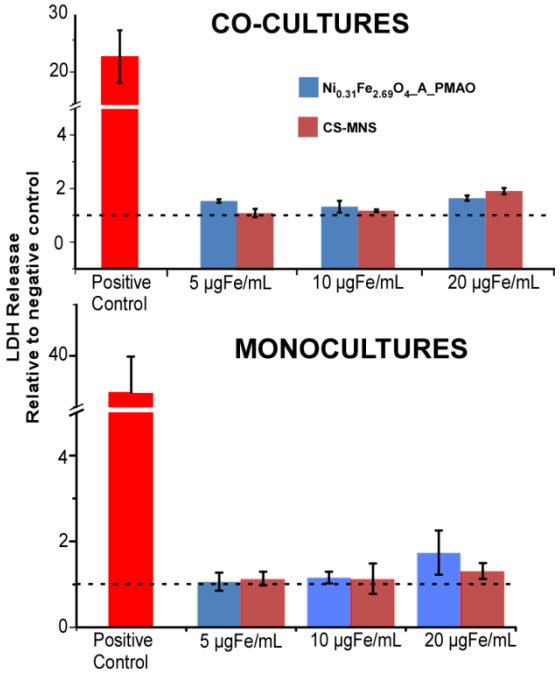

Figure 4.7. *LDH release of different concentrations of $Ni_{0.31}Fe_{2.69}O_4$_A_PMAO and CS-MNS exposed at blood vessel model co-cultures (up) and endothelial cell monocultures (down), relative to negative control (value=1, marked with discontinuous line), compared with a positive control exposed to a 0.2% PBS solution.*

Similar results have been obtained for endothelial cell monocultures, as the exposed monocultures have shown nearly the same LDH release values as the negative control.

On summary, the lack of direct cytotoxicity of both tested samples in blood vessel model culture has been confirmed, in good agreement with the lack of morphological changes observed by LSM analysis.

4.3.6. Assessment of the cell layer integrity

Nanocompounds could affect to the blood vessel integrity by inducing a higher wall permeability of its primary endothelial cell layer. This effect

would increase the exchange process between the blood stream and internal tissues, and also allow the insertion of toxic or non-desirable particles or compounds. Therefore, the absence of this kind of effects needs to be ensured. Hypothetic changes in the cell layer permeability after nanoparticles treatment have been tested by means of the Blue Dextran experiment. This assay is based on the determination of Blue Dextran dye molecule translocation through the mono- and co-culture cell layer.[28] This is a widely used simple and effective method to verify the cell layer integrity by passing a known concentration of dye through the cell culture. In this way, a reduction in the cell viability value is usually connected with an increase in the cell layer permeability. Hence, a decrease of cell permeability is directly proportional to the cytotoxicity of the material.[28,29]

To perform this test, the cell media was removed after the exposures and the samples with the mono- and co-cultures were washed with PBS. A total of 2 mL of phenol red free Roswell Park Memorial Institute (RPMI) cell media were added to the lower chamber and 0.5 mL to the upper chamber. Phenol red free cell media was employed to avoid interferences in the final absorbance measurements. A total of 0.5 mL of a 1 % Blue Dextran solution in PBS were added to the upper chamber and incubated at 37 °C and 5 % CO_2 in 6 well plates for 2 h. The contents from the lower chambers were collected and the absorbance at 600 nm was quantified using a multimode plate reader (BioRad Benchmark Plus, R&D Systems) in 96 well plates. As positive control, the translocation of Blue Dextran molecules through an empty insert was measured under the same conditions.

As it can be observed in Figure 4.8, neglectable increments of cell layer permeability can be noticed in the blood vessel model co-cultures. All permeability values for the NP and nanosphere at different concentrations are in the same range as the negative control value.

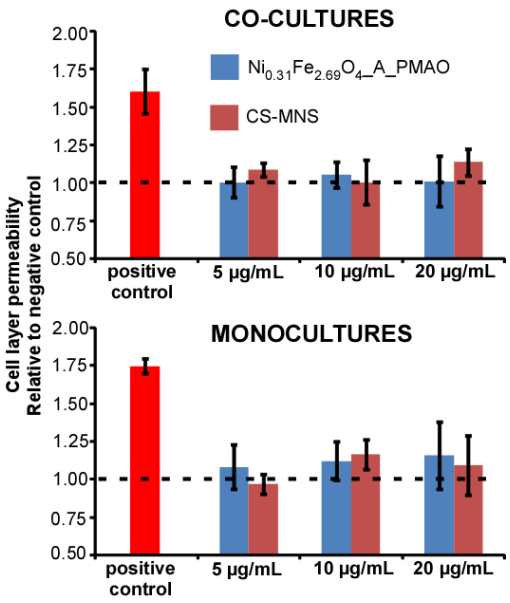

Figure 4.8. *Cell permeability values determined by Dextran Blue experiments of exposed blood vessel model co-cultures (up) and endothelial (down) cell monocultures and positive control performed by an empty insert. The negative control (value=1) is marked by a discontinuous line.*

It is important to highlight that the error of this methodology could be attributed to the Dextran Blue translocation, as well as to the heterogeneity of porous size and density from insert to insert.

Similar results have been obtained in endothelial cell monocultures treated with the nanocompunds. Obtained Dextran Blue translocation values after treatment are similar to the negative control value.

In good agreement with the cytotoxicity analysis of LDH release measurements, the absence of any kind of direct effect of nanocompounds on the cell culture density or thickness can be assured. Hence, no changes in the blood vessel exchange process would be induced, by exposing $Ni_{0.31}Fe_{2.69}O_4$_A_PMAO and CS-MNS samples.

4.3.7. Oxidative stress

In many cases, the presence of external compounds could induce modifications in the cell metabolism, which could alter the cellular behaviour and cause the necrosis or apoptosis in middle or long time periods. One of the most frequently discussed negative effect is the introduction of an oxidative damage, either due to the generation of reactive oxygen species (ROS) or by inactivation of the antioxidant defense system.[30] Under conventional conditions, the ROS are generated in low quantities and are easily neutralized by the antioxidant defenses such as glutathione (GSH) and antioxidant enzymes. However, under an excess of ROS production, the natural antioxidant defenses may be overwhelmed.[30] Oxidative stress refers to a state in which the GSH is depleted while the oxidized glutathione (GSSG) accumulates.[31] The experimental evidences have shown that this kind of oxide based nanoparticles induced DNA damages and apoptosis through oxygen species generation and oxidative stress.[31]

The induced oxidative stress was analysed by measuring the intracellular reduced glutathione (GSH) antioxidant levels with a diagnostic glutathione assay kit provided by Cayman Chemical Company, Ann Arbor, MI, according to the manufacturer's manual (Appendix III). All GSH obtained values were compared with the protein expression measured by a BCA protein determination (Pierce Protein research Products, Thermo Scientific, Rockford, IL), as its activity is related with the cytoplasmic protein reduction. As positive control, a cell culture was exposed to a 7.3 M tert-butyl hydrogen peroxide (^{t}BHP) oxidant solution in PBS for 24 hours (Figure 4.9).

The GSH levels of the blood vessel model co-cultures after $Ni_{0.31}Fe_{2.69}O_4$_A_PMAO nanoparticle and CS-MNS nanosphere exposures were in the same value range of the negative control.

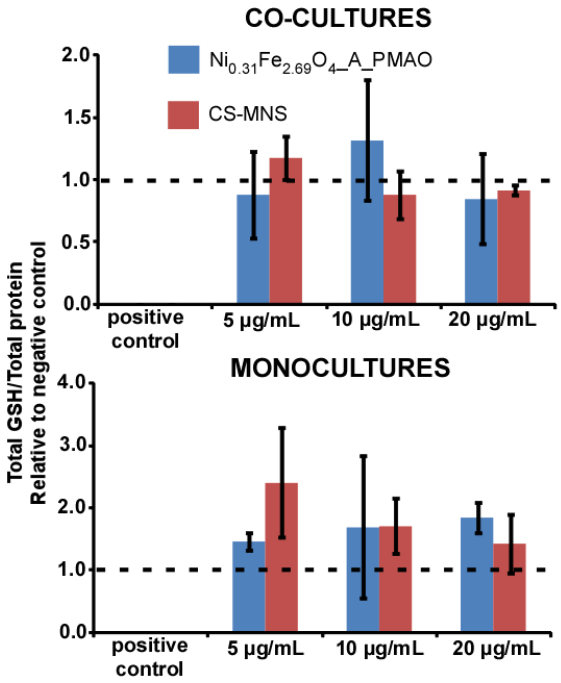

Figure 4.9. *GSH levels, relative to negative control (marked with a discontinuous line), of exposed co-cultures (up) and monocultures (down) exposed to $Ni_{0.31}Fe_{2.69}O_4$_A_PMAO and CS-MNS samples at different concentrations and exposed to a 7.3 M ^{t}BHP solution (positive control).*

There were not evidences of oxidative stress induced by nanocompounds for this time range and concentration, as it can be observed in Figure 4.9. However, low reproducibility was obtained as in the case of previous experiments. Similar results have been obtained for the exposed endothelial cell monocultures, showing slightly highly GSH values compared with co-cultures.

Taking the positive control as a reference of an oxidative stress inductor, it can be concluded that the exposed nanocompounds are not producing significant oxidative stress in the applied concentration range and exposure time.

4.3.8. Inflammatory response analysis

Inflammation is a usual answer of some tissues against an internal or external stimuli. The role of pro-inflammatory cytokines, chemokines, adhesion molecules and inflammatory enzymes have been linked with chronic inflammation. Some cells express and secrete a number of interleukins, growth factors and chemotactic molecules in response to chemical irritants, physical agents or pathogenic organisms. These products, including the interleukin 8 (IL-8), have an important role in many diseases, by mediating the activation of the immune reactions in the presence of toxicological agents.[32,33] The pro-inflammatory response of the co-cultures after the exposures was checked by measuring the release of the interleukin 8 (IL-8) pro-inflammatory mediator.[32,33]

The experiment was assessed via the use of a commercially available IL-8 ELISA assay kit (R&D Systems, Switzerland) following the provided protocol (Appendix III). As positive control, the mono- and co-cultures were treated with a 1 µg/mL Lipopolysaccharide (LPS) solution in DMEM for 24 hours to induce the IL-8 pro-inflammatory protein release. The obtained IL-8 release values for the exposed mono and co-cultures are expressed as relative to negative control in Figure 4.10.

A significant increase of interleukin 8 release was measured after both nanocompound exposures. As was previously explained, the higher measured IL-8 mediator concentration in co-cultures is directly connected with an inflammatory damage in the cell culture, as this molecule activates the immune response.

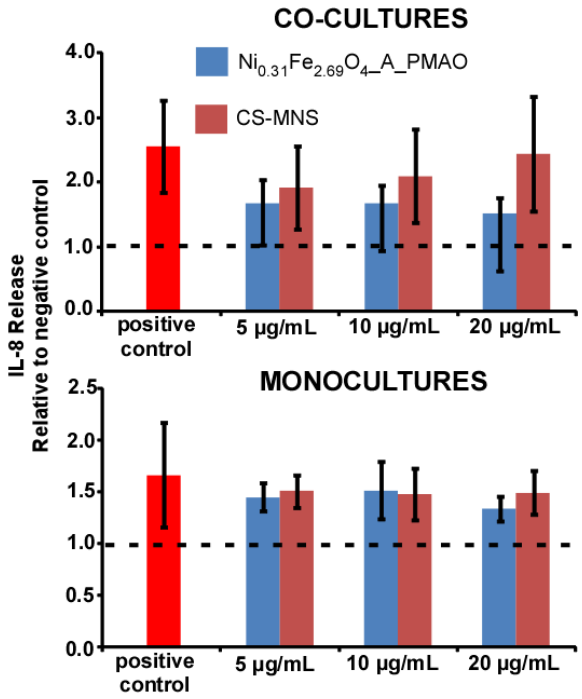

Figure 4.10. *Inflammatory response of mono and co-cultures after $Ni_{0.31}Fe_{2.69}O_4$_A_PMAO and CS-MNS different concentration exposures, relative to negative control, marked with a discontinuous line. Cell cultures were treated with a lipopolysaccharide solution as positive control.*

Thus, according to the results represented in Figure 4.10, higher relative IL-8 release has been induced by the CS-MNS nanospheres, comparing with the $Ni_{0.31}Fe_{2.69}O_4$_A_PMAO NPs in the three tested concentrations. This effect could have been induced, on the one hand, by the higher size of the CS-MNS magnetic nanospheres, which could hinder the normal function of the cell metabolism. On the other hand, this response could be due to the positive surface charge of the nanospheres.

Several studies have previously shown similar pro-inflammatory response of endothelial cell cultures exposed to different NPs.[29,34] Some of these

works support that particles with smaller sizes usually have a stronger pro-inflammatory effect.[35] In contrast, the results shown in Figure 4.10 conclude that the CS-MNS, which have much higher particle diameter, induce more IL-8 release than the $Ni_{0.31}Fe_{2.69}O_4$_A_PMAO nanoparticles. In this case, the increasing of the exposed concentration also rises the IL-8 release, which means that the nanocompounds are definitely the inductors of the release. Actually, the chemokine release in the co-culture exposed to the highest CS-MNS concentration provided similar release value as the positive control (2.5). These results are in good agreement with previously reported results using ultrafine polyestyrene NP.[35]

4.4 *In Vivo* CS-MNS biodistribution in mice

Although the nanocompound short-term effects on a specific tissue have been estimated, their influence in complex organisms also needs to be studied. In this case, the CS-MNS chitosan nanospheres were chosen for the *in vivo* experiments, as their stability and functionability is more suitable than the $Ni_{0.31}Fe_{2.69}O_4$_A_PMAO nanoparticles. The potential applicability of these nanospheres is also higher, since as drug delivery and release biocompatible agents, they could be eventually used in treatments for many kind of diseases. However, before planning future applications, it is necessary to have a better knowledge about the effects of the nanospheres in complex organisms. Thus, the effects that the nanospheres could have in different organs, functions and enzymes must be analysed. Furthermore, it would be helpful to acquire information about the normal biodistribution of the nanospheres.

Although these *in vivo* experiments could be performed in many different kind of animals, during this thesis we used mice.[36] 5 controls without

nanospheres and 5 exposed mice have been used, which were intravenously injected with 150 µL of 1mg/mL CS-MNS 0.9 % NaCl solution through the tail vein. To discard the injection shock effect, the control mice were injected with 150 µL of physiological serum. The injections, as well as the animal treatment and organ and blood extractions, have been performed by Dr. María Moros and Dr. Grazyna Stepien in the Centro de Investigaciones Médicas de Aragón (CIBA). The mice were weighted every day to control any changes in their mass. After 48 hours of exposure, the mice were scarified and the major organs (spleen, heart, lung, livery, testicles and kidney) were extracted and weighed. The blood was also extracted from the neck vein after the sacrifice. After the extraction, the blood was centrifuged at 9 000 rpm for 10 min to obtain the plasma from the supernatant. From this plasma, the concentration of some biochemistry relevant parameters as glucose, creatinine, aspartate, aspartate aminotransferase (AST), bilirubin, total protein, alkaline phosphatase (ALP) and cholesterol were determined in the Servei de Bioquímica Clínica Veterinaria (Universitat Autònoma de Barcelona).[37,38,39] The biodistribution of nanocapsules in the organs was checked by means of ICP measurements of Fe and Ni metals, in the same way as in the blood vessel model experiment. The main scheme of the whole experiment is resumed in Figure 4.11.

The organs were washed, calcined and digested before measuring the metals concentrations by ICP. First, the organs were washed 4 times with distilled water to remove the blood, before being lyophilized. After that, the organs were calcined at 600 °C for 50 min. After the calcination, the organs were digested with 500 µL of aqua regia (1000 µL for livers) at 60 °C for two hours. The non-digested organ pieces were filtered and the metal solution was diluted 30 times. The Fe and Ni concentration was measured by means of the ICP-MS (Appendix I).

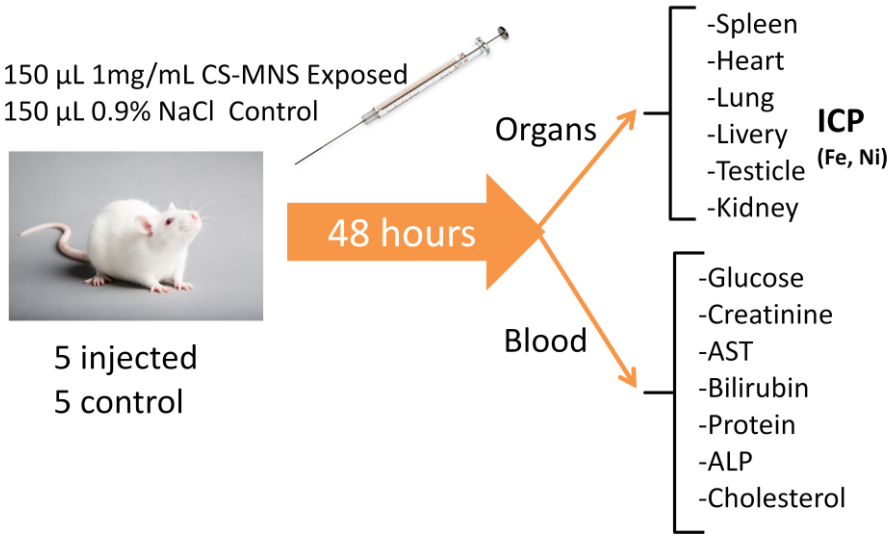

Figure 4.11. *Schematic resume of in vivo experiment carried out with CS-MNS nanospheres*.

The analysed parameters have been divided in two different groups. Firstly, the effects of the CS-MNS injection in the animal's behaviour, physiology and metabolism have been analysed by the animal weight control and the blood analysis. Additionally, the CS-MNS biodistribution in mice has been analysed by iron and nickel ICP measurements.

4.4.1. CS-MNS toxicity in mice

No one of the tested mice died after the injection, before being sacrificed. However, the exposed animals showed more active behaviour during the following minutes, due to the shock of the nanospheres injection. The weight values of the control and CS-MNS exposed mice measured at three different times (0, 24 and 48 hours after the injection) are represented in Table 4.5 and Figure 4.12. It can be observed that treated and non-treated animal weights decreased during the first 24 h. In average, all mice recovered their

original weight 48 h after the injection, having passed the shock effect induced by the injection.

Table 4.5. *Time dependant mice weights of control and CS-MNS exposed mice.*

SAMPLE	0 h	24 h	48 h
Control (g)	28.4	27.6	28.5
	25.4	24.2	24.9
	27.9	28.0	27.6
	25.4	25.8	26.8
	28.1	27.3	28.5
Exposed (g)	28.8	30.4	30.6
	30.3	27.6	30.5
	26.6	26.8	26.2
	27.7	26.2	27.6
	28.8	28.0	29.1

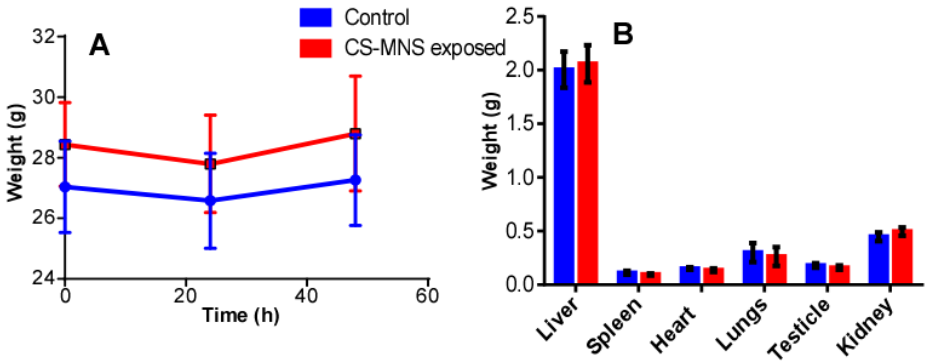

Figure 4.12. *Average weight values of control and CS-MNS exposed mice at different times (A) and average weights of single organs of exposed and non- exposed mice (B).*

Some organs were extracted and weighted after the mice slaughter. The average results, as well as the error values, are shown in Figure 4.12B. No significant differences can be appreciated between the CS-MNS exposed and the non-exposed organs. However, the treatment could induce damages or

metabolism changes in some organs. In this experiment, no visual or mass changes have been noticed in any organ.

Some representative enzymes, proteins and chemical compounds present in the bloodstream have been measured from the blood plasma in order to monitor differences in metabolism.[40] Changes in creatinine or total protein concentration could be a signal of kidney disease. Creatinine is a chemical waste protein derived from creatine metabolism in the muscle tissues. The concentration of this protein in the bloodstream is controlled by the kidneys activity, which filters this molecule to maintain a constant concentration in the bloodstream. Thus, higher creatinine concentrations are usually caused by a non-proper kidney function. In the same way, lower total protein blood concentration can also be connected with a kidney or liver disease, malnutrition or fatigue. Whereas an excess of total protein concentration is related to a chronic inflammation or viral infection. Consequently, when unusual total protein contents are obtained, further analysis is required (as differentiated protein analysis) to find the specific source of this anomalous concentration. Liver diseases can be also noticed by higher AST, bilirubin or ALP blood concentrations. Aspartate aminotransferase (AST) and alkaline phosphatase (ALP) enzyme higher concentrations are directly connected with the liver disease grade. Both enzymes are present in most of body tissues and organs, and a small concentration is present in the bloodstream. As both enzymes are involved in the aminoacid metabolism by protein decomposition, anomalous concentrations in blood indicates a wrong liver activity. Livers function also maintains the blood bilirubin concentration stable. This yellow pigment is released to bloodstream when old erythrocytes start discomposing, and the excess is eliminated from the bloodstream by the liver. Thus, a liver disease or damage could induce a higher bilirubin presence in the bloodstream,

which can be noticed by yellow colored skin and eyes. Nevertheless, this effect can also be caused by an abnormal hemolysis.[41,42]

Finally, glucose and cholesterol concentrations have been measured, as these molecules are the best indicators of a correct metabolic behavior. The average concentration of creatinine, glucose, aspartate aminotransferase (AST), total bilirubin, total protein, alkaline phosphatase (ALP) and cholesterol, together with the error bars, are represented in Figure 4.13.

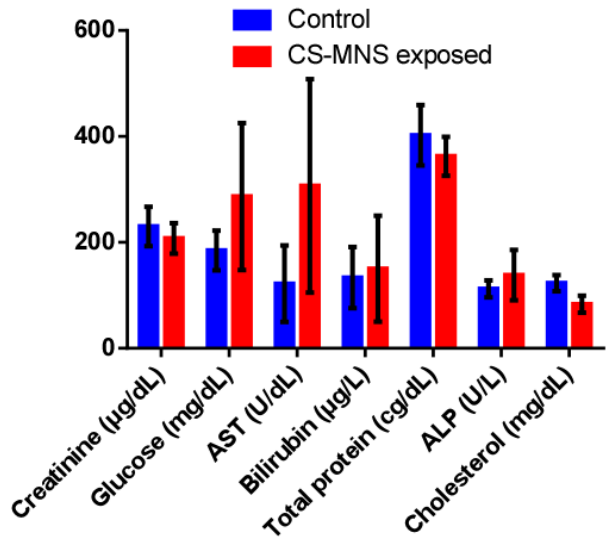

Figure 4.13. *Hematology and blood chemistry data averages and error bars of 5 control and 5 CS-MNS exposed mice. Concentration units of each quantified factor have been modified to obtain an easily interpretable graph.*

All data has been collected for the control mice and those treated with CS-MNS. The statistical study has been performed by means of the two way ANOVA statistical analysis using the GraphPad Prism software with a 0.05 alpha value.[20] Apparently, there is not a general relation between the treated and non-treated animals. According to this statistical analysis, only the AST enzyme value has shown a significant difference between the control and

the CS-MNS exposed mice. Although there are great differences in the AST concentration from one mouse to another in the same group, a considerably higher main concentration can be observed in Figure 4.13 for the CS-MNS exposed mice. As it has been explained, this enzyme plays an important role in the aminoacide metabolism by catalyzing the reversible transfer of the α-amino group between the aspartate and glutamate, and it is present in the kidney, pancreas, muscle tissue, heart, liver and erythrocytes. A strong increment in the AST levels is usually related to liver diseases, being linearly proportional to hepatic tissue damages, as their release to bloodstream came from the hepatocyte collapse. However, the observed value is only two times higher than the control AST value, whereas the liver diseases derived from the AST values are usually around 10-100 times higher than the normal values.[43] Therefore, the observed slight increase is probably caused by damages in the muscle or heart tissues, that are releasing AST from the destroyed cells mitochondrias.[44]

Although no more significant differences between the control and the CS-MNS exposed mice have been found by statistical analysis, the Figure 4.13 also shows a slight hyperglycemia phenomena in the exposed mice. Nevertheless, these differences are not significant if we consider the error bars associated in each case. On balance, no big evidences of damages have been found in the CS-MNS exposed mice after two days of exposure.

4.4.2. CS-MNS biodistribution in mice

The second objective of this *in vivo* study was to achieve information about the biodistribution of the CS-MNS nanospheres over the mouse body. Specifically, it is important to know the organs where the nanospheres tend to accumulate preferentially. Hence, the nanosphere biodistribution has been analyzed by measuring the metal content in each organ (liver, spleen,

heart, lungs, testicles and kidneys) by ICP, relating the extra metal content of the exposed mice to the nanosphere presence. The most abundant metal in the nanosphere structure is the iron. However, most organs have a great amount of intrinsic iron, which could also be considerably different from one mouse to another. This fact makes even more difficult to obtain trustworthy conclusions from the iron content data. For this reason, the Ni content has been also measured by ICP, as the analyzed organs should not have detectable amounts of Ni. Thus, the Fe and Ni total amounts in the organs were calculated and expressed as proportions per total dry organ weight (Figure 4.14).

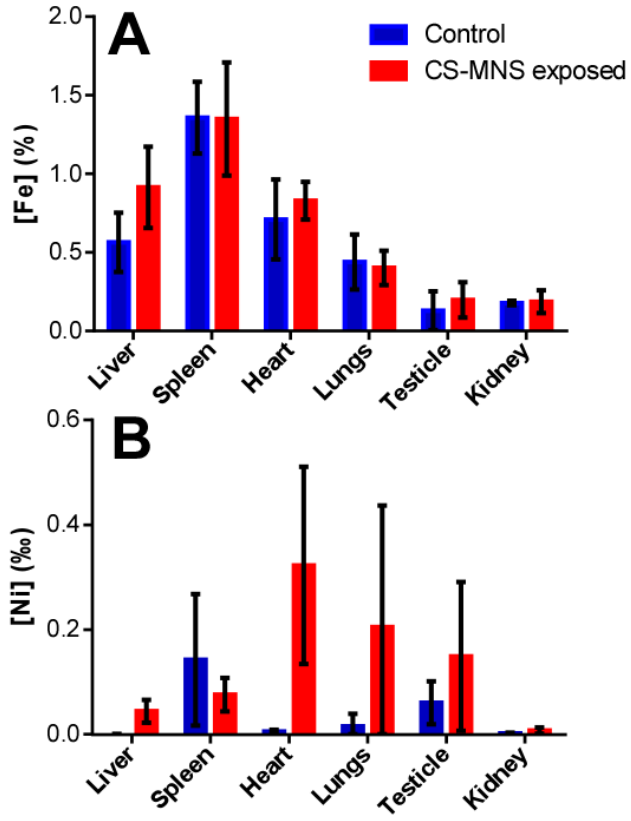

Figure 4.14. *Iron (A) and nickel (B) content of control and CS-MNS exposed mice organs, together with error bars, expressed as metal mass proportion per total dry organ mass.*

As it was expected, the high iron content of some organs makes difficult to assert if the iron increase is due to the presence of nanospheres or to differences between mice. As it can be observed in Figure 4.14A, the organs with higher iron proportions are the spleen, liver, heart and lungs, as these are the organs which present most interaction with the erythrocytes.[45,46] The comparison of iron amount in these organs is even more difficult, as the intrinsic iron amount deviation between different animals would be statistically higher. The correlation analysis between both mice groups, as well as the two-way ANOVA statistical analysis (comparing two mice group for individual organ analysis) were therefore carried out to evaluate the significance of the observed differences (0.05 alpha confidence level). No statistically relevant differences have been found in these terms between the exposed and non-exposed mice. However, the ANOVA analysis performed for single organ iron proportion values show that the most significant difference is present in the liver iron amount. Thus, much higher iron proportion has been found in the CS-MNS exposed mice livers, fact that suggests that the liver could be filtering the nanospheres from the bloodstream. Nevertheless, taking into account the obtained high error values and the used short mice population, this result should not be taken as conclusive.

Therefore, the Ni metal analysis was also performed. However, large error values have also been obtained for the Ni content analysis. Furthermore, many of the measured concentrations were below the ICP-MS detection limit, as the Ni weight in the nanospheres represents only the 5 %. Thus, even considering a high nanosphere presence in mice organs, the low nickel proportion would be easily confused with small Ni contaminations during the organ digestion. The Ni proportion for the different organs and mice groups

is represented in Figure 4.14B. Although the obtained error values are quite high, significant proportions of Ni have been detected in some CS-MNS exposed mice organs, especially in heart, lungs and testicles. However, a relatively high Ni presence has been detected in the spleen of control mice, which would be a certain signal of an external contamination. The global correlation analysis for different mice groups determines in this case a statistically significant difference between the non-exposed and the CS-MNS exposed mice organs. Specifically, the differences have been found in heart and lungs by means of the ANOVA analysis, fact which disagrees with the iron proportion analysis.

It must be highlighted that the nanosphere accumulation depends on the time.[37] Initially, the nanocompounds tend to accumulate in heart, spleen, lungs, kidneys and bloodstream. Around 24-48 hours after the injection, the nanocompounds could have been removed from the heart, lungs and bloodstream, maintaining the tendency to accumulate in the liver and spleen. Although different biodistribution is expected for different kind of nanocompounds, the same behavior has been displayed by other compounds, as carbon nanotubes, graphene or gold NPs.[37,38,39] The nanoparticle size has also been revealed as an important factor, as bigger NPs accumulates easier (quicker) in the organ tissues, especially in the liver and spleen.[47]

Taking all these studies into account, the preferential organs to accumulate the 100 nm nanospheres after 48 hours should be the liver and the spleen. However, the great irreproducibility of the obtained Ni and Fe values from one mouse to another makes impossible to confirm this statement. Although high concentrations of Fe and Ni have been found in the CS-MNS exposed mice spleens, great proportions have also been detected in control mice. These irregular proportions are related to differences between

mouse physiology and metabolism in the case of iron and to small Ni contaminations in the case of Ni. Nonetheless, higher Ni and Fe proportions have been found in the exposed mice livers, which is in good agreement with the previously results of other similar studies.[47]

4.5 Summary

On balance, the suitability of the $Ni_{0.31}Fe_{2.69}O_4$_A_PMAO NPs and the CS-MNS nanospheres to be applied in biomedical applications has been assured by a broad toxicity analysis in Vero and in blood vessel model co-cultures. None of the nanocompounds has shown any cytotoxicity in Vero cells in 24 h exposure, determined by the MTT assay.

Moreover, after being exposed to the simulated blood vessels for 24 h, no cytotoxicity, changes in cell morphology, cell layer permeability increase or oxidative stress has been observed. Only a slight increase of the Interleukin 8 inflammatory mediator has been detected.

Finally, a toxicity and biodistribution test in mice has been carried out for the CS-MNS nanospheres. This test has proved the lack of toxicity of these nanospheres in complex organisms, in short periods of time (48 hours). However, it has not been possible to assess their biodistribution accurately over the mice body.

References

(1) Ito, A.; Shinkai, M.; Honda, H.; Kobayashi, T. Medical Application of Functionalized Magnetic Nanoparticles. *J. Biosci. Bioeng.* **2005**, *100* (1), 1–11.

(2) Mornet, S.; Vasseur, S.; Grasset, F.; Duguet, E. Magnetic Nanoparticle Design for Medical Diagnosis and Therapy. *J. Mater. Chem.* **2004**, *14* (14), 2161.

(3) Corot, C.; Robert, P.; Idée, J.-M.; Port, M. Recent Advances in Iron Oxide Nanocrystal Technology for Medical Imaging. *Adv. Drug Deliv. Rev.* **2006**, *58* (14), 1471–1504.

(4) Moore, T. L.; Rodriguez-Lorenzo, L.; Hirsch, V.; Balog, S.; Urban, D.; Jud, C.; Rothen-Rutishauser, B.; Lattuada, M.; Petri-Fink, A. Nanoparticle Colloidal Stability in Cell Culture Media and Impact on Cellular Interactions. *Chem. Soc. Rev.* **2015**, *44* (17), 6287–6305.

(5) Balog, S.; Rodriguez-Lorenzo, L.; Monnier, C. A.; Michen, B.; Obiols-Rabasa, M.; Casal-Dujat, L.; Rothen-Rutishauser, B.; Petri-Fink, A.; Schurtenberger, P. Dynamic Depolarized Light Scattering of Small Round Plasmonic Nanoparticles: When Imperfection Is Only Perfect. *J. Phys. Chem. C* **2014**, *118* (31), 17968–17974.

(6) Baalousha, M. Aggregation and Disaggregation of Iron Oxide Nanoparticles: Influence of Particle Concentration, pH and Natural Organic Matter. *Sci. Total Environ.* **2009**, *407* (6), 2093–2101.

(7) Edwards, S. A.; Williams, D. R. M. Double Layers and Interparticle Forces in Colloid Science and Biology: Analytic Results for the Effect of Ionic Dispersion Forces. *Phys. Rev. Lett.* **2004**, *92* (24), 248303–1.

(8) Lozsán, A.; García-Sucre, M.; Urbina-Villalba, G. Steric Interaction between Spherical Colloidal Particles. *Phys. Rev. E - Stat. Nonlinear, Soft Matter Phys.* **2005**, *72* (6), 1–13.

(9) McClements, D. J. Theoretical Analysis of Factors Affecting the Formation and Stability of Multilayered Colloidal Dispersions. *Langmuir* **2005**, *21* (21), 9777–9785.

(10) Moros, M.; Hernáez, B.; Garet, E.; T. Dias, J.; Sáez, B.; Grazú, V.; González-Fernández, Á.; Alonso, C.; M. de la Fuente, J. Monosaccharides versus PEG- Functionalized NPs: Influence in the Cellular Uptake. *ACS Nano* **2012**, *2*, 1565–1577.

(11) Mosmann, T. Rapid Colorimetric Assay for Cellular Growth and Survival: Application to Proliferation and Cytotoxicity Assays. *J. Immunol. Methods* **1983**, *65* (1–2), 55–63.

(12) Huang, J.-H.; Parab, H. J.; Liu, R.-S.; Lai, T.-C.; Hsiao, M.; Chen, C.-H.; Sheu, H.-S.; Chen, J.-M.; Tsai, D.-P.; Hwu, Y.-K. Investigation of the Growth Mechanism of Iron Oxide Nanoparticles via a Seed-Mediated Method and Its Cytotoxicity Studies. *J. Phys. Chem. C* **2008**, *112* (40), 15684–15690.

(13) Mosmann, T. Rapid Colorimetric Assay for Cellular Growth and Survival: Application to Proliferation and Cytotoxicity Assays. *J. Immunol. Methods* **1983**, *65* (1–2), 55–63.

(14) Ahamed, M.; Akhtar, M. J.; Siddiqui, M. a.; Ahmad, J.; Musarrat, J.; Al-Khedhairy, A. a.; AlSalhi, M. S.; Alrokayan, S. a. Oxidative Stress Mediated Apoptosis Induced by Nickel Ferrite Nanoparticles in Cultured A549 Cells. *Toxicology* **2011**, *283* (2–3), 101–108.

(15) Yancopoulos, G. D.; Davis, S.; Gale, N. W.; Rudge, J. S.; Wiegand, S. J.; Holash, J. Vascular-Specific Growth Factors and Blood Vessel Formation. *Nature* **2000**, *407* (6801), 242–248.

(16) Dickhout, J. G.; Basseri, S.; Austin, R. C. Macrophage Function and Its Impact on Atherosclerotic Lesion Composition, Progression, and Stability the Good, the Bad, and the Ugly. *Arterioscler. Thromb. Vasc. Biol.* **2008**, *28* (8), 1413–1415.

(17) Schrijvers, D. M.; De Meyer, G. R. Y.; Herman, A. G.; Martinet, W. Phagocytosis in Atherosclerosis: Molecular Mechanisms and Implications for Plaque Progression and Stability. *Cardiovasc. Res.* **2007**, *73* (3), 470–480.

(18) Müller, K.; Skepper, J. N.; Posfai, M.; Trivedi, R.; Howarth, S.; Corot, C.; Lancelot, E.; Thompson, P. W.; Brown, A. P.; Gillard, J. H. Effect of Ultrasmall Superparamagnetic Iron Oxide Nanoparticles (Ferumoxtran-10) on Human Monocyte-Macrophages in Vitro. *Biomaterials* **2007**, *28* (9), 1629–1642.

(19) Rothen-Rutishauser, B. M.; Kiama, S. G.; Gehr, P. A Three-Dimensional Cellular Model of the Human Respiratory Tract to Study the Interaction with Particles. *Am. J. Respir. Cell Mol. Biol.* **2005**, *32* (4), 281–289.

(20) Bisig, C.; Steiner, S.; Comte, P.; Czerwinski, J.; Mayer, A.; Petri-Fink, A.; Rothen-Rutishauser, B. Biological Effects in Lung Cells In Vitro of Exhaust Aerosols from a Gasoline Passenger Car With and Without Particle Filter. *Emiss. Control Sci. Technol.* **2015**, *1* (3), 237–246.

(21) Koley, D.; Bard, A. J. Triton X-100 Concentration Effects on Membrane Permeability of a Single HeLa Cell by Scanning Electrochemical Microscopy (SECM). *Proc. Natl. Acad. Sci. U. S. A.* **2010**, *107* (39), 16783–16787.

(22) Chortarea, S.; Clift, M. J. D.; Vanhecke, D.; Endes, C.; Wick, P.; Petri-Fink, A.; Rothen-Rutishauser, B. Repeated Exposure to Carbon Nanotube-Based Aerosols Does Not Affect the Functional Properties of a 3D Human Epithelial Airway Model. *Nanotoxicology* **2015**, *5390*, 1–11.

(23) Digigow, R. G.; Vanhecke, D.; Rothen-Rutishauser, B.; Clift, M. J. D.; Petri-Fink, A. Uptake and Intracellular Fate of Peptide Surface-Functionalized Silica Hybrid Magnetic Nanoparticles In Vitro. *Part. Part. Syst. Charact.* **2015**, *32* (2), 188–196.

(24) Verma, A.; Stellacci, F. Effect of Surface Properties on Nanoparticle-Cell Interactions. *Small* **2010**, *6* (1), 12–21.

(25) Villanueva, A.; Cañete, M.; Roca, A. G.; Calero, M.; Veintemillas-Verdaguer, S.; Serna, C. J.; Morales, M. D. P.; Miranda, R. The Influence of Surface Functionalization on the Enhanced Internalization of Magnetic Nanoparticles in Cancer Cells. *Nanotechnology* **2009**, *20* (11), 115103.

(26) Chan, F. K.-M.; Moriwaki, K.; De Rosa, M. J. Detection of Necrosis by Release of Lactato Dehydrogenase (LDH) Activity. *Methods Mol Biol* **2013**, *979*, 65–70.

(27) Clift, M. J. D.; Gehr, P.; Rothen-Rutishauser, B. Nanotoxicology: A Perspective and Discussion of Whether or Not in Vitro Testing Is a Valid Alternative. *Arch. Toxicol.* **2011**, *85* (7), 723–731.

(28) Horváth, L.; Umehara, Y.; Jud, C.; Blank, F.; Petri-Fink, A.; Rothen-Rutishauser, B. Engineering an in Vitro Air-Blood Barrier by 3D Bioprinting. *Sci. Rep.* **2015**, *5*, 7974.

(29) Klein, S. G.; Serchi, T.; Hoffmann, L.; Blömeke, B.; Gutleb, A. C. An Improved 3D Tetraculture System Mimicking the Cellular Organisation at the Alveolar Barrier to Study the Potential Toxic Effects of Particles on the Lung. *Part. Fibre Toxicol.* **2013**, *10* (1), 31.

(30) Nel, A.; Xia, T.; Mädler, L.; Li, N. Toxic Potential of Materials at the Nanolevel. *Science* **2006**, *311* (February 2006), 622–627.

(31) Park, E.-J.; Yi, J.; Chung, K.-H.; Ryu, D.-Y.; Choi, J.; Park, K. Oxidative Stress and Apoptosis Induced by Titanium Dioxide Nanoparticles in Cultured BEAS-2B Cells. *Toxicol. Lett.* **2008**, *180* (3), 222–229.

(32) Wilmer, J. L.; Luster, M. I. Chemical Induction of Interleukin-8, a Proinflammatory Chemokine, in Human Epidermal Keratinocyte Cultures and Its Relation to Cytogenetic Toxicity. *Cell Biol. Toxicol.* **1995**, *11* (1), 37–50.

(33) Aggarwal, B. B.; Shishodia, S.; Sandur, S. K.; Pandey, M. K.; Sethi, G. Inflammation and Cancer: How Hot Is the Link? *Biochem. Pharmacol.* **2006**, *72* (11), 1605–1621.

(34) Lenz, A. G.; Karg, E.; Lentner, B.; Dittrich, V.; Brandenberger, C.; Rothen-Rutishauser, B.; Schulz, H.; Ferron, G. a; Schmid, O. A Dose-Controlled System for Air-Liquid Interface Cell Exposure and Application to Zinc Oxide Nanoparticles. *Part. Fibre Toxicol.* **2009**, *6*, 32.

(35) Brown, D. M.; Wilson, M. R.; MacNee, W.; Stone, V.; Donaldson, K. Size-Dependent Proinflammatory Effects of Ultrafine Polystyrene Particles: A Role for Surface Area and Oxidative Stress in the Enhanced Activity of Ultrafines. *Toxicol. Appl. Pharmacol.* **2001**, *175* (3), 191–199.

(36) Moros, M.; Ambrosone, A.; Stepien, G.; Fabozzi, F.; Marcherano, V.; Castaldi, A.; Tino, A.; M. de la Fuente, J.; Tortiglione, C. Deciphering Intracellular Events Triggered by Mild Magnetic Hyperthermia in Vitro and in Vivo. *Nanomedicine (Lond.)* **2015**, *10* (14), 2167–2183.

(37) Zhang, Y.; Wen, S.; Zhao, L.; Li, D.; Liu, C.; Jiang, W.; Gao, X.; Gu, W.; Ma, N.; Zhao, J.; et al. Ultrastable Polyethyleneimine-Stabilized Gold Nanoparticles Modified with Polyethylene Glycol for Blood Pool, Lymph Node and Tumor CT Imaging. *Nanoscale* **2016**, *8* (10), 5567–5577.

(38) Yang, K.; Gong, H.; Shi, X.; Wan, J.; Zhang, Y.; Liu, Z. In Vivo Biodistribution and Toxicology of Functionalized Nano-Graphene Oxide in Mice after Oral and Intraperitoneal Administration. *Biomaterials* **2013**, *34* (11), 2787–2795.

(39) Liu, Z.; Cai, W.; He, L.; Nakayama, N.; Chen, K.; Sun, X.; Chen, X.; Dai, H. In Vivo Biodistribution and Highly Efficient Tumour Targeting of Carbon Nanotubes in Mice. *Nat. Nanotechnol.* **2007**, *2* (1), 47–52.

(40) Diehl, K.-H.; Robin Hull Rudolf Pfister, Yvon Rabemampianina, D. M.; Smith, D. A Good Practice Guide to the Administration of Substances and Removal of Blood,Including Routes and Volumes. *J. Appl. Toxicol.* **2001**, *21* (September 2000), 15–23.

(41) Mahl, a; Heining, P.; Ulrich, P.; Jakubowski, J.; Bobadilla, M.; Zeller, W.; Bergmann, R.; Singer, T.; Meister, L. Comparison of Clinical Pathology Parameters with Two Different Blood Sampling Techniques in Rats: Retrobulbar Plexus versus Sublingual Vein. *Lab. Anim.* **2000**, *34* (4), 351–361.

(42) Haschek, W. M.; Rousseaux, C. G.; Wallig, M. A. *Fundaments of Toxicologic Pathology*, second edi.; ELSEVIER: San Diego, 2007.

(43) Whitehead, M. W.; Hawkes, N. D.; Hainsworth, I.; Kingham, J. G. A Prospective Study of the Causes of Notably Raised Aspartate Aminotransferase of Liver Origin. *Gut* **1999**, *45* (1), 129–133.

(44) Goessling, W.; Massaro, J. Aminotransferase Levels and 20-Year Risk of Metabolic Syndrome, Diabetes, and Cardiovascular Disease. *Gastroenterology* **2008**, *135* (6), 1935–1944.

(45) Elvehjem, C. A.; Peterson, W. H. The Iron Content of Animal Tissues. *J. Biol. Chem.* **1927**, *74*, 433–441.

(46) Valenzuela, C.; de Romaña, D.; Olivares, M.; Morales, M. S.; Pizarro, F. Total Iron and Heme Iron Content and Their Distribution in Beef Meat and Viscera. *Biol. Trace Elem. Res.* **2009**, *132* (1), 103–111.

(47) Liao, W.-Y.; Li, H.-J.; Chang, M.-Y.; Tang, A. C. L.; Hoffman, A. S.; Hsieh, P. C. H. Comprehensive Characterizations of Nanoparticle Biodistribution Following Systemic Injection in Mice. *Nanoscale* **2013**, *5* (22), 11079–11086.

4. *In vitro* and *in vivo* experiments

5. CONCLUSIONS

In the following points, the main conclusions obtained from this work are summarized.

- The thermal decomposition of metalorganic metal precursors has revealed as an ideal method to prepare controlled sized, high crystallinity and colloidal stable hydrophobic ferrite magnetic nanoparticles. Furthermore, the seeded mediated growth process allowed us to control the increase of the NP size to obtain higher NP diameters.

- The presence of Ni^{2+} and Mn^{2+} cations in the prepared NPs has been demonstrated by ICP measurements. However, the insertion of Mn^{2+} cations was not complete due to its different ionic radius comparing with Fe^{2+} cations. The Mn presence affects the final morphology of the obtained particles, as more prismatic shapes have been obtained.

- The Ni^{2+} cations tend to occupy the tetrahedral holes at doping levels up to 10%, what increases the saturation magnetization value, comparing with the magnetite. Nevertheless, at higher doping levels the Ni cations tend to occupy the octahedral holes, decreasing the Ms value.

- The doping induce a softening effect in the magnetic structure as lower magnetocrystalline anisotropy values have been obtained at increasing doping grades for both cations. This effect induces lower blocking temperatures comparing with magnetite.

5. Conclusions

- Disappointing results have been obtained from the core-shell structured sample analysis. The magnetic characterization (M (H), M (T) and EMR) did not show any significant differences with homogeneous magnetite or Ni ferrite systems caused by the two phase interaction. Furthermore, the obtained magnetic hyperthermia response was insufficient to be considered as promising materials for biomedical applications.

- As expected, the particle diameter has a major relevance in the magnetic hyperthermia response. The seeded mediated growth particles show, by far, the greatest magnetic hyperthermia response. Between them, the system which showed the biggest Ms value ($Ni_{0.31}Fe_{2.69}O_4$_A) has the greatest magnetic hyperthermia response.

- A method to encapsulate the $Ni_{0.31}Fe_{2.69}O_4$_A hydrophobic NPs in chitosan shell has been successfully developed and optimized to obtain ≈100 nm chitosan magnetic nanospheres (CS-MNS). Based on the same mechanism, a promising fibroin magnetic nanosphere formation experiment has been carried out, presenting this protein as an appealing option for future experiments.

- An interesting change in the CS-MNS magnetic properties has been measured comparing with its single particle counterparts ($Ni_{0.31}Fe_{2.69}O_4$_A). The interactions generated between different NP inside nanosphere due to its proximity result in a higher g effective value and in a broadening of the M (T) signal.

- High amounts of Nile red hydrophobic dye and Rhodamine b isothiocyanate have been fruitfully encapsulated or bonded to CS-

MNS nanospheres, presenting them as promising agents for drug delivery based therapies.

- The *in vitro* toxicity experiments performed in Vero and endothelial cell monocultures and in blood vessel model co-cultures support the non-toxicity of $Ni_{0.31}Fe_{2.69}O_4$_A and CS-MNS samples, only showing a slight inflammatory response after exposures.

- The higher cellular uptake of $Ni_{0.31}Fe_{2.69}O_4$_A nanoparticles comparing with the CS-MNS for the blood vessel model co-cultures has been verified due to their smaller size.

- The results obtained from the toxicity and biodistribution *in vivo* experiment performed in CS-MNS injected mice only show a statistically relevant increase of AST enzyme levels in blood. From the biodistribution analysis, a tendency of CS-MNS nanospheres to accumulate preferentially in the liver has been concluded.

5. Conclusions

APPENDIX I. CHARACTERIZATION TECHNIQUES

In this appendix, the main characterization techniques performed in this thesis have been descried. Most of these characterization have been carried out in the SGIKER analysis services of the UPV/EHU.

- **Fourier Transform Infrared Spectroscopy (FTIR):**

Nanosphere compositions were measured in powder in a JASCO FT/IR – 4100 Fourier transform infrared spectrometer in a frequency range of 600-4000 cm^{-1} with a resolution of 2 cm^{-1} and a scanning number of 32.

- **UV/Vis Spectroscopy:**

The absorbance values of CS-MNS amino group determinations and Iron concentration were measured on a Cary 50 prove UV-VISIBLE VARIAN spectrophotometer at the given wavelengths. Glucosamine concentration measurements and MTT assays absorbance values were obtained from a Biotek ELX800 microplate reader at the given wavelengths in 96 well plates. Finally, all the absorbances of colorimetric analysis performed to endothelial cell monocultures and endothelial cell-macrophage co-cultures were quantified using a multimode plate reader (BioRad Benchmark Plus, R&D Systems) in 96 well plates.

- **Transmission Electron Microscopy (TEM):**

TEM micrographs of different magnetic NPs were acquired by means of a Philips CM200 microscope at an acceleration voltage of 200 kV. Chitosan nanospheres were visualized in a FEI Tecnai T20 electron microscope operating at 200 kV.

The sample preparation was carried out by dropping-cast toluene NP dispersion onto carbon covered copper grids. For all cases, concentration of

NP toluene dispersion was around 0.05 mgFe/mL to avoid an eventual NP saturation in micrographs, which could difficult the proper analysis of NP size dispersion.

- **Environmental Scanning Electron Microscopy (ESEM):**

Environmental Scanning Electron Microscopy (ESEM) micrographs were collected using a Quanta FE6-250 (FEI Company) field emission ESEM for high-resolution imaging working at low vacuum mode using a STEM and GSED detectors. Samples were prepared in the same way as for TEM analysis.

- **X Ray Diffraction (XRD):**

XRD analysis of all magnetic NP samples was performed in powder using a Phillips PW1710 diffractometer equipped with copper anodes. The X-ray source operated at 40 kV and 40 mA, and the 2θ scan was performed in the 10°< 2θ<90° range each 0.02° with scan step speed of 1.25 s.

- **Inductively Coupled Plasma spectroscopy (ICP):**

ICP-MS (7700x, Agilent Technologies, Palo Alto, USA) was used for the determination of Ni and Fe trace metals using a MicroMist micro-uptake glass concentric nebulizer (Glass Expansion, Victoria, Australia). In order to reduce MO^+ formation in the plasma, the spray chamber was Peltier cooled at 2°C. A standard quartz torch (2.5 mm internal diameter injector) and standard nickel cones were employed. The optimization of the *ICP-MS* conditions was achieved by adjusting the torch position and instrument set up to reduce oxide and doubly charged ion formation with a standard tuning solution containing 1.0 µg L^{-1} of ^{7}Li, ^{24}Mg, ^{59}Co, ^{89}Y, ^{140}Ce and ^{205}Tl in 1.0% HNO_3. This equipment includes a collision cell (He gas, ORS3 system, Agilent Technologies ©) to eliminate, with high efficiency, the spectral

interferences that may affect the elements studied. All elements were measured using the same single set of operating conditions without switching off cell gas modes. Operating conditions are shown in Table A1 and gave more than required sensitivity to meet all certified values. As estimation, total analysis time per sample, including wash-in and wash-out, was 2.5 min.

Table A1. Operating parameter values used *for ICP-MS* and *OID-ICP-MS*.

Instrumental conditions	
RF power (W)	1550
Plasma gas flow (L min^{-1})	15
Helium collision flow (mL min^{-1})	4.5
Kinetic energy discrimination (V)	2.0
Spray chamber temperature (ºC)	2.0
Data acquisition	
Mode	Spectrum
Integration time (ms)	0.2
Point/mass	1
Replicates	3
Analytical detection	
Isotopes^{+}	**52**,53Cr (Y), **56**, 57Fe (Y),**60**,61Ni (Y), **66**,67Zn (Y),**111**,113,114Cd (Rh), 206+207+208 =**208**Pb (Ho),

Appendix I

- **Thermogravymetric analysis (TG):**

Thermogravymetric analysis of magnetic NP samples and nanosphere samples was performed in a NETZSCH STA 449 C thermogravymetric analyzer, by heating 10-20 mg of sample at 10 °C heating rate up to 800 °C under Argon atmosphere.

- **Dynamic Light Scattering (DLS):**

Dynamic Light Scattering (DLS) is a really useful tool since, based on the size dependant light dispersion angle on particles, is able to determine the dynamic NP size based on the diffusion constant (D) of material by means of Stokes-Einstein relation:

$$D = \frac{k_B T}{3\pi\eta\, d_h}$$

Where k_B is Boltzman's constant ($1.38 \cdot 10^{23}$ J/K), T is the measurement temperature and η the fluid viscosity.

Magnetic NP colloidal dispersions in toluene were measured in a Malvern's Zetasizer Nano ZS instrument which works in 0.3 nm - 10 µm range using a He-Ne laser (633 nm), whereas DLS measurements of nanospheres were performed in a Brookhaven 90Plus DLS instrument using particle sizing software by means of the photocorrelation spectroscopy (PCS) technique and using a 0.1 mg/mL nanosphere suspension in water. All the measurements were performed in the following conditions: 0.01 mg/mL, 90°, 6 runs and 3 min/run.

Zeta potential measurements of nanocompounds were measured in water media (10 mM KCl) and DMEM cell culture media in a BI 90 Plus Particle Size Analyzer (Brookhaven Instruments Corporation) using Zeta PALS software at 0.05 mg/mL concentration (8 runs, 30 cycles/run).

Appendix I

- **Field dependant magnetization measurements:**

All magnetic NP samples were measured at 5 and 300 K in powder (≈ 15 mg) in a Vibrating Sample Magnetometer (VSM) from Cryogenic Ltd. up to a maximum field of 100 kOe with a 2-300 K working temperature range. Sample powder was compressed in a gelatine capsule to avoid vibrations during the measurement. The matrix effect in the final magnetization value has been discarded by diminishing the mass corresponding to organic matter. Magnetic nanospheres were measured at room temperature in a home-made VSM magnetometer up to a maximum field of 18 kOe with high field resolution.

- **Temperature dependant magnetization measurements:**

Magnetization measurements of magnetic NPs and CS-MNS as a function of temperature after cooling at zero field (ZFC curve) and field (10 Oe, FC curve) were performed in a commercial Superconducting Quantum Interference Device (SQUID) magnetometer from Quantum Design (MPMS-7T), equipped with a 7 T superconducting magnet. NPs diluted in toluene dispersion (0.05 mgFe/mL), were dyed in a filter paper to avoid great dipolar and magnetic interactions between NPs, which could disturb the obtained result. The diamagnetic contribution of filter paper was removed.

- **Electronic Magnetic Resonance spectroscopy (EMR):**

Mn, Ni ferrite and core shell nanoparticle samples have been measured in 0.05 mgFe/mL toluene dispersions (CS-MNS nanospheres in 0.05 mgFe/mL water dispersion) at room temperature by means of a Bruker ELESYS spectrometer which operates in x band, equipped with a Bruker BNM 200 Gaussometer and a Hewlett-Packard 5352B microwave frequencimeter.

Appendix I

- **Magnetic hyperthermia measurements:**

Measurements of the Specific Absorption Rate (SAR) were carried out by Dr. Eneko Garaio in the "departamento de electricidad y electrónica" of UPV/EHU in a homemade device able to operate up to ca. 1 MHz with magnetic field amplitudes up to 30 kA/m in 1 mg/mL magnetic NP toluene suspensions.

- **Relaxivity measurements:**

Magnetic relaxivity measurements were performed using a minispec m1-one Analyzer from Bruker at 1.41 T. The longitudinal (T_1) and transversal (T_2) relaxation times have been measured at five different iron concentrations in 0.1-1 mgFe/mL range for $Ni_{0.31}Fe_{2.69}O_4$_A_PMAO and CS-MNS samples dispersed in 10% gelatine aqueous solution in order to obtain a more suitable *in vivo* media.

- **Fluorophore fluorescence measurements:**

Fluorsescence measurements in fluorophore encapsulation tests were performed in a PerkinElmer LS 55 120 V Fluorescence spectrometer at room temperature, temperature operating in 200 -800 nm range. The dilution grade was adjusted in each case to obtain an optimal emission measurement.

APPENDIX II. Reactants

The empirical formula, as well as the purity and the supplier of the reactant used in this thesis are shown in this appendix:

Reactant	Empirical formula	Supplier	Purity (%)
Iron (III) acethylacetonate	$Fe(C_5H_7O_2)_3$	Sigma-Aldrich	99
Nickel (II) acethylacetonate	$Ni(C_5H_7O_2)_2$	Sigma-Aldrich	95
Oleic acid	$C_{18}H_{34}O_2$	Sigma-Aldrich	100
Oleylamine	$C_{18}H_{35}NH_2$	Acros Organic	80-90
1,2-hexadecanediol	$CH_3(CH_2)_{13}CHOHCH_2OH$	Sigma-Aldrich	90
Benzyl ether	$(C_6H_5CH_2)_2O$	Sigma-Aldrich	98
Ethanol	C_2H_5OH	Panreac	96
Toluene	$C_6H_5CH_3$	Sigma-Aldrich	99.5
Manganese (II) acethylacetonate	$Mn(C_5H_7O_2)_2$	Sigma-Aldrich	100
poly(maleic anhydride-alt-1-octadecene) (PMAO)	$(C_9H_{12}O_3)_n$	Sigma-Aldrich	
Chloroform	$CHCl_3$	Sigma-Aldrich	99
Sodium hydroxide	NaOH	Panreac	98
Hexane	C_6H_{14}	Sigma-Aldrich	95
Tetrahydrofuran (THF)	C_4H_8O	Sigma-Aldrich	99
Acetic acid	CH_3COOH	Sigma-Aldrich	99
Chitosan	$(C_6H_{11}NO_4)_n$	Sigma-Aldrich	-
Sodium sulphate	Na_2SO_4	Sigma-Aldrich	99
Potassium thiocyanate	K(SCN)	Sigma-Aldrich	99
Fibroin	$(C_{15}H_{23}N_5O_6)_n$	-	-
Hydrochloric acid	HCl	Panreac	37
Sodium	$C_{26}H_{44}NNaO_7S$	Sigma-	

taurocholate		Aldrich	
Sodium chloride	NaCl	Sigma-Aldrich	99.5
Potassium chloride	KCl	Sigma-Aldrich	99
Potassium phosphate monobasic	KH_2PO_4	Sigma-Aldrich	99
Sodium phosphate dibasic	Na_2HPO_4	Sigma-Aldrich	98
Maleic acid	$C_4H_4O_4$	Sigma-Aldrich	99
Potassium ferricyanide	$C_6N_6FeK_3$	Sigma-Aldrich	99
Glucosamine	$C_6H_{13}NO_5$	Sigma-Aldrich	98
n-propanol	C_3H_8O	Sigma-Aldrich	98
Ammonium hydroxide	NH_4OH	Sigma-Aldrich	29
Ninhidrin	$C_9H_6O_4$		100
Nile Red	$C_{20}H_{18}N_2O_2$	Sigma-Aldrich	100
Rhodamine b isothiocyanate	$C_{29}H_{30}ClN_3O_3S$	Sigma-Aldrich	Mixed isomers
Methanol	CH_3OH	Panreac	98
Tween® 20	$C_{58}H_{114}O_{26}$	Sigma-Aldrich	-
(3-(4,5-dimethylthiazol-2-yl)-2,5-diphenyl tetrazolium bromide (MTT)	$C_{18}H_{18}BrN_5S$	Invitrogen	-
Triton X100	$C_{14}H_{22}O(C_2H_4O)_n$(n=9-10)	Supelco	-
Dimethyl sulfoxide (DMSO)	C_2H_6OS	Sigma-Aldrich	98
Paraformaldehyde (PFA)	$OH(CH_2O)_nH$	Sigma-Aldrich	95
Glycine	$C_2H_5NO_2$	Sigma-Aldrich	99
4',6-diamidino-2-phenylindole (DAPI)	$C_{16}H_{15}N_5$	Sigma-Aldrich	-
Phalloidin rhodamine (phRh)	$C_{35}H_{48}N_8O_{11}S$	Life technologies	-
Nitric acid	HNO_3	Panreac	65
Hydrogen peroxide	H_2O_2	Panreac	30

Dextran blue	$(C_6H_{10}O_5)_n$	Sigma-Aldrich	100

Appendix III

APPENDIX III. Manufacturer Manuals

In the third appendix, the suppliers manuals followed to perform the LDH, oxidative stress and IL-8 analysis described in the forth chapter are shown.